EIDESSTATTLICHE ERKLÄRUNG

Ich erkläre an Eides statt, dass ich die vorliegende Arbeit selbstständig verfasst, andere als die angegebenen Quellen/Hilfsmittel nicht benutzt, und die den benutzten Quellen wörtlich und inhaltlich entnommenen Stellen als solche kenntlich gemacht habe. Das in TUGRAZonline hochgeladene Textdokument ist mit der vorliegenden Dissertation identisch.

_____	_____
Datum	Unterschrift

Für meine Familie

Danksagung

An dieser Stelle mochte ich mich bei allen Menschen bedanken, die mich während der gesamten Zeit meines Studiums und meiner Doktorarbeit so großartig unterstütz haben.

Mein besonderer Dank gilt Herrn Ass.-Prof. Dr. Stefan Spirk und Em. Univ.-Prof. Dr. Franz Stelzer, für Ihrer großartigen Betreuung während des Verfassens dieser Doktorarbeit. Des Weiteren möchte ich mich bei Ihnen für die interessanten Gespräche, sowie für die Möglichkeit meine Forschungsergebnisse auf zahlreichen internationalen Konferenzen präsentieren zu können, bedanken.

Außerdem möchte ich mich bei all meinen ArbeitskollegenInnen für tolle Zusammenarbeit in den letzten 3 Jahren bedanken. Mein besonderer Dank gilt dabei meinen Kollegen aus den AG Spirk und AG Slugovc Kati, Mani, Kathrin, Mathias, Michi, Wolfgang, Michael, Chrisi, Betti, Alexej und Simone für ihre ständige Hilfsbereitschaft und den Spaß den wir jeden Tag miteinander hatten.

Mein Dank gilt außerdem meinen StudienkollegenInnen mit denen ich in den letzten 8 Jahren eine wunderbare Zeit verbracht habe und welche Zeit hatten mich auf andere Gedanken zu bringen,wenn mir die Arbeit zu viel wurde.

Des Weiteren möchte ich mich bei Prof. Karin Stana-Kleinschek und Prof. Eero Kontturi bedanken, dass sie mich in Ihren Arbeitsgruppen so herzlich aufgenommen haben und mir mit Rat und Tat bei meinen Problemen zur Seite gestanden sind. Dies gilt auch für die Kollegen Ihrer AGs Rupert, Silvo und Matej bzw. Minna und Tekla.

Weiters möchte ich mich bei Birgit Ehmann und Josefine Hobisch für Ihre Hilfe im Labor und bei den diversen Messungen bedanke.

Bei Prof. Roland Resel, Dr. Harald Pichler, Dr. Wolfgang Fischer, Jürgen Sattelkow, Sandra Moser und speziell Prof. Harald Plank möchte ich mich bedanken mir diverse Messmethoden näher gebracht zu haben und diese im Rahmen von Kooperationen verwenden zu dürfen.

Abstract

This dissertation is devoted to a broad field of cellulose research ranging from fundamental research on the macromolecular structure to the development of new applications based on cellulose supports.

The first part deals with a a comprehensive review article summarizing the research activities on deuteration of cellulosic materials. Deuteration of cellulose has been employed to obtain information on the accessiblility, function and structure of this biopolymer. Moreover, this article is a theoretical preliminary work for further experiments in this disseratation which are described directly after the review.

The second part aims at a better understanding of the interaction behavior between cellulose and water vapor. As model systems for regenerated cellulose, amorphous cellulose thin films, have been used and the impact of different physical treatments on the response in dependence of the humidity level was investigated. These processes were investigated in real time with XRR and QCM-D to obtain information about changes of the thickness, roughness, and electron density of the films.

In the third part, hyrbid materaisl have been syntehsized using trimethylsilyl cellulose thin films which acted as matrix material for the *in-situ* synthesis of Bi_2S_3 or $CuInS_2$ nanoparticles. These thin hybrid layers were characterized (e.g GI-SWAXS, ATR-IR, TEM, AFM) and further tested for their application in optoelctronical devices .

In the fourth chapter, TMSC derived films were exploited to develop a detection platform for terpenoids using Nile red as dye.

In the last part of the thesis, papers as coauthors were appended.

Einleitung

Diese Doktorarbeit beschäftigt sich mit einem breit gefächerten Bereich der Celluloseforschung beginnend bei der Grundlagenforschung über die makromolekularen Strukturen und der Entwicklung von auf Cellulose basierenden Anwendungen.

Der erste Teil ist ein Review Artikel und beschäftigt sich mit der Deuterierung von Cellulose zum Zweck der Analyse von Zugänglichkeit, Funktion bzw. Strukturzusammensetzung. Des Weiteren stellt der Artikel eine Einführung für die folgende Forschungsarbeit dar, welche im Anschluss beschrieben wird.

Im zweiten Teil wurde der Einfluss von steigender relativer Feuchte auf amorphe Cellulosefilme untersucht. Die Filme stellen ein Modell für regenerierte Cellulose dar und wurden vor den Experimenten mittels Quellung und Trocknung behandelt um Phänomene aus der Natur und Industrie zu simulieren. Durch die Behandlung resultierenden Effekte wurden mittels XRR und QCM-D in Echtzeit beobachtet um mögliche Änderungen der Schichtdicke, Oberflächenrauigkeit und Elektronendichte festzustellen.

Im Bereich der angewandten Celluloseforschung wurde Trimethylsilylcellulose als Matrixmaterial für die In-Situ Synthese von Bi_2S_3 bzw. $CuInS_2$ Nanopartikeln verwendet. Diese dünnen Hybridschichten wurden vollständig charakterisiert und als optoelektronische Anwendung getestet (z.B. TMSC/$CuInS_2$ in einer Solarzelle).

Im letzten Teil der Arbeit wird gezeigt, dass Cellulose bzw. dessen Derivate in Verbindung mit dem Farbstoff Nil Rot als Detektionsblatten für Terpene verwenden werden kann.

Zusammenfassend stellt diese Doktorarbeit einen eleganten Übergang zwischen grundlegender und angewandter Forschung dar.

List of Abbreviations

AFM	atomic force microscopy
ATR-IR	attenuated total reflectance infrared spectroscopy
$Cell_A$	microcrystalline cellulose
$Cell_S$	Spruce cellulose
$CDCl_3$	deutero-chloroform
$CHCl_3$	chloroform
D_2O	deuterium oxide
DCl	deuterium chloride
H_2O_2	hydrogen peroxide
H_2SO_4	sulphuric acid
HCl	hydrochloric acid
RH	relative humidity
SAXS	small angle X-ray scattering
TEM	transmission electron microscope
THF	tetrahydrofuran
TMSC	trimethylsilyl cellulose

QCM-D   quartz crystal microbalance and dissipation

WAXS   wide angle X-ray scattering

%wt   weight percentage

XRR   X-ray reflectivity

List of Publications

First author:

I. Reishofer David and Stefan Spirk. *Cellulose Chemistry and Properties: Fibers, Nanocelluloses and Advanced Materials*. Springer International Publishing, **2015**. 93-114.

II. David Reishofer, Jürgen Sattelkow, Wolfgang J. Fischer, Heinz Amenitsch, Katrin Niegelhell, Harald Plank, Roland Resel, Tekla Tammelin, Eero Kontturi, Stefan Spirk, Submitted to *Biomacromolecules*, **2016**

III. David Reishofer, Heike M. Ehmann, Heinz Amenitsch, Christian Gspan, Roland Fischer, Harald Plank, Gregor Trimmel, Stefan Spirk, Submitted to *Carbohydrate Polymers*, **2016**

IV. David Reishofer, Thomas Rath, Heike M. Ehmann, Heinz Amenitsch, Christian Gspan, Sebastian Dunst, Harald Plank, Alonso Bruno, Emmanuel Belamie, Gregor Trimmel, Stefan Spirk, Submitted to *ACS Sustainable Chemistry & Engineering*, **2016**

Co-author:

V. Mohan, T.; Rathner, R.; Reishofer, D.; Koller, M.; Elschner, T.; Spirk, S.; Heinze, T.; Stana-Kleinschek, K.; Kargl, R. *Biomacromolecules* **2015**, *16*, 2403–2411.

VI. Elschner, T.; Reishofer, D.; Kargl, R.; Grießer, T.; Heinze, T.; Kleinschek, K. S. *RSC Adv.* **2016**, *6*, 72378–72385.

VII. Ganner, T.; Sattelkow, J.; Rumpf, B.; Eibinger, M.; Reishofer, D.; Winkler, R.; Nidetzky, B.; Spirk, S.; Plank, H. *Sci. Rep.* **2016**, 1–11.

Herein, the contributions as first-author to the following publications are described.

I.   Deuterium and Cellulose – A Comprehensive Review

   • David Reishofer was responsible for the literature research and wrote the review
     article together with Stefan Spirk.

II. Tuning the Humidity Response of Two Dimensionally Confined Biopolymer Thin
     Films

   • David Reishofer was responsible for the experimental work, and analyzed the
     corresponding results. The manuscript was written in cooperation with the co-
     authors. The AFM images were recorded by Jürgen Sattelkow.

III. Study on the Formation of Bi_2S_3-Cellulose Nanocomposite Films from Bismuth
     Xanthates and Trimethylsilyl-Cellulose

   • David Reishofer was responsible for the experimental work, and analyzed the
     corresponding results. The manuscript was written in cooperation with the co-
     authors. The TEM images were recorded by Christian Gspan.

IV. Biobased Nanocomposites for Optoelectronic Applications

   • David Reishofer was responsible for the experimental work, and analyzed the
     corresponding results. The manuscript was written in cooperation with the co-
     authors. The TEM images were recorded by Christian Gspan and the solar cell
     prepared by Sebastian Dunst.

Herein, the contributions as co-author to the following publications are described. The full version of the manuscripts can be found in the appendix.

V.   Designing Hydrophobically Modified Polysaccharide Derivatives for Biocatalytic Applications

- David Reishofer was responsible for AFM measurements and result interpretation.

VI.   Reactive cellulose-based thin films – a concept for multifunctional polysaccharide surfaces

- David Reishofer was responsible for AFM measurements and result interpretation.

VII.   Direct-Write Fabrication of Cellulose Nano Structures via Focused Electron Beam Induced Nanosynthesis

- David Reishofer was responsible for ATR-IR measurements and result interpretation.

Table of Contents

Introduction

Cellulose is one of the most important renewable resources and nowadays used in a very broad context in both, industry and academia. Cellulose is the primary ingredient of wood plants and obtainable around the whole world. Therefore, it can be designated as one of the most influential materials in the history. For many centuries in mankind it was predominantly used for housing, for heating, clothing (textiles from cotton, hemp or flax) or from conserving cultural heritage. Nevertheless, in the last decades cellulose has been becoming again an interesting research object. In this context, the industry started to collaborate more intensive with the academia to get deeper into the matter for obtaining answers about problems during the manufacturing processes. Moreover, the academic world recognized the high potential of cellulose and correlated synthesized derivatives. Thereof, beside a various number of new developed applications the cellulose fundamental research made a major step forward. Nowadays, cellulose is used commercially as fibers, membranes, hygienic products, papers and in life science applications. Cellulose is also utilized for polymer blends, photolithographic patterning or immobilization of biomolecules in order to tune, for example, protein adsorption, attachment of biomolecules and creation of multi-functional polysaccharide based materials.

In this context, this dissertation concerns with new aspects in fundamental and applied cellulose research.

Chapter 1

## 1. State of the Art

1.1 Cellulose

1.1.1 Structure

Cellulose, discovered and coined by the French chemist Anselme Payen in 1838, is the most abundant biopolymer on earth.[1] It is composed of several hundred to thousands chair-conformed anhydro–β-D-glucopyranose units (AGU; $(C_6O_5H_{10})_n$) which are linked together by $(1\rightarrow4)$ glycosidic bonds to form the final polymer chain (see Figure 1.1.1). Furthermore, each polymer chain features a non-reducing end and a reducing end. In this configuration cellulose is the major component in the cell wall of plants ($\geq 50\%$) and some algae.

Non-Reduced End Group   **Reduced End Group**

Anhydroglucose; AGU
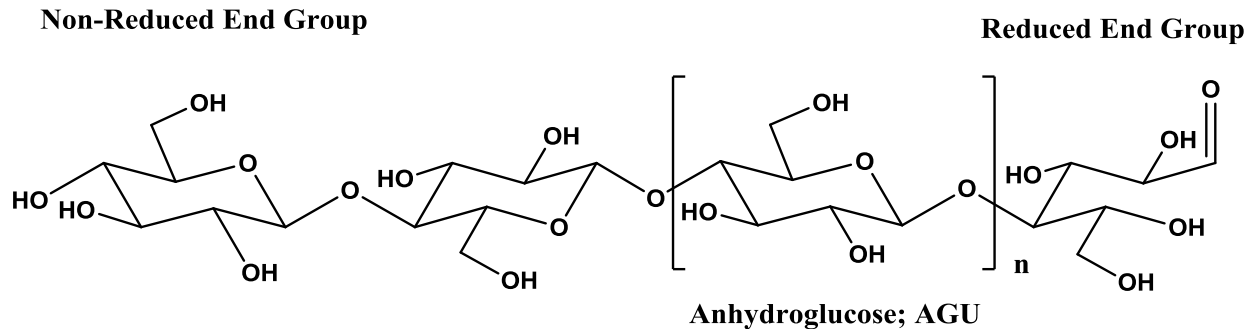
Figure 1.1.1. Molecular structure of cellulose.

The rigid $(1\rightarrow4)$ glycosidic bonds, the degree of polymerization (DP) and the hydrogen bonding network determine the character of the cellulose. Therefore, the supramolecular structure of cellulose comprises interactions of crystalline and amorphous regions in the solid state. The degree of polymerization depends on the source of the cellulose and the processing steps during the isolation. For example cotton or bacterial cellulose have DP values in the range of 800-10000, wood pulp from 300-1700 and regenerated cellulose fibers exhibit DPs of ca. 250-500. Already

20–30 (1→4) glycosidically linked glucose monomers offer most of the properties of cellulose.[2] Moreover, cellulose chains can stack parallel to form elementary fibrils that further aggregate into larger microfibrils (5–50 nm in width) to be the main reinforcement phase for plants, trees, algae, and bacteria (see Figure 1.1.2).
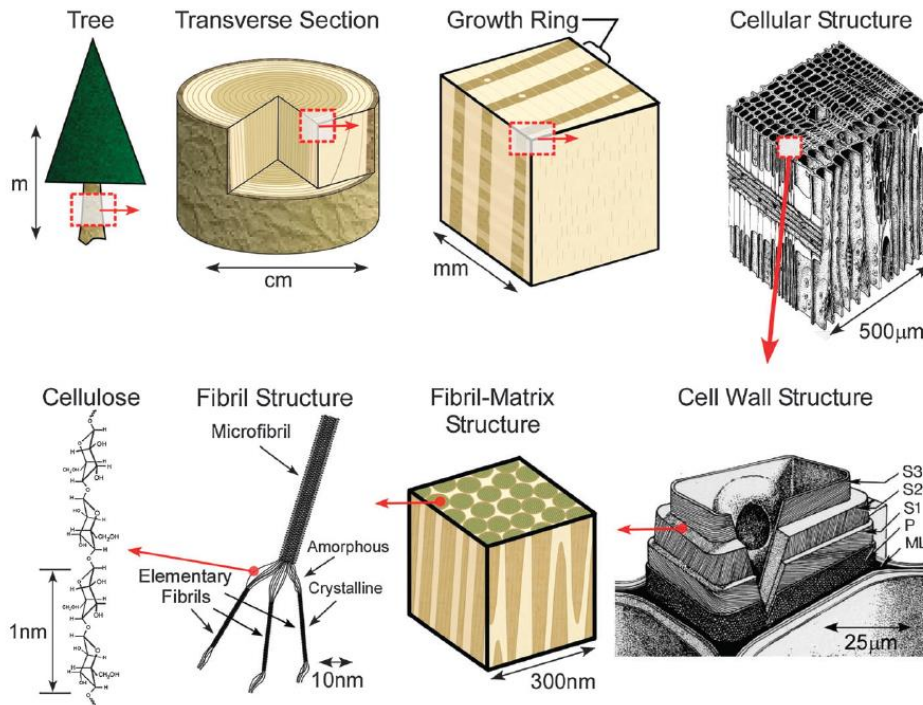
Figure 1.1.2. Schematic of the tree hierarchical structure.[3]

Cellulose shows amphiphilic character, since both hydrophobic and hydrophilic intercations are present. Therefore, cellulose is insoluble in water and the most organic solvents, for that reason special combination of solvents (e.g. lithium chloride/dimethylacetamide or ionic liquids) have to be used for dissolution of cellulose. All three hydroxyl groups in the positions C2, C3 (both secondary, equatorial), and C6 (primary) are involved in the above mentioned hydrogen bonding network. The possibility of various inter- and intramolecular hydrogen bonding of the crystalline cellulose leads to four different polymorphs, namely cellulose I, II, III, and IV. Native cellulose I occurs in nature and is a mixture of two allomorphs.[4] To obtain cellulose II, the thermodynamically most stable crystalline forms, cellulose I_α and I_β have to be recrystallized or mercerized with aqueous sodium hydroxide.[5] With a further liquid ammonia treatment cellulose I or II can be transformed into Cellulose III_I and III_{II} (see Figure 1.1.3).
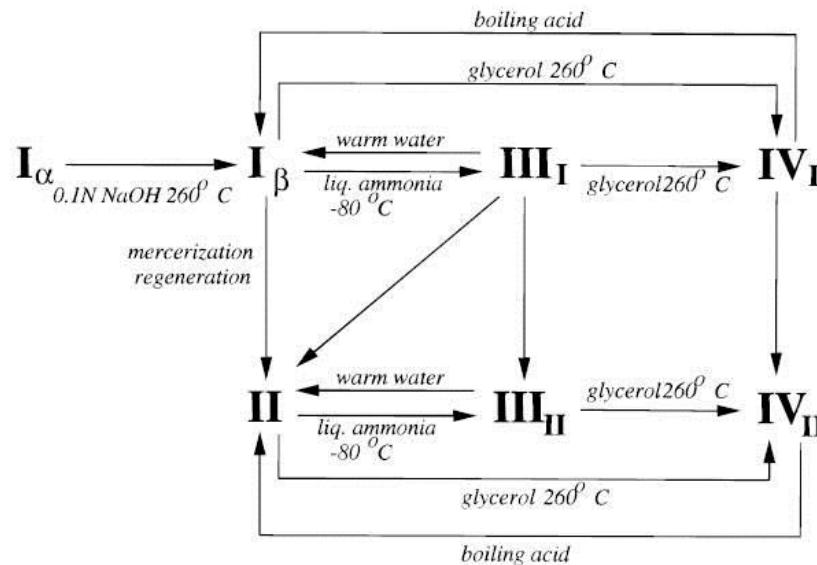
Figure 1.1.3. Polymorphism of cellulose.[6]

Furthermore, cellulose IV is a result from heating cellulose III[7] however recent reports consider it as disordered form of the cellulose I phase. Compared to amorphous cellulose, the different crystalline polymorphs exhibit low diffusion accessibility due to their strong hydrogen bonding network. A more detailed description of the differences between the polymorphs is shown from page xx –xx.

1.1.2 Cellulose Thin Film Preparation

Cellulose and biopolymer thin films in general can be used for many different purposes. Potential applications range from interaction studies using proteins, enzymes, surfactants and polymers to simulation of effects in nature or industrial processes to the preparation of new hybrid materials. Furthermore, cellulose thin films have also been used as moisture sensors, in wetting studies,[8] organic-inorganic hybrid materials[9] and in catalysis research.[10] To analyze these well-defined model surfaces different interfacial characterization methods are available. These are for example stylus profilometer,[11] atomic force microscopy (AFM),[12] surface force apparatus quartz crystal microbalance with dissipation (QCM-D)[8] and surface plasmon resonance (SPR)[13]. Depending on the application, cellulose thin films have to fulfill certain requirements like surface

roughness or film thickness for the above mentioned applications and related characterization methods. As mentioned in the previous section, the supramolecular structure of cellulose is rather complex. There are a variety of methods to prepare such thin films. Beside Langmuir–Blodgett (LB) and Langmuir Schaefer deposition,[14] cellulose thin films have been prepared mostly by spin-coating.[15] Cellulose samples prepared by these two established methods lead, to thin and smooth films under the right condition (e.g. solvent). A distinction can be drawn between the preparation of films directly (i.e. by dispersion of cellulose) and readily soluble cellulose derivatives which are regenerated after the processing step to cellulose. Furthermore, thin films can be divided into open films and closed films where the substrate is completely covered by the cellulose.

1.1.3   Direct preparation of cellulose films

In the first section, the amphiphilic character and inter- and intra-molecular hydrogen bonds which are responsible for the poor solubility were already described which further disable the usage of standard organic or aqueous solvents. Therefore, one of the most common solvents for the non-derivatizing dissolution of cellulose is a N-methylmorpholine-N-oxide (NMMO) water mixture (1:1).[16] As a result of the strong N-O dipoles, NMMO is able to destroy the cellulose inter-molecular hydrogen bonds above 85°C, further leading to dissolution.[17] Furthermore, lithium chloride/dimethylacetamide is a well-established, non-derivatizing solvent combination for the dissolution of cellulose. Moreover, LiCl/DMAc is non-aqueous and can dissolve different cellulose types without significant degradation but requires heating (ca 100°C) during spin coating due to the high boiling point of DMAc.[18,19] As an example, in the literature it is reported that LiCl/DMAc can dissolve molecular weight of cellulose above 1.000.000 g*mol[-1] without noticeable degradation at ambient temperature.[20] Aulin et al.[21] used NMMO and LiCl/DMAc as solvents for the preparation of cellulose thin films by spin coating and Langmuir-Schaefer onto oxidized silicon wafers. These films were then analyzed with AFM and XRD to determine the surface roughness, morphology and degree of crystallinity. Moreover, the interaction with water was examined by QCM-D. Figure 1.1.4 shows the images and the height profiles of the AFM measurements.
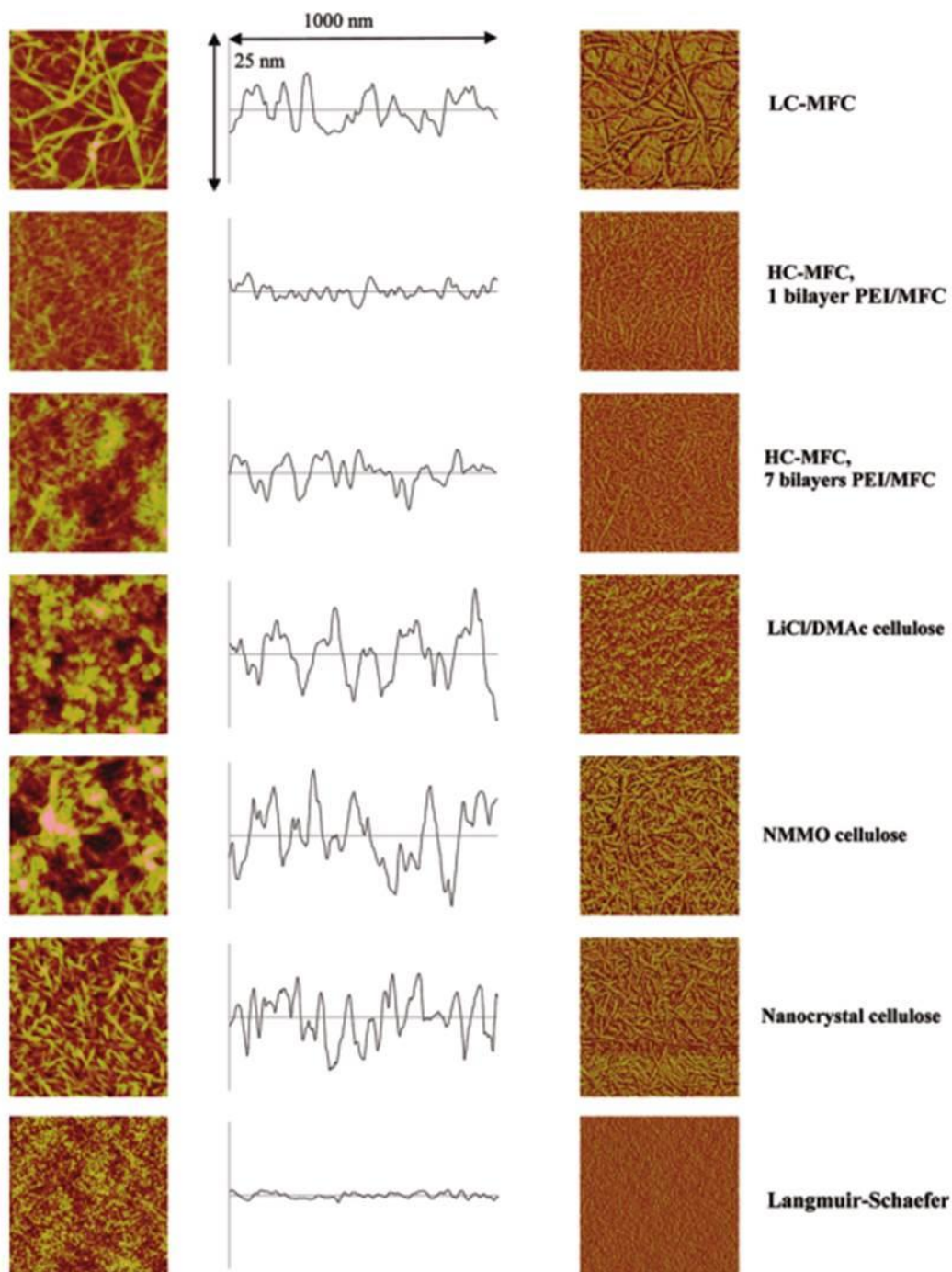
Figure 1.1.4. AFM tapping mode phase (right) and height (left) images of the cellulose films on silicon wafers. Image size 1 x 1 μm^2; z-ranges: 25 nm for nanocrystal surfaces, LC-MFC, and HC-MFC; 40 nm for the NMMO and LiCl/DMAc surfaces; 3 nm for the LS surfaces. Typical height profiles are shown in the middle, all with a z range of 25 nm.[21]

The NMMO as well the LiCl/DMAc and LS prepared cellulose model films revealed smooth surfaces with a RMS of approximately 0.4 – 6.2 nm. Furthermore, the LiCl/DMAc films had a very low degree of crystallinity (<15%) determined by XRD compared to the other films. The measurement of the water interaction by QCM-D correlates with the XRD results and proves the amorphous character of the LiCl/DMAc. Accordingly, the NMMO and LS-deposited samples had a lower degree of swelling due to their higher crystalline character.

Beside the above described solvents also ionic liquids,[22,23] NaOH aqueous solutions[24] and NaOH–urea aqueous solutions[25] have been exploited as solvents for the dissolution and film preparation of cellulose. A disadvantage is that after the spin coating the films have to be washed with water to remove solvent residues. Moreover, the cellulose/solvent mixture has to be heated during the preparation. Another option is the usage of cellulose nanocrystals (CNC),[26] macrofibrillated cellulose (MFC)[27] and nanofibrillated cellulose (NFC)[28] in aqueous suspension.

1.1.4 Indirect preparation of cellulose films

In the recent years the preparation of cellulose thin films has been also performed by using soluble cellulose derivatives which are converted back to cellulose after the processing step. This approach is a more elegant way to prepare such films. The hydroxyl groups of the cellulose are (partially) derivatized leading to increased solubility in common solvents. To obtain water-soluble derivatives the cellulose can be modified with a charged substituent like carboxymethyl groups for example but without the opportunity of conversion. The common point for all derivative systems is the reversibility of the initial reaction (e.g. regeneration to cellulose) which must be relatively straightforward. However, this would be possible with cellulose acetate and liquid NaOH.[29] All these modifications of cellulose are already discussed in extensive reviews.[19,30]

The most important derivative for indirect preparation of cellulose model films is trimethylsilyl-cellulose (TMSC). Trimethylsilyl-cellulose can be relatively easy synthesized by using hexamethyldisilazane (HMDS) as reactant and ionic liquids as solvent.[31,32] The solubility of this derivative can be tuned over a wide range depending in its degree of siubstitution. At high DS

values it dissolves well in common organic solvents, such as toluene, chloroform or THF.[33] The first TMSC thin films (DS: 2.7) have been reported by Klemm in 1993.[34] The paper describes the preparation using the Langmuir-Blodgett (LB) technique on hydrophobic substrates and the regeneration to cellulose by 10 wt% HCl vapor (Figure 1.1.5).
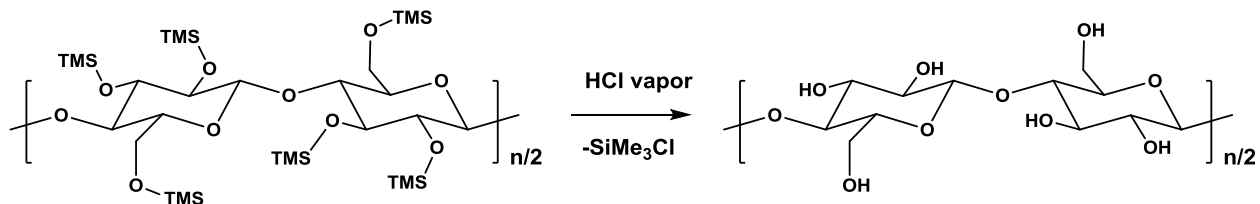
Figure 1.1.5. Regeneration of TMSC to cellulose with HCl vapor.

Therefore, compared to other derivatives like cellulose acetate (regenerated by KOH solution) this method works without any detrimental interaction of liquid. The reported films had a film thickness of approximately 7.8 nm with surface roughnesses of ca 0.8 nm. Moreover, the films lost 60% of their initial thickness during the desilylation and the surface water contact angle decreased from approximately 90° to 35°.

Publications in the following years showed that the thickness of TMSC films is tunable between approximately 5-50 nm.[13,35] In 2000, Geffroy et al.[36] were the first to use spin coating instead of LB to prepare TMSC films but the work of Kontturi et al[37,38] advanced this technique to a powerful tool. Kontturi et al. investigated the influence of different solvents, substrates and the spin coating parameters (e.g. acceleration) on the film thickness, roughness and morphology by AFM (Figure 1.1.6).
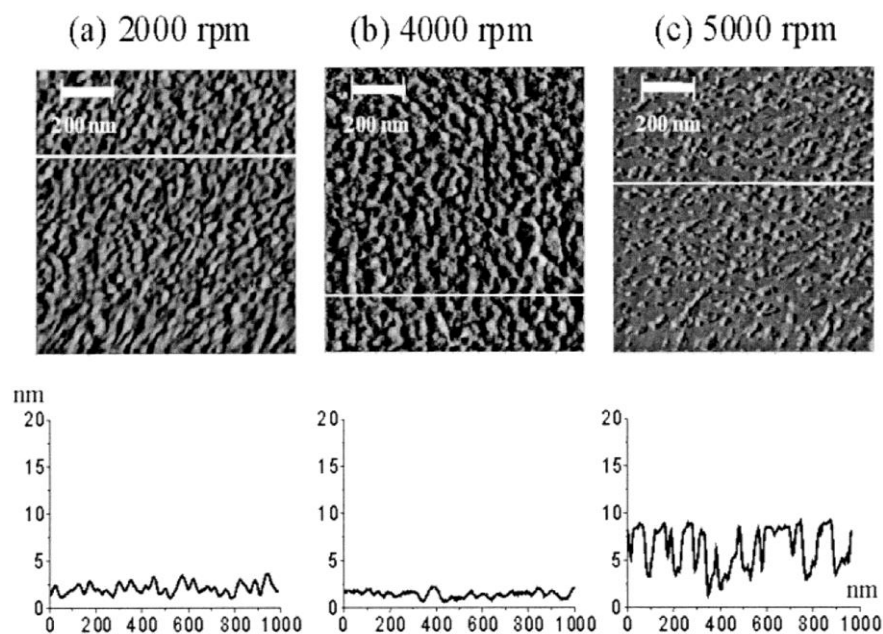
Figure 1.1.6. AFM images of Konturri et al.[37] for hydrolyzed TMSC samples with varying spinning speed during spin coarting.

Furthermore, the samples were analyzed by XPS, ATR-IR and ellipsometry to monitor the purity and regeneration process. Compared to Langmuir–Blodgett the preparation of cellulose thin films by spin coating is faster and leads to amorphous films[39] and a higher degree of reproducibility. However, the LB-deposition leads to a lower surface roughness for thin films (> 20 nm).[34]

Moreover, in the recent years also the desilylation process of the TMSC was investigated in a more distinguished way to understand the obtained cellulose films better. The first step was done by Woods et al.[40] and their usage of TIR Raman spectroscopy to monitor the kinetics during the regeneration process. The authors revealed that the process proceeds in two steps; a fast removal for the first phase is followed by a slower kinetic for the second phase. In contrast Kontturi et al employed ex-situ measurements using XRR and only one rate constant could be detremiend. These results were proven by Mohan et al.[41] using a gravimetric detection method (QCM-D) and HCl vapor instead of liquid. Ehmann et al.[42] investigate the mechanism of the HCl vapor induced conversion on a supramolecular structure level by GI-SAXS. They showed that the correlation length first increases during the regeneration until the conversion to cellulose is complete. This could be explained with remaining voids from the cleaved off trimethylsilyl-groups. However, at

the same time, these voids are partly closed by hydrogen bonding leading to the shrinkage of the cellulose film. Additionally, the authors showed that the cellulose chains start to hydrolyze if the material is exposed to hydrochloric acid for a longer period of time (40 minutes). This process decreased the correlation length of film due to higher mobility of the cellulose chains and caused rearrangements of the films.

The development of these preparation systems for cellulose thin film and also other biopolymers led to several applications and new research fields (see Chapters 4, 5 and 6). Moreover, these techniques allow for the interpretation of chemical changes in cellulosic materials and the supramolecular structure on a basic level where other effects (morphology, accessibility etc.) of real samples are cancelled out.

1.1.5   Cellulose water interaction in thin films

The interaction of cellulose and water is an important issue for the understanding of natural and industrial processes.[43] Especially, for the processing and manufacturing industry of papers and fibers the swelling and drying behavior of the material is an important aspect in correlation to the costs and properties of the final product. Therefore, these processes have been the subject of many studies.[44,45] Fundamental studies concerns with naturel aspects like the transport of the water in the cell wall or water vapor adsorption behavior of a cell wall.[46–48] These studies are very sophisticated do to the complexity of structural hierarchy of wood plants. Mostly, the investigations in these fields were done with fibers and pulp material but also LB-deposit or spin coated films were analyzed. The absorption is affected by the accessibility of hydroxyl-groups, for that reason amorphous cellulose is available for swelling compared to crystalline regions. Therefore, the degree of crystallinity is important for the investigated process. The crystallinity of cellulose films can be tuned by the chosen cellulose source or by doping of amorphous cellulose with various materials (e.g. nanocrystals).[47] In this context Driemaier et al. showed a linear relation (R^2 = 0.98) between monolayer hydration and reciprocal crystallite width.[48] The advantage of thin films as testing system is that they can be treated (e.g. heat treatment) and characterized easily in different ways to simulate the above mentioned processes. Neuman et al.[49]

were the first who reported the swelling behavior of cellulose thin films. The disadvantage of the produced films and furthermore of the study was that the authors used trifluoroacetic acid (TFA) which interacts with the cellulose. Nevertheless, they showed that the films did swell in aqueous solutions. Afterwards, Holmberg et al.[35] were able to use the more stable LB produced films to demonstrate the swelling of cellulose in water. For the monitoring of the swelling degree the authors used surface force apparatus (SFA) and ellipsometry. The effect of the pH value of aqueous solutions and the charge density of the cellulose on the degree of swelling was demonstrated by Österberg and Claesson.[50] The most important study in early 2000er was carried out by Rehfeldt and Tanaka[51] who investigated the hydration force as a function of the deposition technique (LB-deposition vs spin coating). Moreover, they compared different films thicknesses to show whether the number of layers effects on the degree of swelling. Surprisingly, swelling ratios of 1.4-1.7 were obtained regardless to the film thickness or preparation method. Additionally, the paper reports the swelling kinetics of the films and showed a fast swelling ($\tau = 14$ s). The first time QCM-D was used for the monitoring of swelling processes was done by Fält et al.[8] This was an advantage for further investigations on the swelling behavior of cellulose and other biopolymers due to the simple handling. This study concentrated on swelling and de-swelling ability of the cellulose films, depending on the charge density, electrolyte concentration, pH and different electrolytes. Tammelin et al.[52] used similar films as Holmberg et al.[35] and investigated the samples by QCM-D to compare the results with the work of Fält et al.[8] The results of the studies revealed that for low charge density the samples do not swell and deswell during the procedure. Moreover, the films showed a layer softening and only a slight water binding capability. Aulin. et al.[21] prepared samples out of regenerated cellulose and nanocrystalline cellulose (NC) and analyzed them by QCM-D. In comparison, Kontturi et al.[53] investigated fully amorphous cellulose samples before and after drying with GIXD. The results of both studies show that morphology and charge density have an effect on the water content. Furthermore, neutron reflectivity showed that the thickness doubled by taking up 86% of water in its structure during water contact.[53] The study showed that after swelling/drying the morphology, roughness and thickness remained unchanged (see Figure 1.1.7).

Figure 1.1.7. Swelling and drying of amorphous cellulose. Image from Kontturi et al.[53]

Kittle et al.[54] used D_2O/H_2O exchange in a QCM-D to demonstrate a linear relation between the water content and amount of cellulose in a film. In addition, the used procedure should be applicable to other polymer films. This linear relation was further used by Mohan et al.[44] to compare their water content values of different treated cellulose films (e.g. heat and water). Kontturi et al.[55] used the same D_2O/H_2O exchange method to investigate nanofibrillar cellulose (NFC) and the influence of charged groups like cationic polyelectrolyte or carboxymethyl cellulose (CMC). An increased charge (adsorption of CMC) led to an additional swelling of the NFC and negative charge to a decreased swelling amount. Further examples which use D_2O/H_2O exchange and the deuteration of cellulose are described from page 29 to 36 (Review).

In conclusion, cellulose thin films can be a versatile tool for simulation of swelling and drying processes in industrial and natural processes. Especially, the fundamental research helps to understand different phenomena in these fields. Chapter 3 extensive described the influence of increasing humidity to water and heat treated amorphous thin films.

1.1.6 Applications of cellulose thin films

The previous section described the wetting and drying behavior of cellulose which is important to understand phenomena in the papermaking and textile industry. Moreover, cellulose is commercially used as hygienic products, papers, fibers, membranes[56] and in life science applications.[57] The high amount of various additives which can be combined with cellulose or other biopolymers facilitates the preparation and manufacturing of a wide range of hybrid materials and related applications. Therefore, in the following a selection of applications of cellulose thin films and cellulose hybrid materials with inorganic nanoparticles is discussed.

One of the main ideas in this area is to use cellulose thin films as supports for the detection of biomolecules. In this way either patterned ort non-patterned materials have been prepared and equipped with a variety of biomolecules (proteins, DNA, polysaccharides). For some examples[58,59] fully working biosensors have been reported. In different contexts patterned cellulose materials have been reported, macroscopic and microscopically patterned materials have been reported by Spirk[60] and Kargl.[61] Furthermore, Wolfberger et al.[62,63] used photoacid induced desilylation reaction of TMSC to prepare films with sub-micron sized features by photo lithography. Moreover, these films were used as dielectric gate materials in OTFTs with rather good performance. Even smaller structures can be obtained by FIB (down to 70 nm) as reported by Ganner et al.[64]

Another option to create cellulose structures is phase separation by polymer blending. Polymer blends are bicomponent films which generate different surface morphologies by phase separation. These films can then be used in optics (antireflective coating), electronics or biotechnology like cell scaffolds and microarrays. In the literature combinations of TMSC/CTA (useful in emerging nanotechnologies),[65] TMSC/PMMA (for pore size tuning by ratio of polymers)[66] and TMSC/PS (exchange of PS with other polymers to obtain various chemical functionalities) have been reported.[67] A recent example also investigated the effect of enzymes to act as biodevelopers on PHB/cellulose films.[68]

As mentioned above, cellulose thin films can be used as models for processes in nature. In this context Martín-Sampedro et al.[69] analyzed the influence of lignin on enzymatic hydrolysis of

cellulose by QCM-D. The adsorption of different cellulases onto cellulose with varying lignin content is useful to elucidate effective pretreatments for enzymatic hydrolysis in order to obtain cost-effective methods for bioconversion of cellulose.[70] Strasser et al. prepared films from hydrophilic cellulose und hydrophobic lignin esters, to investigate the interaction of these lignocellulosics films and proteins in order to gain better insight into complex interaction of polysaccharides, lipids and proteins in plant cell walls.[71] Furthermore, these films can be functionalized or used for immobilization of biomolecules in order to tune protein adsorption, develop bioanalytical devices, microarrays, controllable attachment of biomolecules, creation of multi-functional polysaccharide based materials, basis for further development in biosensor development or engineering of diverse polysaccharide surfaces.[58,72–75]

Moreover, the usage of cellulose or other biopolymers as matrix material for different inorganic nanoparticles became more common but is still a minor field. In this context often used nanoparticles are titanium dioxide,[76–79] bismuth,[80] silver,[26] gold[81] or iron.[82] Furthermore, it was possible to biosynthesise bacterial cellulose in the presence of inorganic nanoparticles.[83] These hybrid materials are used as electronicdevices, antifouling materials or photocatalysts. The in-situ synthesis of Bi_2S_3 and $CuInS_2$ nanoparticles in a TMSC matrix and further usage as hybrid material is extensively described in chapter 4 and chapter 5.

1.1.7 References

(1)   Payen, A. *Comptes rendus* **1838**, *7*, 1052–1056.

(2)   Kobayashi, S.; Sakamoto, J.; Kimura, S. *In vitro synthesis of cellulose and related polysaccharides*; 2001; Vol. 26.

(3)   Moon, R. J.; Martini, A.; Nairn, J.; Simonsen, J.; Youngblood, J. *Cellulose nanomaterials review: structure, properties and nanocomposites*; 2011; Vol. 40.

(4)   Atalla, R. H.; Van der Hart, D. **1965**, *5*, 5–8.

(5)   Andress, K. R. *Z. Phys. Chem.* **1929**, *4*, 190.

(6)   Kroon-Batenburg, L. M. J.; Bouma, B.; Kroon, J. *Macromolecules* **1996**, *29*, 5695–5699.

(7)   Hayashi, J.; Sufoka, A.; Ohkita, J.; Watanabe, S. **1995**, *16*, 23–27.

(8)   Fält, S.; Wagberg, L.; Vesterlind, E. L. *Langmuir* **2003**, *19*, 7895–7903.

(9)   Naka, K.; Chujo, Y. *Chem. Mater.* **2001**, *13*, 3245–3259.

(10)   Libuda, J.; Freund, H.-J. *J. Phys. Chem. B* **2002**, *106*, 4901–4915.

(11)   Williamson, J. B. P. *Proc. Inst. Mech. Eng.* **1967**, *182*, 21.

(12)   Kontturi, E.; Johansson, L.-S.; Kontturi, K. S.; Ahonen, P.; C, T. P.; Laine, J. *Langmuir* **2007**, *23*, 9680.

(13)   Buchholz, V.; Wegner, G.; Stemme, S.; Odberg, L. *Adv. …* **1996**, *8*, 399–402.

(14)   Roberts, G. G. *Langmuir-Blodgett Films*; Plenum Press: New York, 1990.

(15)   Larson, R. G.; Rehg, T. Kistler, S. F., Schweizer, P. M., Eds.; Chapman & Hall: London, 1997.

(16)   Fink, H.-P.; Weigel, P.; Purz, H. J.; Ganster, J. *Prog. Polym. Sci.* **2001**, *26*, 1473–1524.

(17)   Gagnaire, D.; Mancier, D.; Vincendon, M. *J. Polym. Sci. Polym. Chem. Ed.* **1980**, *18*, 13–25.

(18)   Eriksson, J.; Malmsten, M.; Tiberg, F.; Callisen, T. H.; Damhus, T.; Johansen, K. S. *J. Colloid Interface Sci.* **2005**, *284*, 99–106.

(19)   Heinze, T.; Liebert, T. *Prog. Polym. Sci.* **2001**, *26*, 1689–1762.

(20)   Matsumoto, T.; Tatsumi, D.; Tamai, N.; Takaki, T. *Cellulose* **2001**, *8*, 275–282.

(21)   Aulin, C.; Ahola, S.; Josefsson, P.; Nishino, T.; Hirose, Y.; Osterberg, M.; Wågberg, L. *Langmuir* **2009**, *25*, 7675–7685.

(22)   Kargl, R.; Mohan, T.; Ribitsch, V.; Saake, B.; Puls, J.; Kleinschek, K. S. *Nord. Pulp Pap. Res. J.* **2015**, *30*, 6–13.

(23)   Swatloski, R. P.; Spear, S. K.; Holbrey, J. D.; Rogers, R. D. *J. Am. Chem. Soc.* **2002**, *124*, 4974–4975.

(24)   Kamide, K.; Okajama, K.; Matsui, T.; Kowsaka, K. *Polym J* **1984**, *12*, 857–866.

(25)   Wang, Y. Y.; Cai, K. F.; Yao, X. *J. Nanoparticle Res.* **2012**, *14*, 848-.

(26)   Chu, G.; Yin, H.; Jiang, H.; Qu, D.; Shi, Y.; Ding, D.; Xu, Y. *J. Phys. Chem. C* **2016**,

acs.jpcc.6b09052.

(27) Siró, I.; Plackett, D. *Cellulose* **2010**, *17*, 459–494.

(28) Kontturi, K. S.; Kontturi, E.; Laine, J. *J. Mater. Chem. A* **2013**, *1*, 13655.

(29) Kargl, R.; Mohan, T.; Bračč, M.; Kulterer, M.; Doliška, A.; Stana-Kleinschek, K.; Ribitsch, V. *Langmuir* **2012**, *28*, 11440–11447.

(30) Klemm, D.; Heublein, B.; Fink, H. P.; Bohn, A. *Angew. Chemie - Int. Ed.* **2005**, *44*, 3358–3393.

(31) Kostag, M.; Köhler, S.; Liebert, T.; Heinze, T. *Macromol. Symp.* **2010**, *294*, 96–106.

(32) Cooper, G. K.; Sandberg, K. R.; Hinck, J. F. *J. Appl. Polym. Sci.* **1981**, *26*, 3827–3836.

(33) Greber, G.; Paschinger, O. **1981**, *35*, 547.

(34) Schaub, M.; Wenz, G.; Wegner, G.; Stein, A.; Klemm, D. *Adv. Mater.* **1993**, *5*, 919–922.

(35) Holmberg, M.; Berg, J.; Stemme, S.; Ödberg, L.; Rasmusson, J.; Claesson, P. *J. Colloid Interface Sci.* **1997**, *186*, 369–381.

(36) Geffroy, C.; Persello, J.; Foissy, A.; Lixon, P.; Tournilhac, F.; Cabane, B. *Colloids Surfaces A Physicochem. Eng. Asp.* **2000**, *162*, 107–121.

(37) Kontturi, E.; Thu, P. C.; Niemantsverdriet, J. W. H. *Langmuir* **2003**, *19*, 5735–5741.

(38) Kontturi, E.; Thüne, P. C.; Niemantsverdriet, J. W. *Polymer (Guildf).* **2003**, *44*, 3621–3625.

(39) Kontturi, E.; Lanklnen, A. *J. Am. Chem. Soc.* **2010**, *132*, 3678–3679.

(40) Woods, D. a.; Petkov, J.; Bain, C. D. *Colloids Surfaces A Physicochem. Eng. Asp.* **2011**, *391*, 10–18.

(41) Mohan, T.; Spirk, S.; Kargl, R.; Doliška, A.; Ehmann, H. M. A.; Köstler, S.; Ribitsch, V.; Stana-Kleinschek, K. *Colloids Surfaces A Physicochem. Eng. Asp.* **2012**, *400*, 67–72.

(42) Ehmann, H. M. a. H. M. a.; Werzer, O.; Pachmajer, S.; Mohan, T.; Amenitsch, H.; Resel, R.; Kornherr, A.; Stana-Kleinschek, K.; Kontturi, E.; Spirk, S. *ACS Macro Lett.* **2015**, *4*, 713–716.

(43) Björneholm, O.; Hansen, M. H.; Hodgson, A.; Liu, L. M.; Limmer, D. T.; Michaelides, A.; Pedevilla, P.; Rossmeisl, J.; Shen, H.; Tocci, G.; Tyrode, E.; Walz, M. M.; Werner, J.; Bluhm, H. *Chem. Rev.* **2016**, *116*, 7698–7726.

(44) Mohan, T.; Spirk, S.; Kargl, R.; Doliška, A.; Vesel, A.; Salzmann, I.; Resel, R.; Ribitsch, V.; Stana-Kleinschek, K. *Soft Matter* **2012**, *8*, 9807–9815.

(45) Zeronian, S. H. In *Cellulose Chemistry and Technology*; ACS Symposium Series; AMERICAN CHEMICAL SOCIETY, 1977; Vol. 48, pp 13–189.

(46) Niinivaara, E.; Faustini, M.; Tammelin, T.; Kontturi, E. *Langmuir* **2016**, *32*, 2032–2040.

(47) Niinivaara, E.; Faustini, M.; Tammelin, T.; Kontturi, E. *Langmuir* **2015**, *31*, 12170–12176.

(48) Driemeier, C.; Bragatto, J. *J. Phys. Chem. B* **2013**, *117*, 415–421.

(49) Neuman, R. D.; Berg, J. M.; Claesson, P. M. *Nord. Pulp Pap. Res. J.* **1993**, *8*, 96.

(50) Österberg, M.; Claesson, P. M. *J. Adhes. Sci. Technol.* **2000**, *14*, 603–618.

(51) Rehfeldt, F.; Tanaka, M. *Langmuir* **2003**, *19*, 1467–1473.

(52) Tammelin, T.; Saarinen, T.; Österberg, M.; Laine, J. *Cellulose* **2006**, *13*, 519–535.

(53) Kontturi, E.; Suchy, M.; Penttilä, P.; Jean, B.; Pirkkalainen, K.; Torkkeli, M.; Serimaa, R. *Biomacromolecules* **2011**, *12*, 770–777.

(54) Kittle, J. D.; Du, X.; Jiang, F.; Qian, C.; Heinze, T.; Roman, M.; Esker, A. R. *Biomacromolecules* **2011**, *12*, 2881–2887.

(55) Kontturi, K. S.; Kontturi, E.; Laine, J. *J. Mater. Chem. A* **2013**, *1*, 13655–13663.

(56) Sackmann, E.; Tanaka, M. *Trends Biotechnol.* **2000**, *18*, 58–64.

(57) Fragal, E. H.; Cellet, T. S. P.; Fragal, V. H.; Companhoni, M. V. P.; Ueda-Nakamura, T.; Muniz, E. C.; Silva, R.; Rubira, A. F. *Carbohydr. Polym.* **2016**, *152*, 734–746.

(58) Orelma, H.; Filpponen, I.; Johansson, L. S.; Laine, J.; Rojas, O. J. *Biomacromolecules* **2011**, *12*, 4311–4318.

(59) Mohan, T.; Ristić, T.; Kargl, R.; Doliska, A.; Köstler, S.; Ribitsch, V.; Marn, J.; Spirk, S.; Stana-Kleinschek, K. *Chem. Commun. (Camb).* **2013**, *49*, 11530–11532.

(60) Spirk, S.; Ehmann, H. M.; Kargl, R.; Hurkes, N.; Reischl, M.; Novak, J.; Resel, R.; Wu, M.; Pietschnig, R.; Ribitsch, V. *ACS Appl. Mater. Interfaces* **2010**, *2*, 2956–2962.

(61) Kargl, R.; Mohan, T.; Köstler, S.; Spirk, S.; Doliška, A.; Stana-Kleinschek, K.; Ribitsch, V. *Adv. Funct. Mater.* **2013**, *23*, 308–315.

(62) Wolfberger, A.; Kargl, R.; Griesser, T.; Spirk, S. *Molecules* **2014**, *19*, 16266–16273.

(63) Wolfberger, A.; Petritz, A.; Fian, A.; Herka, J.; Schmidt, V.; Stadlober, B.; Kargl, R.; Spirk, S.; Griesser, T. *Cellulose* **2015**, *22*, 717–727.

(64) Ganner, T.; Sattelkow, J.; Rumpf, B.; Eibinger, M.; Reishofer, D.; Winkler, R.; Nidetzky, B.; Spirk, S.; Plank, H. *Sci. Rep.* **2016**, 1–11.

(65) Taajamaa, L.; Rojas, O. J.; Laine, J.; Kontturi, E. *Soft Matter* **2011**, *7*, 10386–10394.

(66) Kontturi, E.; Johansson, L. S.; Laine, J. *Soft Matter* **2009**, *5*, 1786–1788.

(67) Nyfors, L.; Suchy, M.; Laine, J.; Kontturi, E. *Biomacromolecules* **2009**, *10*, 1276–1281.

(68) Niegelhell, K.; Süßenbacher, M.; Jammernegg, K.; Ganner, T.; Schwendenwein, D.; Schwab, H.; Stelzer, F.; Plank, H.; Spirk, S. *Biomacromolecules* **2016**, acs.biomac.6b01263.

(69) Martín-Sampedro, R.; Rahikainen, J. L.; Johansson, L. S.; Marjamaa, K.; Laine, J.; Kruus, K.; Rojas, O. J. *Biomacromolecules* **2013**, *14*, 1231–1239.

(70) Hoeger, I. C.; Filpponen, I.; Martin-Sampedro, R.; Johansson, L. S.; Österberg, M.; Laine, J.; Kelley, S.; Rojas, O. J. *Biomacromolecules* **2012**, *13*, 3228–3240.

(71) Strasser, S.; Niegelhell, K.; Kaschowitz, M.; Markus, S.; Kargl, R.; Stana-Kleinschek, K.; Slugovc, C.; Mohan, T.; Spirk, S. *Biomacromolecules* **2016**, *17*, 1083–1092.

(72) Taajamaa, L.; Rojas, O. J.; Laine, J.; Yliniemi, K.; Kontturi, E. *Chem. Commun. (Camb).* **2013**, *49*, 1318–1320.

(73) Mohan, T.; Zarth, C. S. P.; Doliška, A.; Kargl, R.; Griesser, T.; Spirk, S.; Heinze, T.; Stana-Kleinschek, K. *Carbohydr. Polym.* **2013**, *92*, 1046–1053.

(74) Ristić, T.; Mohan, T.; Kargl, R.; Hribernik, S.; Doliška, A.; Stana-Kleinschek, K.; Fras, L. *Cellulose* **2014**, *21*, 2315–2325.

(75) Mohan, T.; Findenig, G.; Höllbacher, S.; Cerny, C.; Ristić, T.; Kargl, R.; Spirk, S.; Maver, U.; Stana-Kleinschek, K.; Ribitsch, V. *Colloids Surfaces B Biointerfaces* **2014**, *123*, 533–541.

(76) Tomšič, B.; Jovanovski, V.; Orel, B.; Mihelčič, M.; Kovač, J.; Francetič, V.; Simončič, B.; *Cellul. (Dordrecht, Netherlands)* **2015**, *22*, 3441–3463.

(77) Kraev, A. S.; Agafonov, A. V.; Davydova, O. I.; Nefedova, T. A.; Trusova, T. A.; Zakharov, A. G. *Colloid J.* **2007**, *69*, 620–626.

(78) Maniruzzaman, M.; Mahadeva, S. K.; Khondoker, A. H.; Kim, J. 2012; Vol. 8344, p

83440J–83440J–5.

(79)   Nsib, M. F.; Hajji, F.; Mayoufi, A.; Moussa, N.; Rayes, A.; Houas, A. *Comptes Rendus Chim.* **2014**, *17*, 839–848.

(80)   Breitwieser, D.; Kriechbaum, M.; Ehmann, H. M. a.; Monkowius, U.; Coseri, S.; Sacarescu, L.; Spirk, S. *Carbohydr. Polym.* **2015**, *116*, 261–266.

(81)   Vasil'kov, A. Y.; Rubina, M. S.; Gallyamova, A. A.; Naumkin, A. V.; Buzin, M. I.; Murav'eva, G. P. *Mendeleev Commun.* **2015**, *25*, 358–360.

(82)   Giese, M.; Blusch, L. K.; Schlesinger, M.; Meseck, G. R.; Hamad, W. Y.; Arjmand, M.; Sundararaj, U.; MacLachlan, M. J. *Langmuir* **2016**, acs.langmuir.6b02974.

(83)   Erbas Kiziltas, E.; Kiziltas, A.; Blumentritt, M.; Gardner, D. J. *Carbohydr. Polym.* **2015**, *129*, 148–155.

1.2 Deuterium and Cellulose – A Comprehensive Review[1]

The following section is published as a book chapter in Nanocelluloses and Advanced Materials and describes the research of deuterated cellulose.

(1)   Reishofer David and Stefan Spirk. "Deuterium and Cellulose: A Comprehensive Review." *Cellulose Chemistry and Properties: Fibers, Nanocelluloses and Advanced Materials*. Springer International Publishing, **2015**. 93-114.

This contribution summarizes the achievements in the understanding of cellulose accessibility, structure and function with a particular focus on its interactions with deuteration. This review is the first to explicitly devote a discussion to deuteration of cellulose and highlights the remarkable new findings in cellulose research as a result of the development of new experimental approaches, from simple weighing of deuterated samples to sophisticated techniques, including small angle neutron scattering and ^{2}H-NMR spectroscopy.

1.2.1   Initial efforts in cellulose deuteration

The first report on deuteration experiments on cellulose dates back to the early 1930s when Bonhoeffer[1] investigated the reaction of heavy water and cellulose. More than a polymer scientist, Bonhoeffer can be considered as an electrochemist who during his career studied processes occurring at electrode interfaces. It is not surprising that he was not very interested in the structural details and arrangements of cellulose but in the (electro)chemical behavior and reactivity of D_2O itself, particularly its interaction with platinum electrodes. His experiments did not address the understanding of the polymeric structure of cellulose, just determined by Staudinger some years before in 1920.[2] Particularly, on the basis of Staudinger's viscosity measurements, his finding of the supramolecular structure of cellulose as a linear arrangement of

the polymeric molecule. Very early after Staudinger's discovery, the amorphous-crystalline nature of cellulose was investigated by means of electron diffraction and X-ray scattering experiments. These methods prompted discussions on the potential differences in reactivity of crystalline and amorphous domains and the methods to be used for such explorations. One of the first attempts to measure reactivity differences was made by Goldfinger et al.[3] who showed that there are two rate constants in the course of the oxidation with periodate solutions of various cellulose samples. The rate constants differed significantly and the faster one has been determined to take place preferentially in the amorphous domains, while the second one is related to the crystalline ones. In the second attempt to investigate the reactivity differences, thallous ethylate was used to treat cellulose in a variety of solvents. As it turned out, only a fraction of the hydroxyl groups of the cellulose was converted into the thallium salt while the other portion remained unchanged. Besides these two reactions, a third oxidative degradation method employed analyses of the rate constant of CO_2 evolution; it was observed that after a rapid linear degradation a much slower reaction rate takes place until a stable equilibrium is reached. As we know today the plateau value they observed is connected to the LODP, which is a very important characteristic in the course of cellulose nanocrystal preparation.

However, all the methods employed thus far were laborious, the analyses were pretty complicated and most importantly they were destructive. Champetier and Villard[4] were the first to recognize the potential importance of Bonhoeffer's observation and performed the first detailed studies on exchange reactions of cellulose. However, one of the problems in their experimental setup was the exposure of the samples to ambient atmosphere during the analyses, which changed to some extent the interpretation of the obtained results due to rehydrogenation of the samples. The analyses of the samples at that time were performed by using gravimetry, taking advantage of the difference in density between D_2O and H_2O and the accuracy was in the range of 5%. It took another ten years until Frillette et al.[5] revived the idea to employ D_2O for the characterization of cellulosic samples. They used a variety of different sources such as cotton, cotton linters, viscose rayon fibers and wood fibers and studied the exchange reaction as a function of the pH value and, to some extent, the temperature. In order to avoid ambiguous results, they took great care to prevent the samples from rehydrogenation by carrying out the experiments in a dry box. For all samples, very similar curves were obtained, featuring a fast exchange in the very beginning of the

reaction (ca. 1 h), followed by a very slow second phase that lasted several hours until a stable plateau was reached. Since the curves looked very similar in shape they tried to extract information that could be potentially useful for further characterization of the cellulose samples, particularly the degree of crystallinity. This was done by extrapolating the plateau part of the curve to zero time, yielding the so called "*a*" value. Other values they used were the "*b*" value (degree of exchange after 4 h) and the "*c*" value (exchange after one week) (Figure 1.2.1).
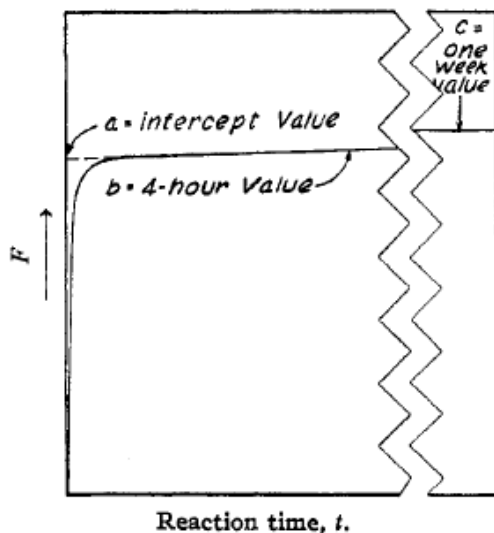
Figure 1.2.1. Generalized reaction curve and characterization values in the deuteration of cellulose samples made by Mark et al.; *a* = the intercept of the horizontal portion of the curve extrapolated to zero time; *b* = at four hours; *c* = at one week.[5]

The authors already had a very good idea of how the supramolecular structure of cellulose was, even several years before the Fringe model was introduced. They proposed that the amorphous domains of cellulose should be easily accessible to water whereas the crystalline domains should not; from their obtained data, they made a distinction of the two considering the role of surface hydroxyls. They realized that the crystalline domains are not that large in diameter, therefore the surface hydroxyls account for a rather high percentage of the total volume of a crystallite, which was expressed by Eq. (1.2.1):

$$F' = \sigma * \alpha + (100 - \alpha) \quad \text{and} \quad \alpha = \frac{100 - F'}{1 - \sigma} \qquad (\textbf{1.2.1})$$

where F' is the percentage of all the hydroxyls that react rapidly with D_2O, σ corresponds to the available surface hydroxyls of the crystalline parts and α is the resulting crystallinity of the sample. At this time also the first reports on the dimensions of crystallites were already available from Mark and Kratky[6] work who indicated values between 50 to 100 Å on edge. The authors were aware that wrong assumptions of σ would lead to some deviation, however the agreement is quite impressive if ones compares the obtained degrees of crystallinity with those available nowadays (Table 1.2.1).

Table 1.2.1. Available data on the degree of crystallinity for several samples in 1955, as determined by gravimetric analyses.

Sample	% accessibility to liquid D_2O					% of amorphous material
	Champetier and Villard, 1938 [4]	Mark 1948 [5]	Rowen and Plyler, 1950 [7]	Mann and Marrinan, 1955 [8]		
				first deuteration	second deuteration	
Viscose		81		83	78	75
Viscose treated with 18% NaOH				[74]	70	66
Cellophane			<50			
Cellulose from acetate			<50			
Bacterial cellulose				39		[30]
Cotton linters	100	61				

The differences they observed with the Nickelson method,[9] described above, were explained by the fact that it depolymerizes cellulose, leading to more mobile chains capable to rearrange and form laterally-ordered structures that undergo recrystallization. However this was a misconception since later the method turned out to be unreliable. Additionally, it was thought that prolonged acid treatment of cellulose, as firstly described by Ingersol in 1946,[9] induced

crystallization since Ingersol observed a significant sharpening of the X-ray patterns after treatment, possibly the first indirect observation of cellulose nanocrystals.

1.2.2 IR Efforts

The next breakthrough in the use of D_2O exchange involved the use of infrared spectroscopy, giving also insight into the hydrogen bonding pattern and allowing for an elegant way to quantify the accessibility and subsequent estimation of crystallinity. Rowan and Plyler [7] employed this technique for the first time on cellophane and regenerated cellulose obtained from cellulose triacetate using regeneration with NaOD. They found very low deuteration degrees even after treatment in liquid D_2O for several days at 52°C. However, Almin[10] later on showed in detailed studies that the samples were rehydrogenated before analysis, giving rise to low deuteration degrees.

Later on, it was shown that the shape of the absorption band can be exploited to directly distinguish between amorphous and crystalline domains during the measurement. Mann and Marrinan investigated different aspects of deuteration in a series of publications.[8,11,12] The first focused on gas and liquid phase deuteration of several cellulose samples (viscose, bacterial cellulose) by using *in situ* IR spectroscopy. Similar to the observations made by Frillette et al., after one hour the H/D exchange slowed down, and was accompanied by the replacement of a broad OH band with four distinct bands in the area assigned to crystalline cellulose I, also with bands evolving at ca 2500 cm^{-1}, corresponding to OD stretching vibrations. Even though the reaction speed was faster in liquid-based systems, deuteration using D_2O vaporous yielded the same IR spectra after 4 h. However, the authors noticed distinct differences upon deuteration between the viscose sample and the one derived from bacterial cellulose. While viscose readily exchanged, the bacterial cellulose did to a much lesser extent. Interestingly, rehydrogenation without drying revealed another difference, namely so called resistant OD groups, that were exclusively observed in samples of bacterial cellulose and assigned to hydroxyls on the crystal surfaces. Like in Plyler's experiments, drying the sample after the D_2O exchange leads to an irreversible incorporation of deuterium into the supramolecular structure of viscose. Even

extensive exposure to liquid H_2O could not rehydrogenate OD groups. These results clearly indicated that incorporation of water into the crystalline domains of cellulose does not take place. While this question had been solved already unambiguously for cellulose I by X-ray data[13], for cellulose II the situation was unclear since X-ray experiments showed a widening of the (101) reflection during wetting with water, which was interpreted by the formation of stoichiometrically formed hydrates.[14] The authors argued that that the resistant OD groups are located in apparently perfect crystalline domains (sharp bands), and their resistance against rehydrogenation suggests that their formation cannot take place by penetration into the lattice.[11]

Since it was now possible to accurately estimate the amount of hydroxyls exchanged, it was possible to determine cellulose accessibly with much higher precision; the same was true for the crystallinity since several assumptions were avoided (see discussion below). The imprecisions were recognized as far as the equilibrium constant K of the exchange reaction (Eq. 1.2.2).

$$K = \frac{D_{acc}/H_{acc}}{D_{H_2O}/H_{H_2O}} = 1 \text{ for the equilibrium HOD + ROH} \leftrightarrow \text{ROD+ROH} \qquad (\mathbf{1.2.2})$$

Mark et al.[11] stated that K = 1, which was not the case since the zero point energies are changed by the H/D exchange (at that time K values were reported between 1.04 and 1.10, depending on which hydroxyls are exchanged)[15]. The zero-point energy differences of R-OH and R-OD in turn are connected to the difference of vibrational energies of their ground state and can be in principle calculated from their frequencies of vibration. Since the hydroxyls have a wide range of vibrational frequencies, a wide range of K values for these and the overall equilibrium could only be obtained by performing the exchange with extremely high mole fractions of D_2O. Mann et al. proved for viscose and bacterial cellulose a difference of about 30-40 % between the crystallinity and the accessibility of cellulose.[8] They recognized that under the condition that all OD in the crystalline domains are located on the surface (and not at the imperfections in the lattice), it is was possible to estimate the crystallite size by using their approach.

Anyway, the use of infrared spectroscopy and a related definition of crystallinity were introduced by the same authors by employing the ratio of the intensities at a given wavelength for OD and

OH corrected by the extinction coefficient according to the Beer's law (Eqn. 1.2.3 and Table 1.2.2).

$$\log\left(\frac{I_0}{I}\right)_\lambda = k_\lambda * c * l \qquad (\textbf{1.2.3})$$

where I_0 is the intensity of the radiation incident on the film, I the intensity of the transmitted radiation, c the concentration of material absorbing at wavelength λ expressed as a mole fraction, l the path length of the radiation through the film, and k the extinction coefficient per unit mole fraction. As a result, the crystallinities of several cellulose I and II materials (cotton, bacterial cellulose, saponified acetate, viscose oriented/unoriented/hydrolyzed, precipitated cellulose, mercerized bacterial cellulose) was determined and compared with previously determined results, derived from X-rays. The same authors were aware that results should be different, since methods based on scattering are do not give reasonable results for crystallite surfaces. In all cases, crystallinities lower than those obtained by X-ray were obtained; however, the relative ratio was rather similar.

Table 1.2.2. Percentage of amorphous OH groups obtained by FT-IR spectroscopy.[11]

Sample	$\dfrac{\log(I_0/I)_{OD}}{\log(I_0/I)_{OH}}$	% amorphous OH
Saponified acetate	3.35	75
Viscose oriented	3.18	74
Viscose unoriented	3.10	73.5
Viscose hydrolyzed in H_2SO_4	2.42	68.5
Precipitated cellulose	2.34	68
Mercerized bacterial cellulose	2.28	67
Viscose treated with NaOH	2.20	66.5
Fortisan micelles	0.96	46.5 ± 5
Bacterial cellulose		30
Cotton micelles		31 ± 5

Further progress in IR spectroscopy was made by Tsuboi,[16] who investigated the effect of polarization, *i.e.* the orientation of the cellulose molecules in regard to their response on deuteration. He obtained spectra for ramie cellulose swollen in NaOD that allowed him to assign

bands in the OD regime to certain vibrations and to correlate them to the corresponding OH vibration, most of which are parallel to the fiber axis. As a result, Tsuboi found out that the ratio of νOD/νOH was always between 1.33-1.35.
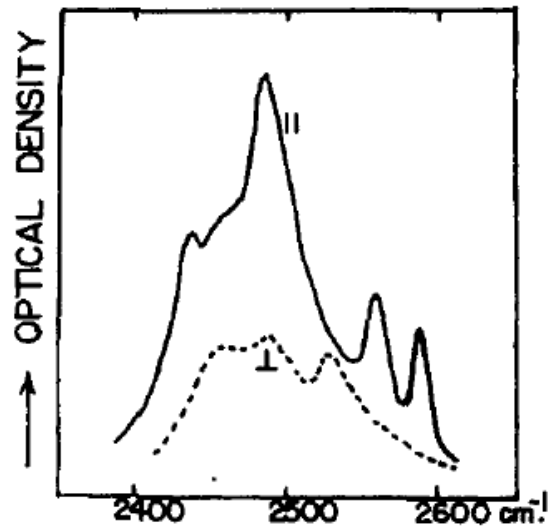

Figure 1.2.2: Infrared spectrum of NaOD-swelled ramie fiber in the O-D stretching region; (∥) Electric vector parallel to fiber axis; (⊥) Electric vector perpendicular to fiber axis.[16]

Table 1.2.3. OD band shifts compared with OH band shifts

OD bands observed by Tsuboi,**Fehler! Textmarke nicht definiert.** cm^{-1}	OH bands observed by Marrinan and Mann,[12] cm^{-1}		Frequency ratio	Dichroism
	Cellulose I	Cellulose II		
2585		3484	1.35	∥
2551		3444	1.35	∥
2527	3410		1.35	⊥
2484	3350		1.35	∥
2462	3288		1.34	∥
2440	3250		1.33	∥

Although Tsuboi was not able to assign which hydroxyls are oriented along the fiber axis and which are perpendicularly oriented, their results gave the first insight into the preferred hydrogen bonding pattern in cellulose.

A rather exotic method was used some time after Tsuboi's report, namely, a combination of D_2O and T_2O to determine the accessibility of cellulosic samples.[17,18] In fact, the incorporation of T_2O led to radioactivity whose decay over time can be exploited to determine the accessibility of cellulose and other biopolymers. The results the authors obtained were in good agreement with studies on deuterated samples, which was necessary in order to exclude roughness effects that may influence the radioactivity measurements. Furthermore, the H/D and H/T exchange was studied in detail[19] with regard to supramolecular arrangements. As a result, it was shown that heating of cellulose leads to a rearrangement of the molecules and results in partial interchange of accessible and inaccessible regions if a variety of drying/wetting procedures are performed. The authors argued that heating may cause mechanical stresses that lead to disruption of crystallites, followed by recrystallization that forms new crystalline domains.

A complementary, interesting approach was carried out by Okajima and Kai, who investigated the H/D exchange behavior of native and regenerated cellulose from *Valonia* before and after heat treatment.[20] According to the early definitions of Frilette, they analyzed the deuteration curves according to the different phases (a, b, c). For native samples, *a* fast exchange was observed, which corresponded to about 20% of exchange, while for the mercerized cellulose, the decay was down to ca 75%. The deuteration of the *a* region was considered to occur directly by exchange with diffused D_2O molecules, but this was not yet clear for the *b* and *c* regions. Because of the relation between the amount of OD (OH) and the logarithmic integrated time *t* it was clear that there no dominant role of the diffusion of D_2O existed for the *b* region.

### 1.2.3 Scattering and diffraction

The next milestone in the investigation of deuterated cellulose was the use of neutron scattering. Particularly, compared to hydrogen deuterium is a very good isotope for such studies

since it provides a high scattering contrast and provides a way to stain the amorphous domains of cellulose, and, as will be shown later on, also to stain the crystalline domains.

E. Fischer was the first to report on the long spacing in cellulose,[21] which had been postulated but not measured since the electron density differences between the amorphous and the crystalline domains in cellulosic fibers were too small for SAXS or SANS elucidation. For this purpose Fischer employed gas phase deuteration, which mainly takes place in the amorphous domains. As was the case of other reports, the exchange was complete after a very short time (30 min) and no increase in scattering intensity was observed after prolonged exposure times. Meridional long spacing was determined for the deuterated samples (16.5 and 19.3 nm for Fortisan and rayon) whereas native cellulose samples (ramie) did not give any result. The authors explained this observation by diffuse scattering, which plays a large role if the long spacing reach values in the range of 50-70 nm, as has been found for such materials by electron microscopy. In addition, the experiments gave rise to the cross sections of crystalline arrays in regenerated cellulose (3.4 nm), which compared well with data available from other sources such as electron microscopy (3.5 nm) and was superior to SAXS data (5.0 nm) available at that time by evaluation and data acquisition at large angles. In addition, a large monodisperse component was identified in the range of 9.8 nm, which was assigned to bundles of eight elementary fibrils. Besides insights in dimensions, these experiments also shed light on how voids and pores could be organized. Due to presence of continuous equatorial scattering (which leads to elongated scattering patterns) the authors concluded that elongated microvoids are present in the sample.

After Fischer's findings, there were only isolated reports on deuterated cellulose until the end of the 1990's when Nishiyama, Isogai, Langan and Chanzy, to name some contributors, revisited the topic at hand. The motivation for related work was probably driven by discoveries some years before when it was demonstrated via ^{13}C solid state NMR spectroscopy[22] that the earlier reported crystal structure of Valonia cellulose was imprecise. This was because it was not taken into account that Valonia cellulose is composed of cellulose I_α and I_β.[23] The main challenge in the determination of crystal structures of native cellulose is that fibers consist of microcrystallites that are preferentially aligned along the fiber axis, while along that axis they employ a random orientation. As a consequence, reflection spots tend to overlap in diffractograms due to

cylindrical averaging, making the separation of distinct reflections from different phases doubtful. Progress has been made by electron microscopy on individual cellulose microcrystals resulting in the unambiguous identification of two distinct crystal phases corresponding to cellulose I_α und I_β.[24] In a first series of experiments, Nishiyama and coworkers investigated a series of highly crystalline cellulose samples (Cladophora, I_α and I_β; Halocynthia, exclusively I_β)[25] and mercerized cellulose and compared the neutron diffraction data before / after deuteration and obtained a resolution of 0.9 (native celluloses) and 1.2 Å (mercerized cellulose). Their report was accompanied with new investigations to elucidate if deuterium can be incorporated into the crystal structure of these materials.[17,26] Substrates of choice included acid hydrolyzed microcrystals that had been processed into oriented films. It was demonstrated by X-ray experiments using synchrotron radiation that exposure to elevated temperature (210°C/30 min) leads to intracrystalline H/D exchange without converting cellulose I_β to I_α. In addition to scattering data, the polarized FT-IR proved that there was not any significant amount of OH groups present in the samples. These OH groups nearly quantitatively converted to OD groups that in turn were assigned very precisely. On the basis of these results, it was subsequently possible to determine the precise crystal structures and to locate the hydrogen bonding system in cellulose I_β (Halocynthia)[27] and later on also in I_α (Glaucocystis).[28,29] A major contribution in these studies was the excellent quality of data from both X-ray and neutron scattering experiments. For example, the use of deuterated samples allowed the precise determination of the atomic coordinates and the localization, with atomic resolution, of the hydrogen bonded network in Fourier difference maps for both, the deuterated and the hydrogenated data. The resulting hydrogen bonding pattern and the geometric details are given in Figure 1.2.3 and Table 1.2.4 for cellulose I_β. The resulting hydrogen bonding pattern for cellulose I_α is given in Table 1.2.5.
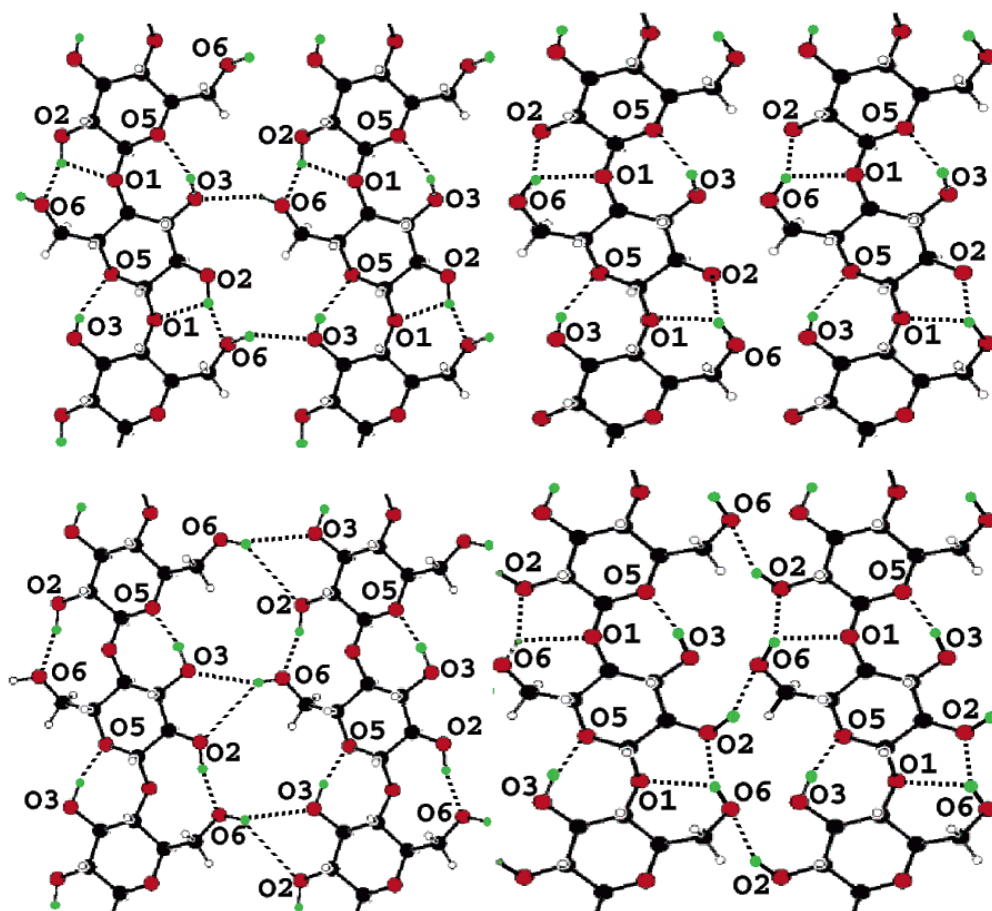
Figure 1.2.3. Schematic representation of the hydrogen bonds in the origin (top) and center (bottom) sheets of cellulose Iβ. Carbon, oxygen, hydrogen, and deuterium atoms are colored black, red, white, and green, respectively. Hydrogen bonds are represented by dotted lines. Only the oxygen atoms involved in hydrogen-bonding have been labeled for clarity. Deuterium atoms D2oA, D3o, and D6oA are included in the top left view (O2o-D2oA···O6o, O2o-D2oA···O1o, O3o-D3o···O5o, O6o-D6oA···O3o), D3o and D6oB in the top right view (O3o-D3o···O5o, O6o-D6oB···O2o, O6o-D6oB···O1o), D2cA, D3c, and D6cA in the bottom left view (O2c-D2cA···O6c, O3c-D3c···O5c, O6c-D6cA···O3c, O6c-D6cA···O2c), and D2cB, D3c, and D6cB in the bottom right view (O2c-D2cB···O6c, O3c-D3c···O5c, O6c-D6cB···O2c, O6c-D6cb···O1c).[27]

Table 1.2.4. The hydrogen bonding parameters for cellulose I$_\beta$ determined by Nishiyama et al.[27]

| D-H	d(D-H)	d(H···A)	∠DHA	d(D··A)	A
O2o-D2oA	0.977	1.832	158.72	2.765	O6o [-x, -y, z+½]
O2o-D2oA	0.977	2.304	110.28	2.797	O1o [-x, -y, z+½]
O3o-D3o	0.979	1.966	137.08	2.764	O5o [-x, -y, z-½]
O6o-D6oA	0.979	2.040	144.26	2.892	O3o [x, y+1, z]
O6o-D6oB	0.974	1.876	150.23	2.765	O2o [-x, -y, z+½]
O6o-D6oB	0.974	2.152	121.59	2.789	O1o
O2c-D2cA	0.982	1.904	165.12	2.865	O6c [-x+1, -y+1, z+½]
O2c-D2cA	0.978	2.440	135.44	3.211	O6c [x, y-1, z]
O3c-D3c	0.983	1.752	162.23	2.705	O5c [-x+1, -y+1, z-½]
O6o-D6cA	0.985	1.779	156.61	2.711	O3c [x, y+1, z]
O6o-D6cA	0.985	2.544	124.98	3.211	O2c [x, y+1, z]
O6o-D6cB	0.975	1.967	152.06	2.865	O2c [-x+1, -y+1, z-½]
O6o-D6cB	0.975	2.243	123.21	2.894	O1c

Table 1.2.5. The hydrogen bonding parameters for cellulose I$_\alpha$ determined by Nishiyama et al.[28]

D-H	d(D-H)	d(H··A)	∠DHA	d(D··A)	A
O3d-D3d	0.989	1.954	163.94	2.918	O5u [x-1, y, z]
O3d-D3d	0.989	2.386	119.05	2.994	O1u [x-1, y, z]
O2d-D2dA	0.974	1.689	133.83	2.465	O6u
O2d-D2dB	0.983	2.283	116.94	2.866	O3d
O2d-D2dB	0.983	2.679	157.47	3.606	O6d [x, y-1, z+1]
O2u-D2uA	0.980	1.763	127.07	2.480	O6d [x+1, y, z]
O2u-D2uA	0.980	2.181	118.44	2.784	O1u
O2u-D2uB	0.985	2.357	110.37	2.853	O3u
O2u-D2uB	0.985	3.019	122.21	3.641	O6u [x, y+1, z-1]
O6d-D6dA	0.977	2.176	122.20	2.821	O3d [x, y+1, z-1]
O6d- D6dA	0.977	2.791	141.32	3.606	O2d [x, y+1, z-1]
O6d- D6dB	0.976	1.894	150.36	2.785	O1u [x-1, y, z]
O6d- D6dB	0.976	1.967	110.23	2.480	O2u [x-1, y, z]
O6u- D6uA	0.983	1.853	153.99	2.770	O3u [x, y-1, z-1]
O6u- D6uA	0.983	2.881	134.82	3.641	O2u [x, y-1, z-1]
O6u- D6uB	0.976	1.956	145.03	2.812	O1d
O3u-D3u	0.976	2.072	137.59	2.868	O5d

It was demonstrated that the intra-sheet hydrogen bonding involving O2 and O6 donors is disordered over two possible sites in both cellulose I_α and I_β. Most of the hydrogen bonds in these networks are either strong (D···A: 2.2-2.5 Å) or medium strong (2.5-3.2 Å) according to Steiner[30] and Jeffrey[31] (compare Tables 4 and 5). The situation is rather complicated since there are at least two different networks, probably in a dynamic equilibrium (see Figure 3). In both networks, the intramolecular O3-H3···O5 hydrogen bonds are relatively strong in both I_α and I_β (H···A: 1.966 and 2.072 Å) featuring in addition DHA angles close to 180° (162.23 and 163.94°). In network I, the intramolecular O2-H2···O6 bonds are quite different (H···A: 1.689 and 1.763 Å for I_α; 1.832 and 1.904 Å for I_β) as well as the O6-H6···O3 interchain bonds (H···A: 1.853 and 2.176 Å for I_α; 1.779 and 2.040 Å for I_β). In contrast, in network II there is only one intramolecular hydrogen bond for I_α (O6-H6…O2) whereas there are two in I_β; for the interchain hydrogen bond O2-H2···O6 the situation is opposite. For all hydrogen bonds, the distances are shorter (H···A are 2.679, 3.019 and 1.967 Å for I_α; 1.876, 2.440 and 1.967 Å for I_β).

The use of deuteration in cellulose II combined with neutron diffraction allowed the distinction between two conformational models (A and B). While model A features equivalent backbone conformations, having different ones at the hydroxymethyl group (tg and gt, respectively), model B (cellotetraose-like) has different backbone conformations and the hydroxymethyl group has always nearly the same conformation (Figure 4). Langan and coworkers showed that model B is correct and identified the hydrogen bonding pattern of cellulose II. There are intermolecular hydrogen bonds between origin and center chains involving O2c (D) and O2o (A) and O6o (D) that form a four-center hydrogen bond, with O6c, O5c, and O3c as potential acceptors. There is a rather strong intramolecular hydrogen bond between O3 and O5 (O3o-O5o: 2.66 Å and O3c-O5c: 2.73 Å) and a much weaker one between O3 and O6 (O3o-O6o: 3.31 Å and O3c-O6c: 3.22 Å). Both values for these hydrogen bonds are very similar for those reported by Gessler et al.[32] who studied hydrogen bonding in D-cellotetraose (compare: O3o-O5o: 2.84 Å, O3c-O5c: 2.91 Å, O3o-O6o: 3.32 Å, and O3c-O6c: 3.09 Å) An summary of hydrogen bonding parameters is given in Table 1.2.6.
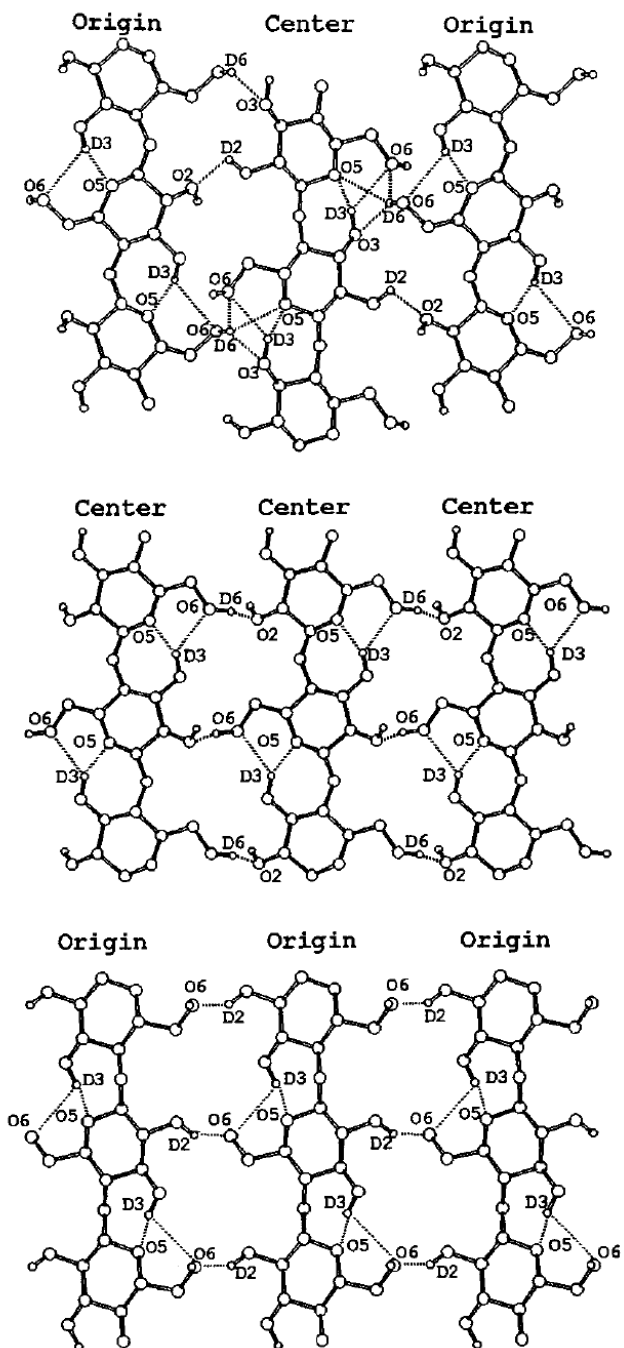
Figure 1.2.4. A schematic representation of the hydrogen bonds in cellulose II. Only atoms involved in hydrogen bonding are labeled. Hydrogen bonds are represented by dotted lines. Intermolecular hydrogen bonds are O2-D···O6 in sheets containing only origin molecules and O6-D···O2 in sheets containing only center molecules. In the sheet containing both center and

origin molecules there are O6-D⋯O6 and O2-D⋯O2 intermolecular hydrogen bonds. The former has minor components involving O5 and O3 as acceptors. Intramolecular hydrogen bonds are O3-D⋯O5 in each molecule with a minor component involving O6 as acceptor.[29]

Table 1.2.6. Hydrogen bonding parameters for cellulose-II determined by Langan et al.[29]

D-H	d(D-H)	d(H⋯A)	∠DHA	d(D⋯A)	A
O2o-D2oA	0.981	2.015	119.75	2.643	O6c [-x+1, -y,z+½]
O2o-D2oA	0.981	2.223	141.49	3.053	O3c [-x, y-1, z]
O3o-D3o	0.981	2.489	122.08	3.123	O5c [-x+1, -y,z+½]
O6o-D6oA	0.980	1.918	130.45	2.660	O5o [-x, -y,z-½]
O6o-D6oB	0.980	2.803	113.07	3.312	O6o [-x, -y,z-½]
O6o-D6oB	0.979	1.817	150.67	2.713	O6o [x-1, y, z]
O2c-D2cA	0.981	1.784	150.44	2.682	O2c [x+1, y, z]
O2c-D2cA	0.980	1.848	148.43	2.731	O5c [-x + 1, -y+1, z+½]
O3c-D3c	0.980	2.500	130.02	3.219	O6c [-x + 1, -y+1, z+½]
O6o-D6cA	0.981	2.212	115.84	2.783	O2o [-x, -y+1, z-½]

Although cellulose I and II are the most prominent polymorphs, others are possible as well. In a similar approach as for cellulose I and II, deuterated cellulose III[33] was produced by employing ND_3 instead of NH_3 for conversion. A comparison of the different polymorphs is depicted in Figure 1.2.5. It is clear that compared to cellulose I_β, cellulose III has a chain reorientation that significantly reduces the distance between neighboring chains in a sheet (8.20 to 7.85 Å) and increases the sheet separation (from 3.87 to 4.29 Å). Other differences between cellulose I_β and cellulose III_I include the number of weak inter-sheets in I_β and that I_β sheets are tightly packed. The combination of difference in sheet separation and the nature of the inter-sheet stacking interactions may contribute to the enhanced accessibility of cellulose III_I for polar guest molecules.
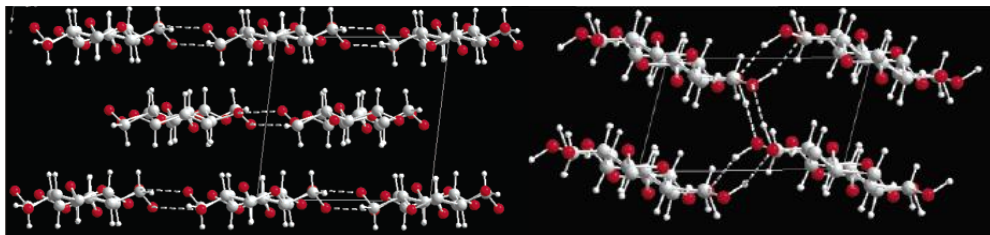
Figure 1.2.5. Projections of the crystal structures of cellulose I$_\alpha$ (left) and cellulose III$_\mathrm{I}$ (right)[33]

Besides the crystal structures of cellulose, the distribution of the I$_\alpha$ and I$_\beta$ polymorphs in the elementary fibrils is of large interest from a biological point of view. Horikawa and Sugiyama developed an elegant technique using FT-IR that allows localization of I$_\alpha$ and I$_\beta$ domains in a single microcrystallite.[34] Their approach converted part of cellulose I$_\alpha$ from *Glaucocystis* into the I$_\beta$ form by heating to 255°C for 30 minutes, leading to only partial inter-conversion. The resulting material included a I$_\beta$ skin and a I$_\alpha$ core. Afterwards, the procedure was completed by intra-crystalline deuteration, as described already above. For the sake of comparison, other samples (*Cladophora* and *Valonia*) that contain a large portion of I$_\beta$ were subjected to intra-crystalline deuteration.[35] After rehydrogenation at elevated temperatures the I$_\alpha$/I$_\beta$ localization was predicted according to the H/D exchange rate (faster for the I$_\beta$ skin) and supported by electron micro-diffraction experiments. The authors expected to observe a similar behavior for the native celluloses, however, the H/D exchange rates were identical for the two crystalline phases, meaning that native celluloses do not exhibit a skin-shell structure.

Other approaches used neutron scattering and used commercial samples including e.g. TENCEL fibers[36] and polysaccharide films[37] but were not aimed to unveil a deep understanding of cellulose structure and reactivity.

1.2.4 Current efforts

Efforts to unravel the crystalline domains of cellulose include those of Kondo and coworkers who studied the amorphous nature of cellulose. In 1996, they reported a model for amorphous cellulose that was featured by isotropic hydrogen bonds whereas some domains exhibited a short range order via intermolecular hydrogen bonding.[38] However, these interactions are weaker than in the crystalline cellulose and lack long-range order. Later on, same authors investigated the deuteration behavior of cast and coagulated cellulose films and indicated 0 and 13.8% crystallinity by X-ray diffraction patterns, respectively. The amorphous films revealed an interesting behavior, since they did not undergo H/D exchange to a full extent. While it was already reported by Wadehra[39] and Jeffries[40] that probably the materials could recrystallize upon D_2O vapor exposure, Kondo et al. argued in a different way. One of their arguments was that upon recrystallization the H/D exchange rate changed significantly, as well as the absorption band of the νOH vibrations. Furthermore, the use of different model compounds (methylcelluloses) allowed them to model and to determine the possible hydrogen bonding modes of amorphous cellulose.[41] In a subsequent report, the same group employed two-dimensional correlation spectroscopy to characterize amorphous cellulose.[42] They assigned three different non-crystalline domains in the IR spectrum to OH vibrations and were able to distinguish between inter- and intramolecular hydrogen absorption bands. More or less at the same time, inelastic neutron scattering and neutron time-of flight spectroscopy was employed to study this question in more detail.[43] It was shown that the accessible regions may unambiguously be identified with the disordered regions of a specimen, which show universal low frequency dynamical signatures that have a unique response to water molecules.[43] The main result of these studies was that the share of D_2O accessible functional groups in cellulose rather correlates to disordered domains, whereas the inaccessible ones are assigned to crystalline areas. However, the disordered domains retain a preferential orientation parallel to the microfibril orientation.

Another approach investigated nematically ordered cellulose films (NOC), which were obtained by stretching water swollen, gelly cellulose films using a draw ratio of two.[44] As a result, highly oriented films were obtained (crystallinity ca 20%), as shown by high resolution transmission

electron microscopy. By using deuteration experiments in combination with polarized IR spectroscopy, Kondo and coworkers showed that the main chains (along stretching direction) only show a moderate degree of order, while the OH groups remained unordered.

After the refinement and investigation of the different cellulose crystal structures revealing the hydrogen bonding pattern in the corresponding polymorphs, the study of cellulose in its native environment (i.e. wood cell walls) became a major focus. In related approaches, a main motivation was to understand the changes that take place upon industrial processing steps, namely drying, hydrothermal degradation or aging, as well as to learn how the cell wall acts in biology. Although Tsuchikawa and Siesler have investigated diffusion of D_2O into wood already in 2003,[45–47] the first detailed studies on bulk wood were performed by groups in Helsinki. The same groups studied the influence of drying on the accessibility of fresh wood and never dried pulp fibers using/HD exchange by IR spectroscopy.[48,49] The novelty in this work was the fact that changes upon drying could be followed in situ, *i.e.* it was not required to process the sample after heat treatment for analysis, which obviously could influence the results. It was found that the behavior of the samples was very similar, particularly in terms of inaccessibility. Therefore, the authors stated that the fundamental mechanisms behind the supramolecular rearrangements in cellulose are qualitatively the same, namely aggregation of microfibrous bundles, which is believed to play a key role in drying of papermaking fibers. In a recent report, the same authors investigated the behavior of fibers during heat treatment.[50] They succeeded in determining the kinetics behind deuteration allowing them to detect the equilibrium state of accessibility reduction. Furthermore, the effect of pH and temperature was thoroughly studied. Under acidic conditions (pH of 3), heat treatment below 100°C caused similar alterations as in wood fibers (reduction by aggregation of microfibrils). Alkaline treatments (pH 12, T<100°C) led to an equilibrium state of aggregation that originated from either the equilibrium between the microfibrils and the aggregates or the equilibrium between crystalline and amorphous domains. Based on these results, further details have been investigated by using NaOD for digestion in Kraft processing. It was found that during digestion an irreversible deuteration occurs, which was mainly connected to the heating of wood causing aggregation of the microfibrils. The removal of lignin could play a role but this takes place also in the other stages of pulping. Therefore, it was suggested that hemicelluloses that are dissolved from the fibers are play critical roles in cellulose

microfibril aggregation. Atalla investigated recently the effects of fiber processing type and compared those that are air-dried to those dried at elevated temperatures.[51] The important finding was that the accessibility, as studied by D_2O exchange, is altered already during air drying, a fact that is often neglected in many studies since drying effects are usually investigated at elevated temperature. In a related study, Inagaki and coworkers studied degradation effects by hydrothermal and aging procedures on the crystallite sized and microfibril arrangement.[52] Their main interest was to understand how cellulose in old woods (Hinoki wood, in their particular case) crystallized and how the treatments affected the structure over time. XRD and near infrared spectroscopy (NIR) were used, and the different hydroxyl groups from amorphous and crystalline domains, respectively, are well resolved. Mid infrared has been widely used in the analysis of deuteration process in cellulose. In contrast and despite the possibility to directly distinguish between the amorphous and the crystalline domains, NIR has not been used for this purpose. The reason originates from sample requirement: it must be thick due to the low absorption of cellulose in this region, which is disadvantageous for the investigation of fibers. However, it can be exploited for the analysis of whole wood samples. The main results indicated that hydrothermal treatment leads to an increase in the crystallite size while ageing results in smaller crystallites in the microfibrils. On the basis of the data, a morphological model that explains the observed differences was established. While non-degraded wood microfibrils are composed of elementary fibrils, which are glued by hemicelluloses and lignin, in archeological wood these components are depolymerized, oxidized and finally removed, whereas the crystalline domains are unaffected in terms of size (2.8 nm). Therefore, gaps are created between the elementary fibrils that, according to the proposed model, are larger than those in native wood (from 0.3 to 0.5 nm). In contrast, the distances between elementary fibrils in hydrothermally altered cellulose are the same as in native cellulose (0.3 nm) whereas the crystallite size increases from 2.8 to 3.3 nm, which is a result of amorphous cellulose undergoing crystallization. In a study with a similar background, "Washi" paper samples were investigated.[53] Washi paper is a very durable form of paper that is mainly used in Japan. The authors were interested in the diffusion of D_2O and the saturation accessibility. They studied archeological papers (AD 1615, AD 1791) and compared their accessibility to D_2O vapors with modern Washi paper (AD 2003). One of their main results is that old papers have a much lower accessibility, which probably originates from the beating

procedures performed in the past. Beating in combination with oxidative degradation of the hemicelluloses formed a skin that acts as a diffusion barrier preventing D_2O penetration into the material.

A different approach was followed by Hofstetter et al.[54] and Sturcova et al.,[55] who studied changes in IR spectra upon deuteration during mechanical stress. The main objective was to obtain information how hydrogen bonding strength is altered during mechanical stress and to provide molecular insights, which are of crucial importance for other fields such as composites. While Hofstetter et al. investigated the behavior under dynamic conditions and under a wide range of D_2O vapor pressures, Sturcova et al. mainly focused on the development of a routine under constant mechanical stress. The effects of background fluorescence in Raman spectroscopy and scattering in FT-IR spectra were considered. Changes upon mechanical stress were rather small and interpretation and extraction of bandshifts from complex spectra thorough background corrections and peak fitting procedures were discussed. As a result, a qualitative description of the dependence of the mechanical strain along fiber direction was given. FT-IR absorbance and Raman scattering are dependent on $\cos^2\alpha$ whereas the strain of the polymer chains varies with $\cos\alpha$, leading to non-linear effects. Hofstetter investigated oriented sheets from spruce fibers, mounted in a specially designed sample chamber, which was capable to measure IR spectra in parallel and perpendicular modes while (static or dynamic) mechanical analyses are performed. Moreover, the chamber had inlets to vary the D_2O vapor pressure during the measurement, which allowed for an investigation on how the system responds under changes in humidity.
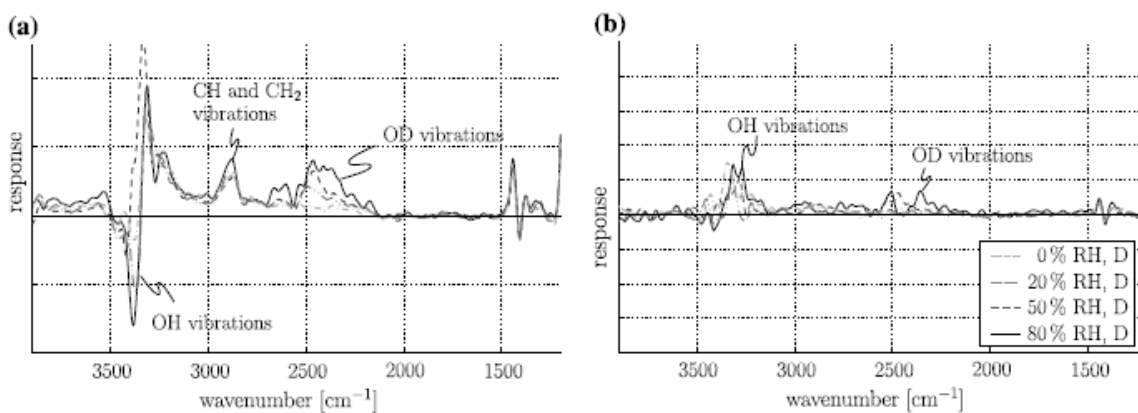
Figure 1.2.6. Dynamic response of cellulose sample in parallel mode during increasing relative humidity to 80% with deuterium vapor: (a) in-phase response; (b) out-of-phase response.[54]
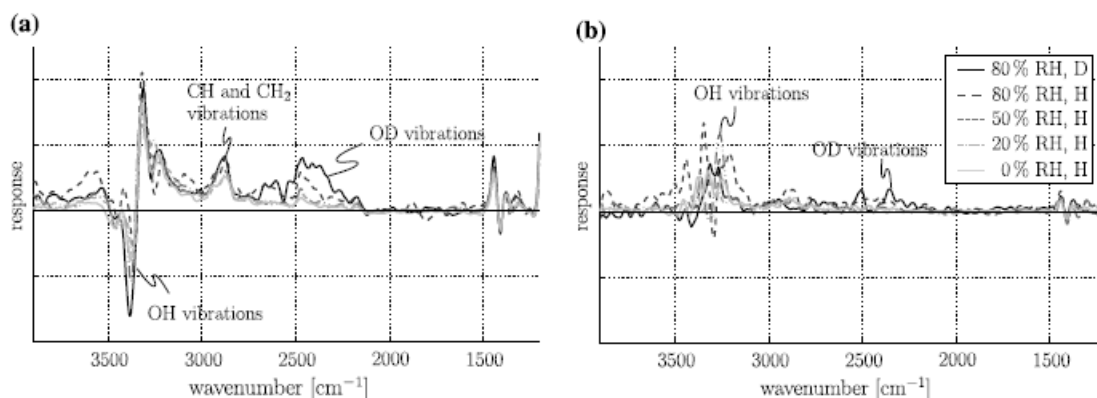
Figure 1.2.7. Dynamic response of cellulose sample in parallel mode during rinsing with normal water vapor and a subsequent decrease of the relative humidity to 0%: (a) in-phase response; (b) out-of-phase response.[54]

The same authors identified several bands, namely, the C-O-C bridge (1160 cm^{-1}), the O5···H3-O3 (3340 cm^{-1}) and the C-OH bending at 1435 cm^{-1}; no large differences between high and low humidity conditions were evident. Furthermore, the intensity of the band at 3230 cm^{-1} corresponding to the O3-H3···O6 intermolecular hydrogen bonds slightly increased, meaning that there were rearrangements under mechanical stress. On the other hand, the peak at 3470 cm^{-1}, assigned to O2-H2···O6 was considerably reduced under high humidity, indicating that this

hydrogen bond is not involved as cellulose softens due to swelling. In addition to these observations, the authors were able to distinguish between reorientation and stretching, at least for surface accessible OD groups. As an outcome the OH bands were assigned to the corresponding vibrations and compared with literature (Table 1.2.7).

Table 1.2.7. Wavenumbers (cm^{-1}) of absorption bands in dynamic spectra upon deuteration assuming a pure translation by 850 cm^{-1} and a shift by a ratio of 1.34, respectively.[54]

Functional group	Wavenumber H [cm^{-1}]	Wavenumber D [cm^{-1}] shifted by 850 cm^{-1} (Nishiyama et al.[25])	Wavenumber D [cm^{-1}] shifted by the ratio 1.34 (Jarvis and McCann[56])
Free O-H(2)	3513-3560	2663-2710	2622-2657
Free O-H(6)	3577-3579	2727-2729	2669-2671
O2-H(D)···O6	3410-3455	2560-2595	2545-2578
O3-H(D)···O5	3340-3375	2490-2525	2492-2519
O3-H(D)···O6	3230-3310	2380-2460	2410-2470
Absorbed water (directly bound)	3200	2350	2388
Absorbed water (indirectly bound)	3600	2750	2687

Lately, deuterated bacterial cellulose was produced by performing the cultivation in completely deuterated media.[57] By this approach deuterium was incorporated at positions that are usually not prone to exchange. The exchange of hydrogen against deuterium did not influence the accessibility; the molecular weight was not affected not the morphology of the material. Besides the first reports of C-D vibrations determined by IR spectroscopy, ^{2}H NMR spectroscopy was used to characterize the deuterated bacterial cellulose leading only to negligible isotope chemical shifting. Since these materials possess a large amount of deuterium, they were proposed as model substrates for further studies with small angle neutron scattering.

^{2}H-NMR spectroscopy was employed to investigate cellulose films[58] and fibers, and to gain insights about the residence time and mobility of D_2O in cellulose, which was determined to be ca 1.5 ms in oriented fibers.[59] Furthermore, the diffusion behavior of water close to a solid cellulose surface was investigated by the same technique.[60-62] The basis for these measurements is the fact that liquid molecules close to a solid surface have different relaxation profiles

compared to those in the bulk liquid, due to interactions at the solid-liquid interface. The main advantage of ^{2}H compared to ^{1}H in this respect is the relaxation mechanism that is governed by quadrupolar interactions for D_2O (I=1). Therefore, mainly intramolecular relaxation mechanisms are favored, which are hardly affected by paramagnetic impurities as for H_2O. As a consequence, for systems with an intrinsic porosity such as cellulose that contain water, the averaged longitudinal relaxation times are proportional to the surface-area-to-volume ratio of the pores. Models can be employed in order to distinguish between freely moving water and constrained water.[62–69] In a very convenient set of experiments, the change in porosity of biomass samples during sulfuric acid hydrolysis at 160°C was determined. It was shown that the relaxation times of populus biomass decreased from 23.9 to 36.3 ms after exposure for 60 minutes to H_2SO_4. These values correspond to an increase in pore size by a factor of 3.5 and that for the pore volume of 6.5. Also the effect on pore size of fibers upon drying and pressing was followed.[63] A decrease in the water content (e.g. by pressing or drying) leads to a decrease in the average pore size and results in a narrowing of the pore size distribution.

Finally, H/D exchange reactions on a variety of thin films have been performed in order to determine the water equilibrium content by a quartz crystal microbalance with dissipation unit. For this purpose the films are swollen in water for an extensive time before water is exchanged with D_2O. The difference in density and viscosity of D_2O and H_2O leads to large frequency shift. According to the equations firstly described by Kazagawa, the water equilibrium content can be simply obtained. The differences in viscosity/density of H_2O and D_2O have an impact on the resonance frequency of the respective solvent fraction and the changes of the solvent fraction $\Delta f_{solvent}$ can be expressed by the Kanazawa-Gordon equation (Eqn. 1.2.4)[70]:

$$\frac{\Delta f_{solvent}}{n} = -f_0^{3/2} \sqrt{\frac{\eta_l \rho_l}{\pi \rho_p \mu_p}} \qquad (1.2.4)$$

where n is the overtone number, f_0 the Eigenfrequency of the crystal (5 MHz), ρ_l is the density of the liquid (0.9982 g cm^{-3} for H_2O and 1.1050 g cm^{-3} for D_2O at 20°C, respectively), η_l is the viscosity of the liquid (1.002 cP for H_2O and 1.25 cP for D_2O at 20 °C respectively) while ρ_p and μ_p are the density and shear modulus of the quartz. The frequency of the bare substrate, $\Delta f_{bare,}$ can

be calculated by subtraction of Δf_{H2O} from Δf_{D2O} and the frequency shift due to the water content can be determined according to (Eqn. 1.2.5):

$$\frac{\Delta f_{H_2O}}{n} = \frac{\dfrac{\Delta f_{film}}{n} - \dfrac{\Delta f_{bare}}{n}}{\dfrac{\rho_{D_2O}}{\rho_{H_2O}} - 1} \qquad (\mathbf{1.2.5})$$

and the total water content Γ_{water} (also referred to as the surface concentration) can be calculated according to the Sauerbrey equation (Eqn. 1.2.6)[70]

$$\Gamma_{water} = -C \frac{\Delta f_{H_2O}}{n} \qquad (\mathbf{1.2.6})$$

where C is the Sauerbrey constant (17.7 ng cm^{-2} for a 5 MHz crystal). An overview of the behavior of the resonance frequency upon H_2O/D_2O solvent exchange is depicted in Figure 1.2.8. It turns out that the water equilibrium content of amorphous cellulose thin films is ca 50-70% related to the dry mass, whereas pre-dried films and pre-swollen/dried films show lower Γ (30 and 45% respectively).[71] Lately also thin films of nanofibrillar cellulose have been investigated with this approach, yielding values of 70-85%.[72]
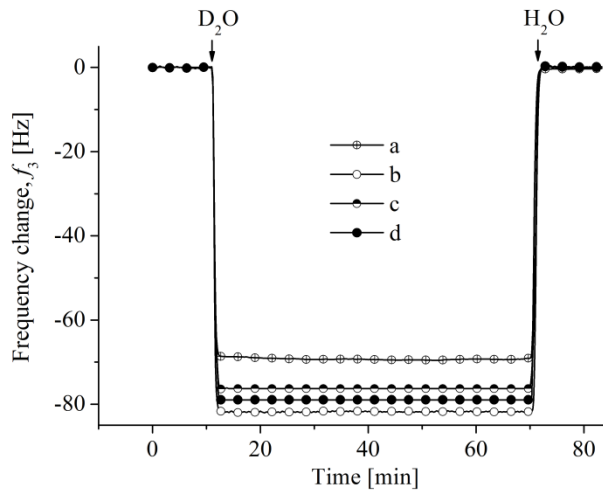
Figure 1.2.8. Effect of H_2O/D_2O solvent exchange on the QCM resonance frequencies. *a*: bare gold substrate, *b*: cellulose film (non-heat treated), *c*: cellulose film (heat treated), *d*: cellulose film (swollen and heat treated)

1.2.5 Summary and conclusion

Over the past 80 years the application of deuteration to cellulose has contributed significantly to the understanding of its supramolecular structure. The developments came in waves and in parallel to advances in analytical techniques. While the first studies by Bonhoeffer in 1938 mainly considered gravimetry, giving the first proof of the potential of heavy water in cellulose science, the use of FT-IR, particularly using polarized waves, allowed band assignment to given hydrogen bonds in cellulose. Later, the use of neutron scattering provided a tool to distinguish between amorphous and crystalline domains and later on also allowed a detailed analysis to unravel the hydrogen bonded network in different cellulose polymorphs. The last wave of efforts have focused on more complex systems such as wood samples and to understand how mechanical properties are influenced by changes at the molecular level. Most recently, the use of D_2O allowed the estimation of the amount of water in cellulose thin films, and open the way to learn about cellulose hydration and its behavior during the adsorption and interactions with biomolecules.

1.2.6 References

(1)   Bonhoeffer, K. F. *Z. Elektrochem.* **1934**, *40*, 469–474.

(2)   Staudinger, H. *Ber. Dtsch. Chem. Ges.* **1920**, *53*, 1073–1085.

(3)   Goldfinger, G.; Siggia, S.; Mark, H. *Ind. Eng. Chem.* **1943**, *35*, 1083–1086.

(4)   Champetier, G.; Viallard, R. *Bull. Soc. Chem.* **1938**, *5*, 1042–1048.

(5)   Frilette, V. J.; Hanle, J.; Mark, H. *J. Am. Chem. Soc.* **1948**, *70*, 1107–1113.

(6)   Kratky, O.; Mark, H. *Z. Phys. Chem.* **1937**, *B86*, 129–139.

(7)   Rowen, B. J. W.; Plyler, E. K. *Res. Pap. RP2080* **1950**, *44*, 313–320.

(8)   Mann, B. Y. J.; Marrinan, H. J. *Trans. Faraday Soc.* **1955**, *52*, 487–492.

(9)   Nickerson, R. F. *Ind. Eng. Chem.* **1942**, *84*, 1480–1485.

(10)   Almin, K. E. *Sven. Papp-Tidn.* **1952**, *55*, 767–770.

(11)   Mann, B. Y. J.; Marrinan, H. J. *Trans. Faraday Soc.* **1955**, *52*, 481–487.

(12)   Mann, B. Y. J.; Marrinan, H. J. *Trans. Faraday Soc.* **1955**, *52*, 492–497.

(13)   Hermans, P. H. *Makromol. Chem.* **1951**, *6*, 25–29.

(14)   Kratky, O.; Treiber, E. *Z. Elektrochem.* **1951**, *55*, 716–717.

(15)   Sidgwick, N. V. In *Chemical Elements and Their Compounds (Oxford University Press, London)*; 1950; Vol. I, p 56.

(16)   Tsuboi, M. *J. Polym. Sci.* **1957**, *25*, 159–171.

(17)   Sepall, O.; Mason, S. G. *Can. J. Chem.* **1961**, *39*, 1934–1943.

(18)   Sepall, O.; Mason, S. G. *Can. J. Chem.* **1961**, *39*, 1944–1955.

(19)   Sepall, O.; Lang, A. R. G.; Mason, S. G. *Can. J. Chem.* **1961**, *39*, 827–834.

(20)   Okajima, S.; Kai, A.; Technology, F. *J. Appl. Polym. Sci.* **1968**, *6*, 2801–2817.

(21)   Fischer, E. W.; Herchenroder, P.; Manley, R. S. J.; Stamm, M. *Macromolecules* **1978**, *11*, 213–217.

(22)   Atalla, R.; Van der Hart, D. *Science (80-.).* **1984**, *223*, 283–284.

(23)   Gardner, K. H.; Blackwell, J. *Biopolymers* **1974**, *13*, 1975–2001.

(24)   Sugiyama, J.; Chanzy, H.; Vuong, R. *Macromolecules* **1991**, *24*, 4168–4175.

(25)   Nishiyama, Y.; Okano, T.; Langan, P.; Chanzy, H. *Int. J. Biol. Macromol.* **1999**, *26*, 279–283.

(26)   Wada, M.; Okano, T.; Sugiyama, J. *Cellulose* **1997**, *4*, 221–232.

(27)   Nishiyama, Y.; Langan, P.; Chanzy, H. *J. Am. Chem. Soc.* **2002**, *124*, 9074–9082.

(28)   Nishiyama, Y.; Sugiyama, J.; Chanzy, H.; Langan, P. *J. Am. Chem. Soc.* **2003**, *125*, 14300–14306.

(29)   Langan, P.; Nishiyama, Y.; Chanzy, H. *J. Am. Chem. Soc.* **1999**, *121*, 9940–9946.

(30)   Steiner, T. *Angew. Chem.* **2002**, *114*, 50–80.

(31)   Jeffrey, G. A. In *Oxford University Press: Oxford*; 1997; p 272.

(32)   Gessler, K.; Krauss, N.; Steiner, T.; Betzl, C.; Sarko, A.; Saenger, W. *J. Am. Chem. Soc.*

1995, *117*, 11397.

(33)   Wada, M.; Chanzy, H.; Nishiyama, Y.; Langan, P. *Macromolecules* **2004**, *37*, 8548–8555.

(34)   Horikawa, Y.; Sugiyama, J. *Biomacromolecules* **2009**, *10*, 2235–2239.

(35)   Horikawa, Y.; Sugiyama, J. *Cellulose* **2007**, *15*, 419–424.

(36)   Crawshaw, J.; Vickers, M.; Briggs, N.; Heenan, R.; Cameron, R. *Polymer (Guildf).* **2000**, *41*, 1873–1881.

(37)   Evmenenko, G.; Alexeev, V.; Reynaers, H. *Polymer (Guildf).* **2000**, *41*, 1947–1951.

(38)   Kondo, T.; Sawatari, C. *Polymer (Guildf).* **1996**, *31*, 393–399.

(39)   Wadehra, I. L.; Manley, Rs.-J. *J. Appl. Polym. Sci.* **1965**, *9*, 2627–2630.

(40)   Jeffries, R. *J. Appl. Polym. Sci.* **1968**, *12*, 425–445.

(41)   Hishikawa, Y.; Togawa, E.; Kataoka, Y.; Kondo, T. *Polymer (Guildf).* **1999**, *40*, 7117–7124.

(42)   Hishikawa, Y.; Inoue, S.-I.; Magoshi, J.; Kondo, T. *Biomacromolecules* **2005**, *6*, 2468–2473.

(43)   Muller, M.; Czihak, C.; Schober, H.; Nishiyama, Y.; Vogl, G. *Macromolecules* **2000**, *33*, 1834–1840.

(44)   Hishikawa, Y.; Togawa, E.; Kondo, T. *Cellulose* **2010**, *17*, 539–545.

(45)   Tsuchikawa, S.; Siesler, H. W. *Appl. Spectrosc. Vol. 57, Issue 6, pp. 667-674* **2003**, *57*, 667–674.

(46)   Tsuchikawa, S.; Siesler, H. W. *Appl. Spectrosc.* **2003**, *57*, 675–681.

(47)   Tsuchikawa, S.; Yonenobu, H.; Siesler, H. W. *Analyst* **2005**, *130*, 379–384.

(48)   Suchy, M.; Virtanen, J.; Kontturi, E.; Vuorinen, T. *Biomacromolecules* **2010**, *11*, 515–520.

(49)   Suchy, M.; Kontturi, E.; Vuorinen, T. *Biomacromolecules* **2010**, *11*, 2161–2168.

(50)   Pönni, R.; Kontturi, E.; Vuorinen, T. *Carbohydr. Polym.* **2013**, *93*, 424–429.

(51)   Atalla, R. S.; Crowley, M. F.; Himmel, M. E.; Atalla, R. H. *Carbohydr. Polym.* **2014**, *100*, 2–8.

(52) Inagaki, T.; Siesler, H. W.; Mitsui, K.; Tsuchikawa, S. *Biomacromolecules* **2010**, *11*, 2300–2305.

(53) Yonenobu, H.; Tsuchikawa, S.; Sato, K. *Vib. Spectrosc.* **2009**, *51*, 100–104.

(54) Hofstetter, K.; Hinterstoisser, B.; Salmén, L. *Cellulose* **2006**, *13*, 131–145.

(55) Sturcová, A.; Eichhorn, S. J.; Jarvis, M. C. *Biomacromolecules* **2006**, *7*, 2688–2691.

(56) Jarvis, M. C.; McCann, M. C. *Plant Physiol. Biochem.* **2000**, *38*, 1–13.

(57) Bali, G.; Foston, M. B.; O'Neill, H. M.; Evans, B. R.; He, J.; Ragauskas, A. J. *Carbohydr. Res.* **2013**, *374*, 82–88.

(58) Matsumura, K.; Hayamizu, K.; Yamamoto, O. *J. Polym. Sci., B Polym. Phys.* **1989**, *27*, 2407–2418.

(59) Li, T.-Q. *Appl. Spectrosc.* **1996**, *50*, 1512–1518.

(60) Foston, M.; Ragauskas, A. *Energ. Fuels* **2010**, *24*, 5677–5685.

(61) Li, T.-Q.; Henriksson, U.; Eriksson, J. C.; Odberg, L. *Langmuir* **1992**, *8*, 680–686.

(62) Vittadini, E.; Dickinson, L. C.; Chinachoti, P. *Carbohydr. Polym.* **2001**, *46*, 49–57.

(63) Haggkvist, M.; Li, T.-Q.; Odberg, L. *Cellulose* **1998**, *5*, 33–49.

(64) Gallegos, D.; Munn, K.; Smith, D.; Stermer, D. *J. Colloid Interface Sci.* **1987**, *119*, 127–140.

(65) Gallegos, D.; Smith, D. *J. Colloid Interface Sci.* **1988**, *122*, 143–153.

(66) Gallegos, D.; Smith, D.; Brinker, J. *J. Colloid Interface Sci.* **1988**, *124*, 186–198.

(67) Glaves, C.; Frye, G.; Smith, D.; Brinker, C.; Datye, A.; Ricco, A.; Martin, S. *Langmuir* **1989**, *5*, 459–466.

(68) Glaves, C.; Smith, D. *J. Membr. Sci.* **1989**, *46*, 167–184.

(69) Li, T.; Henriksson, U. *Nord. Pulp Pap. Res. J.* **1993**, *3*, 326–330.

(70) Kanazawa, K. K.; Gordon, J. G. *Anal. Chem.* **1985**, *57*, 1770–1771.

(71) Mohan, T.; Spirk, S.; Kargl, R.; Doliška, A.; Vesel, A.; Salzmann, I.; Resel, R.; Ribitsch, V.; Stana-Kleinschek, K. *Soft Matter* **2012**, *8*, 9807–9815.

(72) Kontturi, K. S.; Kontturi, E.; Laine, J. *J. Mater. Chem. A* **2013**, *1*, 13655–13663.

Chapter 2

## 2. Infrared Spectroscopy Study on Deuterated Cellulose Thin Films

The following chapter is based on chapter xx and describes the deuteration of cellulose in form of thin films to exclude bulk effects. These films are further characterized by ATR-IR spectroscopy. The replacement of hydrogen against deuterium should lead to better resolved IR spectra and changes in supramolecular structure as well information about accessibility can be easier followed. The main difference between the above described literature and the results of this chapter is the amount of material and the deuteration conditions. Furthermore, for following experiments it is crucial that the cellulose samples have highly amorphous character.

2.1 Materials and Methods

Materials. Trimethylsilyl-cellulose (TMSC; DS: 2.7-2.9) obtained from Avicel pulp, purchased from TITK Rudolstadt MFSA, was used as starting material for the film preparation. Methylene chloride (99 wt%), acetone (99 wt%) and sulfuric acid (95 wt%) were purchased from VWR chemicals, hydrogen peroxide (30 wt%), deutero-chloroform (99 wt%), deuterium oxide (99 wt%), deuterium acid (35 wt%) and hydrochloric acid (37 wt%) from Sigma-Aldrich. All chemicals were used without purification. Au-coated glass slides as substrate (SPR102-AU), Filter Chromafil® Xtra PVDF-45/25 0.45 μm, petri dishes (20 ml; 5 cm diameter) were used as obtained.

Film Preparation. The gold sensor slides (2 x 1 cm²) were cleaned in "piranha" acid ($H_2SO_4:H_2O_2 = 7:3$ (v/v)) for 10 min and neutralized afterwards with distilled water. For the film preparation TMSC was dissolved in $CDCl_3$ (15 mg/ml; 60 mg/ml) filtered and spin coated on the gold substrate at 4000 rpm for 60s (acceleration 2500 rpm/s). The TMSC films were exposed to HCl vapor (12 wt%) for 12 min to obtain full regenerated cellulose thin films.

Deuteration. The deuteration of the cellulose samples were done by two different procedures. The first common possibility is to use D_2O vapor for the direct deuteration of cellulose, in our case after regeneration of TMSC. In the second procedure DCl vapor is used for a one-step regeneration and deuteration of TMSC (scheme 2.1). For both procedures the films were placed in a petri dish beside liquid DCl (12 wt%) or D_2O.
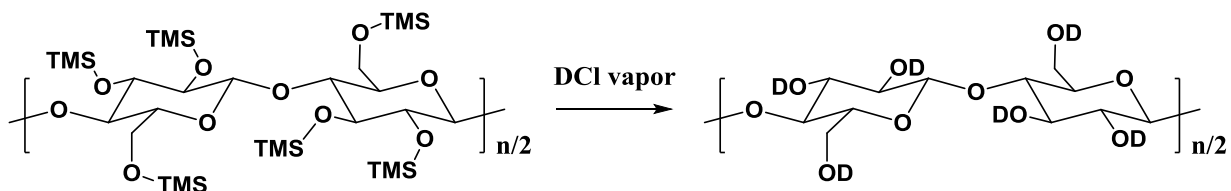

Scheme 2.1. Regeneration and deuteration of trimethylsilyl-cellulose.

ATR-IR Spectroscopy. The experiments were performed with an ALPHA FT-IR spectrometer (Bruker; Billerica, MA, USA). For the measurement an attenuated total reflection (ATR) attachment was used with 48 scans at a resolution of 4 cm^{-1} and a scan range between 4000 and 400 cm^{-1}. The data were analyzed with OPUS 4.0 software.

2.2 Results and Discussion

In a first pioneering experiment, TMSC powder was regenerated and deuterated in a one-step reaction by vapors of DCl. The powder was placed next to freshly prepared DCl solution (17 wt% in D_2O) in a petri dish for 170 min (corresponds to literature for fibers and foils) and monitored by ATR-IR spectroscopy. The obtained results in Figure 2.1 (A) show that it is possible to regenerate TMSC to cellulose with DCl. The cellulose exhibit undeuterated –OH groups (band at 3400 cm^{-1}). This result is surprising, because for fibers longer re-hydration times (hours to days) are reported. A potential explanation might be the accessibility of the film in combination with the abundant atmosphere during the IR measurement. Afterwards, the same experiment was performed with an approximately 50 nm thin cellulose film (12 min regeneration

time). The samples were immediately measured (1-2 sec) after they were taken out of the protective deuterated atmosphere to reduce the possible influence of re-hydration.
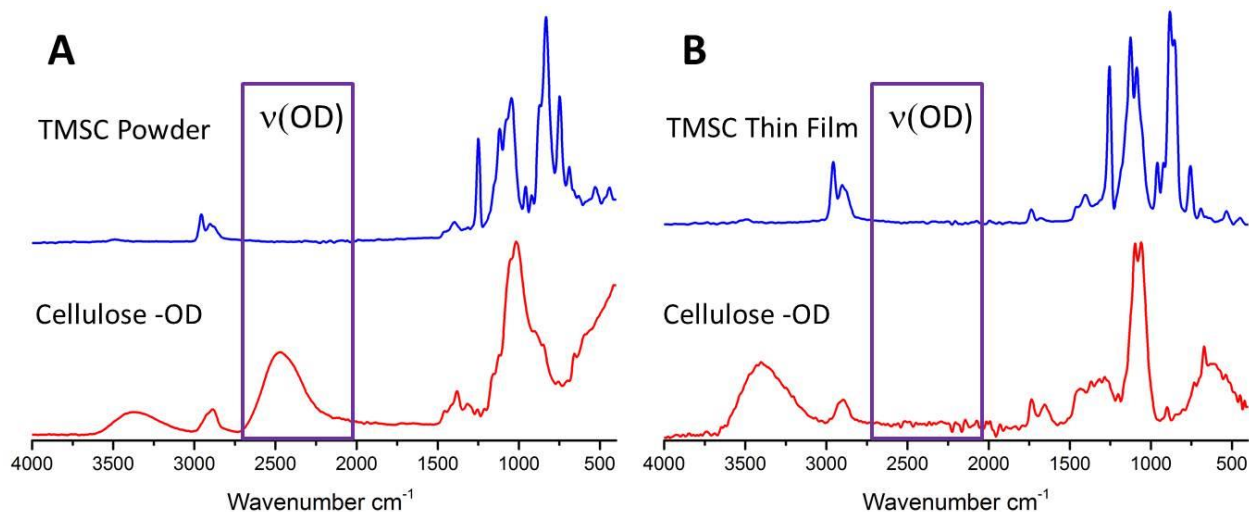
**Figure 2.1.** ATR-IR spectrum of deuterated cellulose powder (A) and cellulose thin film (B).

Surprisingly, IR spectroscopy (Figure 2.1 B) reveals a typical spectrum for cellulose without any deuteration. Although the sample was measured immediately the accessibility of the film and therefore the H/D exchange rate seemed to be too high to accomplish for complete re-hydration. However, for that reason the IR spectrometer was moved into a mobile glovebox and the measurements were performed under nitrogen-purged and phosphor pentoxide dried atmosphere. Beside the equipment also the samples were prepared inside the glovebox to avoid water adhesion on the substrate and the material. Furthermore, the surface of the IR spectrometer was saturated by D_2O. To explore the potential influence of a monolayer of water on the surface of the gold substrate, a 2 μm thick cellulose thin film and a free standing (~ 2 μm) film were also prepared. These two samples were regenerated due to their thickness for 100 min. The results of these four samples are shown in Figure 2.2 (A).
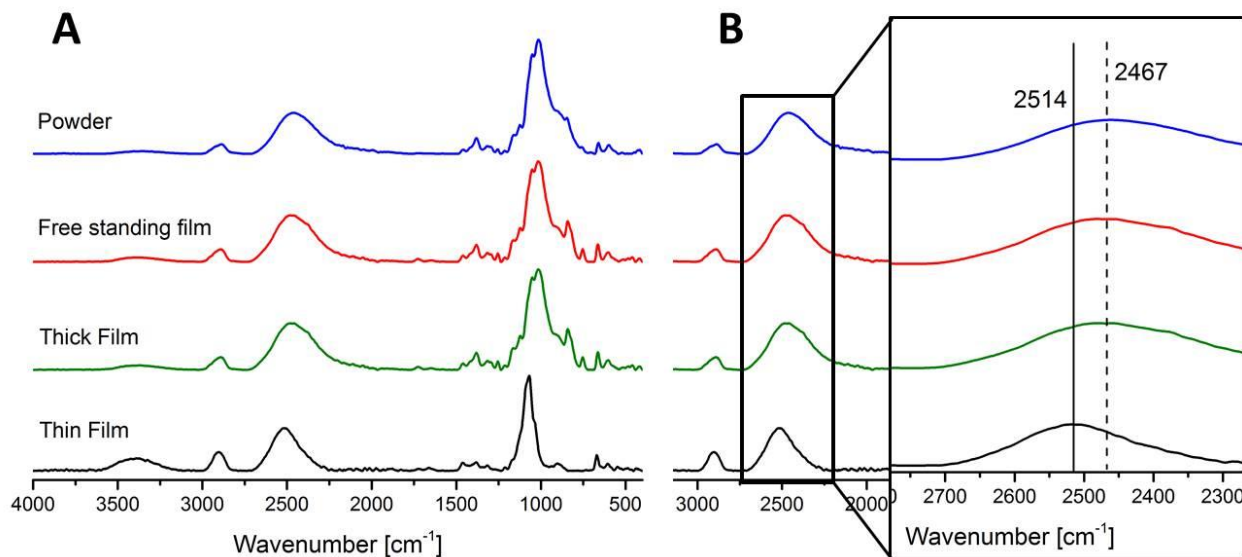
Figure 2.2. Comparison of deuterated cellulose materials (A) and zoom (B).

Under these inert conditions all –OH groups of the cellulose powder had been deuterated. Unfortunately, the thick and free standing cellulose film have again a small amount of re-hydrated –OH groups. Obviously, this effect is coherent with the decreased amount of material and the associated increase of accessibility. However, these results reveal that the substrate has not a large impact on the degree of deuteration. Furthermore, the trend of re-hydration becomes more evident for the 50 nm thin films. Interestingly, the maximum of the –OD band is shifted for the thin film compared to the thicker samples (Figure 2.2 (B)). This indicates a different hydrogen bonding mode which related to the film thickness. A more precise statement about the changes in supramolecular structure is not possible with this data. Moreover, attempts were made to saturate the dry nitrogen atmosphere in the glovebox with deuterium by evaporation of liquid D_2O but also this step did not have any positive influence on the degree of deuteration of the thin samples. The same result was obtained by the interaction of deuterated cellulose samples with D_2O vapor in a covered petri dish for post-regeneration deuteration. The last deliberation to impede the re-hydration was to capture the deuterium by heating inside the structure like it had been reported for pulp in the literature[1,2]. For this purpose, the sample was covered with liquid D_2O after the regeneration and dried at 105°C for 1h on a heating plate. Afterwards the samples

were analyzed by ATR-IR. Surprisingly, the IR measurement revealed that the heating of the thicker sample led to a shift of the -OD (2514 cm^{-1}) band to the same value like the thin samples (Figure 2.3 (A)), indicating a rearrangement of the cellulose structure. For the thicker samples as well for the powder the heat treatment did not have any further influence.
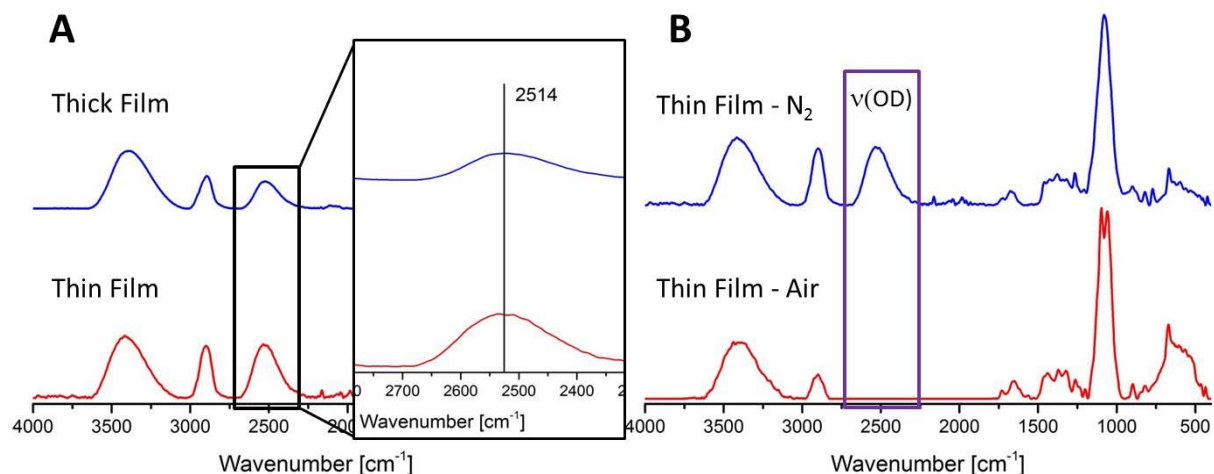
Figure 2.3. A) Heat treated thin film compared with thick samples; B) Heat treated thin film exposed to abundant atmosphere.

Afterwards, the thin samples (heated) were exposed to abundant atmosphere for 30 sec to test the deuterium capturing (Figure 2.3 (B)). Unfortunately, this short period was sufficient for complete re-hydration of the material which reveals that the heat treatment process did not yield in permanent deuteration. Finally, this study showed that the accessibility of cellulose films increase with decreasing film thickness. Furthermore, it seems that the hydrogen bonding mode is depending on the film thickness and further it can be adjusted by heat treatment. Regrettably, also the heat treatment does not lead to permanent deuteration inside the cellulose. For more meaningful statements the conditions which can be provided for the film preparation and ATR-IR measurements were insufficient for a complete deuteration of cellulose samples with high accessibility.

2.3 References

(1)   Pönni, R.; Galvis, L.; Vuorinen, T. *Carbohydr. Polym.* **2014**, *101*, 792–797.

(2)   Pönni, R.; Kontturi, E.; Vuorinen, T. *Carbohydr. Polym.* **2013**, *93*, 424–429.

Chapter 3

3. Tuning the Humidity Response of Two Dimensionally Confined Biopolymer Thin Films[1]

The following chapter is written for the submission in Biomacromolecules:

(1)   David Reishofer, Jürgen Sattelkow, Wolfgang J. Fischer, Katrin Niegelhell, Roland Resel, Gerhard Drexler, Heinz Amenitsch, Harald Plank, Tekla Tammelin, Eero Kontturi, Stefan Spirk, *Biomacromolecules*, **2016**

The humidity response of different dimensionally confined ultrathin cellulose films is investigated as a function of industrially relevant treatments using different techniques. As treatments, drying at elevated temperature, swelling and swelling followed by drying at elevated temperatures were chosen. The cellulose films have been prepared by spin coating a soluble cellulose derivative, trimethylsilyl cellulose onto solid substrates followed by conversion to cellulose using HCl vapors. For the highest investigated humidity levels (97%), layer thickness increased by ca 40% corresponding to the incorporation of ca 3.6 molecules of water per anhydroglucose unit, independently on the used cellulose source. The treatments affected this ratio significantly with drying being the most notable procedure (2.1 and 2.6 molecules per AGU).

This process was investigated in real time with XRR, SAXS and QCM-D equipped with a humidity module to obtain information about changes of the thickness, roughness and electron density of the films.

3.1 Introduction

The interaction of water vapor with surfaces represents one of the crucial aspects to be considered in technology development, exploitation and product engineering.[1] This is particularly prominent with soft materials like polymers because vapor can penetrate the chain network, altering its properties. Indeed, the control over water vapor migration through or into a material (e.g. a membrane or a film) is pivotal in many cases when realizing or triggering certain materials characteristics. For synthetic hydrophobic polymers, the vapor transport is often straightforward to monitor, model, and control.[2] The major interactions comprise diffusion into and out of the polymer as well as adsorption/desorption phenomena.[3] For biopolymers, however, the case is more complicated. They usually form hydrophilic, porous networks that swell considerably when exposed to water vapor, rendering the solution-diffusion model inapplicable.[4] One of the more intricate cases with biopolymers is cellulose, the main ingredient of all plants. Cellulose forms highly specific semi-crystalline microfibrils which are further organized into complex hierarchical superstructures in plant fibers. Water interactions are highly relevant for the fibers in their native growth environment[5] and they are equally important for the manifold applications of cellulose fibers[6-8] as well as for modern usages designed for various nanocellulose grades.[9-13] In this realm, many studies exist on the vapor transport mechanisms in macroscopic products prepared from cellulose fibers, such as paper and textiles or regenerated films and fibers.[3, 14-19] In addition, commendable efforts have been undertaken to model the vapor transport through certain cellulose-based structures.[20, 21]

Such studies are generally driven by industrial applications and they are specific to the relevant macroscopic structures where multi-scale morphology plays a significant role. In this fundamental contribution, we aim at minimizing the morphological contribution to as small as possible by monitoring the water vapor interactions in homogeneous, two-dimensionally confined ultrathin films of highly amorphous cellulose. This way, we are capable to gain fundamental information on the influence of various industrially relevant treatments on the vapor uptake of cellulose and these results are not obfuscated with the morphology factor. The treatments prior to water vapor uptake measurements comprise drying (105°C for 1 h), swelling, and swelling/drying (105°C for 1 h). The films were prepared from trimethylsilyl cellulose

(TMSC) which was regenerated into cellulose after film deposition by spin coating. Two different TMSC grades were employed, featuring different solubility due to a difference in the degree of substitution. Moreover, the film structure was tuned by the use of two different solvents (chloroform and THF) in the spin coating step. The surface morphology of the films was characterized by atomic force microscopy and the mechanical properties (stiffness) by nanoindentation. The water vapor uptake was followed by in-situ by x-ray reflectivity (XRR) and quartz crystal microbalance with dissipation monitoring (QCM-D). This study is related to recently published studies on the water uptake of various cellulose thin films[22-24] but here the approach is more revealing for the molecular arrangements of water molecules inside homogeneous cellulose layers with subtle systematic variations. The results revealed a complex ordering of water to, at times, three different layers within the film, laying the groundwork for profound understanding of vapor-cellulose interactions and their explicit utilization in modern applications.

3.2 Materials and Methods

Materials. Trimethylsilyl-cellulose (TMSC; from MCC, DS: 2.7-2.9; from spruce pulp, DS: 2.0), purchased from TITK Rudolstadt MFSA, were used as starting materials for the thin film preparation. Hydrochloric acid (37 wt%), chloroform (99 wt%), THF (99 wt%) and sulfuric acid (95 wt%) were purchased from VWR chemicals and hydrogen peroxide (30 wt%) from Sigma-Aldrich. All chemicals were used without purification. Silicon wafer, gold QCM-D sensors purchased from Q-Sense, AB, Gothenburg, Sweden (fundamental resonance frequency, $f0 = 5$ MHz; sensitivity constant, $C = -0.177$ mg·m−2·Hz−1), Filter Chromafil® Xtra PVDF-45/25 0.45 µm and petri dishes (20 ml; 5 cm diameter) were used as obtained.

Film preparation. The silicon wafer substrates (native oxide layer, 1.4 x 1.4 cm²) for the XRR measurements were cleaned with "piranha" acid ($H_2SO_4:H_2O_2 = 7:3$ (v/v)) for 30 min and neutralized afterwards with distilled water. QCM-D gold quartz crystals were cleaned with a UV ozone cleaner (Bioforce Nanosciences Inc., California, USA) for a minimum of 20 min. For the preparation of the cellulose thin films two different trimethylsilyl-celluloses (TMSCA, from

MCC, 2.7-2.9; TMSCS, from spruce, DS: 2.0) were employed and dissolved in chloroform (TMSCA: 15 mg·ml-1) and tetrahydrofuran (TMSCS: 9 mg·ml-1). Afterwards, the solutions were filtered and used to prepare thin films via spin coating (4000 rpm, 2500 rpm·s, 60 s) on QCM-D gold quartz crystals and silicon wafers. The film thickness of the TMSC films was approximately 150 nm. In the next step the films were regenerated using 12 wt% HCl vapor for 12 min.[25] After the regeneration, the cellulose samples were subjected to different treatments (drying at 105°C for one hour, swelling with distilled H2O for 30 min, swelling with distilled H2O for 30 min followed by drying at 105°C for one hour).

Atomic force microscopy. Measurements have been performed with a FastScanBio platform operated by a Nanoscope V controller (Bruker Nano Surface Offices, Santa Barbara, CA). Nanomechanical characterization was executed in PeakForce-mode providing additional information on Young modulus, sample adhesion, energy dissipation, and surface deformation with laterally resolved character. All measurements were performed in an air conditioned environment (21°C) under an acoustical enclosure box. All experiment used RTESPA-300 (Bruker AFM Probes, Camarillo, CA) cantilever with nominal spring constants of 40 N/m. Calibration was done for each tip using the calibration kit PFQNM-SMPKIT-12M (Bruker AFM Probes, Camarillo, CA). Deflection sensitivity was ramped against sapphire, cantilevers spring constant were evaluated by thermal tune and tip end radii were estimated via a defined titanium-oxide roughness sample. First TMSC and cellulose samples from spin coating and post treatment were carefully scratched with a sharp razor blade to create a mark in the layer with silicon oxide as level zero. At least four different areas per sample have been investigated with minimum two measurements at the scratched edges and at top layer positions, each. Experimental parameters were optimized to obtain stable imaging conditions with lowest possible energy dissipation and sample deformation.

X-ray reflectivity. X-ray reflectivity (XRR) measurements were performed using a PANalytical Empyrean goniometer system with radiation produced by a copper sealed tube (λ= 0.154178 nm). The primary side of the reflectometer was equipped with a 20 mm beam mask, a multilayer mirror, a 1/32° slit, and an automatic beam attenuator. On the secondary side, a receiving slit of 0.1 mm and a Soller slit of 0.02 rad were used in front the PANalytical PIXEL3D

point detector. The sample stage was a domed DHS 900 from Anton Paar[26], equipped with a SHT15 humidity sensor to monitor the relative humidity and the temperature during the in situ swelling measurements. The relative humidity (RH) was controlled using a S-503 humidity generator from Michell instruments. For each humidity step an equilibration time of 30 minutes was accomplished. XRR measurements were performed in the 2θ region 0.030–9.999° with a step size of 0.006°. The evaluation of the data was performed with the X'Pert Reflectivity (Panalytical, $C_6H_{10}O_5$ for cellulose was used) software package providing information on the electron density, layer thickness and the roughness of the films by applying Parrat[27] formalism and the disturbance term of Nevot–Croce[28].

Quartz crystal microbalance with dissipation (QCM-D). Water vapor absorption experiments were carried out in a QCM-D (Q-Sense, AB, Gothenburg, Sweden) equipped with a humidity module (QHM 401). The frequencies of the pure QCM-D sensor crystal and of the spin-coated starting areal mass were determined in air. At the beginning of the water vapor absorption experiments the samples were allowed to equilibrate at 11 %RH (saturated LiCl solution) for 18 hours to obtain a stable baseline. For the following humidity steps stable values were adjusted by suitable salt solution (11 → 33 → 53 → 75 → 97 %RH) after 30 min of equilibration (100 µl/min at 23°C). For the highest humidity level (97 %RH) equilibration was done for 45 minutes. More information on the used salts can be found in the Supporting Information. The collected frequency data were stitched together using QTools Software and the areal mass as well as the film thickness were calculated according to the Sauerbrey equation (3.1):

$$\Delta m = -C \frac{\Delta f_n}{n} \ \textbf{(3.1)}$$

where n is the measurement overtone number (n = 1, 3, 5, 7, ...), $\Delta f_n = f_n - f_0$ is the resonance frequency, and C is the sensitivity constant of the sensor. For the calculation of the film thickness of the samples the individual starting area mass (Δf_3) of the samples and the calculated densities of the XRR measurements were used. The samples were stored in a desiccator to protect them from environmental influences and taken out 15 min before measurement started.

GI-SAXS. The *in situ* GI-SAXS experiments were performed at the high-flux SAXS beamline at Elettra synchrotrone in Triest, Italy, with an X-ray energy of 8 keV (λ = 1.54 nm). The sample stage was a domed DHS 900 from Anton Paar. As detection system a 2D Pilatus 100k Detector System was used. The sensitive area is 470×200 pixels (72.3×33.3 mm^2) with a pixel size of 172×172 μm^2. As calibration standard silver behenate with a lamellar spacing of 58.38 Å was used. The sample-to-detector distance was determined to be 1911.5 mm and the incidence angle was set to 0.35°. For the generation of the relative humidity a S-503 humidity generator from Michell instruments was used.

3.3 Results and Discussion

A very common procedure to prepare cellulose ultrathin films is to employ acid labile trimethylsilyl cellulose which is deposited by spin coating onto silicon wafers and subsequently exposed to HCl vapors. This exposure cleaves off the silyl groups leaving a rather amorphous cellulose thin film. Since the solvent's vapor pressure can affect the film structure, two different TMSC derivatives featuring a different solubility behavior ($CHCl_3$ and THF) and molecular mass (Mw: 70 vs 120 kDa were selected to prepare cellulose thin films. In the following, the cellulose films derived from $TMSC_A$ are denoted as $Cell_A$ whereas those from $TMSC_S$ are denoted as $Cell_S$.

The AFM images of the two differently prepared cellulose films are depicted in Figure 3.1. All of these surfaces were rather featureless with the exception being the dried $Cell_A$ sample. Here, aggregation into rod like features was observed which was reflected in an increased roughness compared to the other samples as well (2.1±0.1 vs 1.4-1.5±0.1 nm, Table 3.1). However, the $Cell_S$ samples differed in this respect since the non-treated and the dried sample featured nearly the same roughness (1.4 vs 1.5±0.2 nm).

Table 3.1. Comparison of surface roughness determined by AFM and XRR. Further average stiffness determined by AFM is shown.

	$Cell_A$			$Cell_S$		
	XRR	AFM		XRR	AFM	
	RMS [nm]	RMS [nm]	stiffness [Gpa]	RMS [nm]	RMS [nm]	stiffness [Gpa]
non-treated	1.5	1.6	4.0±1.2	1.5	1.5	5.5±0.5
dried	2.1	2.8	4.9±0.8	1.6	1.7	6.0±0.5
swollen	1.5	1.5	4.5±1.3	1.1	1.7	6.0±0.5
swollen/dried	1.4	1.7	4.8±1.0	1.2	1.4	6.0±0.5

This is a very interesting finding since it gives a hint that these two cellulose films differ from each other. In order to explore whether there are further differences, AFM nanoindentation experiments were performed which showed two trends. First, $Cell_S$ samples exhibited much higher stiffnesses than the $Cell_A$ whereas the non-treated films exhibited the largest discrepancy with 4.0±1.2 and 5.5±0.5 GPa respectively. Second, for both films the non-treated samples displayed a lower stiffness than those which had been subjected to different treatments. For $Cell_A$, the treated films were in a range from 4.5±1.3 (swollen) to 4.9±0.8 GPa (dried), while for $Cell_S$ the stiffness did not significantly vary for the differently treated samples (5.9-6.0±0.5 GPa). For all nanoindentation experiments, the calibration of the measurement was done using a calibration kit and further more reference measurements at a scratch in the thin film giving silicon as a reference surface, which allows for obtaining quantitatively comparable data (Table 3.1).
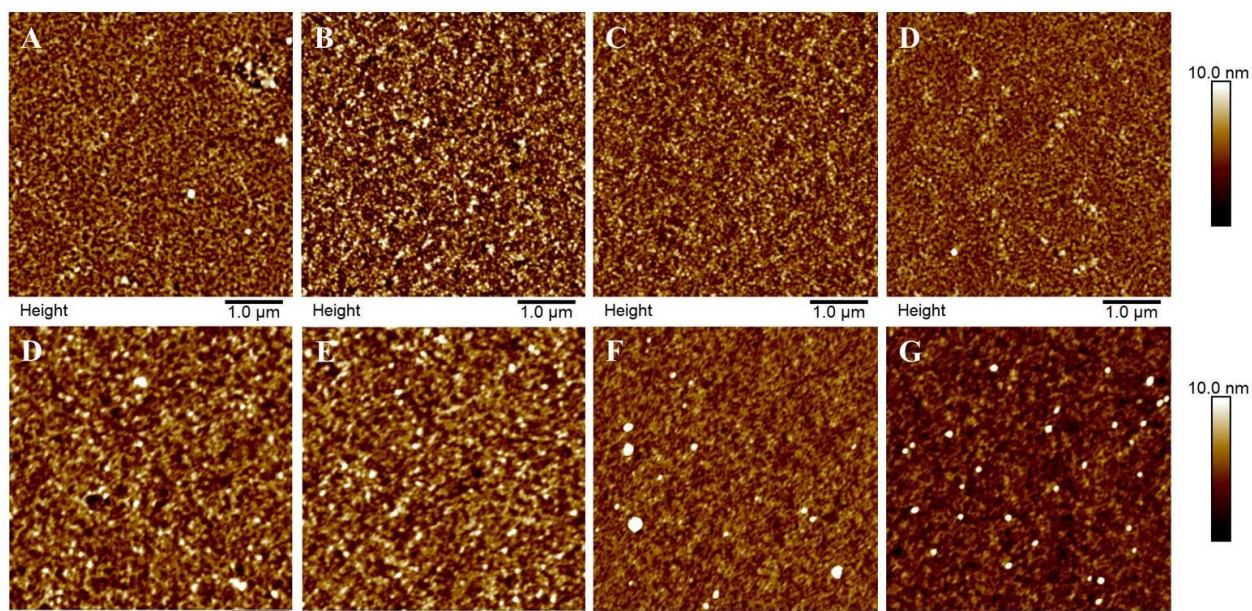
Figure 3.1. AFM topography images (5 x 5 μm^2) of the differently prepared cellulose films before and after the different treatments. A-D: Cell$_A$, A: non-treated, B: dried, C: swollen, D: swollen/dried, E-G: Cell$_S$ E: non-treated, F: dried, G: swollen, H: swollen/dried).

The water vapor uptake was first monitored XRR since it provides insights into changes in film thickness, density as well as on the roughness of the films. The obtained XRR curves and the corresponding layer fits are shown in Figure 3.2 for the non-treated and the dried samples. More data is available in the SI (Figure S3.1).
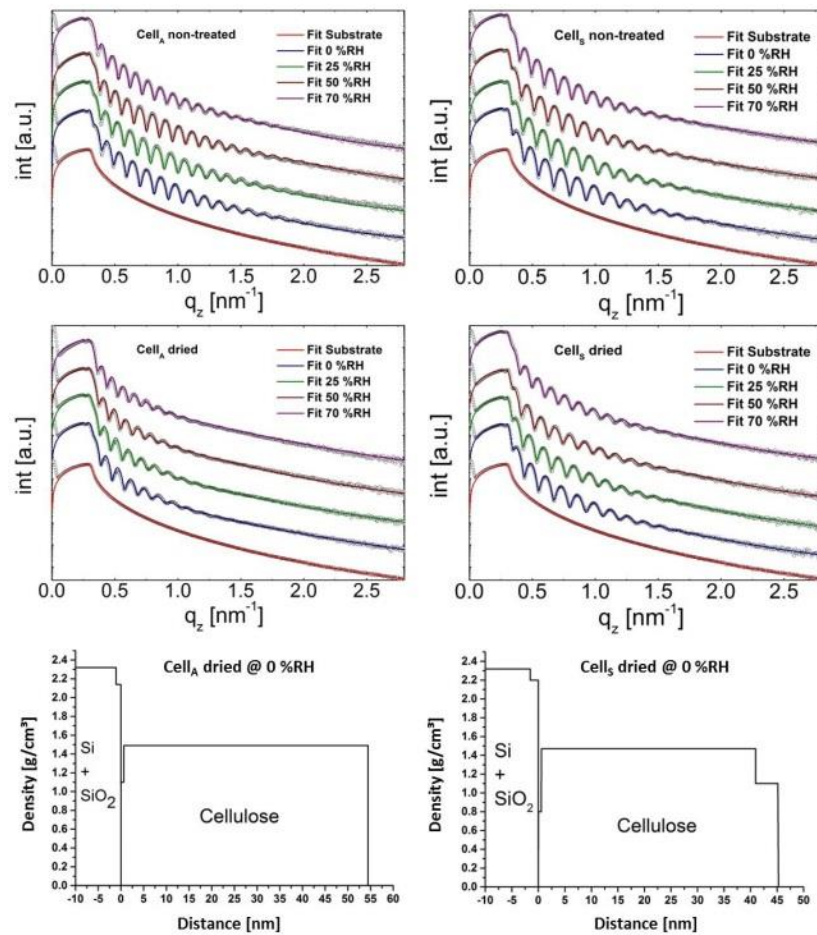
Figure 3.2. XRR curves and corresponding layer fit of the two different cellulose films (Cell$_A$, left column; Cell$_S$, right column) samples.

The XRR data revealed that a multilayer approach with varying densities of the respective layers was required to fit the data. Such multilayer fittings can be physically related to the different mass densities of films at the respective interfaces (e.g., cellulose-substrate or cellulose-air). As a consequence, a local statistical density distribution was obtained as already shown earlier.[29] For the Cell$_A$ samples, a two-layer model fit and for the Cell$_S$ ones a three-layer model fit yielded excellent agreement between the data and the fit. Similar as for the AFM data, also the XRR results revealed some differences between the two different cellulose samples.

The XRR investigations (for comprehensive data see Table S1 and S2; SI) revealed that the initial film thickness at 0 %RH of the $Cell_A$ samples is slightly higher (51±3 nm) than those of $Cell_S$ (43±2 nm). As relative humidity increases, the fringes of the cellulose film shifted to a lower q_z indicating that the films start to incorporate water vapor thereby increasing film thickness. At 25 %RH, all $Cell_A$ samples exhibited a similar relative increase in layer thickness (~3.8%) independently of whether they had been subjected to treatments or not (Figure 3.3). However, at 50 %RH alterations in the behavior of the differently treated samples started to evolve. The dried samples for instance were prone to a lower water vapor uptake compared to the other films (7.2 vs 9.5% thickness increase). This behavior was even more pronounced at 70% RH where the dried films feature a relative film thickness increase of 12.2% whereas the other samples exhibited a higher relative increase (~15.2%). By increasing RH from 50 to 70% water uptake increased non-linearly. The $Cell_S$ samples (Figure 3.3, B) displayed the same trends but there were some distinct differences, particularly for the treated films. While water vapor uptake of the non-treated films equaled the $Cell_A$ films, the extent of water vapor uptake for the swollen films was rather high, particularly at high RH. For instance, the swollen $Cell_S$ samples exhibited a relative thickness increase of 16.8% while for the $Cell_A$ samples only 15% increase was observed. Another remarkable difference was the rather low impact of heating on the water vapor uptake capacity even at high RH for the $Cell_S$ samples (comp. at 70 %RH, 14.8 vs 12% relative increase).
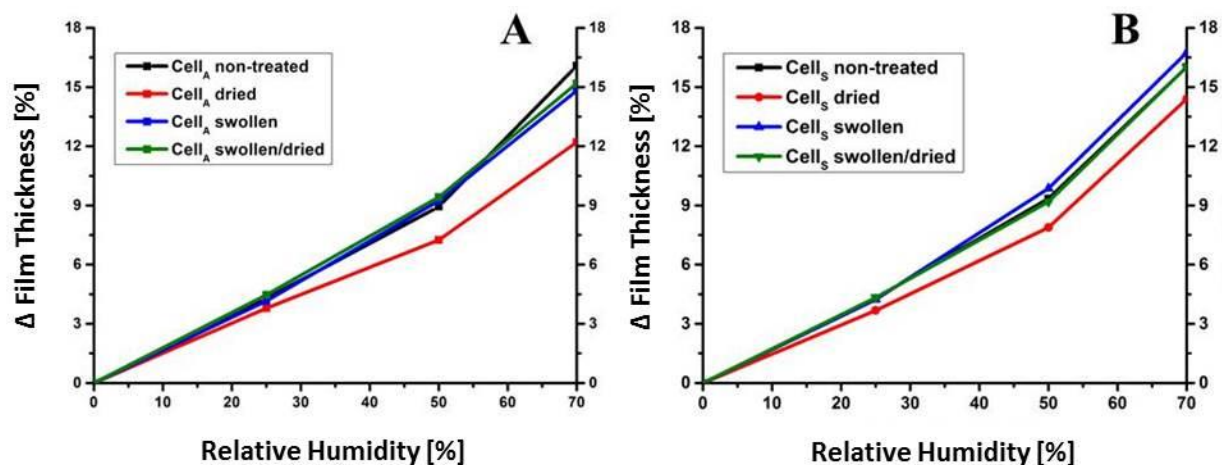
Figure 3.3. Film thickness increase at different humidity levels determined by XRR measurements during the water vapor uptake process. A) $Cell_A$ samples B) $Cell_S$ samples.

An appealing feature of XRR measurements in these experiments is to obtain roughness values as a function of RH. Surprisingly, the impact of humidity on the surface roughness of the films was rather low and just slight changes in the range of max. 0.3 nm were noticeable. As for the AFM studies, the dried $Cell_A$ samples exhibited the highest roughness (2.8 nm at 0 %RH). For the $Cell_S$ samples, similar trends were observed albeit the films were slightly smoother and also the difference in roughness to the heat treated films was not as pronounced (1.6 vs 1.8 nm for non-treated vs dried; Table 1, and Figure S3.1, SI). As mentioned above, the cellulose layer was fitted by a two and three layer model considering the different cases at the interfaces. This is particularly interesting since it allows for making statements on the arrangement of cellulose molecules at the substrate interface. Interestingly, the thickness of the cellulose layer between the substrate and the cellulose 'bulk' was in a range between 0.5 and 0.7 nm at 0 %RH for all films (Table S2, SI), corresponding to a mono- or bilayer of cellulose molecules (compare thickness of graphene monolayers: 0.3 nm). The impact of humidity on this layer in terms of thickness was proven to be negligible for most cases and hardly any variations could be observed. Further, the density of this layer for the non-treated films indicated that the rather rigid cellulose molecules were not able to perfectly cover the whole SiO_2 surface, probably resulting in the formation of voids inaccessible to water vapor.

For the Cell$_S$ samples, the inclusion of an additional layer was required which reflected alterations at the cellulose-air interface. This layer had a thickness in the range of 4.5 nm and showed a decreased density (1.0-1.2 g·cm^{-3} at 0 %RH) compared to the bulk cellulose.

The incorporation of water vapor into the film structure can influence the density in two ways. First, the filling of gaps, i.e. replacement of air against water will increase the density of the films. Second, if the water was directly incorporated into the cellulose supramolecular structure, the resulting electron density should be smaller than those of the cellulose itself.

The density for most of the cellulose 'bulk' layers as determined by XRR is in the range for amorphous cellulose (1.48 g cm^{-3}).[30, 31] Accordingly, the vapor uptake leads to decreasing density of most of the films by increasing humidity levels (Table S3.5, SI). Densities decrease down to 1.35 g cm^{-3} for both samples at humidity levels of 70 %RH. For both samples, there is just one exception, namely the pre-swollen films. For CelL$_A$, the films show already higher densities at 0 %RH than all the other films (1.54 g cm^{-3}) and also the interfacial layer features a rather high density (1.42 g cm^{-3}). When just looking at this data, it seems that the swelling induced some rearrangement of the cellulose chains leading to tighter packing. If we consider that parts of the films may be capable to crystallize, and considering the density of crystalline cellulose (1.6 g cm^{-3}) one may end up with a degree of crystallinity of ca 50%. In contrast, the swelling of the Cell$_S$ sample results in rather low densities even at 0 %RH (1.38 g cm^{-3}) We will discuss these points later on in combination with densities obtained by QCM-D data.

In order to validate the results obtained by XRR, a second technique was employed to determine the water vapor uptake capacity of the cellulose films. For this purpose, QCM-D measurements equipped with a humidity module were performed. Since the setup of the QCM-D uses water vapor permeable membranes to adjust RH, even higher RH (up to 97%) can be realized which is not feasible with our XRR equipment due to condensation at the chamber walls. While XRR is a spectroscopic technique, QCM-D exploits gravimetric principles based on the Sauerbrey equation which relates the Eigenfrequency of a resonating system to its mass. In more detail, the change in frequency (Δf) of a QCM-D sensor allows for monitoring changes in the film mass thereby providing information on the mass of absorbed water vapor on/in the sample.

It can be clearly seen that an increase of the RH leads to a negative change in frequency, which correlates with an increase in film mass (Figure 3.4).
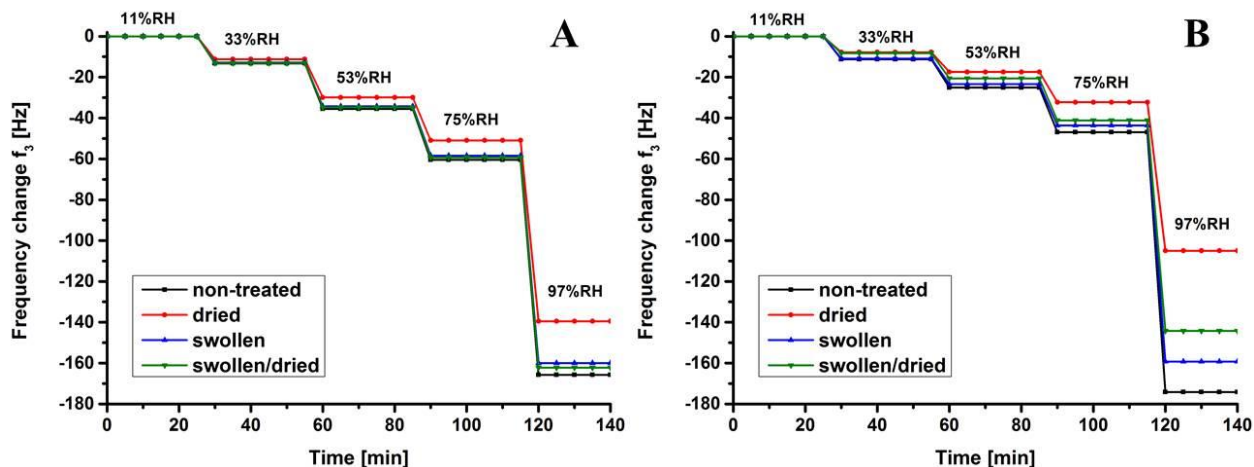
Figure 3.4. QCM-D data highlighting the change in frequency during water vapor uptake experiments on Cell$_A$ (A) and Cell$_S$ (B) films at different humidity levels. Changes in the third overtone are shown. Please note that there are hardly any changes in dissipation (Figure S3.2; SI)

The results of the QCM-D measurements followed the same trends as already shown in the XRR investigations. The dried samples exhibited the lowest water vapor uptake at the different RH for all samples, whereas differences were most pronounced at 97 %RH. The particular difference between the Cell$_A$ and Cell$_S$ derived samples was also reflected in the QCM-D measurements. Except for the dried sample, water vapor uptake was nearly the same for all treated and the non-treated films as those determined by the XRR measurements. For Cell$_S$, situation was similar as for the XRR and the swollen/dried films showed a lower water vapor uptake than the swollen films. Even the relative raise in film thickness for the different films was in good agreement with the XRR data. For instance, the non-treated Cell$_A$ sample featured an increase of film thickness of 15.4% at 75 %RH (compare XRR: 15.2%). However, while trends were represented in a similar manner as in the XRR experiments, for some samples a smaller water vapor uptake is accomplished in the QCM-D studies (dried: 10.4% vs 12.2%, swollen: 13.2 vs 14.8%, swollen/dried 12.8 vs 15.2%, Figure 3.5). After a further increase of the relative humidity up to

97 %RH the difference between the non-treated (42.3%) and dried (30.8%) films was even more distinct. The results for the pristine films were comparable to previous findings.[22, 24]

A convenient means to clarify the obtained results in a more convenient way is to present the results in terms of the mass of absorbed water per mass of cellulose. This also allows for the calculation of the number of water molecules which are embedded per AGU by simply calculating the molar ratio (Figure 3.6, Figure S3.3 and S3.4, SI). The uptake of water vapor into the films at lower humidity levels led to the incorporation of less than one water molecule/AGU. By increasing the humidity to 70 %RH, the ratio of water molecules/AGU in non-treated films raised to 1.0 (Cell$_S$) and 1.4 (Cell$_A$) and at 97% it even accounted for 3.6 for both non-treated films. This is an interesting finding since earlier reports on liquid water uptake on similar regenerated cellulose thin films concluded that in liquid phase five molecules of water were present at each AGU.[32] Drying the films reduced the ratio water/AGU, particularly when rather high relative humidity levels were employed (Figure 3.6). In addition to information on mass changes on films, the dissipation module of the QCM allows for interpreting and monitoring changes in viscoelastic behavior. This is accomplished by determination of dissipated energy at a given overtone, denoted as ΔD_n. One might expect that the incorporation of the water into the film structure will lead to a softening concomitant with the appearance of viscoelastic behavior and an increase in ΔD_n. As in a recent report,[22] we cannot observe any changes in viscoelastic behavior of the films by QCM-D. However, the situation seems to be complex since another report demonstrated the effect of high humidity level on viscoelastic properties of such films.[24] Although it was stated that the origin of the TMSC used for film preparation may affect the dissipation values, this work excludes any influence of the source (spruce vs microcrystalline cellulose). Potentially, the different sample preparation may influence the behavior of the films in terms of viscoelasticity. The authors in that work used a polystyrene (PS) coated QCM sensor to deposit the TMSC from chloroform solutions. Since chloroform is a very good solvent for PS, this may lead to partial dissolution of the PS accompanied by penetration of TMSC into the PS layer during the spin coating step. Partially phase separated domains may form at the PS/TMSC interface as described in other publications.[33] Upon regeneration, the interfacial tension may induce the cellulose domain to rearrange resulting in a different viscoelastic behavior than for a

film directly deposited on the QCM sensor, while surface properties at the air/cellulose interface should remain unaffected.

In principle changes in density of the cellulose films can also be tracked using the QCM-D. Since the mass of water per gram of cellulose has been determined, the changes in density upon water uptake can be easily followed during water vapor uptake. For all the films there is a clear trend, namely that densities significantly decrease with increasing water vapor uptake. The decrease is slightly more pronounced for the $Cell_A$ samples (up to $0.05 - 0.07$ vs $0.03 - 0.04$ g*cm^{-3} for $Cell_S$). Even for the pre-swollen films the densities obtained by QCM-D follow these trends. Since these results are rather plausible, it was attempted to fit the data of the pre-swollen $Cell_A$ films with a three layer model similarly to the one used for the $Cell_S$ samples.
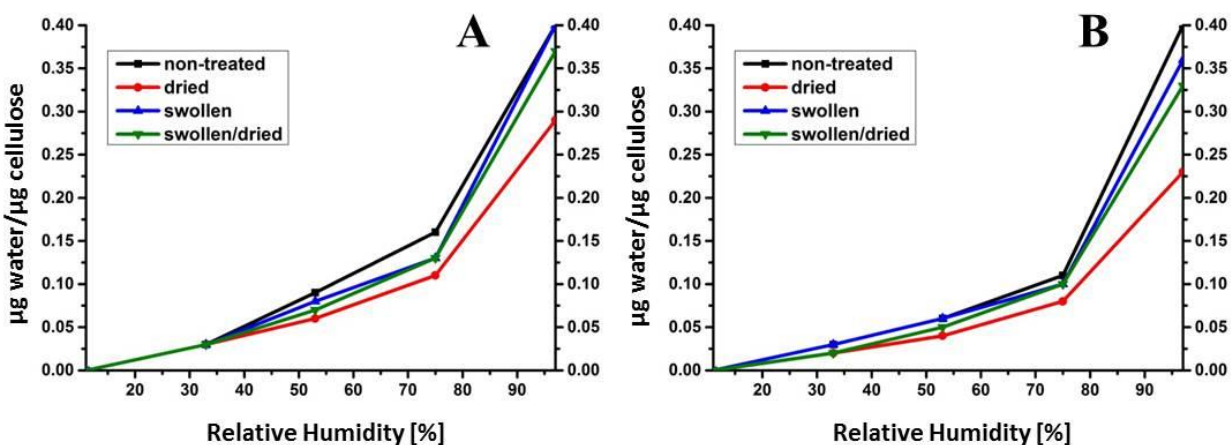
Figure 3.6. Comparison of the hydration of cellulose in dependence of the relative humidity and applied treatments. A: $Cell_A$, B; $Cell_S$

The results can be rationalized concerning two major aspects. The first interesting finding was that the very interface between the substrate and the cellulose 'bulk' layer is rather different to the bulk layer. This is of peculiar interest since in most cases the interaction of the substrate with nanocellulosic substrates is reduced to mere adhesion aspects in order to provide a stable cellulosic support (see above). Although some functionalized cellulose derivatives have been exploited for monolayer formation,[34-38] there are only a few studies available which have

attempted the generation of neat cellulose monolayers. For these cases, either sub-monolayers, fractal structures or open films have been realized.[39, 40] Therefore, the exact nature of such interfaces and their importance for film formation still remains hardly accessible. For all the investigated samples in this work, the interfacial cellulose layer features a thickness of ca 0.5-0.7 nm corresponding to two or three stapled cellulose layers. Probably, the constrained environment (i.e. a smooth, regular, non-swelling, OH rich surface) of the substrate forces the cellulose chains during regeneration into a parallel, flat arrangement with respect to the substrate surface. This interfacial cellulose layer is surprisingly stable and does not vertically extend during exposure to increased humidity levels as shown by XRR. Either the water molecules are incapable to diffuse to this interfacial layer, or they are incorporated in voids between individual macromolecules within the layer structure. It is evident that this layer must feature a rather good interaction with the hydrophilic silicon oxide substrate via hydrogen bonding which may compete with those of water vapor. We gained weak indications earlier that the biochemistry of this interlayer is different to the 'bulk' layer. Some of us noticed that during enzymatic hydrolysis monitored by AFM occasionally an extremely thin layer (< 1 nm) of cellulose was left on the silicon substrates. It seemed that the cellulase cocktail was not capable to degrade this part of the cellulose film.[41] Since in many biological processes interfacial phenomena play a large role, the boundaries to other materials classes are of particular importance for the function of biological systems.

The second aspect concerns the influence of the treatments on the hydration of the cellulose macromolecules. For the non-treated films, 3.6 molecules of water are present per AGU of cellulose for both investigated cellulose films. These values are in excellent agreement with available data on non-treated cellulose thin films which have been prepared the same way as in this study.

In this work, the response of $Cell_A$ and $Cell_S$ at lower humidity levels and the applied treatments differed significantly. The results follow a common, rather unexpected trend: the degree of hydration of $Cell_A$ is higher for all samples at the same humidity level/treatment than those of $Cell_S$. Except for the 97% humidity level, even the non-treated films show differences which are most pronounced at 75 %RH (1.4 vs 1.0 molecules H_2O/AGU for $Cell_A$ and $Cell_S$). This is rather surprising since there is a difference in 40% of water vapor uptake for a material featuring the

same chemistry and similar morphology. It is plausible to relate these differences to the preparation procedure (spin-coating from THF vs chloroform). This is also in line with the results from AFM nanoindentation and topography since the $Cell_S$ films showed higher stiffness than $Cell_A$, thereby requiring more energy for rearrangements to accommodate water into the structure. The differences, however, in terms of relative ratio are larger at humidity levels where capillary condensation takes place. Since capillary forces are rather strong, it can be reasoned that they may partially compensate at elevated humidity levels for the different stiffness of the films. Further, the necessity to induce a third layer for the description of the $Cell_S$ films, also point at differences in the film structure between $Cell_A$ and $Cell_S$. Nevertheless, it is very intriguing that these –on first glance- subtle differences lead to such distinct water vapor uptake phenomena. Besides the different behavior of the films in terms of preparation conditions, the impact of the treatments on the amount of water molecules/AGU is instructive. Non-treated and swollen films show a similar behavior at lower humidity levels, whereas an additional drying step after the swelling reduces the water incorporation into the films. Drying directly after preparation of the films largely reduces the amount of water molecules/AGU at high and medium humidity levels (2.6 vs 3.6 and 2.1 vs 3.6 at 97 %RH, 1.0 vs 1.4 and 0.7 vs 1.0 at 75 %RH for $Cell_A$ and $Cell_S$) but also at lower ones the effect is clearly visible (0.5 vs 0.8 and 0.4 vs 0.5 at 53 %RH). At small humidity levels (33 %RH) the effect of drying on water incorporation is small but not negligible (0.25 vs 0.30 and 0.16 vs 0.24 for $Cell_A$ and $Cell_S$).

3.4 Conclusion

Despite many attempts in the past to unravel interactions of water and cellulose, the rather high complexity makes it rather arduous to assess the basic underlying mechanisms. This is particularly relevant for 'real' cellulosic samples where complex pre- and post- treatments are regularly applied to realize certain material characteristics. However, even for rather simple model film approaches such as mixed crystalline and amorphous cellulose films, unexpected behavior of the cellulose materials is observed. Even if the complexity is further reduced by investigating mostly amorphous cellulose films like in the present study, the preparation conditions largely affect the interaction of the films with water vapors at different humidity

levels. As determined by nanoindentation experiments carried out using AFM instrumentation, the stiffness of the two respective films is rather different which may contribute to the different behavior of the two films. However, there are also distinct differences in the films' structure. While for both films an interfacial layer to the substrate was introduced for the evaluation of the XRR data, for the Cell$_S$ sample a third layer at the cellulose/air interface was required to achieve excellent agreement between the data and the fitting. Such differences certainly stem from the different preparation procedures since the used solvents exhibit rather different vapor pressures. The employed physical treatments give rise that similar processes take place in the thin films approach as for macroscopic samples. Similarly as with liquid water, water vapor incorporation decreases when the samples have been dried at elevated temperatures. This behavior becomes particularly pronounced at elevated humidity levels, where the amount of water molecules/AGU can be significantly reduced from 3.6 to 2.6 / 2.1 for the differently prepared samples.

3.5 References

(1) Björneholm, O.; Hansen, M. H.; Hodgson, A.; Liu, L.-M.; Limmer, D. T.; Michaelides, A.; Pedevilla, P.; Rossmeisl, J.; Shen, H.; Tocci, G.; Tyrode, E.; Walz, M.-M.; Werner, J.; Bluhm, H., *Chem. Rev.* **2016,** *116*, 7698-7726.

(2) Morillon, V.; Debeaufort, F.; Blond, G.; Capelle, M.; Voilley, A., *Critical Reviews in Food Science and Nutrition* **2002,** *42*, 67-89.

(3) Hedenqvist, M.; Gedde, U. W., *Progress in Polymer Science* **1996,** *21*, 299-333.

(4) Wijmans, J. G.; Baker, R. W., *Journal of Membrane Science* **1995,** *107*, 1-21.

(5) Scott, P., In *Physiology and Behaviour of Plants*, John Wiley & Sons: Chichester:, 2008.

(6) Maloney, T. C.; Paulapuro, H., *J. Pulp Pap. Sci.* **1999,** *25*, 430.

(7) Grignon, J.; Scallan, A. M., *Journal of Applied Polymer Science* **1980,** *25*, 2829-2843.

(8) Wistara, N.; Young, R. A., *Cellulose* **1999,** *6*, 291-324.

(9) Olsson, R. T.; Azizi Samir, M. A. S.; Salazar Alvarez, G.; BelovaL; StromV; Berglund, L. A.; IkkalaO; NoguesJ; Gedde, U. W., *Nature Nanotechnology* **2010,** *5*, 584-588.

(10) Benítez, A. J.; Torres-Rendon, J.; Poutanen, M.; Walther, A., *Biomacromolecules* **2013,** *14*, 4497-4506.

(11) Liu, A.; Walther, A.; Ikkala, O.; Belova, L.; Berglund, L. A., *Biomacromolecules* **2011,** *12*, 633-641.

(12) Malho, J.-M.; Ouellet-Plamondon, C.; Rüggeberg, M.; Laaksonen, P.; Ikkala, O.; Burgert, I.; Linder, M. B., *Biomacromolecules* **2015,** *16*, 311-318.

(13) Mautner, A.; Lee, K. Y.; Lahtinen, P.; Hakalahti, M.; Tammelin, T.; Li, K.; Bismarck, A., *Chemical Communications* **2014,** *50*, 5778-5781.

(14) Bandyopadhyay, A.; Ramarao, B. V.; Ramaswamy, S., *Colloids and Surfaces A: Physicochemical and Engineering Aspects* **2002,** *206*, 455-467.

(15) Nilsson, L.; Wilhelmsson, B.; Stenstrom, S., *Drying Technol.* **1993,** *11*, 1205-1225.

(16) Findenig, G.; Leimgruber, S.; Kargl, R.; Spirk, S.; Stana-Kleinschek, K.; Ribitsch, V., *ACS Appl. Mater. Interfaces* **2012,** *4*, 3199-3206.

(17) Nair, S. S.; Zhu, J. Y.; Deng, Y.; Ragauskas, A. J., *Sustainable Chemical Processes* **2014,** *2*, 23.

(18) Hult, E.-L.; Iotti, M.; Lenes, M., *Cellulose* **2010,** *17*, 575-586.

(19) Bedane, A. H.; Eić, M.; Farmahini-Farahani, M.; Xiao, H., *Cellulose* **2016,** *23*, 1537-1552.

(20) Hashimoto, A.; Stenström, S.; Kameoka, T., *Drying Technol.* **2003,** *21*, 1411-1431.

(21) Driemeier, C.; Bragatto, J., *The Journal of Physical Chemistry B* **2013,** *117*, 415-421.

(22) Niinivaara, E.; Faustini, M.; Tammelin, T.; Kontturi, E., *Langmuir* **2016,** *32*, 2032-2040.

(23) Niinivaara, E.; Faustini, M.; Tammelin, T.; Kontturi, E., *Langmuir* **2015,** *31*, 12170-12176.

(24) Tammelin, T.; Abburi, R.; Gestranius, M.; Laine, C.; Setala, H.; Osterberg, M., *Soft Matter* **2015,** *11*, 4273-4282.

(25) Kontturi, E.; Thüne, P. C.; Niemantsverdriet, J. W., *Langmuir* **2003,** *19*, 5735-5741.

(26) Resel, R.; Tamas, E.; Sonderegger, B.; Hofbauer, P.; Keckes, J., *J. Appl. Cryst.* **2003,** *36*, 80-85.

(27) Parratt, L. G., *Physical Review* **1954,** *95*, 359-369.

(28) Nevot, L.; Croce, P., *Revue de Physique Appliquée* **1980,** *15*, 761-779.

(29) Ehmann, H. M. A.; Werzer, O.; Pachmajer, S.; Mohan, T.; Amenitsch, H.; Resel, R.; Kornherr, A.; Stana-Kleinschek, K.; Kontturi, E.; Spirk, S., *ACS Macro Lett.* **2015,** *4*, 713-716.

(30) Mazeau, K.; Heux, L., *J. Phys. Chem. B* **2003,** *107*, 2394-2403.

(31) Chen, W.; Lickfield, G. C.; Yang, C. Q., *Polymer* **2004,** *45*, 1063-1071.

(32) Kittle, J. D.; Du, X.; Jiang, F.; Qian, C.; Heinze, T.; Roman, M.; Esker, A. R., *Biomacromolecules* **2011,** *12*, 2881-2888.

(33) Nyfors, L.; Suchy, M.; Laine, J.; Kontturi, E., *Biomacromolecules* **2009,** *10*, 1276-1281.

(34) Tanaka, M.; Wong, A. P.; Rehfeldt, F.; Tutus, M.; Kaufmann, S., *J. Am. Chem. Soc.* **2004,** *126*, 3257-3260.

(35) Soo, W. C.; Lauer, H.; Wenz, G.; Bruns, M.; Petri, D. F. S., *Journal of the Brazilian Chemical Society* **2000,** *11*, 11-15.

(36) Wenz, G.; Liepold, P.; Bordeanu, N., *Cellulose* **2005,** *12*, 85-96.

(37) Sakakibara, K.; Ogawa, Y.; Nakatsubo, F., *Macromolecular Rapid Communications* **2007,** *28*, 1270-1275.

(38) Niinivaara, E.; Wilson, B. P.; King, A. W. T.; Kontturi, E., *React. Funct. Polym.* **2016,** *99*, 100-106.

(39) Kontturi, E.; Thüne, P. C.; Alexeev, A.; Niemantsverdriet, J. W., *Polymer* **2005,** *46*, 3307-3317.

(40) Niinivaara, E.; Kontturi, E., *Soft Matter* **2014,** *10*, 1801-1805.

(41) Suchy, M.; Linder, M. B.; Tammelin, T.; Campbell, J. M.; Vuorinen, T.; Kontturi, E., *Langmuir* **2011,** *27*, 8819-8828.

3.6 Supporting Information
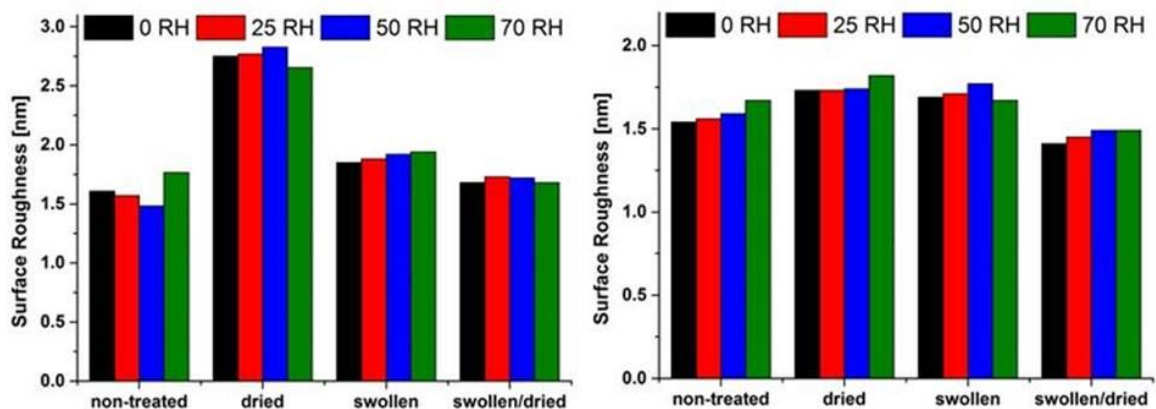
Figure S3.1. Surface roughness of $Cell_A$ (left) and $Cell_S$ (right) samples determined by XRR during water vapor uptake experiment.
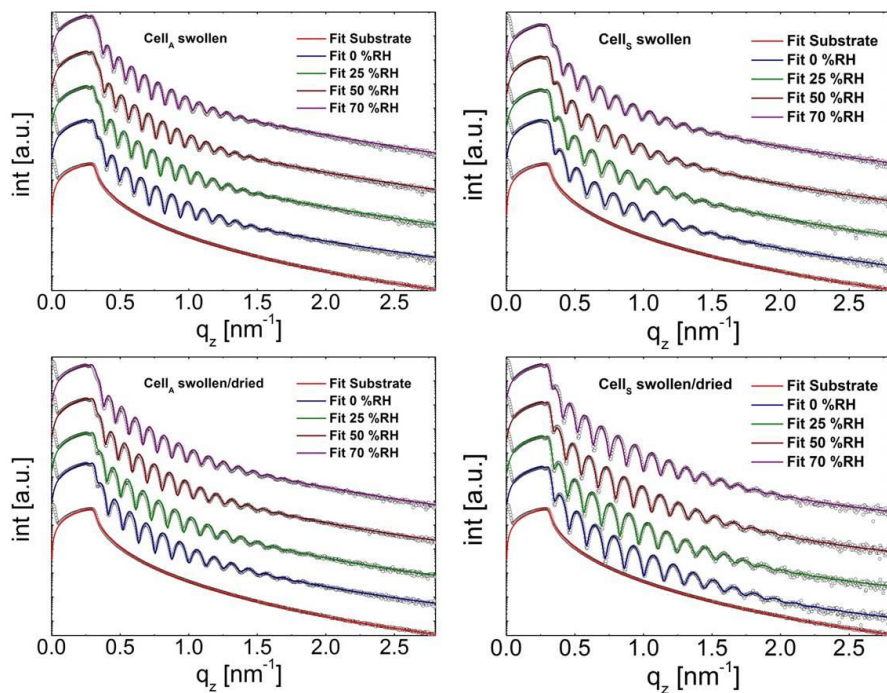
Figure S3.2. XRR curves and corresponding layer fit of the two different cellulose films ($Cell_A$, left column; $Cell_S$, right column) samples after different treatments.

Table S3.1. XRR results of Cell$_A$ samples (two-layer fit).

Cell$_A$	Layer 1			Layer 2			Layer 3			Total Thickness	
% RH	nm		g/cm³	nm		g/cm³	nm		g/cm³	nm	%
non-treated	Thickness	Roughness	Density	Thickness	Roughness	Density				Thickness	Thickness
0	0.6	0.2	0.92	51.9	1.6	1.45				52.5	0.0
25	0.6	0.2	0.90	54.1	1.6	1.43				54.7	4.3
50	0.5	0.3	0.67	56.7	1.5	1.48				57.2	9.0
70	0.5	0.3	0.66	60.8	1.8	1.41				61.3	16.1
dried	Thickness	Roughness	Density	Thickness	Roughness	Density				Thickness	Thickness
0	0.6	0.3	1.10	53.8	2.8	1.49				54.4	0.0
25	0.5	0.2	1.04	56.0	2.8	1.48				56.5	3.8
50	1.0	0.5	1.06	57.4	2.8	1.44				58.4	7.2
70	1.3	0.5	1.04	59.8	2.7	1.40				61.1	12.2
swollen	Thickness	Roughness	Density	Thickness	Roughness	Density	Thickness	Roughness	Density	Thickness	Thickness
0	0.4	0.3	0.99	47.0	3.1	1.45	4.6	1.6	1,17	52.0	0.0
25	0.4	0.3	0.96	48.9	3.1	1.43	4.9	1.6	1,15	54.2	4.4
50	0.4	0.3	0.95	51.0	3.2	1.42	5.4	1.7	1,11	56.8	9.2
70	0.4	0.3	0.94	52.9	3.6	1.39	6.2	1.7	1,10	59.5	14.6
swollen dried	Thickness	Roughness	Density	Thickness	Roughness	Density				Thickness	Thickness
0	0.6	0.2	0.92	47.8	1.7	1.44				48.4	0.0
25	0.6	0.3	0.91	50.0	1.7	1.47				50.6	4.5
50	0.6	0.2	0.89	52.3	1.7	1.45				52.9	9.4
70	0.6	0.2	0.86	55.1	1.7	1.42				55.7	15.2

Table S3.2. XRR results of Cell$_S$ samples (three-layer fit).

Cell$_S$	Layer 1			Layer 2			Layer 3			Total Thickness	
% RH	nm		g/cm³	nm		g/cm³	nm		g/cm³	nm	%
non-treated	Thickness	Roughness	Density	Thickness	Roughness	Density	Thickness	Roughness	Density	Thickness	Thickness
0	0.6	0.3	0.81	40.4	3.0	1.50	4.2	1.5	1.15	45.2	0.0
25	0.6	0.3	0.79	42.2	3.1	1.50	4.3	1.6	1.14	47.1	4.3
50	0.6	0.3	0.75	44.5	3.1	1.48	4.3	1.6	1.12	49.4	9.4
70	0.6	0.2	0.72	46.7	3.3	1.48	5.0	1.7	1.14	52.3	16.0
dried	Thickness	Roughness	Density	Thickness	Roughness	Density	Thickness	Roughness	Density	Thickness	Thickness
0	0.6	0.2	0.80	40.4	2.7	1.47	4.2	1.7	1.10	45.2	0.0
25	0.6	0.2	0.76	41.9	2.3	1.45	4.3	1.7	1.08	46.8	3.7
50	0.7	0.2	0.83	43.9	1.8	1.39	4.2	1.7	1.05	48.7	7.9
70	0.6	0.2	0.86	46.4	2.2	1.40	4.7	1.8	1.01	51.7	14.4
swollen	Thickness	Roughness	Density	Thickness	Roughness	Density	Thickness	Roughness	Density	Thickness	Thickness
0	0.5	0.3	0.84	36.8	2.9	1.47	4.3	1.7	1.05	41.6	0.0
25	0.5	0.2	0.87	38.3	2.8	1.45	4.6	1.7	0.99	43.3	4.2
50	0.5	0.3	0.84	40.3	3.0	1.43	4.6	1.8	0.98	45.7	9.7
70	0.7	0.2	0.75	43.2	2.3	1.40	4.7	1.7	1.03	48.5	16.7
swollen dried	Thickness	Roughness	Density	Thickness	Roughness	Density	Thickness	Roughness	Density	Thickness	Thickness
0	0.5	0.2	0.93	37.4	2.6	1.49	3.7	1.4	1.19	41.6	0.0
25	0.5	0.3	0.93	38.5	3.8	1.47	4.3	1.5	1.17	43.4	4.3
50	0.5	0.2	0.92	40.0	3.8	1.44	4.9	1.5	1.17	45.4	9.2
70	0.5	0.2	0.92	42.5	3.9	1.43	5.2	1.5	1.13	48.2	16.0
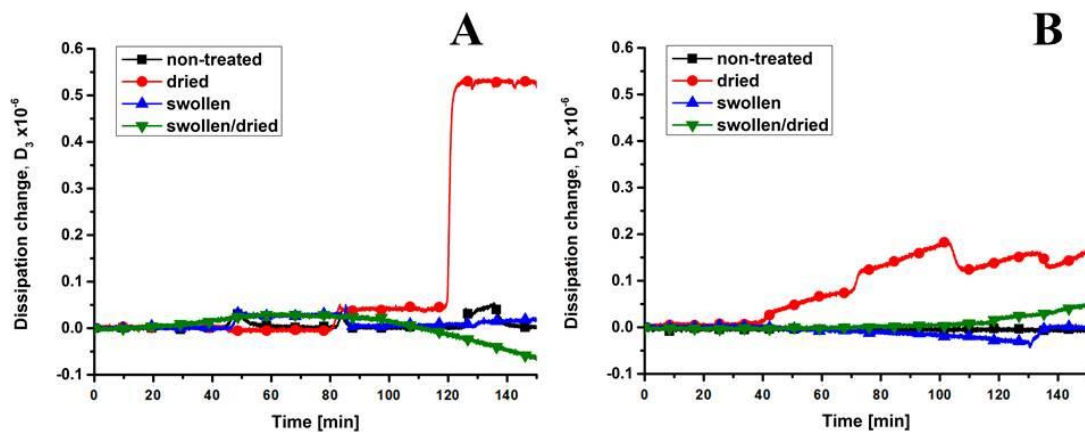
Figure S3.3. QCM-D data highlighting the change in dissipation during water vapor uptake experiments on $Cell_A$ (A) and $Cell_S$ (B) films at different humidity levels and treatments. Changes in the ΔD_3 are shown.
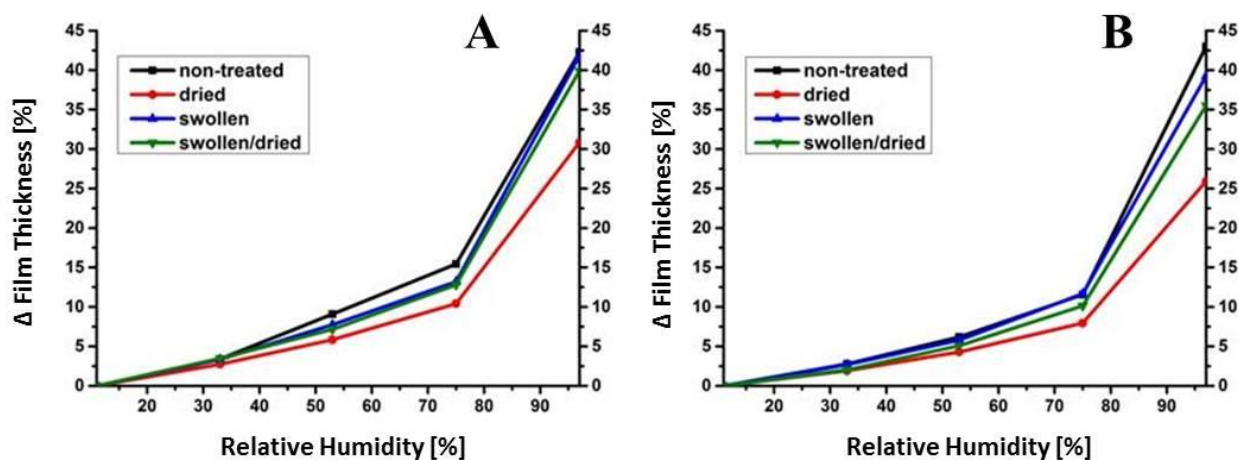
Figure S3.4. Film thickness increase at different humidity levels determined by QCM-D A) $Cell_A$ samples B) $Cell_S$ samples.

Table S3.3. Comparison of the densities of the films determined by XRR and QCM-D. Densities obtained by QCM-D are referred to as the density of amorphous cellulose (1.48 g*cm^{-3}).

Relative Humidity [%RH]		Cell$_A$		Cell$_S$	
XRR	QCM-D	XRR	QCM-D	XRR	QCM-D
non-treated		Density [g*cm³]			
0	11	1.45	1.48	1.45	1.48
25	33	1.43	1.47	1.45	1.47
50	53	1.43	1.44	1.43	1.45
70	75	1.41	1.41	1.43	1.43
	97		1.34		1.34
dried					
0	11	1.49	1.48	1.42	1.48
25	33	1.48	1.47	1.40	1.47
50	53	1.44	1.45	1.34	1.46
70	75	1.40	1.43	1.35	1.44
	97		1.37		1.39
swollen					
0	11	1.41	1.48	1.41	1.48
25	33	1.39	1.47	1.38	1.47
50	53	1.38	1.44	1.37	1.45
70	75	1.35	1.42	1.34	1.44
	97		1.34		1.35
swollen/dried					
0	11	1.44	1.48	1.44	1.48
25	33	1.47	1.47	1.42	1.47
50	53	1.45	1.45	1.39	1.46
70	75	1.42	1.42	1.38	1.44
	97		1.35		1.36

Table S3.4. Relative humidities of each saturated salt solution and water used in the QCM-D relative humidity cycles.[1]

Salt	Relative humidity (RH)
$LiCl_{(aq)}$	11
$MgCl_{2(aq)}$	33
$Mg(NO_3)_{2(aq)}$	53
$NaCl_{(aq)}$	75
$K_2SO_{4(aq)}$	97
$MilliQ_{(l)}$	100

(1) L. Greenspan, *J. Res. Natl. Bureau Stand.* **1977**, *81*, 89.

Chapter 4

4. Study on the Formation of Bi_2S_3-Cellulose Nanocomposite Films from Bismuth Xanthates and Trimethylsilyl-Cellulose[1]

The following chapter is written for the submission in Carbohydrate Polymers:

In this chapter, we explore the synthesis and characterization of bismuth sulfide-cellulose nanocomposite thin films. The films are prepared using highly soluble precursors, namely bismuth xanthates for Bi_2S_3 and trimethylsilyl cellulose (TMSC) for cellulose. Solutions of these precursors were spin coated yielding homogeneous precursor films. Afterwards, a heating step under inert atmosphere leads to thin nanocomposite films of bismuth sulfide nanoparticles within the TMSC matrix. In a second step, the silyl groups can be cleaved off by vapors of HCl yielding bismuth sulfide/cellulose nanocomposite films. The thin films are characterized by a wide range of surface sensitive techniques such as atomic force microscopy, attenuated total reflection infrared spectroscopy, transmission electron microscopy and wettability investigations. In addition, the formation of the nanoparticle directly in the TMSC matrix was investigated *in situ* using GI-SWAXS operated by synchrotron irradiation using a temperature controlled sample stage.

4.1 Introduction

In recent years, research on semiconducting colloidal crystals led to a wide range of solution-processable optoelectronic devices such as photocatalysts, light emitting devices, sensors, and photovoltaic cells. However, many of the used materials contain toxic metals such as cadmium or lead causing negative effects for the environment during manifacturing and after disposal. A sulfide forming element with a rather low reported toxicity is bismuth. Bi_2S_3 nanoparticles and nanocomposites find numerous applications in magnetic resonance imaging[1], thermoelectric devices[2], memory devices[3], photodetectors[4], as electrode material in lithium-ion batteries[5], as well as in electronic, optoelectronic and gas sensor devices[6-9]. In other applications, the low band gap of bismuth sulfide (1.3 to 1.7 eV)[3] is exploited in optoelectronic devices e.g. in nanocrystal-polymer solar cells[10,11]. A very convenient route to produce bismuth sulfide nanoparticles is to use soluble bismuth xanthate (BiXa) precursors which are decomposed after the final processing step such as spin coating or knife blading[12]. These works inspired us to explore whether we could implement polysaccharide derivatives as stabilizing agents to control the growth of the bismuth sulfide nanoparticles from the xanthates to generate a nanocomposite with a better ecologic footprint. The major challenge to obtain homogeneous nanocomposites is to find a common solvent for both, the bismuth xanthate precursor as well as the polysaccharide compound. Since many bismuth xanthates are readily soluble in apolar organic solvents, trimethylsilyl-cellulose (TMSC) was chosen as precursor due to its excellent solubility in aprotic solvents. TMSC has several further advantages in this context: its solubility can be fine-tuned by the degree of substitution, it is rather light- and thermostable under exclusion of air/moisture[13] and it is a good film forming polymer as already explored in literature.[14,15] Further, the conversion into cellulose proceeds via a gas phase reaction.[16,17] In contrast to other regeneration procedures using aqueous acidic or alkaline solutions, the nanocomposite films do not come in contact with any liquids during the regeneration, which may change or even harm the structure of the cellulose film. This regeneration procedure using TMSC was just recently exploited to generate metallic Bi-NP/TMSC and Bi-NP/cellulose nanocomposites in a very efficient way by photoreduction of a bismuth precursor in toluene solution[18]. Here, we combine the TMSC precursor route for cellulosic thin films with the bismuth xanthate precursor route for Bi_2S_3 nanoparticles to generate Bi_2S_3 cellulose nanocomposite thin films.

The work is constructed as follows: after a detailed characterization of the film forming properties of various BiXa/TMSC films, these films are thoroughly analyzed and subjected to a heat treatment. The formation of the particles is monitored by *in-situ* grazing incidence X-ray scattering using a temperature controlled heating stage. All samples have been analyzed in detail after the heating step and conversion to cellulose using HCl vapors was accomplished.

4.2 Experimental

Materials. Trimethylsilyl-cellulose (TMSC; Avicel pulp DS: 2.7-2.9), purchased from TITK Rudolstadt MFSA, and bismuth xanthate (bismuth(III)-O-3,3-dimethylbutan-2-yl dithiocarbonate, denoted as BiXa in the following), synthesized according to a literature procedure,[12] were used as starting materials for the thin film preparation. Hydrochloric acid (37 wt%), chloroform (99 wt%) and sulfuric acid (95 wt%) were purchased from VWR chemicals and hydrogen peroxide (30 wt%) from Sigma-Aldrich. All chemicals were used without purification. Silicon wafer, glass slides (Roth), Au-coated glass slides as substrate (SPR102-AU), Filter Chromafil® Xtra PVDF-45/25 0.45 μm, petri dishes (20 ml; 5 cm diameter) were used as obtained.

ATR-IR Spectroscopy. The experiments were performed with an ALPHA FT-IR spectrometer (Bruker; Billerica, MA, USA). For the measurement an attenuated total reflection (ATR) attachment was used with 48 scans at a resolution of 4 cm^{-1} and a scan range between 4000 and 400 cm^{-1}. The data were analyzed with OPUS 4.0 software.

AFM. Atomic force microscopy (AFM) images are recorded in the tapping mode (non-contact mode) on a Veeco Multimode Quadrax MM AFM (Bruker; Billerica, MA, USA). For the scanning silicon cantilevers (NCH-VS1-W from NanoWorld AG, Neuchatel, Switzerland) were used with an average spring constant of 42 N/m (Force Constant) and with a resonance frequency of 270 − 320 kHz (Coating: none). All measurements were performed at room temperature and under ambient atmosphere. The calculation of the root mean square roughness (calculated from a 6 x 6 μm image) und the image processing was done with the Nanoscope software (V7.30r1sr3; Veeco).

Stylus profilometry/Determination Film Thickness. Layer thickness was measured on a Bruker DekTak XT surface profiler. The scan length was set to 1000 μm over the time duration of 3 seconds. The diamond stylus had a radius of 12.5 μm and the force was 3 mg with a resolution of 0.333 μm/sample and a measurement range of 6.5 μm. The profile was set to *hills and valleys*. For the determination of the film thickness a silicon wafer sample was scratched five times (up to the silicon surface). This measured profile was then used to calculate the thickness of the different coatings.

Contact angle and surface free energy determinations. To determine the static contact angle and the surface free energy (SFE) a drop shape analysis system DSA100 (Krüss GmbH, Hamburg, Germany) with a T1E CCD video camera (25 fps) and the DSA1 v 1.90 software was used. For the measurements 3 μl droplets of Milli-Q water ($\geq$18 MΩ cm^{-1}) and diiodomethane as test liquids in the sessile drop modus at 25 °C were deposited on the substrates. The dispense rate was adjusted to 400 μl/min and the time before the image was captured was 2 seconds. Each sample was measured at least three times. The contact angle calculations were performed with the Young-Laplace equation and the surface free energy calculation with the Owens-Wendt-Rabel & Kaelble method.

UV-Vis spectroscopy. The UV-Vis absorption spectra of the samples (on glass substrate) were measured with a Shimadzu UV-1800 UV spectrophometer. The absorbance was determined from 200 - 1100 nm at 25°C and an ambient atmosphere.

GI-SWAXS. The *in situ* GISAXS and GIWAXS experiments were performed at the high-flux SAXS beamline at Elettra synchrotron in Triest, Italy, which is well suited for studying time-resolved structural transitions with an X-ray energy of 8 keV (λ = 1.54 nm). To realize the *in situ* regeneration of trimethylsilyl cellulose to pure cellulose, a specially designed chemical reaction chamber was used as sample holder, and mounted on a sample stage that can be rotated around 2 axes transversal to the beam (precision ~ 5 μm) and also tilted to set the incidence angle (precision ~ 0.001°). As detection system either Gabriel type detectors, (for simultaneous SAXS and WAXS measurements having windows size 8 x 100 mm, active length 86.1 mm with a resolution of 0.135 mm/channel for the WAXS-range, and either a second linear Gabriel type detector). As calibration standard silver behenate with a lamellar spacing of 58.38 Å was used.

The sample-to-detector distance was determined to be 1516.55 mm and the incidence angle was set to 0.83°. We decided on purpose to have a large grazing angle to be in the kinematic regime and to deal with the simple born approximation - a common approach, when the signal is sufficient in q and intensity to describe the sample scattering as described in the book chapter by P. Müller-Buschbaum.[19].

The *in situ* heating was performed using the Anton Paar DHS1100 heating stage (temperature range 5-1100°C) sealed with a Kapton windows which is continuously rinsed with gaseous nitrogen under steady flow conditions. The heating rate was set to 10°C/min.

2.2.7. Scanning Transmission Electron Microscopy (STEM)

STEM and EDXS. STEM investigations were done on a Titan³ G2 60-300 from the company FEI at 300 keV accelerating voltage. The microscope is equipped with a CS-corrector to correct the spherical aberration in the STEM mode to obtain atomic high resolution with a lateral resolution below 1 Ångström. Bright field (BF) and also high angle annular dark field (HAADF) STEM images were recorded with detectors from the company Gatan. Energy dispersive X-ray spectroscopy (EDXS) was performed with four high-sensitivity SDD X-ray spectrometers (Super-X) from Bruker.

Film Preparation. The different substrates (silicon wafer (1.4 x 1.4 cm), glass wafer (1.4 x 1.4 cm) and gold slide (2.0 x 1.0 cm)) were cleaned with "piranha" acid (H_2SO_4:H_2O_2 = 7:3 (v/v)) for 30 min (10 min for gold slides) and neutralized afterwards with distilled water. For the film preparation, TMSC (1 wt%) was dissolved in $CHCl_3$, filtered and combined (1:1 (v/v)) with the bismuth xanthate solution (1 wt%, 5 wt%, 10 wt% in $CHCl_3$). This solution (180 μl) was spin coated on the different substrates at 4000 rpm for 60 s (acceleration 2500 rpm/s). The in-situ synthesis of the Bi_2S_3-nanoparticles (BiSNPs) was done by thermal conversion (195°C over a period of 30 min, heating rate= 10°C/min) of bismuth xanthate on a heating plate. After the thermal conversion the films were exposed to HCl vapor to obtain full regenerated cellulose/Bi_2S_3-nanoparticle thin films. For that step the Bi_2S_3/TMSC film were placed in a petri dish for 12 min next to 2 ml of 12 wt% hydrochloric acid and covered by the petri dish cap.

4.3 Results and Discussion

4.3.1 Film preparation

The first step in the preparation of the thin films was to evaluate under which conditions homogenous films of TMSC and BiXa can be obtained by spin coating (Figure 1). We chose as starting point, 1 wt% solutions of TMSC in $CHCl_3$ and added different amounts of BiXa (1, 5, and 10 wt% in $CHCl_3$, respectively).
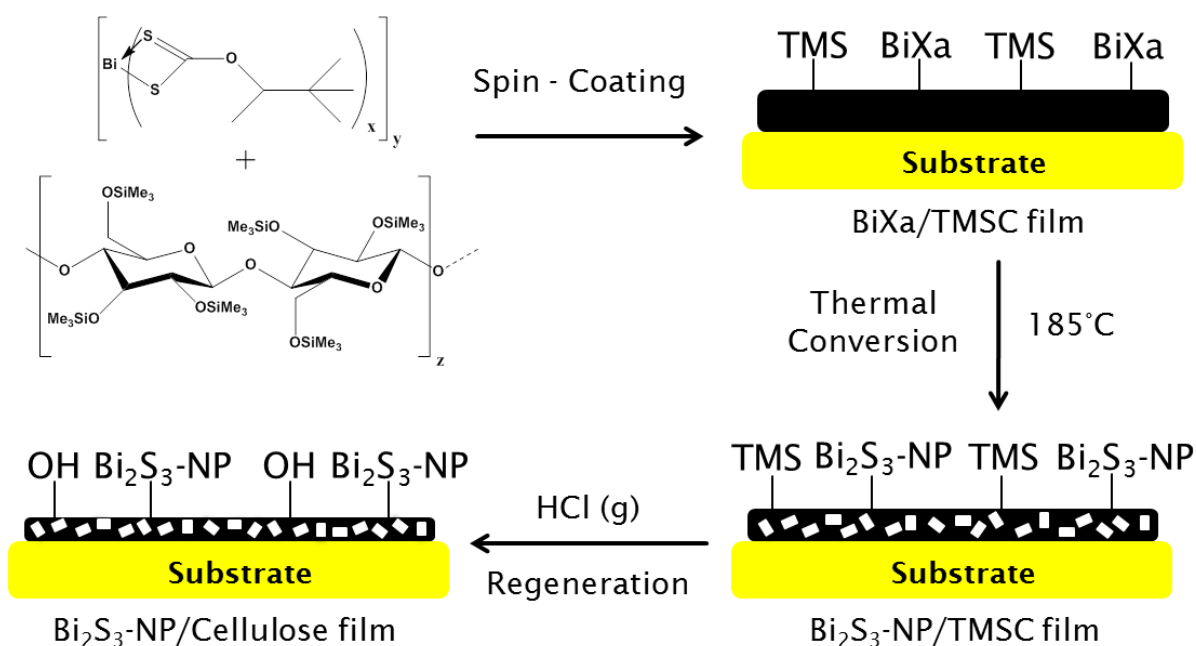
**Figure 4.1.** Schematic representation of the manufacturing steps of BiXa/TMSC nanocomposite films.

In all cases, macroscopically clear solutions were obtained which are stable over a period of more than 30 minutes. These solutions were placed on silicon substrates and subjected to spin coating (4000 rpm, 2500 rpm s, t = 60 s). After spin coating, all prepared films appear rather smooth by naked eye, which already gave a first hint that TMSC and BiXa are compatible in both, solution and solid state. The next step was to evaluate the thermal conversion of the BiXa to the Bi_2S_3 particles inside the films. It is known from literature[12] that BiXa starts decomposing

at ca 150°C to form Bi_2S_3 while forming other volatile compounds such COS and 3,3-dimethylbut-1-ene which are the typical species of the decomposition of xanthates via the Chugaev rearrangement.[20] Although not directly formed via the Chugaev mechanism, traces of H_2S may evolve during the decomposition as well. Important questions in this context were whether the release of rather reactive compounds would affect the TMSC matrix. It is known that HCl vapors for instance are capable to cleave off silyl groups of cellulose, given an exposure time of at least 10 minutes.[21] In the next sections, the chemical reactions as well as the quality of the thin films were analyzed in detail.

4.3.2 ATR-IR spectroscopy

A very suitable method to monitor such changes is ATR-IR spectroscopy. It can be clearly seen in Figure 2 (A) that neither the addition of the xanthate to the TMSC, nor the heating step causes regeneration of the TMSC to cellulose.
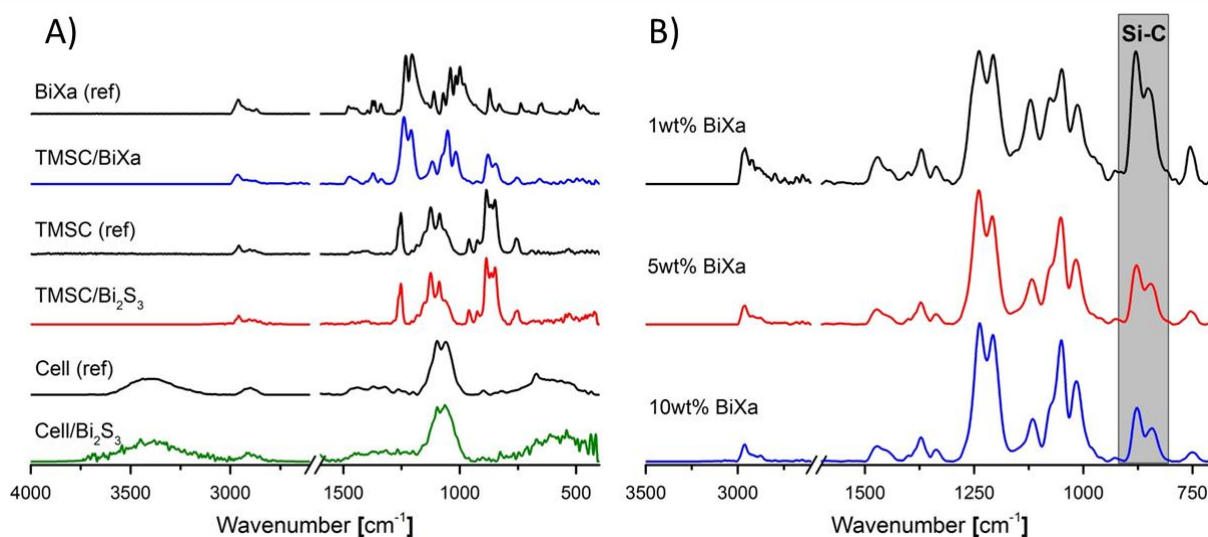
Figure 4.2. A) Comparison of the ATR IR reference spectra (BiXa, TMSC and cellulose) with nanocomposite thin films having a BiXa concentration of 5 wt%. B) Comparison of ATR IR spectra of TMSC/BiXa nanocomposites at different BiXa contents.

For the non-treated BiXa/TMSC film, typical vibrations for xanthates as well as for TMSC were detected. The bands at 1238 cm^{-1} and 1207 cm^{-1} can be attributed to the asymmetric C–O–C stretching vibrations, and those at 1047 and 1017 cm^{-1} to the C–S stretching vibrations of the xanthate. These bands can be unambiguously assigned since their intensity increases by increasing the BiXa content in the films (Figure 2 (B)).

For the TMSC fraction, the Si-C vibration at 852 cm^{-1} is characteristic. The band at 1121 cm^{-1} can be assigned to symmetric C–O–C stretching vibrations of both substances. Bands associated with the BiXa (1238 cm^{-1}, 1207 cm^{-1}) vanish after exposure to elevated temperatures indicating a decomposition of the xanthate, while leaving the TMSC untouched. This is proven by a distinctive spectrum for TMSC exhibiting all characteristic bands for Si-C and Si-O-C vibrations. It can be concluded that neither the heating step at 195°C nor the volatile side products in the conversion of BiXa to Bi$_2$S$_3$ lead to a decomposition of the TMSC films. However, a separate HCl treatment indeed induces regeneration from TMSC to cellulose as proven by the appearance of typical bands associated with cellulose at 1024 cm^{-1} (C–O stretching; aromatic C–H in plane deformation), 1064 cm^{-1} (C–O stretching) and 3000–3600 cm^{-1} (OH stretching).[22]

4.3.3 Particle formation - GI-SWAXS and STEM

In order to get more insights in the heat-induced conversion of the BiXa into the corresponding bismuth sulfides, combined GI-SAXS and GIWAXS studies using monochromatic X-rays have been performed. The setup of the experiment comprised a temperature-controlled sample stage which was flushed with dry nitrogen to prevent oxidation by air during the illumination with the synchrotron beam. After positioning the samples, the temperature was steadily increased and the scattering patterns were recorded. It can be clearly seen that the scattering contrast increases at ca 120°C and reaches a maximum at ca. 195°C. This can be attributed to the formation of bismuth sulfide nanoparticles, which provide small scattering centers, giving rise to much higher contrast compared to the small precursor molecules homogenously distributed in the film. This is further illustrated by simply increasing the amount

of BiXa in the films from 1 to 10 wt% leading to a tenfold increase of intensity after the end of the heating ramp (Figure 4.3). The formation of the nanoparticles is further evidenced in two movies demonstrating the heat induced conversion of BiXa to Bi_2S_3 (SI). Further proof for the presence of the bismuth sulfides is provided by analysis of the reflection planes of the GI-WAXS patterns (Figure 4.4). The main diffraction peaks at 2.8 Å, 3.1 Å, 3.5 Å, 3.7 Å, 3.9 Å, 5.4 and 7.0 Å are nearly identical as those reported for orthorhombic Bi_2S_3 in literature (Joint Committee on Powder Diffraction Standards JCPDS Card No. 17-320).
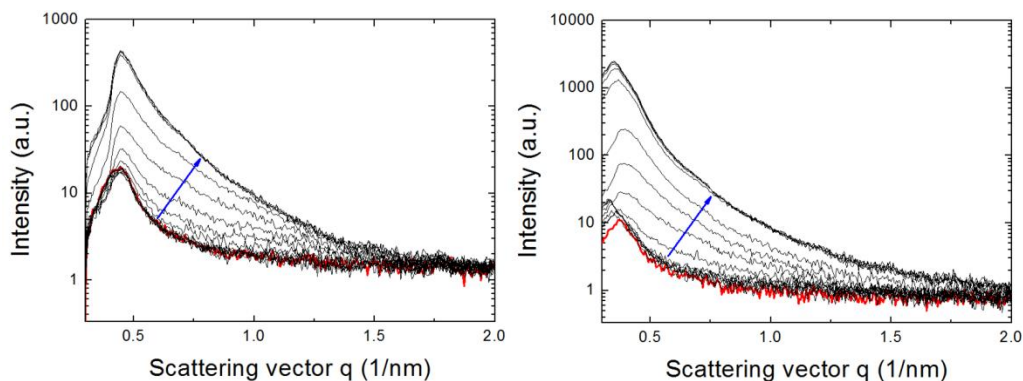
Figure 4.3. Heat induced growth of Bi_2S_3 nanoparticles in a TMSC film upon increase of temperature from 25 to 195° monitored by *in situ* GI-SAXS. Left: TMSC:BiXa ratio of 1:1, Right: TMSC: BiXa ratio of 1:10. Please note the different intensity scales for both scattering curves.
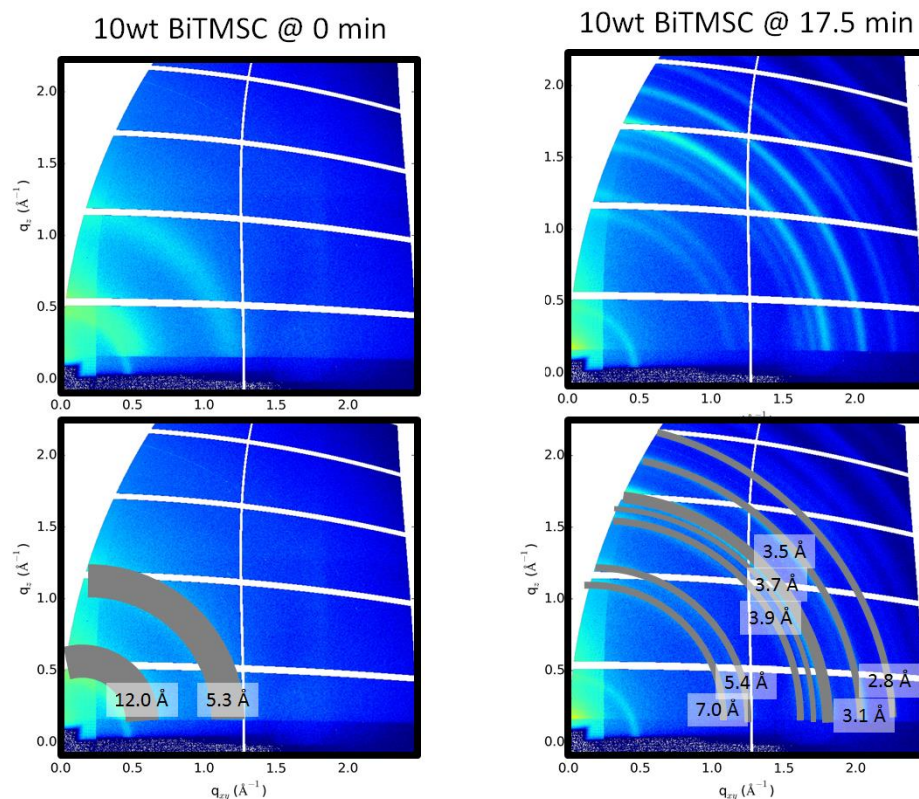
Figure 4.4. Scattering patterns of a TMSC/BiXa film before and after the heating procedure monitored by *in situ* GI-WAXS. The BiXa concentration was 10 wt% in those films.

A crucial question is the shape and the size of the nanoparticles grown in the film. Besides SWAXS, bright field and high angle annular dark field TEM are very suitable methods to determine particle dimensions in thin films. However, sample preparation was a bit tricky, since we had to ensure the same conditions for the TEM sample as for the other films using Si-wafers as support. Since the films cannot be peeled off the substrate nor deposited on carbon grids (the polymer coating melts at 150°C) we decided to deposit the TMSC/BiXa mixture on a NaCl grid, followed by the heating step and subsequent careful dissolution of the grid with water. Figure 5 illustrates the results of the 5 wt% BiXa sample with different magnifications after the heating step. The images indicate that the formed nanoparticles are rod shaped with a diameter of 25±4 nm and a length of 80±7 nm. An EDX spectrum of the Bi_2S_3 nanoparticles is depicted in the supporting information (SI). Most of the particles are homogenously distributed in the matrix, whereas there are some spots having a higher density of particles. It is not clear whether this

higher density is due to sample preparation or whether it is a consequence of the particle growth (Figure 4.5).
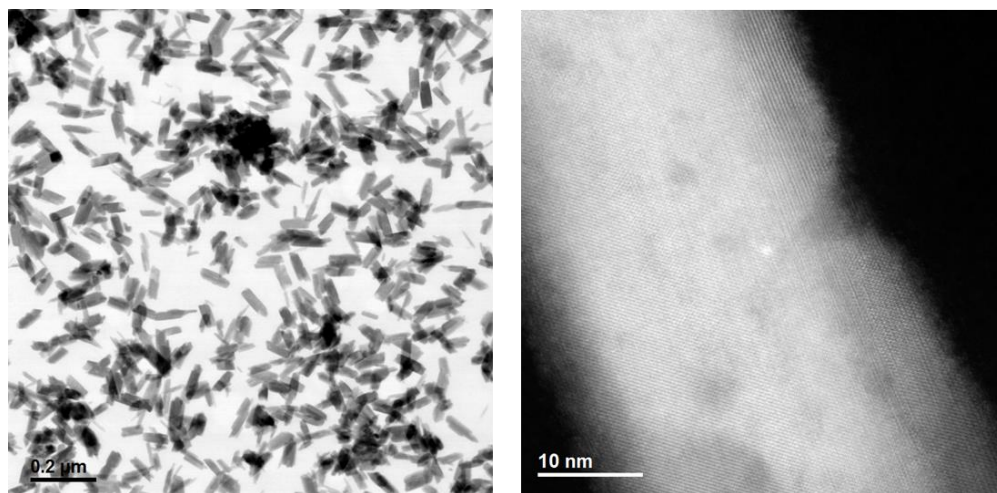
Figure 4.5. Bright field (left) and high angle annular dark field (right) TEM images of 5 wt% Bi_2S_3-NP in a TMSC matrix at different magnifications.

4.3.4 Morphology - AFM

While the above mentioned methods clearly provide proofs for the successful conversion of the BiXa to the sulfides, a very interesting question is to which extent the morphology is affected by the heating process. It can be clearly seen that the heating process itself does not induce changes in neat TMSC. However, the addition of BiXa into the TMSC matrix leads to slightly rougher surfaces. Interestingly, the effect of the concentration on morphology on non-treated films is rather small (Table S4.2; SI). However, situation changes after the heat treatment. All the images show homogenously distributed features and a significant increase in the roughness of the films which relates to the amount of BiXa in the films. Situation changes when higher amounts of BiXa are inside the TMSC, whereas the 1:10 film features a rather high roughness. It can be clearly seen in the images that particulates have been formed.

The morphology of the nanocomposite films was analyzed by atomic force microscopy before and after the modification steps. In Figure 4.6, the AFM images of the non-treated films (A, D,

G, J) at three different xanthate concentrations and there modifications (B, C, E, F, H, I, K, L) are depicted.
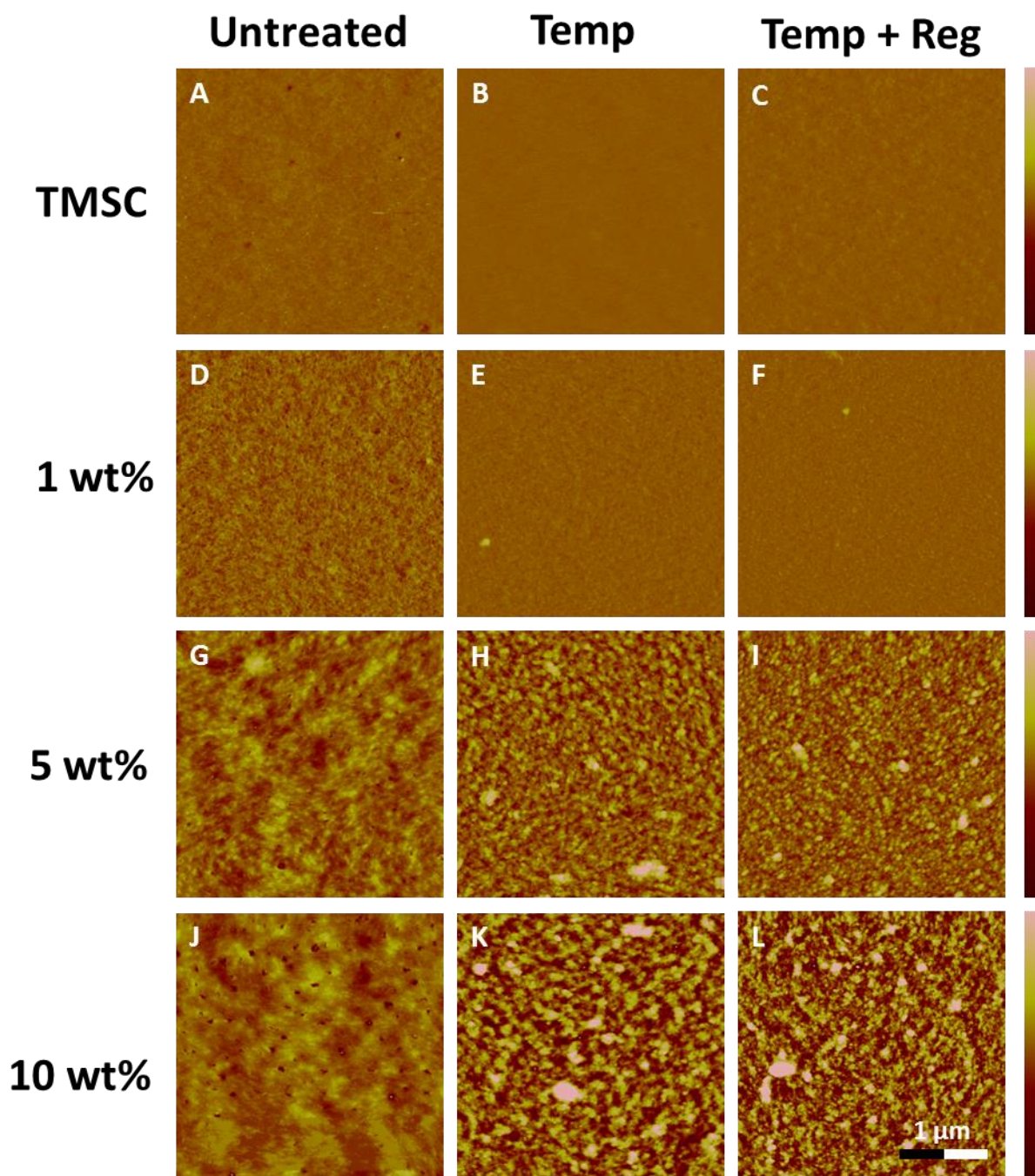
Figure 4.6. TMSC matrix (A, B, C) with 1 wt% BiXa (D, E, F), 5 wt% BiXa (G, H, I), 10 wt% BiXa (J, K, L); Z-scale (A, D, G, J) = 40 nm, Z-scale (B, C, E, F, H, I, K, L) = 130 nm

Based on the good solubility of the starting materials and the spin coating parameters neither the surface morphology nor roughness of the native films is changing by increasing the BiXa concentration (see Table S4.2; SI). After the heating step, the films reveals 80-100 nm small structures on the surface, which can be ascribed to the formed Bi_2S_3 nanoparticles. For the films containing 5 and 10 wt% BiXa, this effect is very pronounced (Figure 6, H and K) while the surface morphology of the film containing 1 wt% BiXa is not affected (for a smaller Z-scale see ESI†). Besides changes in morphology, the film thickness decreases since a large fraction (67 wt%) of BiXa consists of organic material, which is converted to volatile compounds during the heating step, finally leaving the TMSC film. Consequently, the decrease in layer thickness is correlated with the amount of BiXa in the films. The 1 wt% samples featured a decrease of 103 to 62 nm, the 5 wt% from 248 to 92 nm and the largest decrease was observed for the 10 wt% sample (482 to 118 nm). As films shrank, the roughness of the surface increased, especially for the samples containing 5 wt% (2.83 nm to 11.4 nm) and 10 wt% (2.78 nm to 20.9 nm) BiXa.

After the heat treatment step, the TMSC fraction of the nanocomposite can be converted to cellulose by exposing the films to vaporous HCl over a period of 12 minutes. Although the thickness of the films decreased again after the regeneration of the material due to the loss of silyl groups, the morphology as well as the roughness remained unaffected by the treatment. During the entire modification process (heating and regeneration) the films decreased in ca 75-80% of their initial thickness.

4.3.5   Surface wettability and surface free energy

A further aspect when it comes to applications is the wettability of the nanocomposites and their interaction with other materials. Particularly the surface free energy (SFE) is an important parameter in the design of multi-layer applications. Therefore, the contact angles of different liquids (water and diiodomethane (SI)) were determined using the sessile drop approach.
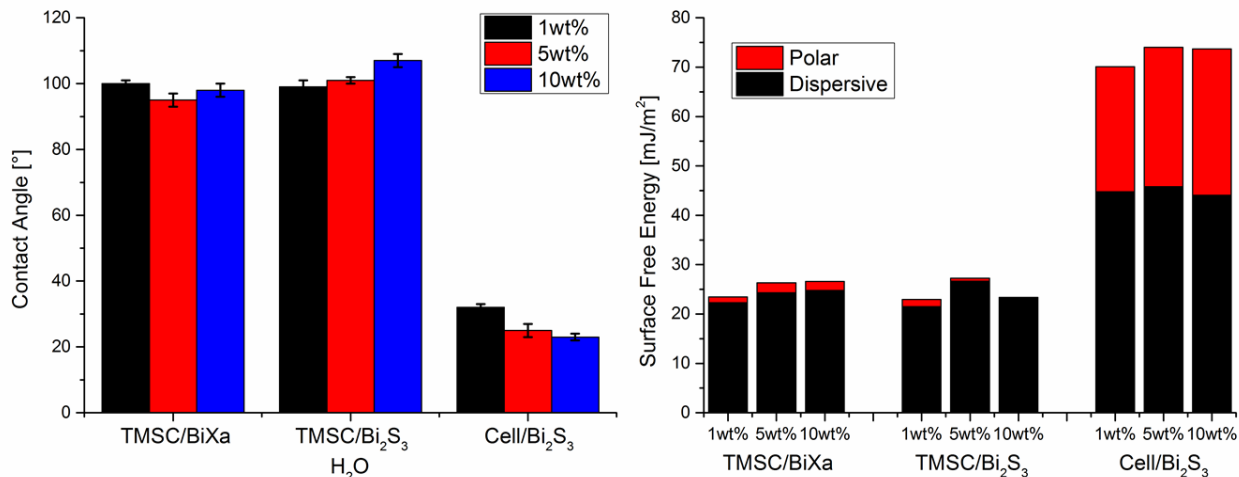
Figure 4.7. Contact angle (dest. H$_2$O) and surface free energy of the native, heat treated and regenerated sample.

As shown in Figure 7, the non-treated TMSC/BiXa films exhibit a static water contact angle of ca 100° regardless of the used concentration of BiXa for film preparation. Interestingly, even after the heat treatment step, i.e. the conversion of BiXa to Bi$_2$S$_3$, the films retain their hydrophobic character, with minor differences to the non-treated ones. These minor differences may be related to alterations in surface roughness, although we do not have hard evidence for this. Moreover, this data is a further proof (besides IR spectroscopy) that the TMS groups are not cleaved off by the formed volatile side products during BiXa decomposition. This is also reflected in the SFE of those films featuring a rather large dispersive and a low polar contribution. After a final HCl treatment step, the water contact angles decreased to values which are typical for cellulose films (25°) in combination with significantly larger SFE (ca 72 mJ/m^2) which now additionally features a rather large polar contribution of ca 30 mJ/m^2. The reason for this effect is the elimination of the nonpolar alkyl chains and TMS groups.

4.3.6 UV-Vis spectroscopy

Since Bi$_2$S$_3$ is known as material with a low band gap, UV-VIS was employed to check the suitability of this material as light absorber in TMSC and cellulose films. For this purpose the films have been deposited on glass slides instead of silicon wafers. Figure 4.7 compares the

TMSC/BiXa films before and after thermal treatment. It can be clearly seen that after the heat treatment the initial absorption band of the BiXa at ca 380 nm vanished while the characteristic spectrum of Bi_2S_3 nanoparticles with an onset between $800 - 900$ nm appears. The TMSC and regenerated cellulose matrix material (for TMSC and TMSC heated see ESI†) do not absorb in this area and therefore do not affect the absorption of the Bi_2S_3 nanoparticles.
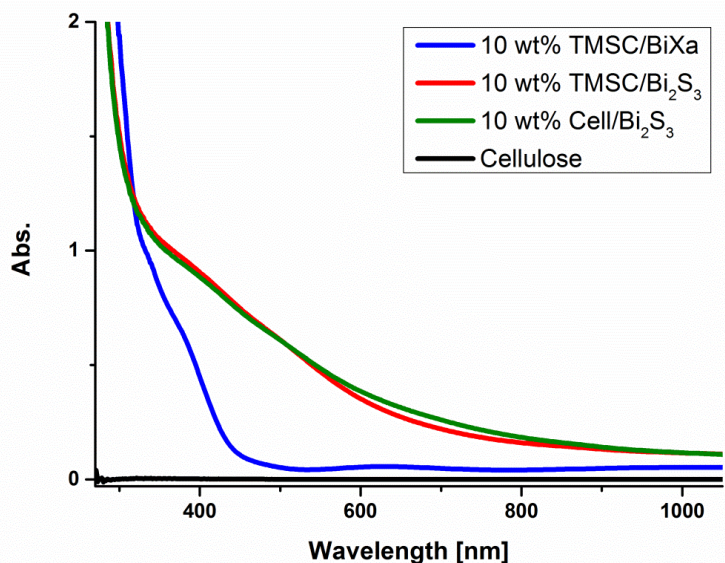
Figure 4.8. UV-VIS absorption spectra of the 10 wt% native, heat treated, regenerated and cellulose reference sample.

4.4 Conclusion

In summary, we demonstrated successfully the generation of bismuth sulfide cellulose based nanocomposites based on BiXa and TMSC. Spin coating of chloroform solutions of these compounds yielded for a variety of BiXa:TMSC ratios homogeneous films, whereas the BiXa could be successfully converted in all cases to Bi_2S_3 nanoparticles in a subsequent heating step under exclusion of oxygen and moisture. The conversion of the BiXa to the Bi_2S_3 nanoparticles was further monitored *in-situ* using GI-SWAXS experiments at a synchrotron facility and yielded together with TEM particle with a diameter of 25 ± 4 nm and a length of 80 ± 7 nm. The morphology of the films depends on the ratio of the initial amount of BiXa in the films and can

be smooth (1 wt%) or rough (10 wt%). After the particles had formed, the silyl groups were cleaved off using HCl vapors to obtain cellulose-Bi_2S_3 nanocomposite films. This procedure affected the roughness as well as the thickness of the films significantly since this conversion is associated with a shrinkage of the film due to the formation of hydrogen bonding [23]. Depending on whether the silyl groups are cleaved or not, the wettability of the nanocomposite films can be classified as either hydrophobic or hydrophilic. This enables a maximum in flexibility in the case these films should be embedded into devices. In principle, it is further possible to obtain partially regenerated films [24] whereas in this case the resulting surface free energies are somewhere in between fully regenerated cellulose and non-regenerated TMSC, opening further the processing window. Finally, the conversion of the BiXa to the bismuth sulfide particles also resulted in a change of color due to the low band gap of the nanoparticles which was quantified by UV-Vis spectroscopy. It clearly turned out that the observed absorptions correspond well to already published spectra of Bi_2S_3 nanoparticles. In future studies, we will focus how to use this approach in the generation of cellulose based photovoltaic devices.

4.5 References

(1) Rabin, O.; Manuel Perez, J.; Grimm, J.; Wojtkiewicz, G.; Weissleder, R., *Nat Mater* **2006,** *5*, 118-122.

(2) Wang, Y. Y.; Cai, K. F.; Yao, X., *J. Nanopart. Res.* **2012,** *14*, 1-7.

(3) Liu, G.-Y.; Xu, L.-Y.; Zhou, F.; Zhang, Y.; Li, H.; Xu, Q. F.; Lu, J. M., *PCCP* **2013,** *15*, 11554-11558.

(4) Konstantatos, G.; Levina, L.; Tang, J.; Sargent, E. H., *Nano Lett.* **2008,** *8*, 4002-4006.

(5) Jung, H.; Park, C.-M.; Sohn, H.-J., *Electrochim. Acta* **2011,** *56*, 2135-2139.

(6) Yao, K.; Zhang, Z. Y.; Liang, X. L.; Chen, Q.; Peng, L. M.; Yu, Y., *J. Phys. Chem. B* **2006,** *110*, 21408-21411.

(7) Yao, K.; Gong, W. W.; Hu, Y. F.; Liang, X. L.; Chen, Q.; Peng, L. M., *J. Phys. Chem. C* **2008,** *112*, 8721-8724.

(8) Ahmad, M.; Rafiq, M. A.; Rasool, K.; Imran, Z.; Hasan, M. M., *J. Appl. Phys.* **2013,** *113*, 043704.

(9) Li, H.; Yang, J.; Zhang, J.; Zhou, M., *RSC Adv.* **2012,** *2*, 6258-6261.

(10) Wang, Z.; Qu, S.; Zeng, X.; Liu, J.; Tan, F.; Jin, L.; Wang, Z., *Appl. Surf. Sci.* **2010,** *257*, 423-428.

(11) Martinez, L.; Stavrinadis, A.; Higuchi, S.; Diedenhofen, S. L.; Bernechea, M.; Tajima, K.; Konstantatos, G., *PCCP* **2013,** *15*, 5482-5487.

(12) Kaltenhauser, V.; Rath, T.; Haas, W.; Torvisco, A.; Muller, S. K.; Friedel, B.; Kunert, B.; Saf, R.; Hofer, F.; Trimmel, G., *J. Mat. Chem., C* **2013,** *1*, 7825-7832.

(13) Wolfberger, A.; Petritz, A.; Fian, A.; Herka, J.; Schmidt, V.; Stadlober, B.; Kargl, R.; Spirk, S.; Griesser, T., *Cellulose* **2015,** *22*, 717-727.

(14) Mohan, T.; Ristic, T.; Kargl, R.; A.Doliska; Köstler, S.; Ribitsch, V.; Marn, J.; Spirk, S.; Stana-Kleinschek, K., *Chem. Comm.* **2013,** *49*, 11530-11532.

(15) Orelma, H.; Filpponen, I.; Johansson, L.-S.; Laine, J.; Rojas, O. J., *Biomacromolecules* **2011,** *12*, 4311-4318.

(16) Kontturi, E.; Lankinen, A., *J. Am. Chem. Soc.* **2010,** *132*, 3678-3679.

(17) Ehmann, H. M. A.; Werzer, O.; Pachmajer, S.; Mohan, T.; Amenitsch, H.; Resel, R.; Kornherr, A.; Stana-Kleinschek, K.; Kontturi, E.; Spirk, S., *ACS Macro Lett.* **2015,** *4*, 713-716.

(18) Breitwieser, D.; Kriechbaum, M.; Ehmann, H. M. A.; Monkowius, U.; Coseri, S.; Sacarescu, L.; Spirk, S., *Carbohydr. Polym.* **2015,** *116*, 261-266.

(19) Müller-Buschbaum, P., Ezquerra, G.-G., Nogales, Gomez, Ed. Springer: Heidelberg, 2009.

(20) Pradhan, N.; Katz, B.; Efrima, S., *J. Phys. Chem. B* **2003,** *107*, 13843-13854.

(21) Kontturi, E.; Thüne, P. C.; Niemantsverdriet, J. W., *Langmuir* **2003,** *19*, 5735-5741.

(22) Mohan, T.; Spirk, S.; Kargl, R.; Doliska, A.; Vesel, A.; Salzmann, I.; Resel, R.; Ribitsch, V.; Stana-Kleinschek, K., *Soft Matter* **2012,** *8*, 9807-9815.

(23) Kontturi, E.; Suchy, M.; Penttilä, P.; Jean, B.; Pirkkalainen, K.; Torkkeli, M.; Serimaa, R., *Biomacromolecules* **2011,** *12*, 770-777.

(24) Mohan, T.; Kargl, R.; Doliška, A.; Vesel, A.; Köstler, S.; Ribitsch, V.; Stana-Kleinschek, K., *J. Coll. Interf. Sci.* **2011,** *358*, 604-610.
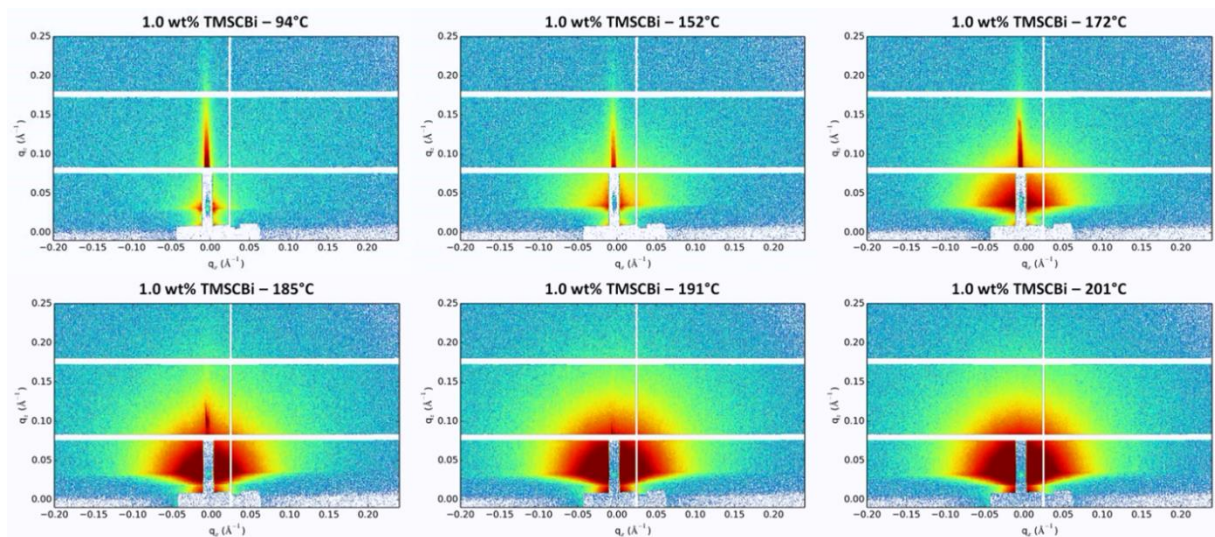
4.6 Supporting Information
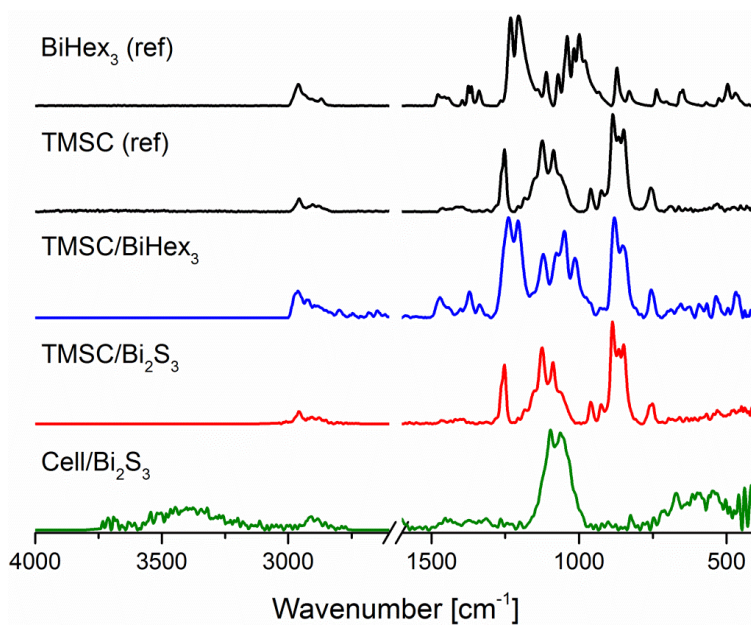
Figure S4.1. Comparison of the ATR IR reference spectra (BiXa, TMSC and cellulose) with nanocomposite thin films having a BiXa concentration of 1 wt%.
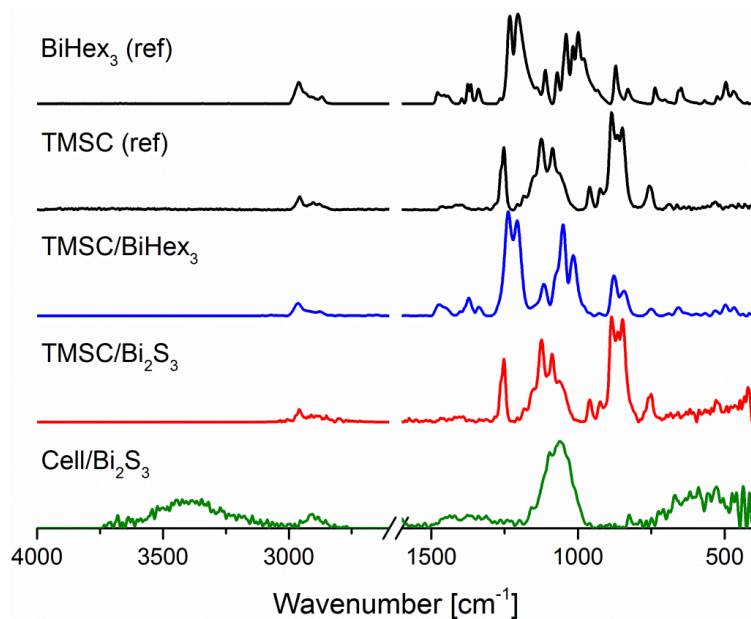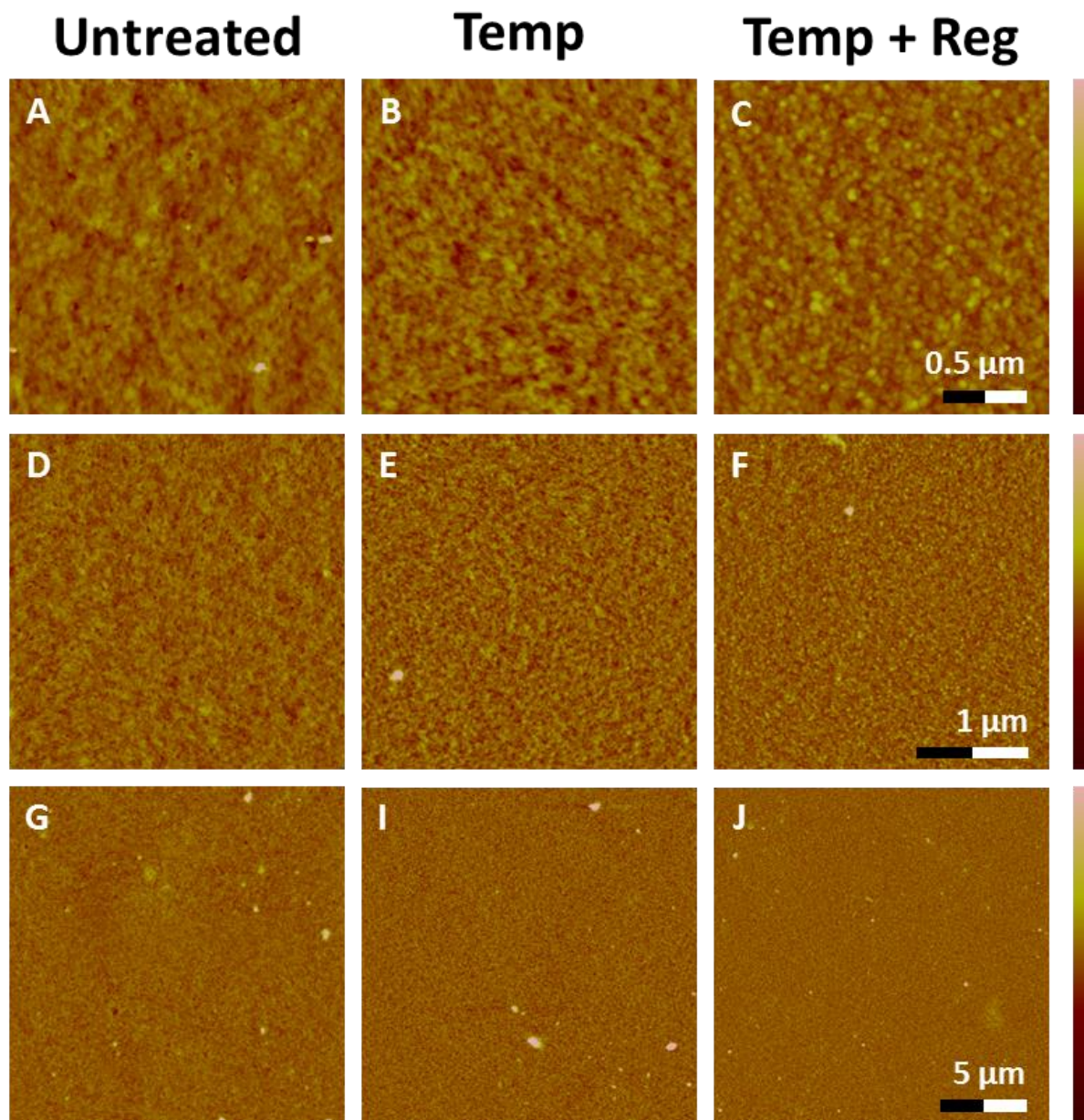
Figure S4.2. Comparison of the ATR IR reference spectra (BiXa, TMSC and cellulose) with nanocomposite thin films having a BiXa concentration of 10 wt%.

Figure S4.3. Heat induced growth of Bi_2S_3 nanoparticles in a TMSC film upon increase of temperature from 94 to 201° monitored by *in situ* GI-SAXS.
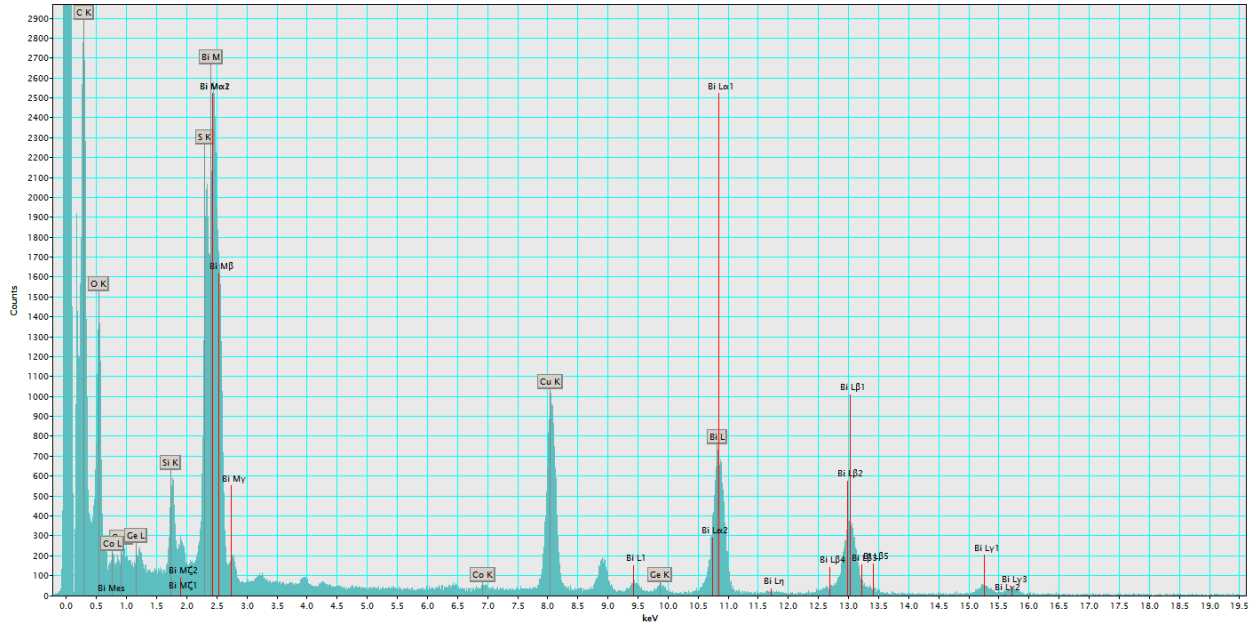
Figure S4.4. EDX spectrum of 5 wt% Bi$_2$S$_3$-NP in a TMSC matrix.

Figure S4.5. AFM images of 1 wt% BiXa (untreated, heat treated, heat treated + regenerated); Z-scale = 40 nm; A, B, C: 2 x 2 cm; D, E, F: 6 x 6 cm; G, I, J: 19 x 19 cm.

Table S4.1. Surface roughness of the nanocomposite films (1 wt%, 5 wt%, 10 wt%) determined by AFM before (TMSC/BiXa) and after heat treatment (ΔT) as well as subsequent HCl exposure (ΔT+HCl).

AFM Image Size	Surface Roughness Rq [nm]								
	2×2 μm^2	6×6 μm^2	19×19 μm^2	2×2 μm^2	6×6 μm^2	19×19 μm^2	2×2 μm^2	6×6 μm^2	19×19 μm^2
Sample	Untreated			Temp			Temp + Reg		
1 wt%	1.8 ±0.1	1.8 ±0.1	1.9 ±0.1	2.1 ±0.1	2.1 ±0.1	2.2 ±0.1	2.2 ±0.1	2.1 ±0.1	2.3 ±0.1
5 wt%	2.1 ±0.1	2.8 ±0.1	3.3 ±0.1	10.3 ±0.2	11.4 ±0.3	11.5 ±0.2	10.2 ±0.2	11.4 ±0.3	11.6 ±0.3
10 wt%	2.3 ±0.1	2.8 ±0.1	3.2 ±0.1	18.3 ±0.3	20.9 ±0.4	21.9 ±0.4	19.8 ±0.3	20.4 ±0.3	21.2 ±0.3
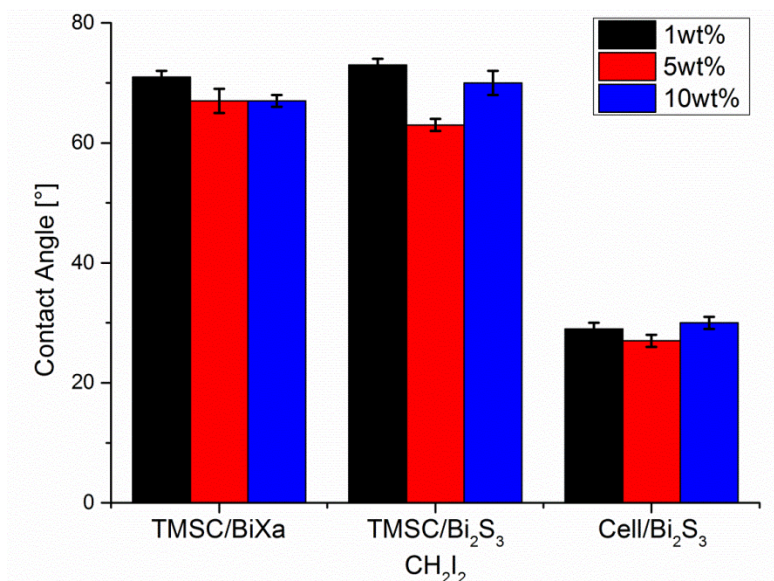
Figure S4.6. Static contact angles (diiodomethane) of the untreated, heat treated and regenerated sample.
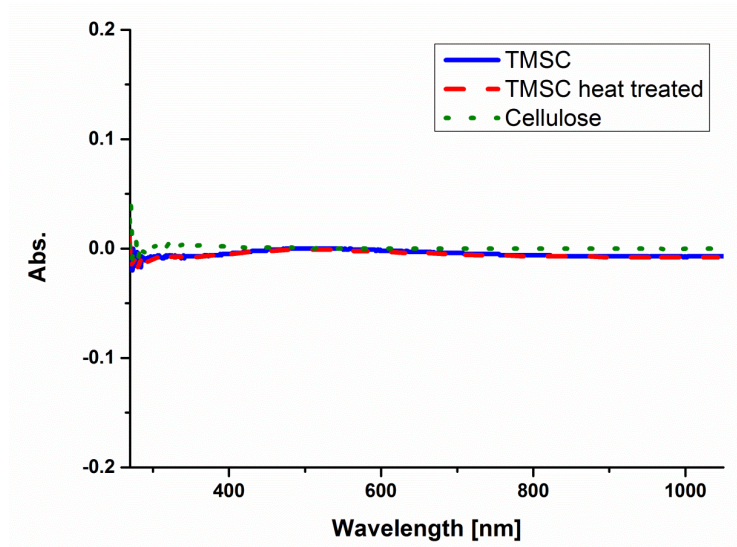
Figure S4.7. UV-VIS absorption spectra of reference matrix samples (TMSC, TMSC heat treated and cellulose).

Chapter 5

5. Biobased Nanocomposites for Optoelectronic Applications[1]

The following chapter is written for the submission in ACS Sustainable Chemistry & Engineering:

(1) David Reishofer, Thomas Rath, Heike M. Ehmann, Christian Gspan, Sebastian Dunst, Heinz Amenitsch, Harald Plank, Bruno Alonso, Emamanuel Belamie, Gregor Trimmel, Stefan Spirk, Submitted to *ACS Sustainable Chemistry & Engineering*, **2016**

A generic approach to design optoelectronic devices using renewable biopolymers is demonstrated. As a proof of principle, a biopolymer/$CuInS_2$ nanocomponent-based solar cell has been assembled by using a cellulose derivative with a reasonable life cycle performance, namely trimethylsilyl cellulose (TMSC). The solar cells are manufactured using a mixture of copper and indium xanthates as precursors, which decompose and form CIS nanoparticles within the biopolymer matrix during a thermal treatment, which was investigated by *in situ* combined grazing incidence small and wide angle X-ray scattering experiments. The growth of the nanoparticles is thereby controlled by the TMSC matrix. The nanocrystals exhibit an average diameter of approx. 4 nm. Using this composite, it was possible to fabricate solar cells, generating current in a wide range of the solar spectrum and exhibiting power conversion efficiencies of ca. 1%.

5.1 Introduction

To meet the challenges of climate change and sustainable use of global resources, tremendous efforts have been made to replace fossil derived energy resources and synthetic petrochemical-based materials by those derived from renewable resources. This development is mainly driven by the rather large CO_2 emissions associated with both, production of energy and of synthetic materials.[1] Among renewable energy resources, photovoltaics are one of the main pillars. One currently followed research area is the use of nanocrystals and nanocomposites in solar cells using at present mainly toxic compounds such as PbS or Cd-based chalcogenides.[2-5] In order to overcome environmental concerns, alternatives have been thoroughly investigated, among which $CuInS_2$ represents a non-toxic alternative.[6-9] However, also in this case, $CuInS_2$ is usually synthesized via wet-chemical/colloidal synthesis routes employing long-chained capping ligands, which have to be removed or exchanged using potentially toxic reagents (e.g. 1,3-benzenedithiol, hexanethiol, etc.) before the nanocrystalline absorber films for the solar cells can be prepared.[10,11] A convenient way to avoid capping agents and ligand exchange reagents is to generate the metal sulfide particles directly in the photovoltaic active layer. In this approach, nanocrystals are formed from precursor compounds which are converted to metal sulfides usually by a mild thermal treatment. Usually, a conjugated polymer matrix is used for controlling the nanocrystal growth.[12] Among the precursors, metal xanthates have proven to be most efficient since they decompose accompanied by the formation of only volatile by-products leaving the layer leading to pure conjugated polymer/nanocrystal nanocomposite thin films which can be directly applied as absorber layers in solar cells.[12-14] In this work, we investigate if it is possible to fully circumvent the use of synthetic capping ligands, ligand exchange reagents and polymers in the fabrication of $CuInS_2$-based nanocrystal solar cells by replacing them in the in-situ route by the bio-based trimethylsilyl cellulose.

Particularly cellulose and its derivatives have an enormous potential to substitute conventional polymers from several viewpoints.[15] Cellulose is a major constituent of lignocellulosic plant cell walls, it occurs in algae as well as in fungi and further it is biodegradable. Currently, it is exploited in a wide range of applications ranging from textiles, papermaking, food additives, and in medicine, to mention just the important ones.

Trimethylsilyl cellulose is a particular congener due to several reasons. It is organosoluble (at high degree of substitution with silyl groups), and further it can be easily converted to cellulose by simple exposure to HCl vapors cleaving off the non-toxic side product hexamethyldisiloxane (HDSO).[16] Life cycle analyses from the early 80ies of the last century revealed a good performance of TMSC in fiber spinning applications.[17,18] Later, its ability to form homogenous thin films on different types of surfaces was exploited to generate cellulose interfaces by exposing them to HCl vapors.[16] This opened the door for a fast production of different types of films with high reproducibility having a variety of applications such as photolithographically patterned dielectric gates in thin film transistors.[19] However, nanocomposite thin films derived from TMSC are much less explored. Such films are potentially interesting as model systems for drug release,[20] for the generation of nanoparticle decorated surfaces,[21,22] as well as for thin film membranes.[23]

The use of TMSC instead of synthetic ligands for such purposes follows several principles of the green chemistry (GC) and engineering (GE) principles, namely the use of a renewable feedstock (GC7, and GE12), better recyclability (GE 3, 6, 9, and 11) and enhanced biodegradability (GC10) compared to commonly employed polymers from fossil sources.[1]

5.2 Materials and Merhods

Materials. Trimethylsilyl-cellulose (TMSC; Avicel pulp DS: 2.7-2.9), purchased from TITK Rudolstadt MFSA, copper xanthate (copper O-2,2-dimethylpentan-3-yl-dithiocarbonate, CuXa) and indium (indium O-2,2-dimethylpentan-3-yl-dithio-carbonate, InXa) xanthate, synthesized according to a literature procedure,[12] were used as starting materials for the thin film preparation. Chloroform (99 wt%) and sulfuric acid (95 wt%) were purchased from VWR chemicals and hydrogen peroxide (30 wt%) from Sigma-Aldrich. All chemicals were used without purification. Silicon wafer, glass slides (Roth), Au-coated glass slides as substrate (SPR102-AU), Filter Chromafil® Xtra PVDF-45/25 0.45 μm, petri dishes (20 mL; 5 cm diameter), glass/ITO substrates (Xinyan Technology Ltd., Hong Kong) and PEDOT:PSS (Clevios P VP.Al 4083, Heraeus) were used as obtained.

Film preparation. For the characterization of the hybrid material, different substrates (AFM, SFE, Stylus profilometry, GISWAXS, STEM: silicon wafer (1.4 x 1.4 cm); UV-Vis: glass wafer (1.4 x 1.4 cm); ATR-IR: gold slide (2.0 x 1.0 cm)) were necessary. At the beginning the substrates were cleaned with "piranha" acid (H_2SO_4:H_2O_2 = 7:3 (v/v)) for 30 min (10 min for gold slides) and rinsed afterwards with distilled water to neutralize the surface. For the film preparation, TMSC (0.5 wt%) was dissolved in $CHCl_3$, filtered and combined (1:1 (v/v)) with the copper and indium xanthate (TMSC:$CuInS_2$ = 1:7 mol) solution (2 wt%, 6 wt%, 12 wt% in $CHCl_3$). This solution (180 µL) was spin coated on the different substrates at 4000 rpm for 60 s (acceleration 2500 rpm/s). The final in-situ synthesis of the $CuInS_2$-nanoparticles ($CuInS_2$-NPs) was done by thermal conversion (195°C over a period of 30 min, heating rate = 10°C/min) of copper and indium xanthate on a programmable heating plate.

ATR-IR spectroscopy. The infrared spectra were recorded with an ALPHA FT-IR spectrometer (Bruker; Billerica, MA, USA). For the measurement an attenuated total reflection (ATR) attachment was used with 48 scans at a resolution of 4 cm^{-1} and a scan range between 4000 and 400 cm^{-1}. The samples were prepared on Au-coated glass slides (SPR102-AU). The data were analyzed with OPUS 4.0 software.

Atomic force microscopy. For the atomic force microscopy (AFM) measurements a Veeco Multimode Quadrax MM AFM (Bruker; Billerica, MA, USA) was used. The images were recorded in the tapping mode (non-contact mode) and silicon cantilevers (NCH-VS1-W from NanoWorld AG, Neuchatel, Switzerland) were used with an average spring constant of 42 N/m (Force Constant) and a resonance frequency of 270 – 320 kHz (Coating: none). All measurements were performed at room temperature and under ambient atmosphere. The image processing and the calculation of the root mean square roughness (calculated from a 6 x 6 µm image) were done with the Nanoscope software (V7.30r1sr3; Veeco).

Profilometry. The determination of the layer thickness was done on a Bruker DekTak XT surface profiler. The scan length was set to 1000 µm over the time duration of 3 seconds. The profile was set to *hills* and *valleys*. The diamond stylus had a radius of 12.5 µm and the force was 3 mg with a resolution of 0.333 µm/sample and a measurement range of 6.5 µm. This measured profile was then used to determine the thickness.

Surface free energy. To determine the static contact angle and the surface free energy (SFE) a drop shape analysis system DSA100 (Krüss GmbH, Hamburg, Germany) with a T1E CCD video camera (25 fps) and the DSA1 v 1.90 software was used. For the measurements 3 µL droplets of Milli-Q water ($\geq$18 MΩcm^{-1}) and diiodomethane as test liquids in the sessile drop modus at 25 °C were deposited on the substrates. The dispense rate was adjusted to 200 µL/min and the time before the image was captured was 2 seconds. Each sample was measured at least three times. The contact angle calculations were performed with the Young-Laplace equation and the surface free energy calculation with the Owens-Wendt-Rabel & Kaelble method.

UV-Vis spectroscopy. The UV-Vis absorption spectra of the samples were measured with a Shimadzu UV-1800 UV spectrophotometer. The absorbance was determined from 270 - 1100 nm at 25°C and an ambient atmosphere.

Grazing incidence small and wide angle X-ray scattering. 2D grazing incidence small and wide angle X-ray scattering (GISAXS, GIWAXS) measurements were conducted at the Austrian SAXS Beamline 5.2L of the electron storage ring ELETTRA (Trieste, Italy),[24] using a similar setup as described before.[25] The beamline has been adjusted to a q-resolution (q=$4\pi/\lambda$*sin($2\theta/2$), 2θ represents the scattering angle) between 0.1 and 3.5 nm^{-1} (GISAXS). The X-ray energy was 8 keV. For the time-resolved measurements, the nanocomposite samples were placed in a heating cell (DHS 1100 from Anton Paar GmbH, Graz, Austria) equipped with a custom-made dome with Kapton polyimide film windows and were heated from 30 °C up to 230 °C at a heating rate of approx. 10 °C min^{-1} under nitrogen atmosphere. During the temperature scan, data were recorded with framing rate of 6 s using a Pilatus 1M detector (Dectris). For detection of the GIWAXS signal, a Pilatus 100K detector from Dectris was used. The angular calibration of the detectors was carried out using silver behenate powder (d-spacing of 58.38 Å) and p-bromo benzoic acid, respectively.

Transmission electron microscopy. Electron diffraction patterns and STEM images (Scanning Transmission Electron Microscopy) were acquired using a Tecnai F20 (operated at 200 kV) and a FEI Titan^3 G2 60-300 (operated at 300 kV). Both microscopes are equipped with a post-column electron energy filter from Gatan Inc. (GIF). The Titan microscope has a Cs probe corrector for the STEM mode and therefore the high resolution STEM images were observed on

the Titan3 G2 microscope. Selected area electron diffraction patterns (SAED) from the nanoparticles were recorded energy-filtered within a range of about 1400 nm in diameter.

Solar cell assembly. The nanocrystal solar cells were fabricated in the device architecture glass/ITO/PEDOT:PSS/biopolymer-CuInS$_2$/Al. Therefore, glass/ITO substrates with a sheet resistance of 10 Ω/sq were used, which were cleaned in deionized water and isopropanol in an ultrasonic bath followed by O$_2$ plasma cleaning (FEMTO, Diener Electronic, Germany). Afterwards, a PEDOT:PSS layer (Clevios P VP.Al 4083, Heraeus) was spin coated on the glass/ITO layer in ambient atmosphere and subsequently annealed at 150 °C for 10 min in a glove box. Next, the nanocomposite films were prepared by doctor blading of a chlorobenzene solution containing copper xanthates, indium xanthates and TMSC (concentration of TMSC in the precursor solution: 5 mg/mL; the weight ratio TMSC:CuInS$_2$ was 1:9) and subsequent thermal treatment (temperature program: 15 min heating from room temperature to 195 °C followed by 15 min at 195 °C) on a programmable heating plate (MCS 66, CAT Ingenieurbüro M. Zipperer GmbH). In the last preparation step, approximately 100 nm thick aluminum electrodes were deposited via thermal evaporation at a base pressure of 5×10^{-6} to 1×10^{-5} mbar. The characteristic values of the prepared solar cells were determined from IV curves recorded using a Keithley 2400 SourceMeter, a custom made Lab-View software and a Dedolight DLH400D lamp providing a spectrum very similar to AM1.5G. The light intensity was set to 100 mW/cm^2 (determined using a KippZonen-CMP-11 pyranometer, no spectral mismatch was considered).

5.3 Results and Discussion

The aim of this paper is to design a nanocrystal solar cell based on CuInS$_2$ and TMSC. In order to realize this goal (Scheme 5.1), different requirements must be met, namely solvent compatibility between the xanthate precursors and TMSC (i), the formation of homogeneous precursor films by spin-coating these solutions onto PEDOT:PSS/ITO (ii), the conversion of the metal xanthates to the metal sulfide nanoparticles in the TMSC matrix (iii), the final assembly of the device (iv) and finally the determination of the photoelectric activity of the assembled solar

cells (v). In all these steps, comprehensive characterization techniques are employed to investigate the underlying processes.
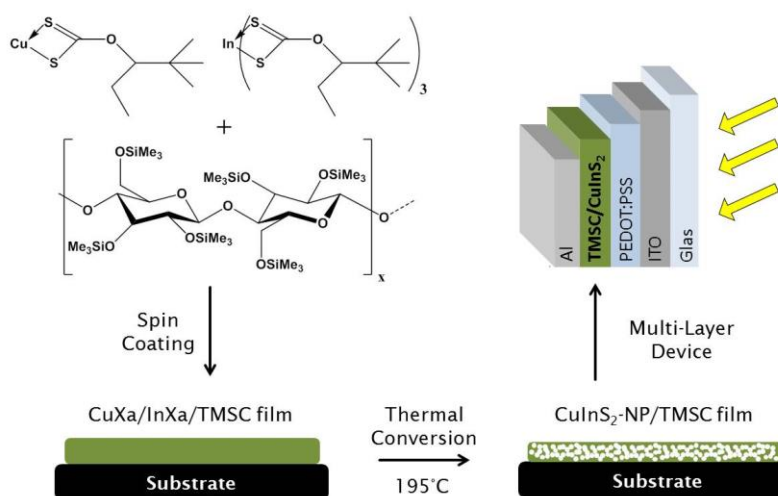

Scheme 5.1. Schematic representation of the manufacturing steps of CuInS$_2$/TMSC nanocomposite films and the multi-layer optoelectronic device.

As mentioned above, solvent compatibility between the xanthates and TMSC needs to be ensured. Based on previous findings in literature to prepare CuInS$_2$ nanoparticles, the ratio between the two xanthates (CuXa/InXa) was fixed at 1.0:1.7.[12] Then, a solubility screening was performed. For this purpose, different amounts of CuXa/InXa (2-12 wt% in chloroform) were added to TMSC solutions (0.5 wt%). All concentrations resulted in clear yellow-brownish solutions. These solutions were further subjected to spin-coating experiments and all the ratios led to films with a rather smooth optical appearance. Afterwards, the nanoparticle growth was induced by exposing the films to elevated temperature (195 °C, up to for 230 °C for GISWAXS). Decomposition of the xanthates via the Chugaev rearrangement[26] is initiated at a temperature of around 155 °C as shown earlier.[12] A benefit provided by the TMSC derivative is the rather high thermal stability (degradation starts at 280°C, see Figure S5.1, SI).

The influence of the heating step on the chemical composition of the films was monitored by ATR-IR spectroscopy. Figure 5.1 compares the different materials before and after the heating

procedure. The obtained results revealed that the TMSC was neither altered by exposure to elevated temperature (e.g. no hydrolysis indicated by the appearance of OH bands associated to ν_{OH} at 3200-3600 cm^{-1}) nor by the addition of copper or indium xanthate. Furthermore, it is demonstrated that the heating step led to decomposition of both xanthates while the TMSC remain unaffected.
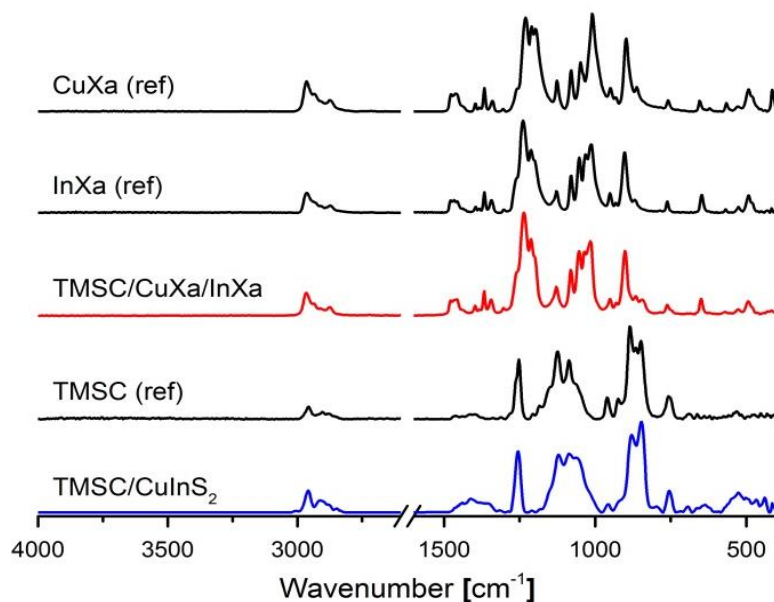
Figure 5.1. Comparison of ATR-IR spectra of the pure films with (CuXa, InXa and TMSC) with nanocomposite thin films before and after heating to 195°C at a CuXa/InXa ratio of 1:1.7 and a concentration of 12 wt%.

For the non-treated TMSC/CuXa/InXa film, characteristic bands for the xanthates as well as those for the TMSC were detected. The bands at 1081, 1054 and 1016 cm^{-1} can be assigned to C-S stretching vibrations and those at 1237 and 1212 cm^{-1} to asymmetric C–O–C stretching vibrations of the InXa.[27,28] The bands associated to the TMSC matrix are present at 848 cm^{-1} which is characteristic for ν_{Si-C}. After the heat treatment, all bands associated with CuXa and InXa vanished, indicating the decomposition of the xanthates and the formation of CuInS$_2$ nanoparticles. The remaining bands (1255, 1119, 1086, 880, 848 cm^{-1}) are distinct for Si-C and Si-O-C vibrations of TMSC. Moreover, these results prove that the TMSC is not regenerated to cellulose and remain untouched during the in-situ synthesis of the nanoparticles at 195°C.

In order to get insights into the formation of the $CuInS_2$ nanocrystals in the TMSC matrix, we conducted combined time resolved GIWAXS and GISAXS experiments using synchrotron radiation on a temperature controlled sample stage. The temperature-dependent evolution of the GIWAXS patterns of a TMSC/metal xanthate sample is shown in Figure 5.2. Between 120 and 150 °C, an intense broad peak between 26 and 32° and a minor one around 47° 2 theta evolved. These peaks can be assigned to the (112) and (204) reflections, which are characteristic for chalcopyrite $CuInS_2$. Therefore, it can be concluded that the conversion of the precursors to the $CuInS_2$ nanocrystals takes place within this temperature range. The corresponding GIWAXS patterns are shown in the SI (Figure S5.3) in higher time resolution. Further, time-resolved GISAXS measurements were performed using 100 nm thick films and a time resolution of 6 s.
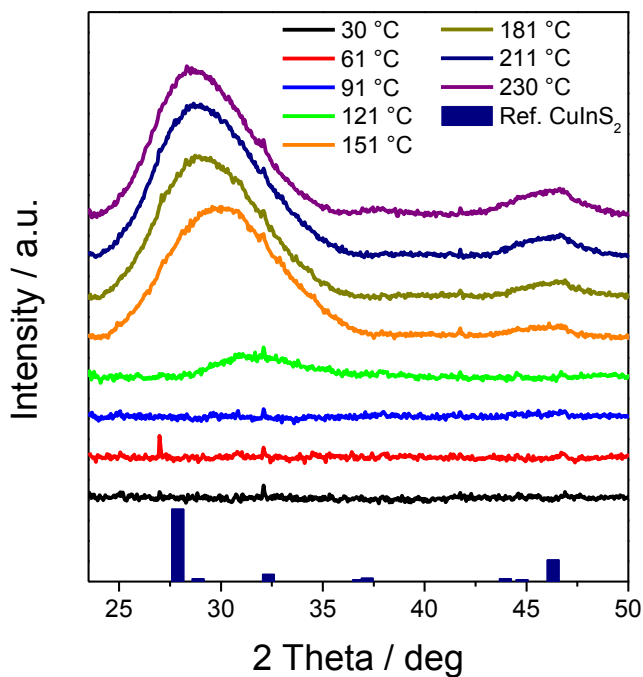
Figure 5.2. Evolution of the GIWAXS patterns of a TMSC/metal xanthate sample during the heating run (the data are shifted horizontally for better visibility) and a reference pattern of tetragonal $CuInS_2$ (PDF 032-0339).

These short intervals are beneficial as the formation of nanocrystalline metal sulfides from metal xanthates proceeds rather fast.[29,30] The GISAXS patterns at different temperatures during the heating run are presented in Figure 5.3 (A) demonstrating a strong increase of scattering due to

the formation of $CuInS_2$ particles. The areas used for horizontal integration are indicated with a red box in the GISAXS images and the resulting vertical cuts at $q_z = 0.35$ nm^{-1} are presented in Figure 5.3 (B).

The evolution of the integrated intensities of the GI-SAXS patterns (Figure 5.3, C), calculated between $q_y = 0.1$ and 2.5 nm^{-1}) revealed that minor structural changes were taking place in the TMSC/metal xanthate film already starting at a temperature of around 120 °C. At approx. 145-150 °C, a significant increase in the integrated intensity was observed. This originated from the decomposition of the metal xanthates, the evaporation of volatile organic decomposition products and the formation of $CuInS_2$ nanocrystals in this temperature range as already revealed by the GI-WAXS investigations. By these processes, the overall electron density in the nanocomposite film was increased, leading to an enhanced scattering intensity in the GISAXS patterns. After the formation of the $CuInS_2$ nanocrystals, the changes in the integrated intensities were minor. Any evidence for further compaction of the nanocomposite film and decomposition of the organic TMSC matrix was not observed until a temperature of 230 °C.
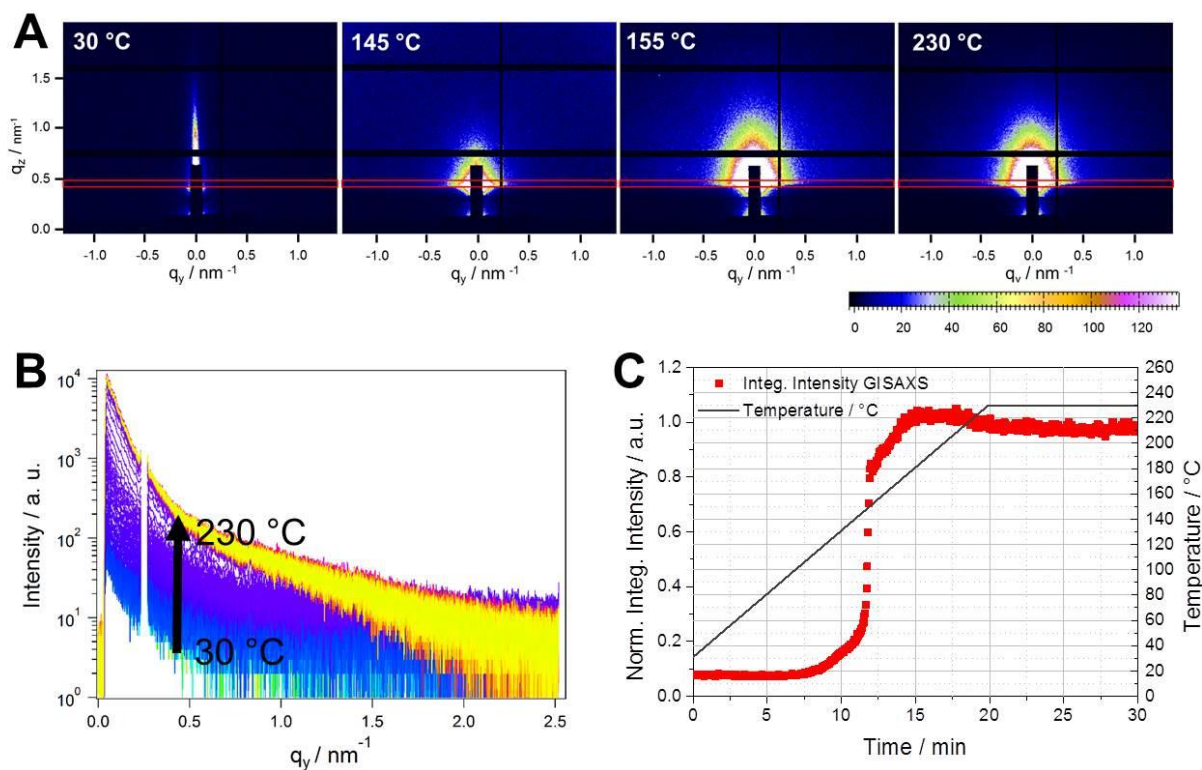
Figure 5.3. (A) GISAXS images of a TMSC/metal xanthate sample at different temperatures during the formation of the $CuInS_2$ nanocrystals in the TMSC matrix (the red boxes indicate the areas used for horizontal integration), (B) temperature-dependent evolution of the horizontal cuts of the GISAXS patterns and (C) the corresponding integrated intensities of the GISAXS curves.

A further important point for the usage of the nanocomposite layers in a solar cell or other optoelectronic devices is the connection of the separate nanoparticles inside the film to ensure a continuous pathway allowing for electronic conduction throughout the material. The bright field TEM images at different magnifications (Figure 5.4. A, B) revealed a dense network of nanoparticles with diameters from 2 nm to 5 nm in the TMSC matrix. Also here crystallographic data on the nanoparticles' structure can be derived by selected area electron diffraction patterns (SAED) (Figure 4, C)). The diffraction patterns feature three main diffraction rings at $r = 3.18\ nm^{-1}$ (112), $r = 5.16\ nm^{-1}$ (204/220) and $r = 6.01\ nm^{-1}$ (116/312) which are in excellent agreement with reference data for chalcopyrite $CuInS_2$ (PDF 032-0339) and a further proof (beside the GI-WAXS data) for the high crystallinity of the nanoparticles inside the film.
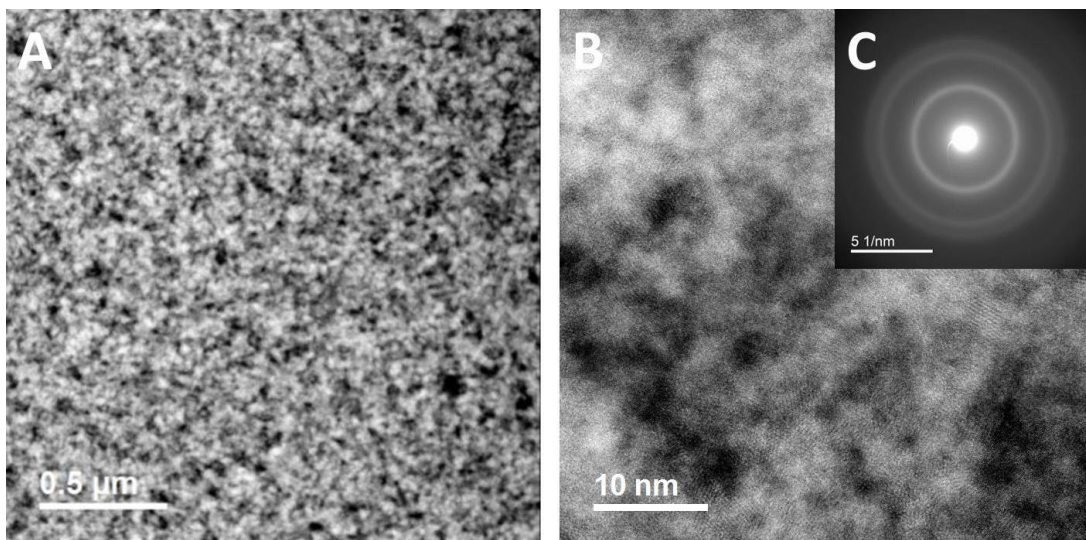
Figure 5.4. Images (A) and (B) represent bright field TEM images of a sample having 12 wt% CuInS$_2$-NP in a TMSC matrix at different magnifications and (C) a corresponding SAED image. More data is available in the SI (Figure S5.4).

An important aspect for the design of optoelectronic devices is the morphology of the hybrid layer. Especially in the assembly of multi-layer devices, the surface roughness of the different layers is crucial for their performance. For that reason the surface was analyzed by atomic force microscopy (AFM) before and after the heat treatment.
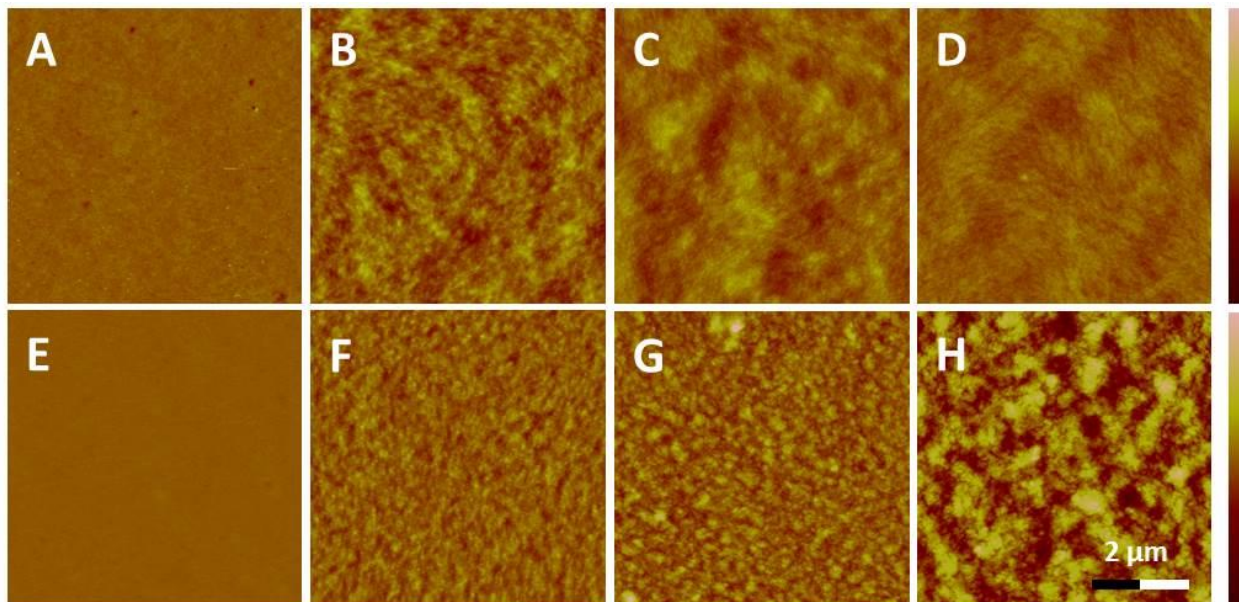
Figure 5.5. AFM images of the different films. Upper row: untreated, A) TMSC matrix, B) 2 wt%, C) 6 wt%, D) 12 wt% TMSC/CuXa/InXa, Z-scale (A, B, C, D) = 40 nm; bottom row: heat treated, E) TMSC matrix heat treated, F) 2 wt%, G) 6 wt% H) 12 wt% TMSC/CuInS$_2$, Z-scale (E, F, G, H) = 100 nm

Figure 5.5 shows the results of the AFM measurements, which reveal a smooth surface for the untreated films (A – D). This can be explained with the good solubility of the starting materials and the good film forming properties of the material. Compared with the pure TMSC reference sample, the TMSC/CuXa/InXa films had some small surface features, but they did not influence the surface roughness (~ 2 nm). Furthermore, also the concentration of CuXa/InXa did not have a significant impact on the morphology. After the heat treatment, the topography of the surface changed and the surface roughness increased, which correlated to the amount of nanoparticles. The surface roughness was 4.4 nm for the lowest concentration (2 wt%), 6.1 nm (6 wt%) and 12.8 nm at 12 wt%. These values imply that the surface is smooth enough for the envisaged use in solar cell applications. During the heat treatment, the film thickness decreased due to the removal of volatile compounds of the xanthates from 220±6 to 76±3 nm (2 wt%), 625±7 to 105±2 nm (6 wt%) and 1241±12 to 193±5 nm for 12 wt%. During the heating process the films lost 65 - 84% of their initial thickness due to the decomposition of the xanthates and the related higher packing density of the CuInS$_2$ nanoparticles.

For the usage in a multi-layer device like a solar cell the wettability of the nanocomposite is important. Especially, the surface free energy (SFE), calculated by contact angle measurements of at least two liquids (H_2O, CH_2I_2; Figure S5.5 and S5.6, SI)), is a crucial parameter whose tuning allows for preventing adhesion problems with connecting layers.

The hydrophobic character of the TMSC/CuXa/InXa film was reflected in a water contact angle of approximately ~97° and a surface free energy of 18-23 mJ/m² with a major apolar contribution. After the heat treatment and the associated formation of $CuInS_2$ nanoparticles, the films retain their hydrophobic character (CA ~90°). Simultaneously, the surface free energies increased depending on the nanoparticle concentration. This effect may originate from roughness effects since SFE increases with increasing $CuInS_2$-NP concentrations in the films. Moreover, these data also confirm the stability of the TMSC during the heat treatment regardless of the starting xanthate concentration.

The UV-VIS absorption of the film was determined to prove the suitability of the hybrid material for the application as an absorber material in a nanocrystal solar cell. The untreated film showed a distinctive absorption band for CuXa/InXa starting at ca. 420 nm, which vanished after the heat treatment Figure 5.6. At the same time, the characteristic spectrum of $CuInS_2$ nanoparticles with an onset between 800-900 nm appeared.[12] Furthermore, the TMSC matrix did not show any absorption in the measured range and did not affect the absorption of the $CuInS_2$ nanoparticles.
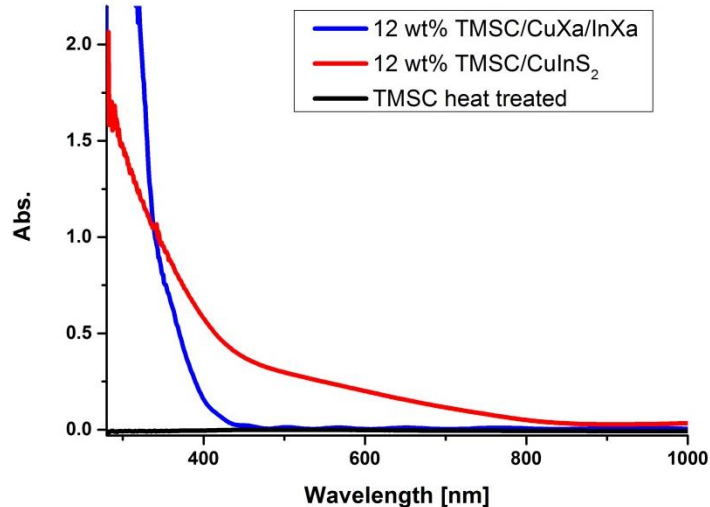
Figure 5.6. UV-VIS absorption spectra of the 12 wt% untreated, heat treated and TMSC reference sample.

To demonstrate the suitability of the prepared TMSC/CuInS$_2$ films for the application in optoelectronic devices, we prepared solar cells using a simple device architecture by sandwiching the TMSC/CuInS$_2$ films between ITO/PEDOT:PSS and aluminum electrodes. In Figure 5.7, typical I/V curves for such a device measured in the dark and under illumination are shown. The solar cell exhibited a V$_{OC}$ of 480 mV, which is in line with other reported solar cells based on nanocrystalline CuInS$_2$/conjugated polymer absorber films.[6] The short circuit current was approximately 5.5 mA/cm². This is significantly lower compared to solar cells with absorber layers in which CuInS$_2$ nanocrystals are embedded in a matrix of a conjugated polymer.[12] However, the observed I$_{SC}$ proves that an interconnected network of CuInS$_2$ nanocrystals was formed in the insulating TMSC matrix allowing for efficient charge transport in the nanoparticle phase to the electrodes. While the control of nanocrystal growth and film formation can be challenging in the formation of nanocrystal solar cells here, the TMSC matrix prevents extensive growth of the nanoparticles during the formation, facilitates the formation of a homogeneous thin film and inhibits short circuiting of the device. Overall, a power conversion efficiency of 0.99% was obtained by the *in situ* prepared TMSC/CuInS$_2$ absorber films.
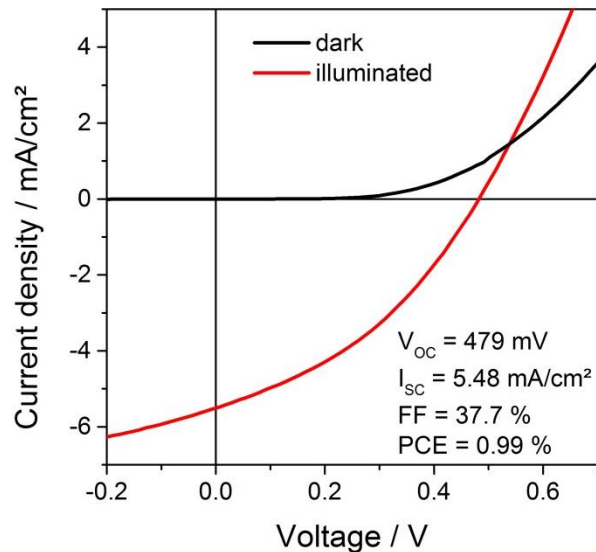
Figure 5.7. IV curves of CuInS$_2$/TMSC solar cells measured in the dark and under 100 mW/cm² illumination.

Further, the chosen approach is in principle scalable to other biopolymers as well, as long as they form stable films, which are not decomposed by the heat treatment required for the generation of the nanoparticles. At the moment, we explore chitin nanocrystals (ChNCs) derived films for such purposes as well. Figure 5.8 illustrates a comparison of the ATR-IR spectra of ChNCs/CuInS$_2$-nanocomposite with the precursor film ChNCs/CuXa/InXa as well as the pure reference materials CuXa, InXa, and ChNCs. The spectrum of the final ChNCs/CuInS$_2$-nanocomposite is dominated by the vibrations of the ChNCs, whereas the significant peaks from the xanthate precursors are absent proving complete conversion to CuInS$_2$.
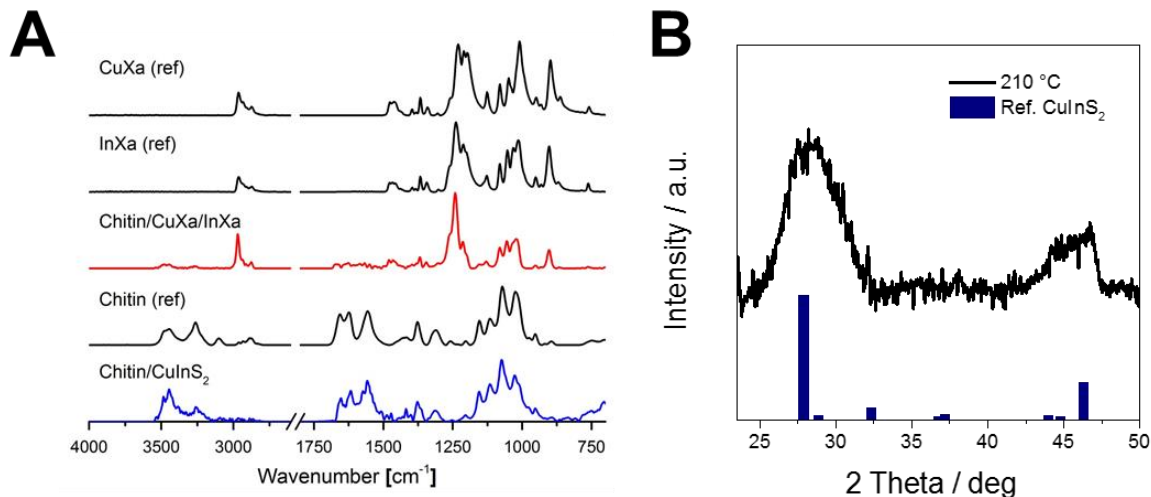
Figure 5.8. A) Comparison of the ATR IR reference spectra (CuXa, InXa and Chitin) with nanocomposite thin films having a CuXa/InXa (1:1.7) concentration of 3.7 wt%; B) GIWAXS pattern of the final ChNC/CuInS$_2$-nanocomposite and a reference pattern of tetragonal CuInS$_2$ (PDF 032-0339).

The formation of CuInS$_2$ - investigated again by combined GIWAXS and GISAXS experiments - takes place at slightly higher temperatures of approx. 170 °C (see Figures S5.9 and S5.10 in the supporting information) compared to the conversion to the CuInS$_2$ nanocrystals in the TMSC matrix. Figure 5.8 (B) shows the final GIWAXS trace (measured at 210 °C) in comparison to the CuInS$_2$ reference pattern proving also the formation of CuInS$_2$ in this system. However, the dispersability and the stability upon heat treatment have been shown insufficient so far to prepare a working solar cell with satisfying performance. Especially the obtained high roughness (see AFM images in Figure S5.7 in the SI) is detrimental for thin film solar cells. Nevertheless, this approach might be interesting for templated porous metal sulfide films analogous to porous silicates obtained by ChNCs-templating.[31]

In summary, we successfully demonstrated the replacement of synthetic ligands by the use of a biopolymer derivative, namely trimethylsilyl cellulose, for the fabrication of CuInS$_2$ nanocrystal solar cells. The solar cells feature a promising power conversion efficiency given the fact that we intended a proof of principle study and any extensive optimization steps of the solar cells were not performed. Further optimization by increasing the nanocrystal content in the biopolymer

matrix, its layer thickness, and the incorporation of interlayers, might lead to competitive solar cells with similar or superior performance than the most efficient $CuInS_2$ nanocrystal-based solar cells reported so far.[7-9]

5.4 References

(1) Tabone, M. D.; Cregg, J. J.; Beckman, E. J.; Landis, A. E., *Environ. Sci. Technol.* **2010,** *44*, 8264-8269.

(2) Yang, J.; Wang, J.; Zhao, K.; Izuishi, T.; Li, Y.; Shen, Q.; Zhong, X., *J. Phys. Chem. C* **2015,** *119*, 28800-28808.

(3) Ren, Z.; Wang, J.; Pan, Z.; Zhao, K.; Zhang, H.; Li, Y.; Zhao, Y.; Mora-Sero, I.; Bisquert, J.; Zhong, X., *Chem. Mater.* **2015,** *27*, 8398-8405.

(4) Chuang, C.-H. M.; Brown, P. R.; Bulović, V.; Bawendi, M. G., *Nat Mater* **2014,** *13*, 796-801.

(5) Yuan, M.; Liu, M.; Sargent, E. H., *Nature Energy* **2016,** *1*, 16016.

(6) So, D.; Pradhan, S.; Konstantatos, G., *Nanoscale* **2016,** *8*, 16776-16785.

(7) Jara, D. H.; Yoon, S. J.; Stamplecoskie, K. G.; Kamat, P. V., *Chem. Mater.* **2014,** *26*, 7221-7228.

(8) Guijarro, N.; Guillen, E.; Lana-Villarreal, T.; Gomez, R., *Phys. Chem. Chem. Phys.* **2014,** *16*, 9115-9122.

(9) Pan, Z.; Mora-Seró, I.; Shen, Q.; Zhang, H.; Li, Y.; Zhao, K.; Wang, J.; Zhong, X.; Bisquert, J., *J. Am. Chem. Soc.* **2014,** *136*, 9203-9210.

(10) Scheunemann, D.; Wilken, S.; Parisi, J.; Borchert, H., *Appl. Phys. Lett.* **2013,** *103*, 133902.

(11) Halpert, J. E.; Morgenstern, F. S. F.; Ehrler, B.; Vaynzof, Y.; Credgington, D.; Greenham, N. C., *ACS Nano* **2015,** *9*, 5857-5867.

(12) Rath, T.; Edler, M.; Haas, W.; Fischereder, A.; Moscher, S.; Schenk, A.; Trattnig, R.; Sezen, M.; Mauthner, G.; Pein, A.; Meischler, D.; Bartl, K.; Saf, R.; Bansal, N.; Haque, S. A.; Hofer, F.; List, E. J. W.; Trimmel, G., *Adv. Energy Mat.* **2011,** *1*, 1046-1050.

(13) Fradler, C.; Rath, T.; Dunst, S.; Letofsky-Papst, I.; Saf, R.; Kunert, B.; Hofer, F.; Resel, R.; Trimmel, G., *Sol. Energy Mater. Sol. Cells* **2014,** *124*, 117-125.

(14) M Arar, M.; Gruber, M.; Edler, M.; Haas, W.; Hofer, F.; Bansal, N.; Reynolds, L. X.; Haque, S. A.; Zojer, K.; Trimmel, G.; Rath, T., *Nanotechnology* **2013,** *24*, 484005.

(15) Klemm, D.; Heublein, B.; Fink, H.-P.; Bohn, A., *Angew. Chem. Int. Ed.* **2005,** *44*, 3358–3393.

(16) Schaub, M.; Wenz, G.; Wegner, G.; Stein, A.; Klemm, D., *Advanced Materials* **1993,** *5*, 919-922.

(17) Cooper, G. K.; Sandberg, K. R.; Hinck, J. F., *Journal of Applied Polymer Science* **1981,** *26*, 3827-3836.

(18) Greber, G.; Paschinger, O., *Lenz. Ber.* **1983,** *55*, 20-25.

(19) Wolfberger, A.; Petritz, A.; Fian, A.; Herka, J.; Schmidt, V.; Stadlober, B.; Kargl, R.; Spirk, S.; Griesser, T., *Cellulose* **2015,** *22*, 717-727.

(20) Maver, T.; Maver, U.; Mostegel, F.; Griesser, T.; Spirk, S.; Smrke, D. M.; Stana-Kleinschek, K., *Cellulose (Dordrecht, Neth.)* **2015,** *22*, 749-761.

(21) Taajamaa, L.; Rojas, O. J.; Laine, J.; Yliniemi, K.; Kontturi, E., *Chem. Commun.* **2013,** *49*, 1318-1320.

(22) Breitwieser, D.; Kriechbaum, M.; Ehmann, H. M. A.; Monkowius, U.; Coseri, S.; Sacarescu, L.; Spirk, S., *Carbohydr. Polym.* **2015,** *116*, 261-266.

(23) Puspasari, T.; Yu, H.; Peinemann, K.-V., *ChemSusChem* **2016,** *9*, 2908-2911.

(24) Amenitsch, H.; Rappolt, M.; Kriechbaum, M.; Mio, H.; Laggner, P.; Bernstorff, S., *Journal of Synchrotron Radiation* **1998,** *5*, 506-508.

(25) Fischereder, A.; Rath, T.; Haas, W.; Amenitsch, H.; Schenk, D.; Zankel, A.; Saf, R.; Hofer, F.; Trimmel, G., *ACS Appl. Mater. Interfaces* **2012,** *4*, 382-390.

(26) Pradhan, N.; Katz, B.; Efrima, S., *J. Phys. Chem. B* **2003,** *107*, 13843-13854.

(27) Socrates, G., *Infrared Characteristic Group Frequences, Tables and Charts*. 2nd ed.; Wiley: Chichester, 1994.

(28) Barreca, D.; Gasparotto, A.; Maragno, C.; Seraglia, R.; Tondello, E.; Venzo, A.; Krishnan, V.; Bertagnolli, H., *Appl. Organomet. Chem.* **2005,** *19*, 1002-1009.

(29) Dunst, S.; Rath, T.; Radivo, A.; Sovernigo, E.; Tormen, M.; Amenitsch, H.; Marmiroli, B.; Sartori, B.; Reichmann, A.; Knall, A.-C.; Trimmel, G., *ACS Appl. Mater. Interfaces* **2014,** *6*, 7633-7642.
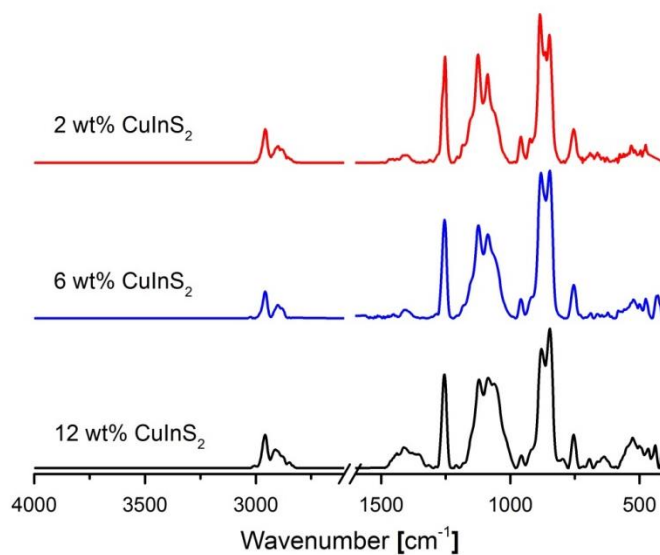
(30) MacLachlan, A. J.; Rath, T.; Cappel, U. B.; Dowland, S. a.; Amenitsch, H.; Knall, A. C.; Buchmaier, C.; Trimmel, G.; Nelson, J.; Haque, S. a., *Adv. Funct. Mater.* **2015,** *25*, 409-420.

(31) Alonso, B.; Belamie, E., *Angew. Chem. Int. Ed.* **2010,** *49*, 8201-8204.
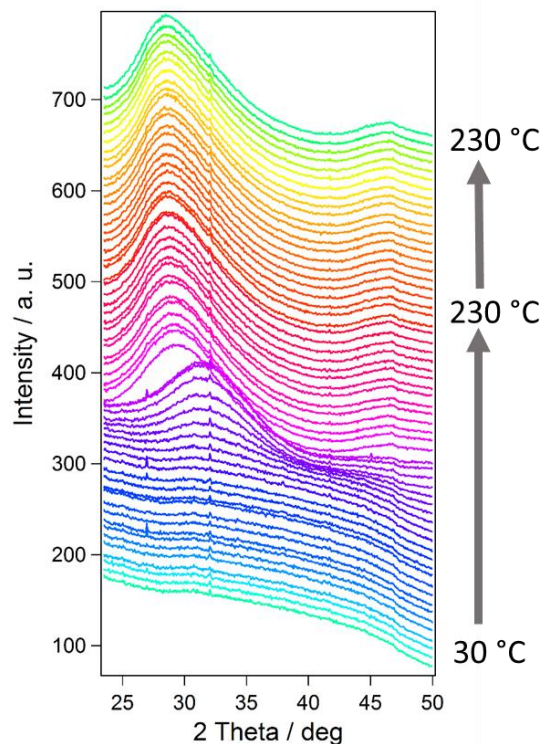
5.5 Supporting Information
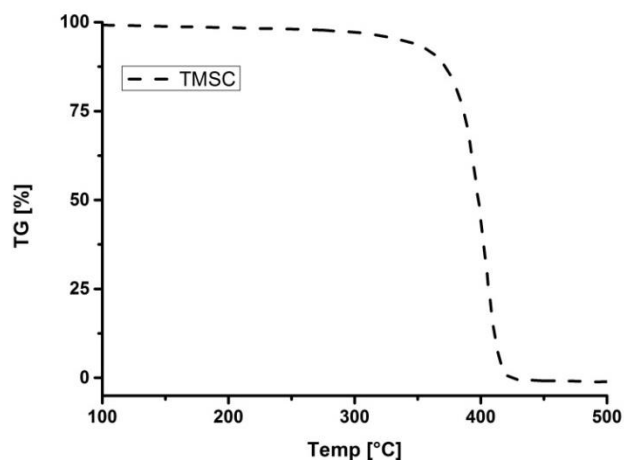
**Figure S5.1**. TGA of the used TMSC in this study.

Figure S5.2. Comparison of ATR IR spectra of TMSC/CuInS$_2$ nanocomposites at different CuXa/InXa concentrations.
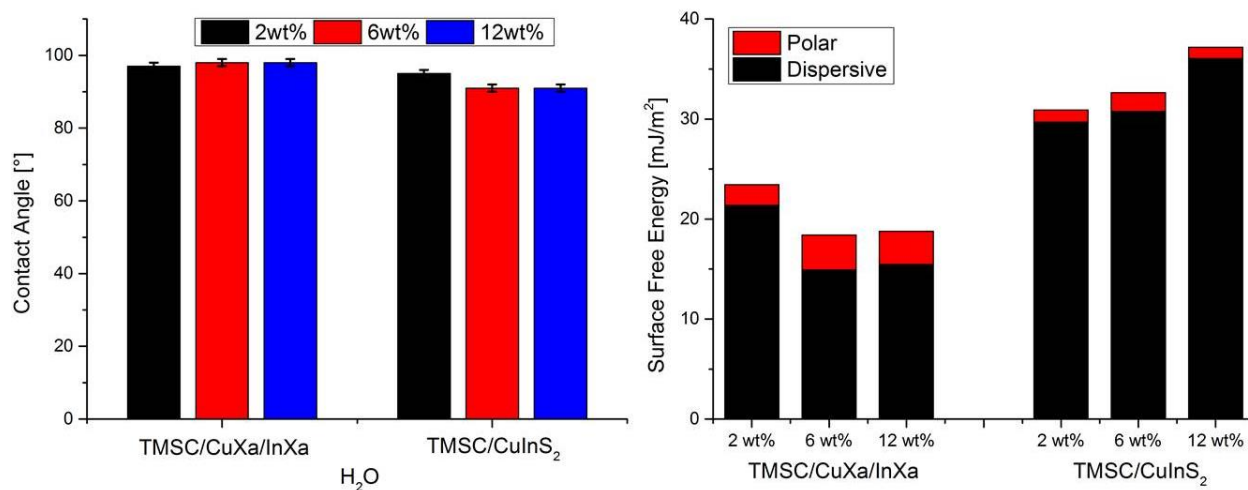
Figure S5.3. Evolution of the GIWAXS pattern during the heating run (raw data, every 10th measurement is shown, data are shifted vertically for better visibility) of a TMSC/metal xanthate sample
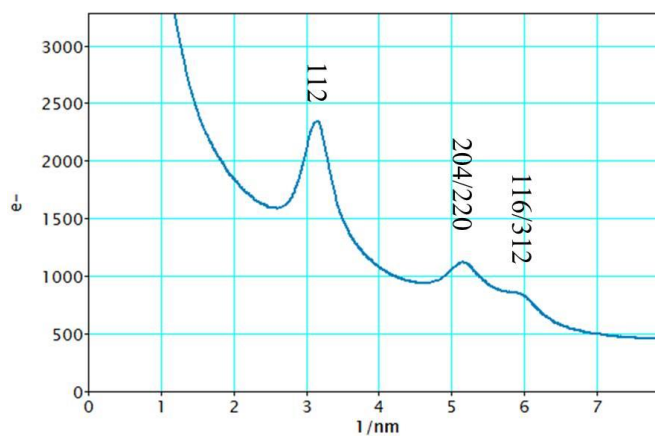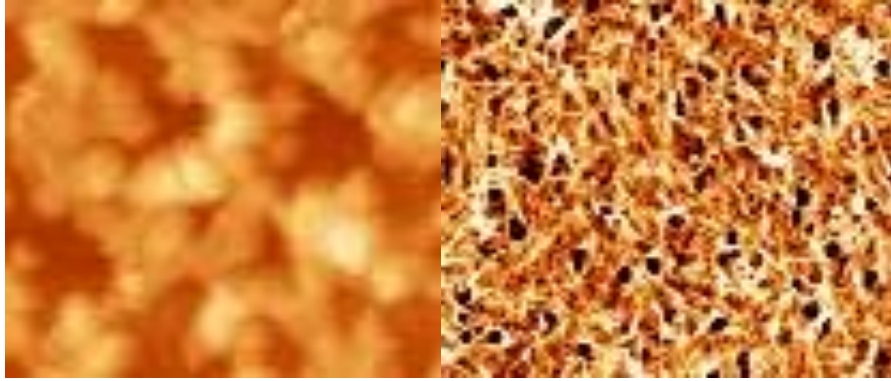

Figure S5.4. Rotational line profile of SAED measurement (12 wt% TMSC/CuInS$_2$)
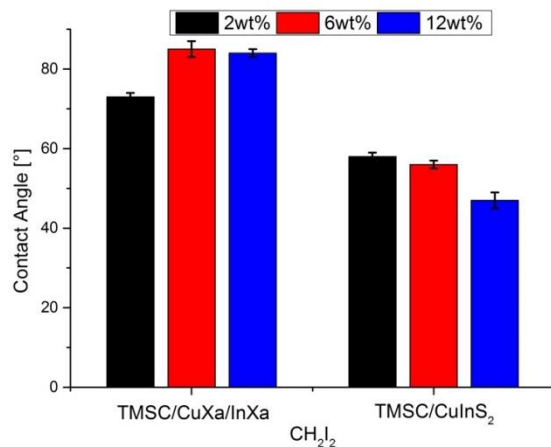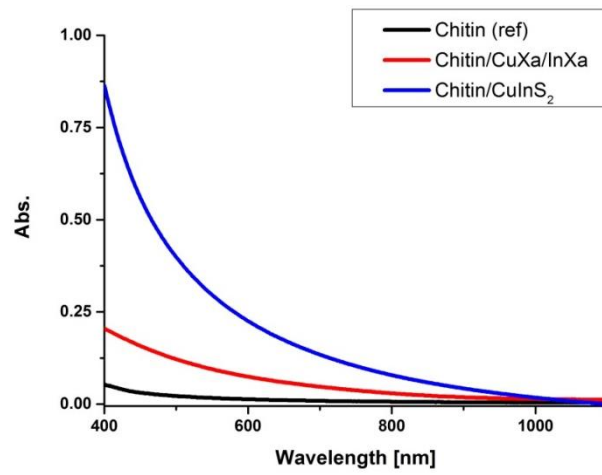
Figure S5.5. Static contact angles (diiodomethane) of the untreated and heat treated 12 wt% CIS/TMSC sample.

Figure S5.6. Static contact angles (dist. H_2O, left) and surface free energy (right) of the untreated and heat treated sample.

Figure S5.7. AFM topography images (5 x 5 μm^2) of a 3.7 and 0.37 wt% CIS/ChNC thin film.

Figure S5.8. UV-VIS absorption spectra of the 3.7 wt% untreated and heat treated sample.
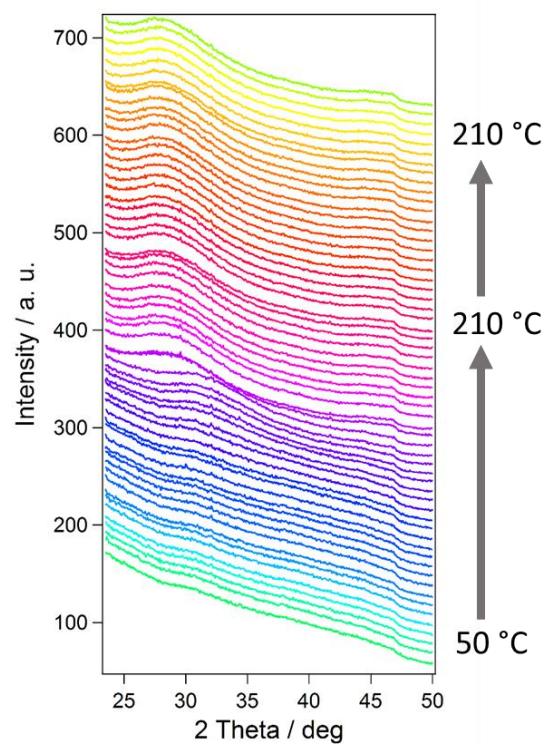
Figure S5.9. Evolution of the GIWAXS pattern during the heating run (raw data, every 10th measurement is shown, data are shifted vertically for better visibility) of a Chitin nanocrystal/metal xanthate sample
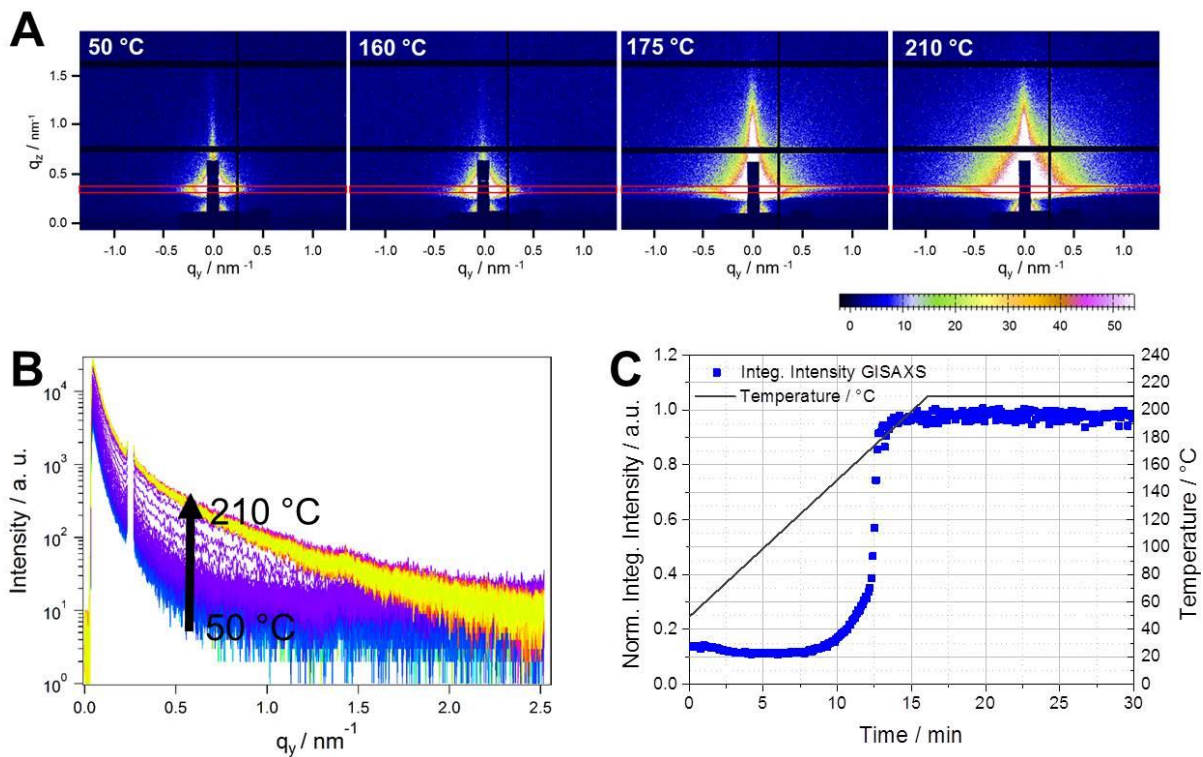
Figure S5.10 (A) GISAXS images of a chitin nanocrystal/metal xanthate sample at different temperatures during the formation of the $CuInS_2$ nanocrystals in the chitin matrix (the red boxes indicate the areas used for horizontal integration at $q_z = 0.35$ nm^{-1}), (B) temperature-dependent evolution of the horizontal cuts of the GISAXS patterns and (C) the corresponding integrated intensities of the GISAXS curves.

Chapter 6

6. Development of an Easy high-throughput Screening Assay for Microbial Terpenoid Production

The following chapter describes the development of a novel detection strategy for terpenoids in cooperation with the Institute of Molecular Biotechnology (group H. Pichler; terpenoid screening by Sandra Moser). The results of this research have been reported in the form of a patent application. Therefore, details are not mentioned here.

6.1 Introduction

Terpenoids are a diverse group of molecules and can be naturally found in insects, bacteria and fungi[1,2,3,4]. Furthermore, due to their wide distribution, terpenoids are interesting for various applications like flavor, fragrances, pharmaceuticals, pesticides, repellents and biofuels[5,6]. Unfortunately, common isolation techniques do not yield to reproducible qualities and quantities of the obtained terpenoids[7,8]. Therefore, metabolic engineering and synthetic biology approaches have been developed in the recent years, but due to the complexity of such systems there are still a lot of unanswered questions for the terpenoid production in microbial organisms. However, terpenoids are colorless (with the exception of carotenoids) and frequently have a hydrophobic, volatile character what makes it virtually impossible to detect them by direct, visual detection methods. Beside the GC(-MS)-based methods for product quantification, prenyl pyrophosphate precursor consumption[9,10] as well the protective properties of terpenoids against detergents[11] or

the measurement of terpene synthase activity by detecting by-products that give a colorimetric read-out[12,13] can be used for detection. Unfortunately, all these assays do not give a direct read-out of terpene synthase activity. These assays are based on colored by-products requiring the preparation of cell lysates, which scales down sample throughput. Literature holds only two approaches (not based on carotenoids) which allow direct detection of terpenes. The first is based on the addition of fluorescent dyes (Nile red or BODIPY) to detect various water-immiscible compounds, including terpenoids.[14] The second system uses the dye 2,2-diphenyl-1-picrylhydrazyl (DPPH) for the detection of an electron transfer to the C-C double bond of the monoterpenoid[15]. Both of these concepts are promising but also limited in different ways.

The following chapter describes the development of the test plates for the direct detection method of terpenoids. Therefore, Nile red was added to solutions of trimethylsilyl-cellulose, which were used as starting material for the preparation of thin detection films. The polysaccharide serves as matrix material. Nile red binds to the terpenoids which results in signals detectable by both eye and UV light. An advantage of this approach is that the detection of terpenoids works without any cellular background signals.

6.2 Materials and Methods

Materials. Trimethylsilyl-cellulose (TMSC; DS: 2.7-2.9) obtained from Avicel pulp, purchased from TITK Rudolstadt MFSA, and Nile-red (Sigma Aldrich) were used as starting materials for film preparation. Chloroform (99 wt%), methylene chloride (99 wt%), acetone (99 wt%) and sulfuric acid (95 wt%) were purchased from VWR chemicals, hydrogen peroxide (30

wt%) and hydrochloric acid (37 wt%) from Sigma-Aldrich. All chemicals were used without purification. For the filtration, Chromafil® Xtra PVDF-45/25 0.45 μm syringe filters were used.

Stylus profilometry/Determination of Film Thickness. To measure the film thickness a DEKTAK 150 Stylus Profiler from Veeco was used. The scan length was set to 1000 μm over the time duration of 3 s. The diamond stylus had a radius of 12.5 μm and the force was 3 mg with a resolution of 0.333 μm/sample and a measurement range of 6.5 μm. The profile was set to *Valleys* and *Hills*. For the determination, the sample was scratched five times up to the substrate surface. This measured profile was then used to calculate the thickness of the film.

Film Preparation. The glass substrate was first rinsed in a pre-cleaning step with methylene chloride, acetone and dist. water. Afterwards, the substrate was placed into "piranha" acid ($H_2SO_4:H_2O_2$ = 7:3 (v/v)) for 30 min to remove organic residues from the surface and then neutralized with dist. water. For film preparation, trimethylsilyl-cellulose (TMSC) and Nile red were dissolved in chloroform, filtered and afterwards spin-coated onto the glass substrate at 4000 rpm for 60 s (acceleration 2500 rpm/s).

6.3 Results and Discussion

Besides Nile red, the matrix material is essential for the performance of the detection plates. Therefore, trimethylsilyl-cellulose (TMSC) was chosen due to the hydrophobicity of the material. Furthermore, the polarity can be switched to a more hydrophilic character by an easy regeneration step to cellulose. For this procedure, TMSC was dissolved in chloroform, afterwards filtered to remove residues and then spin-coated onto the substrate. The obtained

TMSC films were then regenerated to cellulose by HCl vapor. Both, the TMSC and regenerated cellulose materials were then used for the terpenoid detection tests. The Nile red was dissolved and the two different materials were treated (spotted or soaked) with those solutions and analyzed both by eye and under UV light (Figure 6.1 A). The incubation test revealed that compared with the cellulose layer, TMSC gave a better signal (10 ng/µl) for the terpenoid containing line (compared to the controls). A problem during the screening was to homogenously deposit the Nile red on the plate. Therefore, the next step was to incorporate the dye directly into the material. Therefore, TMSC and Nile red were dissolved in a common solvent and spin coated in one step. All prepared films appeared rather smooth by the naked eye, which indicated that TMSC and Nil red were compatible in both, solution and solid state (Figure 6.1 B).
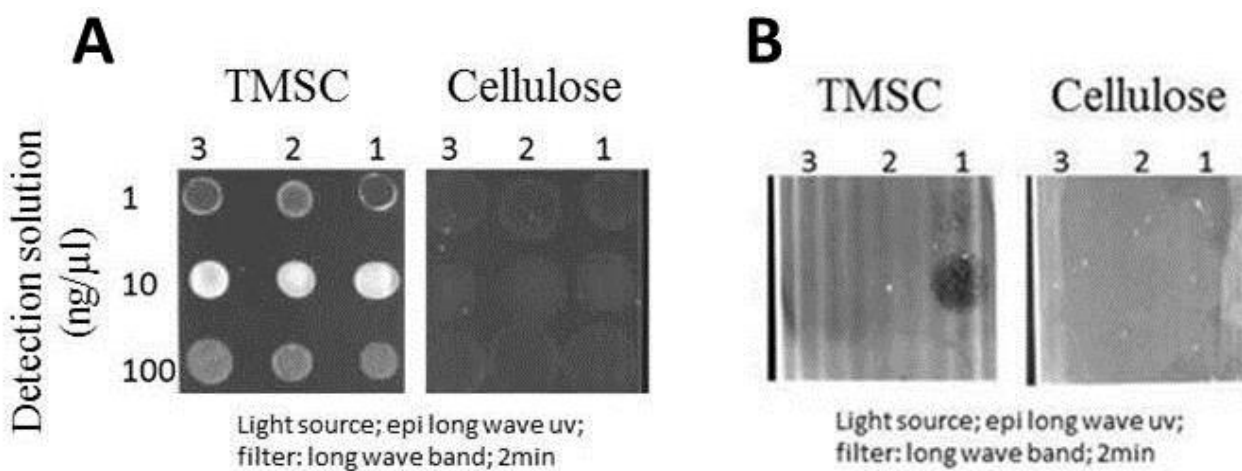
Figure 6.1. A) TMSC and cellulose used for incubation test (overnight) at different Nile red concentrated solutions (spotted or soaked); 1) medium + terpenoid; 2) control medium; 3) empty control. B) TMSC and cellulose containing Nile red used for incubation test (overnight); 1) medium + terpenoid; 2) control medium; 3) empty control. Images acquired by Sandra Moser.

The results for the TMSC/Nil red layer were significantly better due to the more homogenous distribution of the Nile red inside the films. In contrast, for regenerated cellulose films the signals were not as clear as before. A possible explanation might be that the HCl treatment damaged or inhibited the dye. After confirming the TMSC/Nil red films to be a suitable material for the screening, the next measure was the testing of different Nil red concentrations (0.05 wt%, 0.1 wt% and 0.25 wt%) in the film.

Light source; epi long wave uv; filter: long wave band; 2min
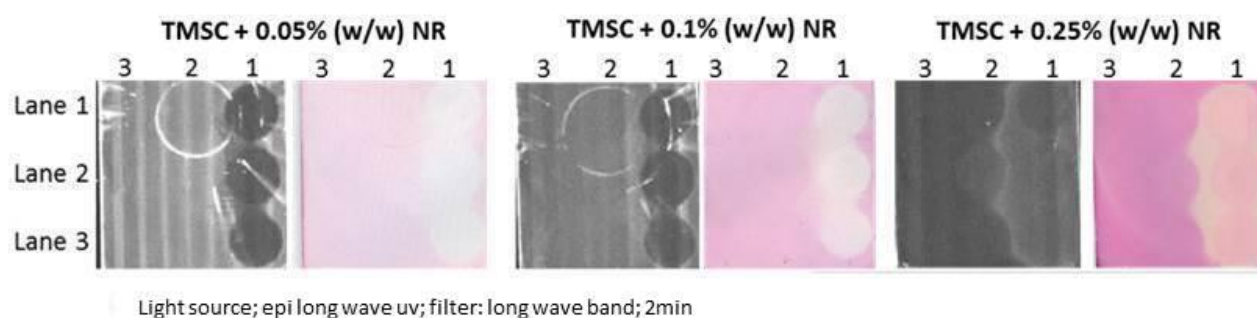
Figure 6.2. TMSC containing Nil Red (0.05 wt%, 0.1 wt% and 0.25 wt%) used for incubation test (overnight); 1) medium + terpenoid; 2) control medium; 3) empty control. Images acquired by Sandra Moser.

Figure 6.2 shows the results of the final incubation test which revealed the strongest signals at a Nile red concentration of 0.05 wt% and 0.1 wt%. Apparently, the 0.25 wt% concentration strongly influenced the polarity of the material and the test solvents started to smear. A minor disadvantage of the system was that the outer area of the test plates could not be used for the screening as they did not give reproducible signals. This behavior originated from the rectangular geometry of the plates since after the spin coating step the layer thickness of the TMSC/Nile red films could differ between the center and the edges of the substrate. The films thicknesses at different Nile red concentrations were analyzed by stylus profilometry. In fact, analysis of a

TMSC film containing 0.1 wt% Nile red demonstrated that the thickness in the center of the film (221±4 nm) was about 10% higher compared to the edges (198±5 nm). The same trends applied also for 0.05 wt% (middle: 170±3 nm; edges: 155±3 nm) and 0.25 wt% (middle: 319±6 nm; edges: 286±5 nm) conditions. Finally, these results show a new opportunity for the detection of terpenoids but further optimization steps need to be performed in order to realize a commercially applicable system.

6.4 References

(1) Chappell, J. *Plant Physiol.* **1995**, *107*, 1–6.

(2) Quin, M. B.; Flynn, C. M.; Schmidt-Dannert, C. *Nat. Prod. Rep.* **2014**, *31*, 1449–1473.

(3) Yamada, Y.; Kuzuyama, T.; Komatsu, M.; Shin-Ya, K.; Omura, S.; Cane, D. E.; Ikeda, H. *Proc. Natl. Acad. Sci. U. S. A.* **2015**, *112*, 857–862.

(4) Sobotník, J.; Jirosová, A.; Hanus, R. *J. Insect Physiol.* **2010**, *56*, 1012–1021.

(5) Bohlmann, J.; Keeling, C. I. Terpenoid biomaterials. *Plant Journal*, 2008, *54*, 656–669.

(6) George, K. W.; Alonso-Gutierrez, J.; Keasling, J. D.; Lee, T. S. *Isoprenoid drugs, biofuels, and chemicals-artemisinin, farnesene, and beyond*; Schrader, J., Bohlmann, J., Eds.; Advances in Biochemical Engineering/Biotechnology; Springer International Publishing: Cham, 2015; Vol. 148.

(7) Ishida, B. K.; Chapman, M. H. *J. Agric. Food Chem.* **2009**, *57*, 1051–1059.

(8) Lapkin, A. A.; Plucinski, P. K.; Cutler, M. Comparative assessment of technologies for extraction of artemisinin. *Journal of Natural Products*, 2006, *69*, 1653–1664.

(9) Furubayashi, M.; Ikezumi, M.; Kajiwara, J.; Iwasaki, M.; Fujii, A.; Li, N.; Saito, K.; Umeno, D. *PLoS One* **2014**, *9*, e93317.

(10) Withers, S. T.; Gottlieb, S. S.; Lieu, B.; Newman, J. D.; Keasling, J. D. *Appl. Environ. Microbiol.* **2007**, *73*, 6277–6283.

(11)   Kirby, J.; Nishimoto, M.; Chow, R. W. N.; Pasumarthi, V. N.; Chan, R.; Chan, L. J. G.; Petzold, C. J.; Keasling, J. D. *Appl. Environ. Microbiol.* **2014**, *80*, 6685–6693.

(12)   Lauchli, R.; Rabe, K. S.; Kalbarczyk, K. Z.; Tata, A.; Heel, T.; Kitto, R. Z.; Arnold, F. H. *Angew. Chem. Int. Ed. Engl.* **2013**, *52*, 5571–5574.

(13)   Vardakou, M.; Salmon, M.; Faraldos, J. A.; O'Maille, P. E. *MethodsX* **2014**, *1*, 187–196.

(14)   Frenz, L.; Ubersax, J. Methods and compositions for detecting microbial production of water-immiscible compounds (WO 2012158466 A1), 2012.

(15)   Behrendorff, J. B.; Vickers, C. E.; Chrysanthopoulos, P.; Nielsen, L. K. *Microb. Cell Fact.* **2013**, *12*, 76.

Chapter 7

7. Conclusion

This thesis covers a broad field of cellulose research beginning with fundamental research of the macromolecular structure over the wetting and drying behavior of treated cellulose thin films and ends up in the usage as matrix material for terpenoid detection dyes and in-situ synthesis of inorganic nanoparticles.

Chapter 2 describes the unsuccessful attempt of a complete deuteration of cellulose layers with different film thicknesses for the characterization with ATR-IR. For this experiment TMSC was spin coated on a substrate regenerated with DCl to obtain deuterated cellulose films. Unfortunately, the thin samples (~20 nm) had a rather high accessibility and the rehydration takes place too fast to perform analytical investigations. Moreover, also the utilization of a nitrogen purged glovebox for the film preparation and the ATR-IR measurements did not lead to better results. With the available equipment it was only possible to deuterated cellulose powder. Probably, highly protective inert as environments may yield better results.

The results of chapter 3 showed that the stiffness of the cellulose film, determined by AFM nanoindentation experiments, is different between $Cell_A$ and $Cell_S$. For both sources the stiffness increased after the treatments. Furthermore, the AFM images revealed that the films have distinct differences in the structure. Interestingly, the evaluated XRR data showed an additional third layer at the cellulose/air interface. These differences certainly stem from the different preparation procedures since the used solvents (THF, $CHCl_3$) have different vapor pressures. The obtained results for the film thickness of the XRR as well for the QCM-D measurement show a decreased water vapor uptake for the dried samples at elevated temperatures. This correlates to results of the literature with liquid water. This behavior becomes particularly pronounced at elevated humidity levels, where the amount of water molecules/AGU can be significantly reduced from 3.6 to 2.6 / 2.1 for the differently prepared samples.

Chapter 4 and chapter 5 describes the *in-situ* synthesis of Bi_2S_3 and $CuInS_2$ nanoparticles in a trimethylsilyl-cellulose matrix. The obtained layers were rather smooth what is important for the usage in multilayer devices. The synthesis of the nanoparticles was monitored with GISWAS (in real-time) and ATR-IR. Furthermore, the ATR-IR spectrum revealed that the matrix was not damaged during the heat treatment procedure (195°C) for both systems. Furthermore, the TMSC/Bi_2S_3 layer was regenerated with HCl vapor to obtain a cellulose/Bi_2S_3 film with a different SFE; the roughness did not changed. In case of the Bi_2S_3 the TEM image showed that the nanoparticles were homogenous distributed in the matrix with a diameter of 25±4 nm and a length of 80±7 nm. In comparison, the $CuInS_2$ nanoparticles were smaller and connected throw the whole material. Therefore, we were able to prepare a working solar cell (TMSC/$CuInS_2$) with a PCE of 0.99%.

Chapter 6 shows that TMSC is an ideal matrix material in combination with Nile red to prepare terpenoid detection plates. The plates reveal better results if the Nile red is directly embedded in the matrix and not added with medium. The ideal amount of Nile red was determined with 0.1 wt%. A disadvantage is that the plates, due to the spin coating procedure, are inhomogeneous and get thinner at the outer regions of the plates. Unfortunately, this leads to inaccurate results in these regions and can further not used for the detection. Finally, these results show a new opportunity for the detection of terpenes but further optimization steps need to be performed in order to realize a commercially applicable system.

Chapter 8

8. Curriculum Vitae

Personal Data

Dipl.-Ing. David Reishofer, BSc
Laimburggasse 27
A – 8010 Graz
+43650/3315886
david.reishofer@tugraz.at
Date of birth: 26.02.1988 (Graz)

Dissertation

TU Graz (ICTM), under the supervision of Ass.Prof. Dipl.-Ing. Dr.techn. Stefan Spirk and Em.Univ.Prof. Dipl.Ing. Dr.techn. Franz Stelzer

02/2014 - 01/2017

Cellulosic Nanomaterials - From Fundamentals to Applications

Diploma Thesis

03/2013 - 12/2013

TU Graz (ICTM), under the supervision of Assoc.Prof. Dipl.-Ing. Dr.techn. Christian Slugovc

Post-functionalization of macroporous pDCPD with tetrazines - the impact on mechanical properties

Education

Doctoral school of Technichal Chemistry, TU Graz (NAWI Graz)

02/2014 - 01/2017

Master programme Technichal Chemistry, TU Graz (NAWI Graz)	10/2011 - 12/2013
Bachelor programme Chemistry, TU Graz (NAWI Graz)	10/2008 - 10/2011
Public secondary academic/technical school (Graz), *Matura*	09/2001 - 06/2007
Private secondary academic school (Graz)	09/1998 - 07/2012
Public elementary school in (Graz)	09/1994 - 07/1998

Work experience

Graz University of Technology, Austria *Project employee at the Institute for Chemistry and Technology of Materials*	02/2014 - 01/2017
University of Maribor, Slovenia *Research assistant at the Institute of Engineering Materials and Design at the Faculty of Mechanical Engineering*	06/2013 - 11/2013
Graz University of Technology *Student assistant at the Institute for Chemistry and Technology of Materials*	07/2013 - 01/2017
Graz University of Technology *Student assistant at the Institute for Organic Chemistry*	03/2013 - 06/2013 10/2012 - 01/2013
Member of the senate at TU Graz (as student)	10/2012 - 09/2015 03/2016 - 01/2017
University Representation of the Students Council at TU Graz *Member and Vice-chairman*	07/2011 - 06/2013

Internships

Short Travel Scientific Mission at VTT Technical Research Centre of Finland Ltd, Aalto, Finland *The Impact of Increased Humidity to Water and Heat Treated Cellulose Thin Films*	05/2016
Research stay at University of Helsinki, Finland	02/2016
Summer school at the Graz University of Technology, Austria	07/2015
Short Travel Scientific Mission at University of Maribor *Trimethylsilyl-cellulose/nanoparticles Hybrid Materials*	11/2014
EuSIP Summer school at Graz University of Technology and Synchrotrone de Trieste, Italy	09/2014

X-ray diffraction (Small and Wide angle X-ray diffraction, Grazing incidence diffraction)

Summer school at the Syracuse University, USA   07 - 08/2012

Scholarships

Short Travel Scientific Mission Grant (European Union) for a research stay at VTT Technical Research Centre of Finland Ltd, Aalto, Finland	05/2016
Short Travel Scientific Mission Grant (European Union) for a research stay at University of Maribor, Slovenia	11/2014
Scholarship pursuant to § 63 *Studienförderungsgesetz* (TU Graz) for the participation at the ACS Meeting 2017 in San Francisco, 2016 in San Diego, 2015 in Denver, USA and APME 2014 in Durham, England	04/2017 03/2016 03/2015 08/2013
Merit-based scholarship of the Faculty of Technical Chemistry, Chemical and Process Engineering and Biotechnology	07/2012

Publications (Paper)

Reishofer, D, Sattelkow, J, Fischer, JW, Amenitsch, H, Niegelhell, K, Plank, H, Resel, R, Tammelin, T, Kontturi, E, & Spirk, S, Submitted to *Biomacromolecules*, **2016**	2016
Reishofer, D, Ehmann, HM, Amenitsch, H, Gspan, C, Fischer, R, Plank, H, Trimmel, G, & Spirk, S, Submitted to *Carbohydrate Polymers*, **2016**	2016
Reishofer, D, Rath, T, Ehmann, HM, Amenitsch, H, Gspan, Dunst, S, Plank, H, Bruno, A, Bellamie, E, Trimmel, G, & Spirk, S, Submitted to *ACS Sustainable Chemistry & Engineering*, **2016**	2016
Ganner, T, Sattelkow, J, Rumpf, B, Eibinger, M, Reishofer, D, Winkler, R, Nidetzky, B, Spirk, S & Plank, H **2016**, 'Direct-Write Fabrication of Cellulose Nano-Structures via Focused Electron Beam Induced Nanosynthesis' *Scientific reports*, S. 1-11.	2016
Elschner, T, Reishofer, D, Kargl, R, Heinze, T & Stana-Kleinschek, K **2016**, 'Reactive cellulose-based thin films - a concept for multifunctional polysaccharide surfaces' *RSC Advances*.	2016

Mohan, T, Rathner, R, Reishofer, D, Koller, M, Elschner, T, Spirk, S, Heinze, T, Stana-Kleinschek, K & Kargl, R **2015**, 'Designing Hydrophobically Modified Polysaccharide Derivatives for highly efficient enzyme immobilization' *Biomacromolecules*, Bd 16, S. 2403-2411.	2015
Reishofer, D & Spirk, S **2015**, 'Deuterium and Cellulose: A Comprehensive Review' *Advances in polymer science*, Bd 271, S. 93–114.	2015
Knall, A-C, Kovacic, S, Hollauf, M, Reishofer, D, Saf, R & Slugovc, C **2013**, 'Inverse electron demand Diels-Alder (iEDDA) functionalisation of macroporous poly(dicyclopentadiene) foams' *Chemical communications*, Bd 49, S. 7325-7327.	2013
Hamner, KL, Alexander, CM, Coopersmith, K, Reishofer, D, Provenza, C & Maye, MM 2013, 'Using Temperature-Sensitive Smart Polymers to Regulate DNA-Mediated Nanoassembly and Encoded Nanocarrier Drug Release' ACS nano, Bd 7, S. 7011-7020.	2013

Publications (Oral Presentation)

Reishofer, D. / Water and Heat Treated Cellulose Thin Films - The Impact of Increased Humidity. 2nd International EPNOE Junior Scientists Meeting, Sophia-Antipolis, France.	2016
Reishofer, D; Ehmann, H; Dunst, S; Rath, T; Trimmel, G; Spirk, S. / In-situ synthesis of copper-indium-sulfide nanoparticles in a cellulose matrix for a semiconductors hybrid material. 6th EuCheMS Chemistry Congress, Sevilla, Spain.	2016
Reishofer, D; Ehmann, H; Werzer, O; Resel, R; Kontturi, E; Tammelin, T; Spirk, S. / The Impact of Increased Humidity to Water and Heat Treated Cellulose Thin Films. 53rd Nordic Polymer Days 2016, Helsinki, Finland.	2016
Reishofer, D; Spirk, S. / Insights into regeneration, drying and hornificiation of amorphous cellulose films. Paper & Biorefineries 2016, Graz, Austria.	2016
Reishofer, D; Ehmann, H; Dunst, S; Trimmel, G; Spirk, S. / In-situ synthesis of semiconductors metal sulfide nanoparticles in a polysaccharide matrix. ACS Spring Meeting 2016 San Diego, USA.	2016
Reishofer, D; Ehmann, H; Dunst, S; Trimmel, G; Spirk, S. / In-Situ Synthesis of Bi$_2$S$_3$-Nanoparticles in a Polysaccharide Matrix. 4th EPNOE International Polysaccharide Conference, Warschau, Polen.	2015
Reishofer, D; Ehmann, H; Trimmel, G; Spirk, S. / Synthesis of Bi$_2$S$_3$-Nanoparticles in a Thin Film Cellulose Matrix. 16. Austrian Chemistry Days 2015, Innsbruck, Austria.	2015
Reishofer, D; Ehmann, H; Kargl, R; Schennach, R; Hribernik, S; Kornherr, A;	2015

Stana-Kleinschek, K; Spirk, S. / Deuterated cellulose thin films - challenges and surprises. 249th ACS National Meeting & Exposition, Denver, USA.

Reishofer, D; Mohan, T; Kargl, R; Niegelhell, K; Hribernik, S; Ehmann, H; Stana-Kleinschek, K; Spirk, S. / Amorphous Nanometric Cellulose Ultra-Thin Films - The Structural Rearrangements Induced by Heat Treatment and Water Interaction. 22nd International Conference on Materials and Technology, Portoroz, Slovenia.	2014

Publications (Poster Presentation)

Reishofer, D., Werzer, O., Ehmann, H., Resel, R., Tammelin, T., Kontturi, E., & Spirk, S. The Impact of Increased Humidity after Water and Heat Treatment of Cellulose Thin Films. 6th EuCheMS Chemistry Congress, Sevilla, Spain.	2016
Reishofer, D., Mohan, T., Kargl, R., Niegelhell, K., Hribernik, S., Ehmann, H., Stana-Kleinschek, K. (2014). Silylcellulose Derivatives as Precursors for Cellulose Model Systems describing Paper Making Processes. EUSIP 2014, Maribor, Slovenia.	2014
Reishofer, D. P., Knall, A-C., Kovacic, S., & Slugovc, C. (2013). Investon on mechanical properties of macroporous pDCPD post-functionalized with tetrazines. 15. Austrian Chemistry Days 2013, Graz, Austria.	2013
Reishofer, D., Hojnik, C., Thonhofer, M., Schalli, M., Stütz, A., & Wrodnigg, T. (2013). Synthesis of multifunktional linker molecules for the Amadori rearrangement. 15. Austrian Chemistry Days 2013, Graz, Austria.	2013
Reishofer, D., Knall, A-C., Kovacic, S., & Slugovc, C. (2013). Post-functionalization of macroporous pDCPD with tetrazines - the impact on mechanical properties. Postersitzung präsentiert bei 10th IUPAC International Conference on Advanced Polymers via Macromolecular Engineering (APME), Durham, Great Britain.	2013

Appendix

Designing Hydrophobically Modified Polysaccharide Derivatives for Highly Efficient Enzyme Immobilization

Tamilselvan Mohan,*[†] Raffael Rathner,[†] David Reishofer,[‡] Martin Koller,[†,§] Thomas Elschner,[$] Stefan Spirk,[‡] Thomas Heinze,[$] Karin Stana-Kleinschek,[β] and Rupert Kargl[β]

[†]Institute for Chemistry, University of Graz, Heinrichstrasse 28, 8010 Graz, Austria

[‡]Institute for Chemistry and Technology of Materials, Graz University of Technology, Stremayrgasse 9, 8010 Graz, Austria

[$]Center of Excellence for Polysaccharide Research, Friedrich Schiller University Jena, Humboldtstraße 10, 07743 Jena, Germany

[β]Institute for Engineering Materials and Design, University of Maribor, Smetanova 17, 2000 Maribor, Slovenia

[§]ARENA − Association for Resource-Efficient and Sustainable Technologies, Inffeldgasse 21b, 8010 Graz, Austria

Ⓢ *Supporting Information*

ABSTRACT: In this contribution, a hydrophobically modified polysaccharide derivative is synthesized in an eco-friendly solvent water by conjugation of benzylamine with the backbone of the biopolymer. Owing to the presence of aromatic moieties, the resulting water-soluble polysaccharide derivative self-assembles spontaneously and selectively from solution on the surface of nanometric thin films and sheets of polystyrene (PS). The synthetic polymer modified in this way bears a biocompatible nanolayer suitable for the immobilization of horseradish peroxidase (HRP), a heme-containing metalloenzyme often employed in biocatalysis and biosensors. Besides the detailed characterization of the polysaccharide derivative, a quartz crystal microbalance with dissipation (QCM-D) and atomic force microscopy (AFM) are used to investigate the binding efficiency and interaction of HRP with the tailored polysaccharide interfaces. Subsequent enzyme activity tests reveal details of the interaction of HRP with the solid support. The novel polysaccharide derivative and its use as a material for the selective modification of PS lead to a beneficial, hydrophilic environment for HRP, resulting in high enzymatic activities and a stable immobilization of the enzyme for biocatalytic and analytic purposes.
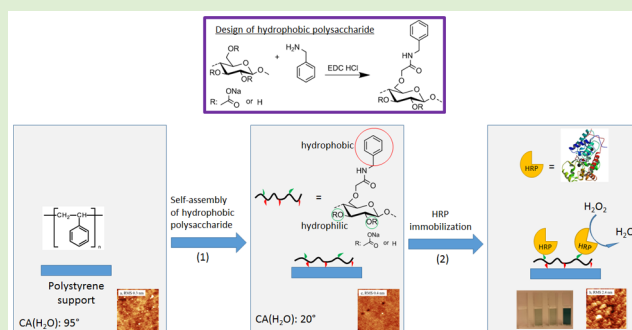
1. INTRODUCTION

Besides the increasing use of living microorganisms as "whole cell biocatalysts" in different fields of biotechnology, we nowadays witness a growing demand for isolated enzymes as powerful biocatalysts for various chemical reactions of industrial significance.[1] Enzymes can be produced at high quantities by biotechnological processes, using both wild-type and genetically tailored organisms. They display the benefit of high catalytic activity and high selectivity for defined reactions, homologues of compounds and even for single substances. Reactions resulting in pure enantiomers, can often exclusively be accomplished by the biocatalytic action of enzymes, either embedded in their producing organisms, or isolated in a pure form.[2] Mild reaction conditions close to the biological optima of enzymes are the main characteristic of these catalytic processes. However, free enzymes are highly prone to activity losses by being exposed to conditions different to those of their optimal natural environments, such as high temperature, salinity, heavy metals and various inhibiting substances. In addition, they are easily susceptible toward deterioration by proteolytic attack. To overcome these disadvantages, soluble enzymes can be immobilized on solid supports, to enable their long time operation in industrial processes. Properties that can be improved by immobilizing enzymes encompass the activity, stability, and resilience against inhibition of heavy metals and other chemicals.[3−5] Various techniques were reported in the past for immobilization of enzymes on diverse surfaces, aiming at the development of so-called "immobilized bed reactors", where the immobilized biocatalyst accomplishes its designated reaction, both in batch or continuous setup.[6−8] An enzyme that received a strong interest for industrial applications and research purposes is horseradish peroxidase (HRP, EC 1.11.1.7), a representative of the oxidase family. This enzyme is well-known for its high potential for oxidative conversion of various eco-pollutants like endocrine disruption compounds and diverse aromatics.[9−11] Hence, HRP displays high potential in the field of bioremediation of polluted water bodies, e.g., by immobilization on devices of wastewater treatment plants, most preferably on fibers in continuously operated filtration modules. In addition, there exists an increasing number of further

potential applications of this enzyme, such as in biosensors,[12,13] for anticancer therapy,[14] neuron labeling,[15] and for coupled enzyme assays, chemo-luminescent assays or immunoassays.[11]

For HRP, several inorganic supports for immobilization were tested, such as gold colloids,[16] nanosized zinc oxide,[17] mesoporous silicas,[18] and ceramic-carbon nanotube composites.[6] Immobilization of HRP on polymeric surfaces is reported on chitosan,[19] poly(acrylonitrile),[20] and sepharose.[21] As a major drawback, it turned out that the sensitivity of HRP immobilized via microencapsulation, e.g., in sol−gel and other polymeric materials (e.g., polyacrylamides), is generally rather poor. Furthermore, the majority of other immobilization methods are cumbersome in terms of complexity, stability, and sensitivity. In the case of nanosized metals, metal-oxides, and carbon nanotubes, the obtained matrix does not display outstanding biocompatibility for the enzyme, thus negatively impacting its catalytic properties as well as its lifetime and stability. As successfully demonstrated by Zhou et al.,[19] covalent linking of HRP to biocompatible polymeric matrices, such as chitosan, is a viable strategy due to the possibility to benefit from their chemical functionalities. In this way, promising enzyme stability and remaining activity can be achieved.[19] The combination of the biocompatible environment of hydrophilic polysaccharides with the availability and chemical stability of synthetic polymer supports (e.g., polystyrene) would allow the full exploitation of the potential of HRP in biocatalytic processes by simple surface immobilization. This work therefore aims at the surface modification of polystyrene (PS) by the adsorption of a partial hydrophobic benzyl-modified derivative of carboxymethyl cellulose and the subsequent covalent or adsorptive immobilization of HRP on these layers. The enzymatic activity is compared with the amounts and structure of immobilized HRP as revealed by quartz crystal microbalance (QCM-D) and atomic force microscopy (AFM) studies.

2. EXPERIMENTAL SECTION

2.1. Materials and Methods. Sodium salt of carboxymethyl cellulose (CMC: DS_{COONa}: 0.7 and M_w: 90.000 g mol^{-1}), 1-ethyl-3-(3-(dimethylamino)propyl)carbodiimide hydrochloride (EDC·HCl), toluene (98%), polystyrene (PS) granulates (M_w: 280.000 g mol^{-1}), horseradish peroxidase (HRP) of herbal origin (145.7 ABTS-units mg^{-1}) and 2,2′-azino-bis(3-ethylbenzothiazoline-6-sulfonic acid) (ABTS) were purchased from Sigma-Aldrich, Austria. Benzylamine (B, 99%) was purchased from Roth, Austria. A PS film with a thickness of 75 μm was purchased from Ergo.fol Norflex, Germany. Twelve Well Advanced TC plates (sterile products) were purchased from Greiner Bio-One, Austria. Sodium acetate p.a. (NaOAc) was purchased from Carl Roth GmbH, Germany. Gold-coated QCM-D sensors (QSX301) were obtained from LOT-Oriel, Darmstadt, Germany. Milli-Q water (18.2 MΩ cm at 25 °C) from a Millipore water purification system (Billerica, USA) was used for all sample preparations and QCM-D measurements.

2.2. Substrate Cleaning and PS Thin Film Preparation. For QCM-D measurements, sensor crystals coated with a gold layer were used as a substrate for spin coating of PS. The crystals were soaked into a mixture of H_2O/H_2O_2 (30 wt %)/NH_4OH (5:1:1; v/v/v) for 10 min at 70 °C. Afterward, they were immersed into a "piranha" solution (H_2O_2 (30 wt %)/H_2SO_4 (98 wt %) (1:3; v/v)) for 60 s, rinsed with Milli-Q water again and finally blow dried with nitrogen gas. For spin coating of PS with a spin coater (Polos MCD wafer spinner, APT corporation, Germany), 70 μL of PS (1% (w/v) solution in toluene) was deposited on the static QCM-D crystal, which was then rotated for 60 s with a spinning speed of 4000 rpm and an acceleration of 2500 rpm s^{-1}. All PS-coated films were dried in an oven at 50 °C overnight. Water contact angles of PS were determined to be 96 ± 1°. The film thickness of the PS was 68 ± 3 nm.

2.3. Conjugation of Benzylamine (B) and CMC. CMC (500 mg, 1.6 mmol COONa) was dissolved in 100 mL of Milli-Q water and stirred overnight. To this solution, 308 mg (1.6 mmol) of EDC·HCl and 860 mg (8.0 mmol) of B were added. The reaction was carried out at pH value of 5 at room temperature for 24 h. The pH value of the solution was kept constant using either 0.1 M NaOH or HCl. The mixtures of CMC, EDC·HCl, and B were stirred constantly during the reaction. The product obtained from this reaction is referred to as BCMC throughout this Article. In separate experiments, the reaction was carried out by mixing EDC·HCl and CMC (without the addition of B, this product is labeled CMCE) and by mixing CMC and B (without the addition of EDC·HCl, this product is called CMCB) in the same way as above. After the reaction, the mixtures were precipitated using an excess amount of absolute ethanol (≥99.8%, Sigma-Aldrich, Austria). The precipitated products were filtered through a sintered G4 glass crucible and washed several times with absolute ethanol. The products were collected and dialyzed against Milli-Q water using dialysis membranes with 14 000 g mol^{-1} MW cutoff (Roth, Germany). The permeate was exchanged every 4 h, and the dialysis was performed for 4 days. Pure CMC solution was precipitated in absolute ethanol and dialyzed in the same way as mentioned above. The dialyzed solutions were lyophilized for 4 days at 10^{-3} mbar and −25 °C.

2.4. UV−Vis Absorption Spectroscopy. Determination of the UV−vis absorption spectra was performed with a Carry 50 spectrophotometer at room temperature. The purified, isolated products of CMC, BCMC and CMCB were dissolved at a concentration of 0.2 mg mL^{-1}. All samples were prepared in Milli-Q water at neutral pH-value. The amount of B in solutions of purified BCMC conjugates was calculated from a linear calibration curve of different B concentrations. B solutions (0.01, 0.005, 0.0025, and 0.00125 mg mL^{-1}) were prepared in water at neutral pH and measured without further purification. The degree of substitution of B for BCMC conjugates was calculated from the amount of B that was found in the BCMC conjugation products.

2.5. FTIR Spectroscopy. Infrared transmission spectra of purified, isolated conjugates were recorded for the pure CMC, CMCE and BCMC products using a PerkinElmer Spectrum GX Series-73565 FTIR-spectrometer at a scan range from 4000 to 650 cm^{-1}. 32 scans were performed for all samples with a resolution of 4 cm^{-1}. All samples were measured as a KBr pellet.

2.6. ^{13}C NMR Spectroscopy. ^{13}C NMR spectra were acquired on a Bruker Avance 400 MHz instrument (Bruker Biospin, Rheinstetten, Germany) applying up to 100 mg sample per mL solvent (D$_2$O). The measurements were carried out at 70 °C with up to 20 000 scans.

2.7. Potentiometric Charge Titration. The potentiometric charge titration of the sample solutions was carried out with a two-buret instrument from Mettler Toledo T70 under inert atmosphere (nitrogen gas bubbling). The isolated purified samples of CMC, CMCE, BCMC, and CMCB (1.5 mg mL^{-1}) were titrated in a forward and back manner between the initial pH-value 2 to the preset pH-value 11. All measurements were repeated three times. A detailed description of the potentiometric charge titration method can be found elsewhere.[22] The amount of carboxylic groups present in the products were expressed in the mmol g^{-1} sample.

2.8. QCM-D Measurements. A QCM-D E4 from Q-Sense AB, Gothenburg, Sweden, was used for interaction studies of the isolated and purified CMC, CMCE and BCMC with thin films of PS. The instrument determines changes in frequency (f) and dissipation (D) on an oscillating quartz crystal. Deposition of mass or changes in the rigidity of the material on the crystals surface can be detected. Negative frequency shifts (Δf) indicate a deposition of mass whereas positive dissipation shifts (ΔD) are caused by a reduced rigidity of the coating. The reduced rigidity is often a result of incorporated solvent molecules and extended swelling. A detailed description of the QCM-D method can be found elsewhere.[23]

2.9. Adsorption of CMC, CMCE, and BCMC on PS Thin Films. The PS-coated gold crystals were assembled in the QCM-D chamber. At each run, Milli-Q water was pumped through the chamber until a stable baseline frequency was obtained. All frequency and dissipation

Table 1. Methods Employed for HRP Immobilization on BCMC-Coated and Bare PS Films (1 × 1 cm^2)^a

Method I	Method II	Method III
(a) incubation with HRP	(a) incubation with HRP + EDC·HCl mixture	(a) incubation with EDC·HCl
(b) incubation with water	(b) incubation with water	(b) incubation with HRP
(c) drying with N$_2$ gas	(c) drying with N$_2$ gas	(c) incubation with water
		(d) drying with N$_2$ gas

^{a}The films are incubated with aqueous HRP (1 mg mL^{-1}), HRP + EDC·HCl mixture (each 1 mg mL^{-1}), EDC·HCl (1 mg mL^{-1}) and water for 180, 180, 20, and 20 min.

values were set to zero and the measurement was started, and a baseline in Milli-Q water was established for 5 min. Following this, either CMC, CMCE or BCMC (0.1 mg mL^{-1} water, filtered using a 5 μm PTFE filter) was introduced and adsorbed for 30 min. After this, Milli-Q water was introduced for 20 min. The temperature during all measurements was set to 21 ± 0.1 °C. Each experiment was carried out on three independent coated crystals. The flow rate was 0.1 mL min^{-1} in any case.

2.10. Immobilization of HRP on the BCMC Coated and Pure PS Surfaces on QCM-D Crystals. Three different methods were used for the immobilization of HRP on bare and BCMC coated PS. In method I, HRP (1 mg mL^{-1}, dissolved in water) was adsorbed for 180 min. Afterward, the surfaces were rinsed with water for 20 min. In method II, a mixture containing HRP (1 mg mL^{-1}, dissolved in water) and EDC·HCl (1 mg mL^{-1}, dissolved in water) was adsorbed for 180 min followed by rinsing the surfaces with water for 20 min. In method III, EDC·HCl (1 mg mL^{-1}, dissolved in water) was adsorbed for 20 min. Then, the surfaces were rinsed with water for 20 min. Subsequently, HRP (1 mg mL^{-1}, dissolved in water) was adsorbed for 180 min. Finally, the surfaces were rinsed with water for 20 min. Each measurement was repeated three times. The flow rate was 0.1 mL min^{-1} and the temperature was 21 ± 0.1 °C for all measurements.

2.11. Determination of Activity of Immobilized HRP. For determining the activity of HRP, the enzyme was immobilized on BCMC-coated and bare PS films with a size of 1 × 1 cm^2. The substrates were rinsed with ethanol and water, and blow dried with nitrogen gas. The coating of BCMC on the PS films were performed using the same sequence as on QCM-D crystals. The cleaned PS films were placed in 12 well plates. Four milliliters of BCMC solution (0.1 mg mL^{-1} dissolved in water, filtered using a 5 μm PTFE filter) was added into the well and shaken for 30 min. After that, the BCMC solution was exchanged for water and shaken for 20 min. Finally, the coated films were taken out, extensively rinsed with water, and blow dried with nitrogen gas. For the immobilization of HRP, the same protocol as on the QCM-D was used. A short description about the HRP immobilization on BCMC coated and bare PS films for each method is presented in Table 1. The detailed procedure is given in the Supporting Information.

For determining the enzyme activity of HRP immobilized on a 2 cm^2 PS substrate area, a protocol described by Morawski et al. (2000) was modified as follows.[24] A 50 mM NaOAc buffer was adjusted to a pH value of 4.5. ABTS (220 mg; 21.4 mM) was dissolved in 20 mL of a NaOAc buffer ("stock solution"). One milliliter of the stock solution and 1.7 μL H$_2$O$_2$ were added to additional 19 mL buffer solution ("ABTS solution", 1.13 mM). Subsequently, a 2 mL ABTS solution was incubated with the PS films placed in well plates for 5 min at room temperature (RT). The increase of the absorption was observed with a UV−vis spectrophotometer during a measurement of 5 min. The measured slope of absorption per time was used to calculate the activity expressed as ABTS-units by the following equation (eq 1). ABTS-unit corresponds to 1 μmol ABTS oxidized per minute.

$$\text{ABTS units} = (A \cdot f)/(\varepsilon \cdot d) \tag{1}$$

where f is the dilution factor for HRP enzyme, A is the absorption units × 10^{-3}, ε is the absorption coefficient of oxidized ABTS (34 700 M^{-1} cm^{-1}), and d is the path length of measuring cuvettes (1 cm).

2.12. AFM. The surface morphology of the coated samples on QCM-D crystals was characterized by AFM in tapping mode with an

Agilent 5500 AFM multimode scanning probe microscope (Agilent, Santa Barbara, CA). The images were acquired after drying the films in a stream of dry nitrogen. The images were scanned using silicon cantilevers (ATEC-NC-20, Nanosensors, Germany) with a resonance frequency of 210−490 kHz and a force constant of 12−110 N m^{-1}. All measurements were performed at room temperature. All images were processed using Gwyddion software package.[25]

2.13. Contact Angle (CA) Measurements. The wettability of pure and BCMC-coated PS films was measured using a Dataphysics contact angle measurement system OCA15+ (Dataphysics, Germany) with the sessile drop method and a drop volume of 3 μL. All measurements were carried out at RT both on uncoated and coated PS films. Determination of the SCA was based on the analysis of the drop shape and was performed with the software provided by the manufacturer (software version SCA 20). All the measurements were performed on at least three independent substrates with a minimum of three drops per surface and an average value was calculated.

3. RESULTS AND DISCUSSION

3.1. Amide Formation via EDC Chemistry. The reaction of benzylamine with CMC is schematically shown in Figure 1.
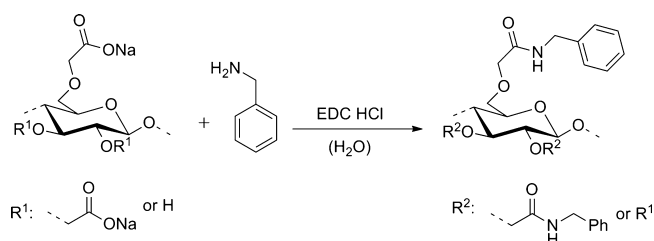
Figure 1. Schematic illustration of the conjugation of benzylamine and CMC in water using EDC·HCl chemistry at RT.

Activation of the carboxylic groups allows the formation of an amide bond leading to a hydrophobization of CMC by the attachment of the benzyl moiety. As a side reaction cross-linking with other carboxylic groups and alcohols and the formation of the N-acyl urea derivative of CMC through rearrangements can occur.[26] In any case, the number of negatively charged carboxylic groups will be reduced. This was confirmed by potentiometric charge titration of the products (CMC: 3.30 ± 0.02 mmol g^{-1}, CMCE: 1.60 ± 0.01 mmol g^{-1}, BCMC: 1.58 ± 0.02 mmol g^{-1}). These values also show that half of all carboxylic groups initially available in CMC are still present in the BCMC product. This fact is advantageous for further covalent binding of HRP on BCMC layers. In addition to covalent reactions, the electrostatic binding of EDC to CMC through the tertiary amine can occur, leading to the presence of the carbodiimide or its hydrolyzed urea derivative in the purified products of CMCE without derivatization of CMC.

3.2. FTIR. The CMC derivatives obtained by the reaction with EDC and benzylamine were analyzed by infrared spectroscopy in the transmission mode. Figure 2 shows the
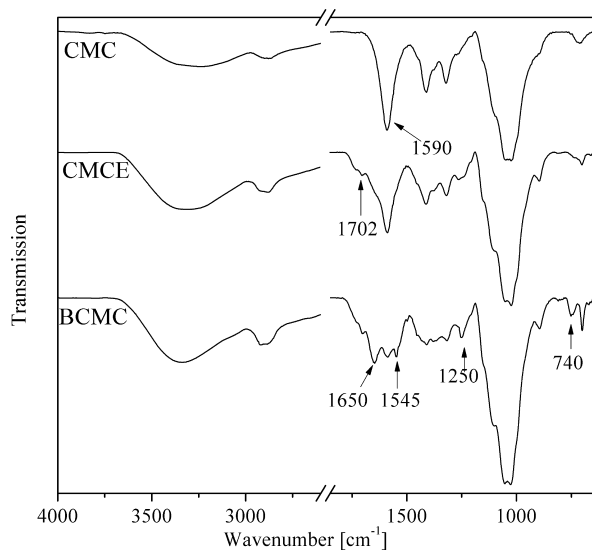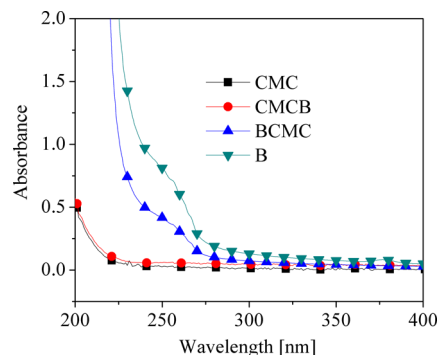
Figure 2. FTIR spectra of the purified and isolated products of CMC, CMCE, and BCMC.

infrared absorbance spectra of CMC, CMCE, and BCMC. Besides the typical OH (ν_{OH}: 3223 cm^{-1}), ring (ν_{ring}: 1021 cm^{-1}), and carboxyl group of CMC ($\nu_{C=O}$: 1590 cm^{-1}), the presence of residual EDC or its hydrolyzed urea form in CMCE is confirmed by the band 1702 cm^{-1} (either at $\nu_{N=C=N}$ or $\nu_{C=O}$) The presence of the benzyl ring in BCMC can further be confirmed by the band at 1650 cm^{-1} ($\nu_{C=C}$ aromatic) and 740 cm^{-1} (ν_{C-H} aromatic). IR peaks visible at 1545 cm^{-1} (ν_{N-H}) and 1250 cm^{-1} (ν_{C-N}) confirm the formation of an amide bond in BCMC.[27]

**3.3. ^{13}C NMR Spectroscopy.** A further confirmation of the covalent bond of B to CMC is obtained by ^{13}C NMR

spectroscopy. Figure 3, CMC shows a typical ^{13}C NMR spectrum of pure CMC.[28] Figure 3, middle spectrum, depicts the CMCE product, which confirms the presence of residual hydrolyzed urea derivative obtained from the hydrolysis of EDC. (^{13}C NMR (D$_2$O): δ = 55.7 and 56.1 (C10); 43.4 (C11); 35.5 (C12), 37.1 (C13); 24.9 (C14), 14.8 (C15) ppm). There are three possible reasons for the persistent presence of EDC signals after thorough purification. The formation of a stable N-acylurea or O-acyl-isourea or the presence of a salt complex formed between CMC and the tertiary amine of EDC.[26] Even though the ^{13}C NMR data presented here cannot prove these structures, charge titration values of the products (section 3.1) suggest the formation of urea derivatives or cross-linking of the carboxylic groups. Evidence for an amide bond formation between B and the carboxymethyl group of CMC is given by a further carbonyl ^{13}C signal at 172.7 ppm (C8b) in addition to the resonance at 177.3 ppm (C8a) arising from carboxylate (Figure 3, BCMC). In addition, the signals at 138 (C17); 130, 128 (C18−20) and 143.4 (C16) ppm demonstrate the

Figure 4. UV−vis absorbance spectra of CMC and purified mixtures of CMC and benzylamine (CMCB), BCMC, and benzylamine (B).
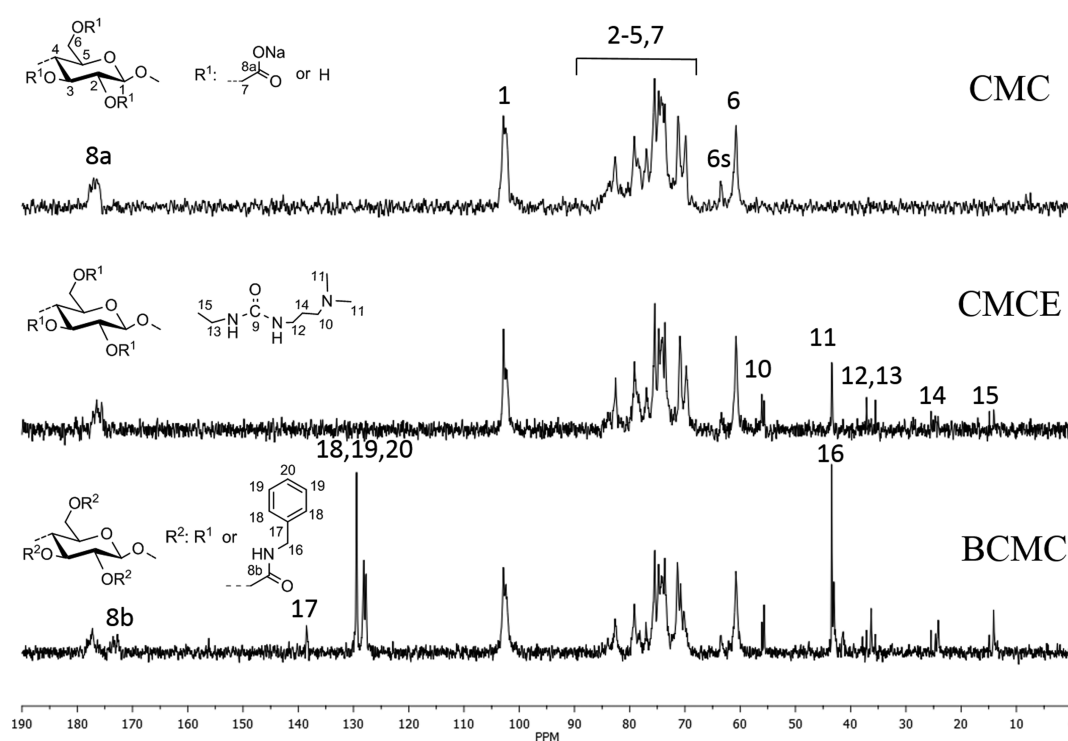
Figure 3. ^{13}C NMR spectra of the purified and isolated products of CMC, CMCE, and BCMC in D$_2$O.
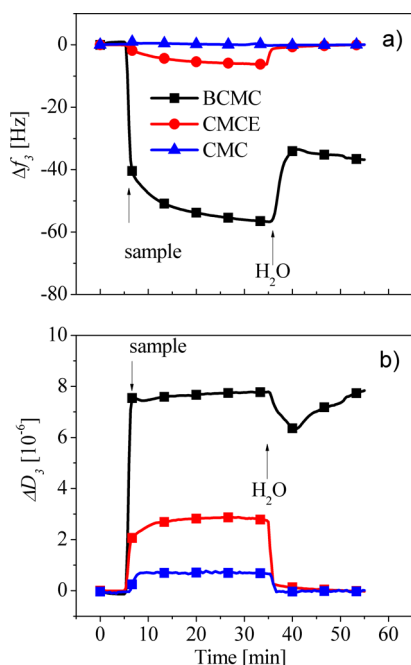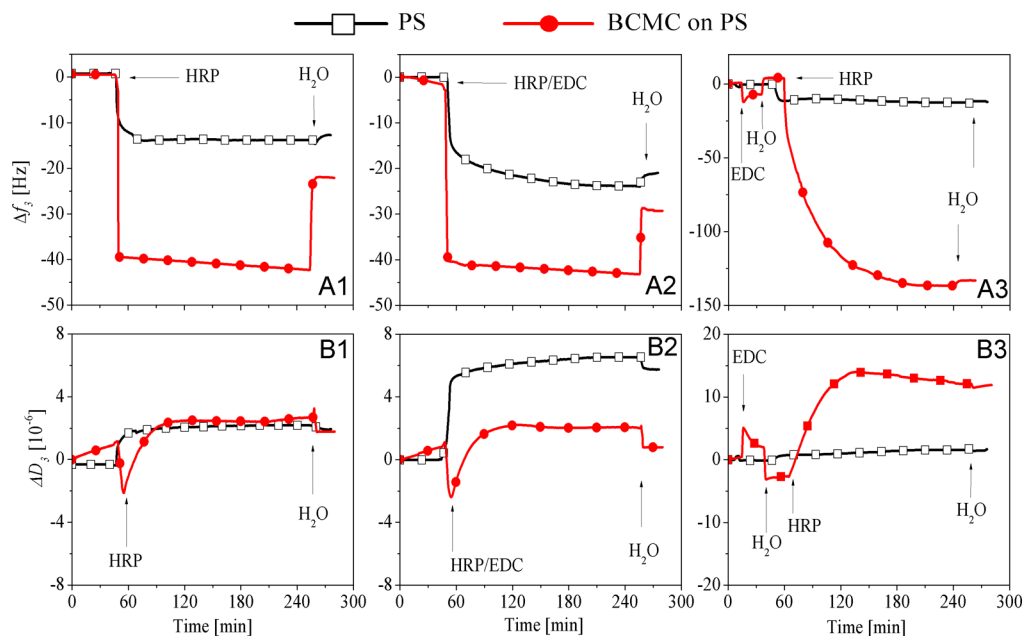
Figure 5. QCM-D frequency and dissipation values for the adsorption of CMC, CMCE, and BCMC on PS thin films.

presence of carbon atoms from the benzyl substituent. However, also in this product, signals of the EDC derivative impurities or side reactions are visible.

3.4. UV−Vis Spectroscopy. The presence of the aromatic ring in the BCMC sample is further confirmed by UV−vis spectroscopy (Figure 4). A strong absorbance of the aromatic ring similar to the pure B is observed at a wavelength of 254 nm. For CMCB no aromatic absorbance can be found confirming the removal of the amine in the absence of the coupling agent EDC. From the UV−vis spectra, a degree of substitution (DS) of 0.05 could be calculated for the aromatic ring in BCMC.

3.5. Adsorption of CMC, CMCE, and BCMC on PS. After confirming the derivatization of CMC with B, adsorption of the polymers was investigated by QCM-D measurements on polystyrene thin films. Figure 5 compares the binding of CMC, CMCE, and BCMC, all 0.1% (w/v) in water on PS. When CMC is introduced into the QCM-D chamber, no frequency change (a) but a slight positive dissipation shift (b) can be observed, indicating minor binding of CMC to PS. Dissipation changes can solely be explained by higher liquid densities and viscosities of the polymer solution. Similar results were obtained on other hydrophobic polymer surfaces in a previous publication.[29] Incubation of PS with CMCE leads to a slight decrease in frequency and a higher dissipation shift. This can be explained by the obvious cross-linking of CMC by EDC resulting in higher molar mass and density.[27] However, no irreversible binding of the product could be observed besides the fact that charges are significantly reduced due to side reactions. The adsorption of BCMC causes a tremendous frequency and dissipation shift when brought into contact with PS. The aromatic ring on the CMC backbone obviously causes stronger interaction with the hydrophobic PS surface leading to the irreversible attachment of the derivative. However, a reduction in the amount of negative charges is not the sole reason for the stronger affinity of the polymer toward PS. Additionally the substitution with the aromatic moiety increases the hydrophobicity and lowers the solubility of the product, making it more prone to adsorption on a hydrophobic surface. Moreover BCMC itself does not spontaneously bind to a hydrophilic surface such as cellulose (Supporting Information Figure S1). After rinsing with water, partial detachment of the BCMC layers is observed (positive Δf_3) and, after a short decrease in dissipation, swelling of the remaining material occurs leading to an increase in D_3. Finally, the layers are stable during extensive rinsing with water for 20 min. These layers of BCMC on PS were subsequently used for the immobilization of HRP in the following sections.

3.6. Immobilization of HRP on BCMC-Coated and Uncoated PS Surfaces. PS surfaces modified by BCMC bear

Figure 6. QCM-D changes in the frequency and dissipation for the adsorption of horseradish peroxidase (HRP) by methods I (A1, B1), II (A2, B2), and III (A3, B3).
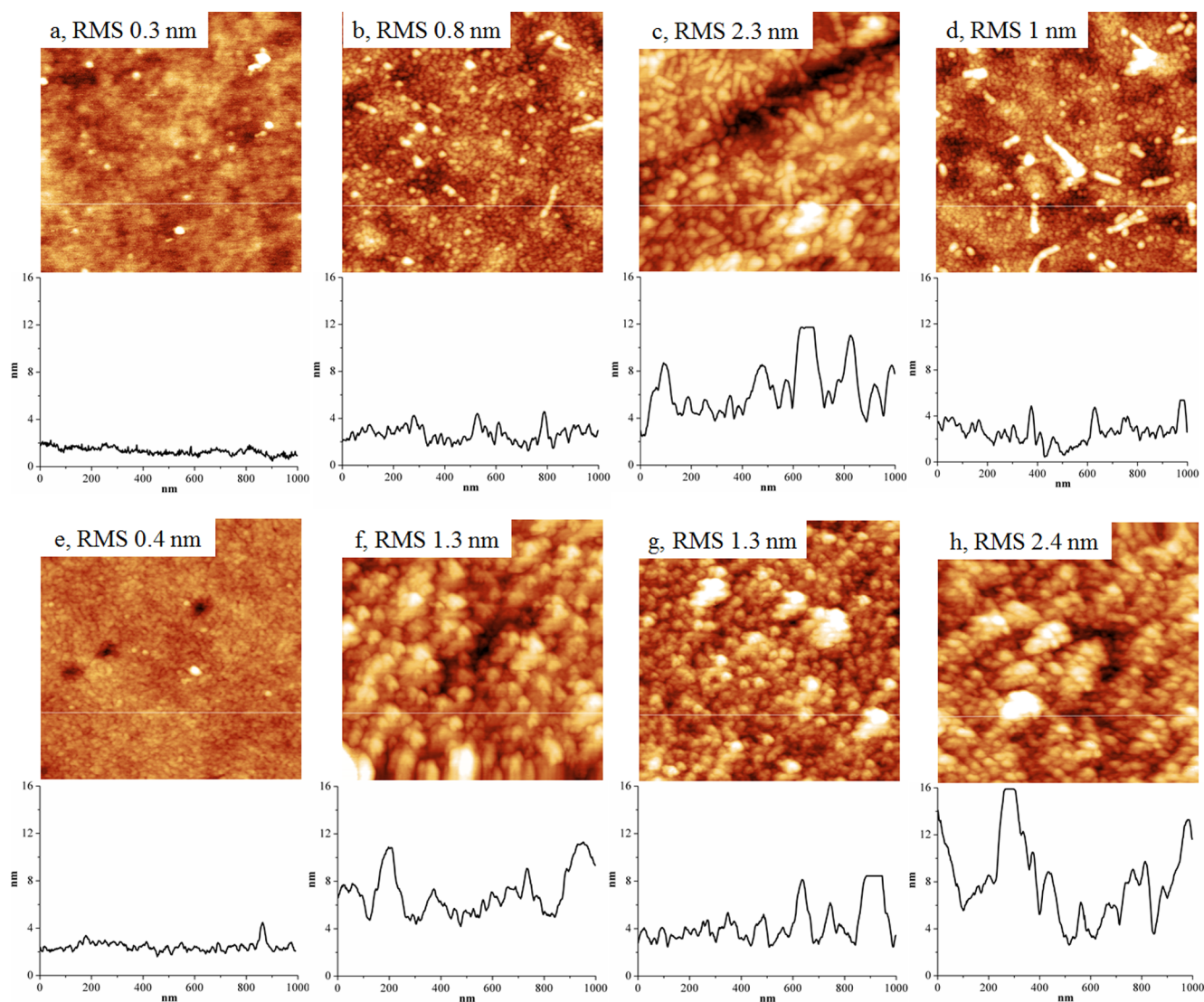
Figure 7. AFM images and their respective cross section profiles of HRP-modified surfaces (1 μm × 1 μm). Upper row: PS; lower row: BCMC-coated PS: (a, e) no HRP, (b, f) method I, (c, g) method II, (d, h) method III. The root-mean-square (RMS) roughness is given in each image. The z-scale is 20 nm.

not only a hydrophilic CMC backbone, but also carboxylic groups available for further modification. Thus, the immobilization of the biocatalytically important enzyme HRP was investigated on BCMC-modified and bare PS layers. Three methods of HRP immobilization were chosen (Figure 6). The first method consists of a simple rinsing step where pure HRP was allowed to adsorb on BCMC and uncoated PS (Figure 6, A1, B1). As expected, larger amounts of HRP are deposited on BCMC-coated PS surfaces. During the initial phase of adsorption, dissipation (B1) is reduced, indicating the release of water and the formation of a denser BCMC-HRP layer. This is not observed on PS films, since this polymer film does not contain water and comprises a solid with low compressibility and a rigid structure. During the whole incubation time with HRP, dissipation is almost constant for both coatings. However, after rinsing with water, a significant amount of HRP is released from the BCMC coating, whereas negligible desorption takes place from the PS surface. Generally more HRP is retained on the BCMC coatings ($\Delta f_3 = -22$ Hz, $\Delta D_3 = 1.8 \times 10^{-6}$) than on the uncoated PS ($\Delta f_3 = -13$ Hz, $\Delta D_3 = 1.9 \times 10^{-6}$).

For coating method II, a mixture of HRP/EDC was applied to both surfaces. In all cases, material is adsorbed on the layers as indicated by the negative frequency (A2) and positive dissipation shifts (B2) shown in Figure 6. On pure PS, cross-linked HRP aggregates are deposited to a higher extent than without EDC as discussed above. On the BCMC coated substrate, more enzyme is irreversibly bound to the surface, which can be explained by cross-linking and covalent binding of the available primary amino groups of HRP with carboxylic groups of BCMC mediated by EDC. The qualitative behavior is comparable to method I with a negative dissipation on BCMC coatings. However, more mass is retained on both surfaces (BCMC: $\Delta f_3 = -29$ Hz, $\Delta D_3 = 0.8 \times 10^{-6}$; PS: $\Delta f_3 = -21$ Hz, $\Delta D_3 = 5.7 \times 10^{-6}$) with a lower dissipation on the BCMC coatings, indicating EDC cross-linking of the layers causing a denser packing and less incorporated water.

A very different behavior was observed when the surfaces were first incubated with EDC, rinsed, and then subjected to the HRP solution (method III, Figure 6A3, B3). After incubation with EDC, frequency (A3) is reduced, which can be attributed to the higher density of the solution and binding

to the surface. This effect is reversible after rinsing the surfaces with pure water.

On BCMC-coated surfaces, reduced dissipation shifts (B3) can be observed after incubation with EDC. This can be explained by the covalent and adsorptive binding of EDC to the carboxylic backbone reducing the negative charge and obviously the water content of the layer, which subsequently leads to a negative dissipation after rinsing. The binding of HRP to layers activated in this way demonstrates the significance of the developed surface modification method. Strong immobilization of HRP obviously occurs on BCMC modified PS (BCMC: $\Delta f_3 = -133$ Hz, $\Delta D_3 = 11.9 \times 10^{-6}$), whereas amounts of HRP deposited on PS are very similar to the immobilization method I (PS: $\Delta f_3 = -12$ Hz, $\Delta D_3 = 1.7 \times 10^{-6}$) since no carboxylic groups are present to be activated by EDC.

3.7. Surface Morphology of Pure and Functionalized PS Films.
To further investigate the deposited BCMC and HRP layers, AFM images were recorded (Figure 7). On PS (a), all three methods of HRP immobilization lead to changes in surface morphology (b−d). Methods I and III (images b and d) give similar results, exhibiting homogeneously adsorbed HRP, whereas method II yields larger enzyme aggregates with a much higher surface roughness (c, RMS roughness: 2.3 nm). This is also reflected in the cross section profile (c, bottom) where an uneven and increase in height distribution are observed, an indication that the HRP is randomly distributed on the surfaces. The higher surface roughness can be explained by prior cross-linking and formation of HRP aggregates in the HRP/EDC solution and the subsequent deposition of these aggregates on the surface. These results strongly confirm the QCM-D results, where method I and III resulted in similarly low frequency shifts on PS. The presence of BCMC on PS can further easily be confirmed by the appearance of a dense homogeneous coating but only results in negligible changes in surface roughness (e, RMS roughness: 0.4 nm). Immobilization of HRP on these layers by the methods I−III (f−h) results in completely different morphologies compared to bare PS.

In particular, on the BCMC surfaces, which were obtained by coating method III, large enzyme aggregates with highest root-mean-square roughness values (h, RMS: 2.4 nm) are observed compared to the coatings produced from method I and II. Although this roughness value is similar to the value obtained for HRP layers on PS by method II (c), clear differences in the cross section profile is observable. The height of the HRP immobilized layer on BCMC coated surfaces is higher (h, bottom: ∼ 12−16 nm) compared to those of HRP-coated PS surfaces (c, bottom: ∼ 8−10 nm), which is indicative of deposition of more and random distribution of HRP on the surfaces. Thus, AFM confirms the findings from the QCM-D measurements on BCMC coated films. Although AFM and QCM-D give information on qualitative structure and immobilized amount, the activity of the bound enzyme is not revealed. Therefore, the catalytic activity of HRP modified PS films were investigated in the next step by a photometric ABTS test in detail.
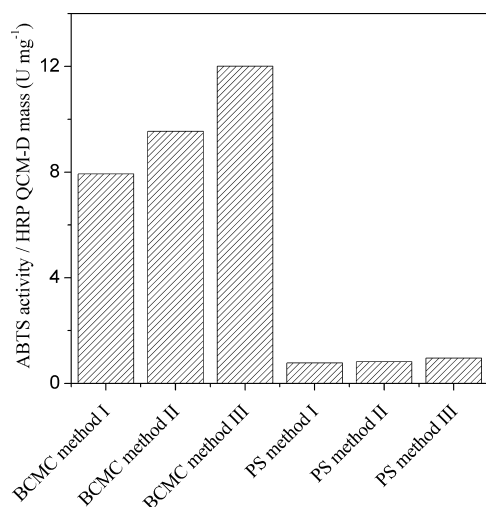
3.8. ABTS-Activity of Immobilized HRP.
The amount and conformation of the immobilized enzyme determines the final activity on the solid substrates. The concentration dependent enzymatic activity for all methods of immobilization was therefore investigated and compared with the results from QCM-D and AFM. Figure 8 shows the ABTS activity of the HRP coated PS surfaces. Without a BCMC coating (Figure 8a), much lower activities are observed. On these surfaces method II
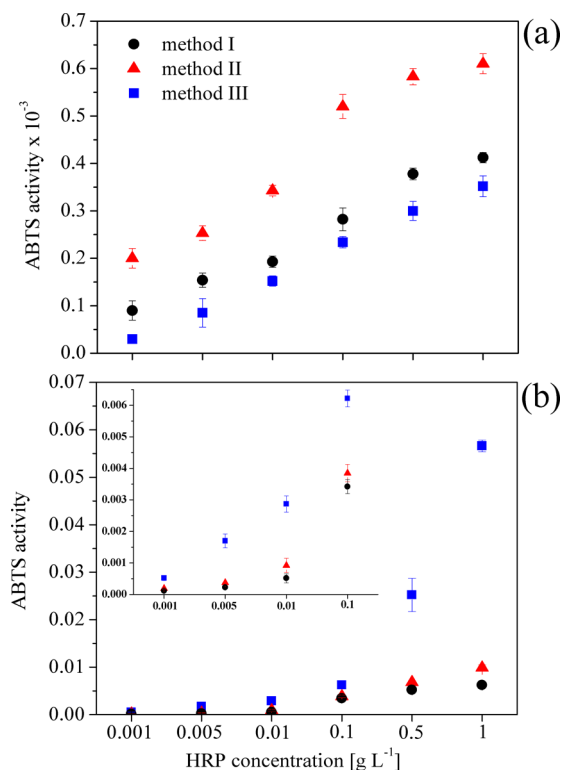
Figure 8. ABTS activity of HRP on PS (a) and on BCMC-coated PS (b) immobilized by method I−III on a 2 cm^2 substrate area. The inset in panel b shows the enlarged lower concentration range of the same figure.

gives the highest activities (on PS: HRP 1 g L^{-1}, ABTS: 0.0006, $\Delta f_3 = -21$ Hz, $\Delta D_3 = 5.7 \times 10^{-6}$). This can be directly related to the QCM-D results where the highest amount of immobilized HRP on PS was obtained by method II (Figure 6) and with the AFM results, where larger agglomerates of HRP were visible (Figure 7c). Contrary to that, the immobilization of HRP on BCMC leads to much higher activities for all methods of immobilization (e.g., method II on BCMC: HRP 1 g L^{-1}, ABTS: 0.01, $\Delta f_3 = -29$ Hz, $\Delta D_3 = 0.8 \times 10^{-6}$). Frequency shifts of immobilized HRP are similar on bare and BCMC-coated PS, but ABTS activity is 16 times higher on BCMC. It can therefore be assumed that the underlying BCMC layer provides a hydrophilic environment (contact angle of water pure PS (95 ± 1°), and CMC-coated PS (94 ± 2°), CMCE-coated PS (92 ± 2°), and BCMC-coated PS (20 ± 1°) beneficial for retaining the activity of HRP. Even though the coated BCMC layer carries hydrophobic benzyl groups (DS of benzyl groups in BCMC is 0.05, as revealed by UV−vis results), BCMC polymer still possess lots of unsubstituted carboxylic groups in addition to the hydroxyl groups that are highly hydrophilic in nature. These hydrophilic groups are responsible for the observed reduced water contact angle. This result is in accordance with the report published by Kargl et al., where a reduced water contact angle is noted for hydrophobic polymeric surfaces (e.g., cellulose acetate and cyclo olefin polymer) that are coated with hydrophilic CMC molecules.[29] For the covalent immobilization with method III, exceptionally high enzymatic activities are observed (on BCMC: HRP 1 g L^{-1}, ABTS: 0.055 U, $\Delta f_3 = -133$ Hz, $\Delta D_3 = 11.9 \times 10^{-6}$). When these values are compared with method II on BCMC, one can see that QCM-D frequency shifts and ABTS activity

correlate well. A 4.6-fold decrease in frequency results into a 5.5-fold increase in activity. Figure 9 depicts the ABTS activity

Figure 9. ABTS activtiy per QCM-D wet mass of immobilized HRP (1 g L^{-1}) for each method of immobilization on BCMC-coated and bare PS.

per QCM-D wet mass of immobilized HRP $(U \text{ mg}^{-1})$. The wet mass was calculated directly using Δf_3 (from Figure 6) following the Sauerbrey equation (see the Supporting Information).[30] The ABTS activity (obtained for 1 g L^{-1} HRP, immobilized on a 2 cm^2 substrate area; see Figure 8) was then normalized to the QCM-D wet mass of HRP according to the following equation: (ABTS activity U cm^{-2}/ QCM-D wet mass mg cm^{-2})/2. An underlying BCMC layer obviously increases the activity of the enzyme, and values up to 12 U mg^{-1} HRP are found. By contrast, HRP reveals a much lower activity on PS substrates. It can finally be stated that the BCMC layer provides a stable hydrophilic environment that much better retains the activity of HRP during adsorptive and covalent immobilization. With the most effective immobilization method III, HRP shows ABTS activities that are 13-fold higher on BCMC than on bare PS. BCMC does not only provide a simple and quick method for the modification of PS, but also allows the efficient immobilization of HRP while retaining its activity. While a direct comparison of one method to other one is always difficulty due to the different immobilization chemistry, substrates, concentration of enzymes, reaction conditions and the techniques used for the determination of ABTS activity, the obtained results from this work can be compared to a certain extent. For instance, a covalent immobilization of HRP on a hydrophilic polyacrylonitrile (PAN) via EDC chemistry showed an ABTS activity of 2.3 U mg^{-1}, which is 80% less when compared with the values obtained for BCMC coated PS surfaces (Figure 9, method III).[31] However, a HRP that was immobilized on other hydrophilic substrates such as silica microbeads and aminated glass slides with EDC displayed a several-fold increased ABTS activity compared to those obtained with our method III, as in their cases a rather higher HRP concentration (15-fold higher) was used for HRP immobilization.[31]

4. CONCLUSIONS

The carbodiimide mediated reaction of benzylamine with CMC yields a water-soluble benzylamide of CMC as confirmed by IR, NMR, and UV−vis measurements. Besides the remaining negative charges, this derivative binds, in contrast to the unmodified polysaccharide, spontaneously and irreversibly to polystyrene surfaces as proven by QCM-D. The favorable hydrophilic environment along with carboxylic groups available for covalent reactions results in a substrate that can be used for the immobilization of enzymes. HRP, immobilized either by adsorption or covalently onto these polysaccharide layers, shows a high enzymatic activity. When comparable amounts of enzymes are adsorbed, activities are always higher on the polysaccharide modified, than on the bare polystyrene. Possible covalent binding of the enzyme to the surface results in enzymatic activities that are 2 orders of magnitude higher than enzymes bound to bare polystyrene. The generic method of surface modification and enzyme immobilization developed here can further be extended to any other kind of (bio)-molecule bearing accessible amino-moieties.

■ ASSOCIATED CONTENT

Ⓢ Supporting Information

QCM-D measurements of BCMC on cellulose and polystyrene, calculation of QCM-D wet mass of immobilized HRP using Sauerbrey equation, and determination of ABTS activity of immobilized HRP. The Supporting Information is available free of charge on the ACS Publications website at DOI: 10.1021/acs.biomac.5b00638.

(PDF)

■ AUTHOR INFORMATION

Corresponding Author
*E-Mail: tamilselvan.mohan@uni-graz.at; Tel: +43 316 380 5413.

Notes
The authors declare no competing financial interest.

■ REFERENCES

(1) Kirk, O.; Borchert, T. V.; Fuglsang, C. C. Industrial enzyme applications. *Curr. Opin. Biotechnol.* **2002**, *13* (4), 345−351.

(2) Bornscheuer, U. T. Immobilizing Enzymes: How to Create More Suitable Biocatalysts. *Angew. Chem., Int. Ed.* **2003**, *42* (29), 3336−3337.

(3) Clark, D. S. Can immobilization be exploited to modify enzyme activity? *Trends Biotechnol.* **1994**, *12* (11), 439−443.

(4) Sheldon, R. A. Enzyme Immobilization: The Quest for Optimum Performance. *Adv. Synth. Catal.* **2007**, *349* (8−9), 1289−1307.

(5) Nidetzky, B.; Steiner, W. A new approach for modeling cellulase−cellulose adsorption and the kinetics of the enzymatic hydrolysis of microcrystalline cellulose. *Biotechnol. Bioeng.* **1993**, *42* (4), 469−479.

(6) Chen, Y.; Xiao, B.; Chang, J.; Fu, Y.; Lv, P.; Wang, X. Synthesis of biodiesel from waste cooking oil using immobilized lipase in fixed bed reactor. *Energy Convers. Manage.* **2009**, *50* (3), 668−673.

(7) Roy, I.; Gupta, M. N. Lactose hydrolysis by Lactozym immobilized on cellulose beads in batch and fluidized bed modes. *Process Biochem.* **2003**, *39* (3), 325−332.

(8) Xu, X.; Balchen, S.; Høy, C. E.; Adler-Nissen, J. Production of specific-structured lipids by enzymatic interesterification in a pilot continuous enzyme bed reactor. *J. Am. Oil Chem. Soc.* **1998**, *75* (11), 1573−1579.

(9) Auriol, M.; Filali-Meknassi, Y.; Adams, C. D.; Tyagi, R. D. Natural and synthetic hormone removal using the horseradish peroxidase enzyme: Temperature and pH effects. *Water Res.* **2006**, *40* (15), 2847−2856.

(10) Tatsumi, K.; Wada, S.; Ichikawa, H. Removal of chlorophenols from wastewater by immobilized horseradish peroxidase. *Biotechnol. Bioeng.* **1996**, *51* (1), 126−130.

(11) Veitch, N. C. Horseradish peroxidase: a modern view of a classic enzyme. *Phytochemistry* **2004**, *65* (3), 249−259.

(12) Azevedo, A. M.; Martins, V. C.; Prazeres, D. M. F.; Vojinović, V.; Cabral, J. M. S.; Fonseca, L. P. Horseradish peroxidase: a valuable tool in biotechnology. *Biotechnol. Annu. Rev.* **2003**, *9*, 199−247.

(13) Wang, L.; Wang, E. A novel hydrogen peroxide sensor based on horseradish peroxidase immobilized on colloidal Au modified ITO electrode. *Electrochem. Commun.* **2004**, *6* (2), 225−229.

(14) Ryan, B. J.; Carolan, N.; Ó'Fágáin, C. Horseradish and soybean peroxidases: comparable tools for alternative niches? *Trends Biotechnol.* **2006**, *24* (8), 355−363.

(15) Adams, J. C. Technical considerations on the use of horseradish peroxidase as a neuronal marker. *Neuroscience* **1977**, *2* (1), 141−145.

(16) Xiao, Y.; Ju, H.-X.; Chen, H.-Y. Hydrogen peroxide sensor based on horseradish peroxidase-labeled Au colloids immobilized on gold electrode surface by cysteamine monolayer. *Anal. Chim. Acta* **1999**, *391* (1), 73−82.

(17) Liu, Y.-L.; Yang, Y.-H.; Yang, H.-F.; Liu, Z.-M.; Shen, G.-L.; Yu, R.-Q. Nanosized flower-like ZnO synthesized by a simple hydrothermal method and applied as matrix for horseradish peroxidase immobilization for electro-biosensing. *J. Inorg. Biochem.* **2005**, *99* (10), 2046−2053.

(18) Chouyyok, W.; Panpranot, J.; Thanachayanant, C.; Prichanont, S. Effects of pH and pore characters of mesoporous silicas on horseradish peroxidase immobilization. *J. Mol. Catal. B: Enzym.* **2009**, *56* (4), 246−252.

(19) Zhou, G.-J.; Wang, G.; Xu, J.-J.; Chen, H.-Y. Reagentless chemiluminescence biosensor for determination of hydrogen peroxide based on the immobilization of horseradish peroxidase on biocompatible chitosan membrane. *Sens. Actuators, B* **2002**, *81* (2−3), 334−339.

(20) Leirião, P. R. S.; Fonseca, L. J. P.; Taipa, M. A.; Cabral, J. M. S.; Mateus, M. Horseradish peroxidase immobilized through its carboxylic groups onto a polyacrylonitrile membrane. *Appl. Biochem. Biotechnol.* **2003**, *110* (1), 1−10.

(21) Hong, H.-C.; Huang, H.-J. Flow injection analysis of uric acid with a uricase- and horseradish peroxidase-coupled Sepharose column based luminol chemiluminescence system. *Anal. Chim. Acta* **2003**, *499* (1−2), 41−46.

(22) Čakara, D.; Fras, L.; Bračič, M.; Kleinschek, K. S. Protonation behavior of cotton fabric with irreversibly adsorbed chitosan: A potentiometric titration study. *Carbohydr. Polym.* **2009**, *78* (1), 36−40.

(23) Marx, K. A. Quartz Crystal Microbalance: A Useful Tool for Studying Thin Polymer Films and Complex Biomolecular Systems at the Solution−Surface Interface. *Biomacromolecules* **2003**, *4* (5), 1099−1120.

(24) Morawski, B.; Lin, Z.; Cirino, P.; Joo, H.; Bandara, G.; Arnold, F. H. Functional expression of horseradish peroxidase in Saccharomyces cerevisiae and Pichia pastoris. *Protein Eng., Des. Sel.* **2000**, *13* (5), 377−384.

(25) Nečas, D.; Klapetek, P. Gwyddion: an open-source software for SPM data analysis. *Cent. Eur. J. Phys.* **2012**, *10* (1), 181−188.

(26) Nakajima, N.; Ikada, Y. Mechanism of Amide Formation by Carbodiimide for Bioconjugation in Aqueous Media. *Bioconjugate Chem.* **1995**, *6* (1), 123−130.

(27) Mohan, T.; Kargl, R.; Köstler, S.; Doliška, A.; Findenig, G.; Ribitsch, V.; Stana-Kleinschek, K. Functional polysaccharide conjugates for the preparation of microarrays. *ACS Appl. Mater. Interfaces* **2012**, *4* (5), 2743−2751.

(28) Käuper, P.; Kulicke, W.-M.; Horner, S.; Saake, B.; Puls, J.; Kunze, J.; Fink, H.-P.; Heinze, U.; Heinze, T.; Klohr, E.-A.; Thielking, H.; Koch, W. Development and evaluation of methods for determining the pattern of functionalization in sodium carboxymethylcelluloses. *Angew. Makromol. Chem.* **1998**, *260* (1), 53−63.

(29) Kargl, R.; Mohan, T.; Bračič, M.; Kulterer, M.; Doliška, A.; Stana-Kleinschek, K.; Ribitsch, V. Adsorption of Carboxymethyl Cellulose on Polymer Surfaces: Evidence of a Specific Interaction with Cellulose. *Langmuir* **2012**, *28* (31), 11440−11447.

(30) Mohan, T.; Niegelhell, K.; Zarth, C. S. P.; Kargl, R. J.; Köstler, S.; Ribitsch, V.; Heinze, T.; Spirk, S.; Stana-Kleinschek, K. Triggering Protein Adsorption on Tailored Cationic Cellulose Surfaces. *Biomacromolecules* **2014**, *15* (11), 3931−3941.

(31) Leirião, P. R.; Fonseca, L. J.; Taipa, M. A.; Cabral, J. M.; Mateus, M. Horseradish Peroxidase Immobilized through Its Carboxylic Groups onto A Polyacrylonitrile membrane: Comparison of Enzyme Performances with Inorganic Beaded Supports. *Appl. Biochem. Biotechnol.* **2003**, *110* (1), 1−10.

CrossMark
click for updates

Reactive cellulose-based thin films – a concept for multifunctional polysaccharide surfaces

Thomas Elschner,[a] David Reishofer,[b] Rupert Kargl,[a] Thomas Grießer,[c] Thomas Heinze[d] and Karin Stana Kleinschek*[a]

Reactive coatings of hydroxyethyl cellulose furoate in the form of thin films, suitable for the covalent immobilization of functional molecules, were developed and characterized in this work. The cellulose furoate derivatives were synthesized under homogeneous conditions by esterification of hydroxyethyl cellulose with 2-furoic acid. Reactive platform layers of these furoates were obtained by chemical surface modification of spin coated thin films with N,N'-carbonyldiimidazole. This chemistry allowed the covalent immobilization of functional molecules bearing primary and secondary amines on the films. The degree of substitution of the furoate thin films and their amino functionalized counterparts was determined gravimetrically by a quartz crystal microbalance (QCM-D) and correlated with infrared and X-ray photoelectron spectroscopy and zeta-potential measurements. Scanning electron- and atomic force microscopy showed changes in the morphologies that were influenced by the chemical reactions on the surface. The concept presented can be seen as a versatile method for immobilizing amine-containing (bio-)molecules to polysaccharide surfaces with the furoates having the potential for further reversible cross-linking in Diels–Alder reactions.

1 Introduction

Surface functionalization methods are important and common tools in manifold applications ranging from antifouling coatings to biosensors,[1] supports and models for living cells,[2] light-emitting or photovoltaic devices, batteries, membranes, corrosion protection, and colloid stability.[3–5] In particular polysaccharide (PS) materials and their surface modifications gained importance during previous years, owing to their biocompatible and renewable character, combined with a large number of possible derivatization reactions.[6] Surface modifications can, besides others, be carried out by chemical reactions on bulk materials or by thin film depositions. They possess the advantage that less chemicals are needed to achieve a significant impact on the functionalities and properties of materials.

For PS, thin film coatings are often obtained by the synthesis of a soluble derivative and subsequent coating on a support using spin coating or layer-by-layer approaches.[1] PS thin film coatings in general can either serve as a model for bulk materials or can subsequently be surface modified by a large number of chemical reactions depending on the targeted application. Surface reactions give accessibility to derivatives that are difficult to produce under homogeneous conditions in solution due to cross-linking, which hampers subsequent processing into thin film coatings. Reactive carbonic acid esters of cellulose for instance form intra- and intermolecular carbonates[7] in solution limiting the applicability of these interesting derivatives.[8]

Cellulose and its derivatives are also appropriate for post-modification of the hydroxyl groups at positions 2, 3, and 6 of the repeating unit. Tailor-made functional surfaces based on cellulose derivatives and solutions were reviewed recently emphasizing the great potential of these materials.[9] Examples are regenerated cellulose from trimethylsilyl cellulose[10,11] or solutions of cellulose in N,N-dimethylacetamide/lithium chloride (DMAc/LiCl)[12] or N-methylmorpholine N-oxide/dimethyl sulfoxide (NMMO/DMSO).[13] Moreover, spin coating of cellulose from aqueous colloidal suspensions was demonstrated successfully.[9] Applications cover basic surface science, biosensors or low-protein adhesion coatings.[11]

A step further in these developments is the design of reactive thin film based platforms allowing post-modification after coating the PS derivative on a substrate. This includes reversible cross-linking reactions or immobilization of e.g. biomolecules and especially the covalent binding of primary amines if biomedical, biotechnological, or biosensoric applications are targeted.[14–16] This work therefore aims at combining the

aFaculty of Mechanical Engineering, Laboratory for Characterization and Processing of Polymers, University of Maribor, Smetanova 17, 2000 Maribor, Slovenia. E-mail: karin.stana@um.si; Fax: +386 2 220 7990; Tel: +386 2 220 7881

bInstitute for Chemistry and Technology of Materials, Graz University of Technology, Stremayrgasse 9, 8010 Graz, Austria

cChair of Chemistry of Polymeric Materials, University of Leoben, Otto Glöckel-Straße 2, 8700 Leoben, Austria

dCenter of Excellence for Polysaccharide Research, Institute for Organic Chemistry and Macromolecular Chemistry, Friedrich Schiller University of Jena, Humboldtstraße 10, D-07743 Jena, Germany

advantages of PS derivatisation in solution with the post-modification of thin films. It develops a new approach for joining two functions in one PS film. An organo-soluble cellulose derivative bearing furoate moieties that could be cross-linked reversibly with maleimides leading to self-healing materials[17,18] is synthesized under homogeneous conditions from hydroxyethyl cellulose. The polymer is characterized by NMR- and IR spectroscopy and spin coated in the form of nanometric thin films on solid substrates. Subsequent reaction of the remaining hydroxyl groups with N,N'-carbonyldiimidazole (CDI), avoiding in this way the negative consequences of cross-linking in solution, then enables the immobilization of primary amines as model substances for biomolecules (peptides, proteins *etc.*). To monitor the reactions on the thin films, surface sensitive techniques such as a quartz crystal microbalance with dissipation monitoring (QCM-D)[19-21] is used and compared with surface analytical results of attenuated total reflectance infrared spectroscopy (ATR-IR) and X-ray photoelectron spectroscopy. Surface charges are investigated by zeta-potential measurements and changes in morphology are analysed by atomic force microscopy. The whole concept would allow the development of reactive PS based platform layers that serve for the immobilization of primary amines and simultaneously provide a (Retro-) Diels–Alder reactive furoate substituent for further modification.

2 Experimental section

2.1 Materials

2-Hydroxyethyl cellulose (2-HEC) with a viscosity average molar mass of 90 000 g mol^{-1} was purchased from Sigma-Aldrich and dried at 60 °C in vacuum. Toluene (99.9%, Sigma) was dried over sodium hydroxide before use. Other chemicals and solvents were purchased from Sigma-Aldrich or Acros Organics and were used without further treatment.

Silicon wafers supplied by Silchem (Germany) were cut into 15 mm × 15 mm pieces. Microscope glass slides (25 mm × 75 mm) were obtained from Sigma-Aldrich. Quartz crystal microbalance (QCM-D) sensors with a gold layer (QSX303) were purchased from LOT-Oriel (Germany). Milli-Q water from a Millipore water purification system (MA, USA, resistivity 18.2 MΩ cm, pH 6.8) was used for the experiments.

All polysaccharide derivatives and the respective thin film are numbered according to the notation of the chemical structures in Fig. 1.

2.2 Syntheses

2.2.1 Synthesis of 2-hydroxyethyl cellulose 2-furoate 2. 2-Furoic acid (6.18 g, 55.1 mmol) was dissolved in 30 mL N-methyl-2-pyrrolidone (NMP) and CDI (8.93 g, 55.1 mmol) was added stepwise. The mixture was allowed to react over night at room temperature under stirring.

2-HEC (**1**, MS 2.5, 5 g, 18.4 mmol) was dissolved in 75 mL NMP at 90 °C for 2 h under stirring. After cooling to room temperature, the activated carboxylic acid was added and the combined solutions were stirred for 24 h at 60 °C. The reaction

mixture was allowed to cool to room temperature and poured into 1.5 L deionized water. Subsequently, the precipitate was filtered off, washed three times with 500 mL water, and dried in vacuum at room temperature.

Yield: 93%, DS$_{furoate}$ 1.72 (determined by ^{1}H NMR after peracetylation[22]), FT-IR (ATR): 1730 cm^{-1} ($\nu_{C=O}$), soluble in DMSO, DMA, DMF, CHCl$_3$, THF, 1,4-dioxane, insoluble in toluene, heptane, acetone. (Solubility was determined by suspending 20 mg product in 0.5 mL solvent at room temperature or 60 °C over night. The product was considered to be soluble, when a clear solution was obtained.) ^{1}H NMR (250 MHz, DMSO-d$_6$): δ [ppm] = 7.95 (CH), 7.29 (CH), 6.67 (CH), 4.34, 3.70, 3.49, 3.35. ^{13}C NMR (63 MHz, DMSO-d$_6$): δ [ppm] = 158.3 (C=O), 148.0 (CH), 144.2 (C), 119.0 (CH), 112.7 (CH), 70.2, 68.7, 64.2, 60.7.

2.2.2 Peracetylation. 250 mg of 2-hydroxyethyl cellulose 2-furoate in 5 mL pyridine was allowed to react with 5 mL of acetic anhydride over night at 60 °C. The polymer was precipitated in 250 mL of an aqueous solution of 0.5% sodium hydrogen carbonate and washed four times with deionized water (150 mL). Subsequently, the product was dried at room temperature in vacuum. FT-IR (KBr): no ν_{OH}.

2.3 Surface modification

2.3.1 Cleaning and coating of support materials. The procedures for cleaning of the substrates were already described in detail by Mohan *et al.*[23] In brief, silicon wafers, glass slides, and QCM-D crystals were treated with piranha solution and rinsed with Milli-Q water extensively. Subsequently, the support materials were spin coated with 2-hydroxyethyl cellulose 2-furoate from solutions in chloroform applying 4000 rpm (acceleration 2500 rpm s^{-1}) for 60 s.

2.3.2 Activation of hydroxyl groups applying N,N'-carbonyldiimidazole (CDI). The coated support materials were immersed in a solution of 1% CDI in toluene at 60 °C for 4 h and subsequently rinsed with 2-propanol and Milli-Q water. The films (**3**) were dried with a stream of nitrogen before measurements. FT-IR (ATR): 1730 cm^{-1} ($\nu_{C=O}$, furoate), 1773 cm^{-1} ($\nu_{C=O}$, 1*H*-imidazole-1-carboxylate), elemental composition (at% obtained by XPS) for DS$_{Im}$ 0.91: calculated: C, 63.0; O, 32.1; N, 4.9 found: C, 65.3; O, 29.8; N, 4.9.

2.3.3 Aminolysis of 1*H*-imidazole-1-carboxylate. The activated films **3** (on solid support) were immersed in triethylene tetramine (TETA, 1% in toluene) at 60 °C for 4 h. Subsequently, the surface **4** was rinsed with 2-propanol and Milli-Q water and dried with a stream of nitrogen. For the blank sample an unmodified film of 2-hydroxyethyl cellulose 2-furoate (**2**) was treated under equal conditions. FT-IR (ATR): 1730 cm^{-1} ($\nu_{C=O}$, furoate, carbamate), elemental composition (at% obtained by XPS) for DS$_{TETA}$ 0.65: calculated: C, 63.0; O, 30.2; N, 6.8 found: C, 66.0; O, 27.0; N, 6.8.

2.4 Measurements

2.4.1 NMR spectroscopy. NMR spectra were acquired on a Bruker Avance 250 MHz with 32 scans for ^{1}H NMR
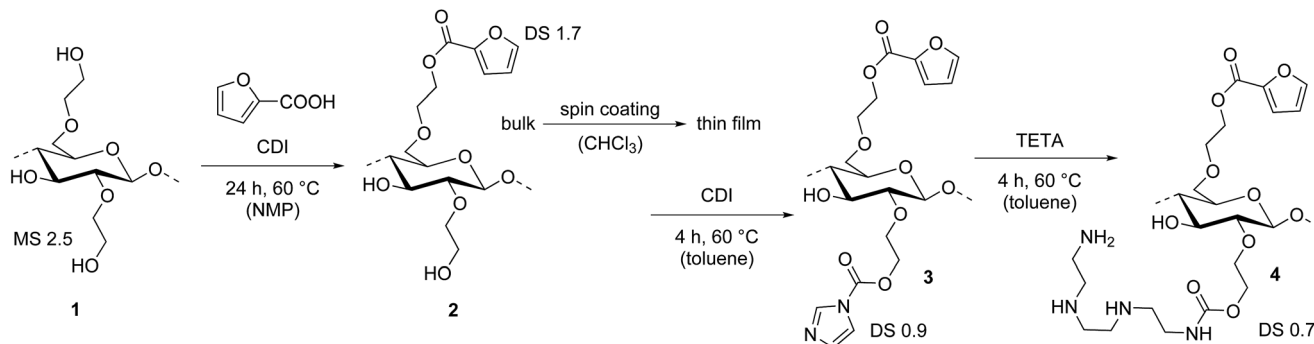
Fig. 1 Reaction scheme of the synthesis of hydroxyethyl cellulose furoate in bulk and subsequent post-modification of the thin film obtained by spin coating.

spectroscopy and 10 000 scans for ^{13}C NMR spectroscopy (27 °C) applying 100 mg sample per mL solvent.

2.4.2 FT-IR spectroscopy. For supporting the complete functionalization of peracetylated **2** the FT-IR spectrum was recorded on a Nicolet AVATAR 370 DTGS spectrometer with the KBr technique. Thin films on QCM-D crystals were measured using a PerkinElmer Spectrum GX Series-73565 FTIR-spectrometer by the ATR technique applying 100 scans.

2.4.3 QCM-D experiments. The gold coated sensor crystals were measured in air with a QCM-D E4 from Q-Sense AB (Gothenburg, Sweden) at 21 °C. The relative resonant frequency (Δf) of the crystals as well as the relative dissipation factor (ΔD) were determined in comparison to the zero values at the beginning of the experiment (third overtone). All adsorption experiments were repeated at least three-times. The quartz crystals were AT-cut quartz with gold plated electrodes and with gold on the active surface. The fundamental frequency of quartz crystals is $f_0 \approx 5$ MHz and the sensitivity constant $C = 17.7$ ng Hz^{-1} cm^{-2}. Previous to measurements the sensors we blow-dried in a stream of nitrogen.

2.4.4 Atomic force microscopy. Atomic force microscopy (AFM) images were recorded in tapping mode (non-contact mode) on a Veeco Multimode Quadrax MM AFM (Bruker; Billerica, MA, USA). Scanning silicon cantilevers (NCH-VS1-W from NanoWorld AG, Neuchatel, Switzerland) possessed an average spring constant of 42 N m^{-1} (force constant) and a resonance frequency of 270 to 320 kHz (coating: none). All measurements were performed at room temperature and under ambient atmosphere. The calculation of the root mean square roughness was done on 5 μm × 5 μm images. The image processing was carried out with the Nanoscope software (V7.30r1sr3; Veeco).

2.4.5 Stylus profilometry. The film thickness was measured using a DEKTAK 150 Stylus Profiler (Veeco). The scan length was set to 1000 μm for a period of 3 s. The diamond stylus possesses a radius of 12.5 μm. The force was adjusted to 3 mg with a resolution of 0.333 μm per sample and a measurement range of 6.5 μm. The profile was set to Hills and Valleys. For the determination of the film thickness each silicon wafer sample was scratched five times with tweezers. The profile was used to calculate the thickness from step height measurement.

2.4.6 X-ray photoelectron spectroscopy. XPS spectra were recorded using a Thermo Scientific instrument equipped with a monochromatic Al K_α X-ray source (1486.6 eV). High resolution scans were acquired at a pass energy of 50 eV and a step size (resolution) of 0.1 eV. Wide scans were acquired with pass energy of 100 eV and a step size of 1.0 eV. All spectra were normalized to the Au 4f7/2 peak. Charge compensation was performed with an argon flood gun. The average chemical composition was calculated from wide scan spectra in two different locations on each surface. The peaks were fitted using a Gaussian/Lorenzian mixed function employing Shirley background correction (Software Thermo Avantage v5.906). All analyses were performed at room temperature.

2.4.7 Contact angle measurements. The surface energies of the films were measured by using Dataphysics contact angle measurement system OCA35 (Dataphysics, Germany) with the sessile drop method and a drop volume of 3 μL. Contact angles of four different solvents, namely water (Erbil), ethylene glycol (van Oss *et al.*), formamide (van Oss *et al.*), and diiodomethane (Gonzales-Martin) were evaluated according to the published surface tension parameters applying the Young–Laplace method. The references written in brackets refer to the used software of the contact angle device. All measurements were carried out at room temperature and were performed at least five times and an average value was calculated (Table 1).

2.4.8 Zeta potential measurements. The zeta potential was determined on microscope glass slides in a self-made apparatus "Zeta-Oszi" using the principle of oscillating streaming potential.[24] The electrolyte was composed of 1 mM KCl solution in water and the pH was adjusted by automatic titration from pH 9 to pH 2. Each measurement was carried out for 60 s recording 600 points and repeated three times at the same pH value.

Table 1 Contact angles (CA) of water, ethylene glycol, formamide, and diiodomethane on thin films **2–4**

Sample	CA_{water} [°]	CA_{glycol} [°]	$CA_{formamide}$ [°]	$CA_{diiodomethane}$ [°]
2 (furoate)	76.6 ± 0.2	52.7 ± 1.3	50.4 ± 2.8	41.9 ± 1.5
3 (Im)	68.2 ± 1.0	44.2 ± 1.6	53.1 ± 2.2	34.0 ± 2.3
4 (TETA)	64.7 ± 0.6	35.5 ± 1.3	36.5 ± 1.5	35.2 ± 0.8

3 Results and discussion

3.1 Synthesis of hydroxyethyl cellulose furoate

The derivatization of polysaccharides (PS) with furoate moieties is an innovative approach to obtain materials, which can be cross-linked reversibly. Up to now, there are only a few examples for PS-based polymer films[17] or hydrogels[18] possessing furoate groups that undergo (Retro)-Diels–Alder reaction with e.g. bis-maleinimides as cross-linker. First synthetic attempts to synthesize hydroxyethyl cellulose furoate were based on the acid chloride, but a low DS value (1.2) was obtained at more than 6-fold excess of reagent.[17] Moreover, the product had to be per-acetylated to increase solubility.

Within this work, the mild and chlorine-free esterification applying N,N′-carbonyldiimidazole (CDI) leads to a highly functionalized product (DS 1.72) at low molar ratio (1 : 3, mol repeating unit : mol reagent). As shown in Fig. 1 (1, 2) the reaction was performed homogeneously in NMP at 60 °C over night. The furoic acid was activated with CDI separately in order to avoid side products or cross-linking. The biopolymer derivative obtained is not colored and possesses good solubility in several organic media, e.g. DMSO, chloroform, THF, and dioxane. Thus, this biopolymer derivative may be easily shaped into films, particles, and fibers.

The molecular structure of hydroxyethyl cellulose furoate (2) was shown by NMR spectroscopy. In the ^1H NMR spectrum the signals arising from the furan ring appear at 7.95, 7.29, and 6.67 ppm, which are well separated from the remaining resonances of the repeating unit (Fig. 2, top). Therefore, the DS could be calculated from the integral intensities of furoate- and methyl protons after peracetylation of the sample.[22] The structure was evidenced by ^{13}C NMR spectroscopy assigning the signals to the corresponding position and the linkage (ester moiety) to the polymer backbone that can be clearly observed due to the carbonyl resonance at 158 ppm (Fig. 2, bottom).
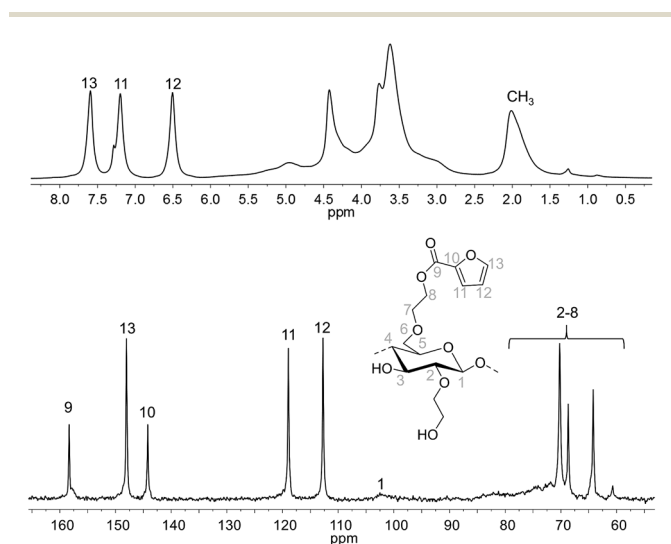

Fig. 2 ^1H NMR spectrum of peracetylated hydroxyethyl cellulose furoate recorded in CDCl$_3$ (top) and ^{13}C NMR spectrum of hydroxyethyl cellulose furoate (2) recorded in DMSO-d$_6$ (bottom).

3.2 Film formation of hydroxyethyl cellulose furoate

In order to obtain thin films of the cellulose derivative, which are uniform and suitable for post-modification, chloroform solutions were applied for spin coating on silicon wafers. Using 0.5% polymer solution, a smooth and evenly distributed film is obtained. According to profilometry the film thickness is 19.7 ± 0.5 nm.

3.3 Post-modification of films

Considering features of thin films obtained from cellulose derivatives, multifunctionality can be achieved by modification of the remaining hydroxyl groups. Thus, next to furoate moieties that could be cross-linked reversibly by Diels–Alder reaction, 1H-imidazole-1-carboxylate groups could be integrated into the film, which provides a reactive platform for various materials by aminolysis. In a first step, the hydroxyethyl cellulose furoate film (2) was allowed to react with a solution of CDI in toluene (Fig. 1). Toluene was found to be an aprotic organic solvent that does not dissolve the film but CDI, which is a prerequisite for this reaction. In the second reaction, the 1H-imidazole-1-carboxylate (3) was allowed to react with triethylene tetramine (TETA) to yield the corresponding hydroxyethyl cellulose furoate carbamate (4). It should be pointed out that this model amine is an example for an inexhaustible pool of amino compounds that may be covalently bound to the surface. TETA provides a high density of amino groups and a relatively high molecular mass, which is advantageous for monitoring the reaction with QCM-D.

3.3.1 Qualitative and quantitative evaluation. For a quantitative analysis of the surface modification, QCM-D experiments were performed in air. To show the applicability of toluene as reaction medium spin coated sensor crystals were immersed twice in pure solvent under reaction conditions (4 h, 60 °C, Fig. 3, top). The frequency shift (Δf) of about −240 Hz (after spin coating) changes to about −190 Hz. Thus, loosely bound molecules were removed from the surface. However, the mass of the films was constant after the first treatment.

The mass increase during the first reaction of films with CDI, Δf changes to −221 Hz (Fig. 3, center). Due to the low dissipation ($\Delta D \approx 0$) the film is rigid and Sauerbrey equation[25] is valid. Thus, the DS of 1H-imidazole-1-carboxylate (DS$_{Im}$) could be calculated according to the following equation. M_2 is the molecular mass of one repeating unit of 2 (g mol^{-1}) and M_{Im}^* represents the net molecular mass increase by 1H-imidazole-1-carboxylate (94.07 g mol^{-1}):

$$DS_{Im} = \frac{M_2 \dfrac{\Delta f(3)}{\Delta f(2)} - M_2}{M_{Im}^*}$$

The change in frequency from −186 to −221 Hz leads to a DS$_{Im}$ of 0.87 assuming a homogeneous esterification in the whole film. The activation is efficient and provides a high density of reactive groups.

Moreover, the formation of covalent bonds on the films could be shown by FT-IR ATR spectroscopy of the QCM-D
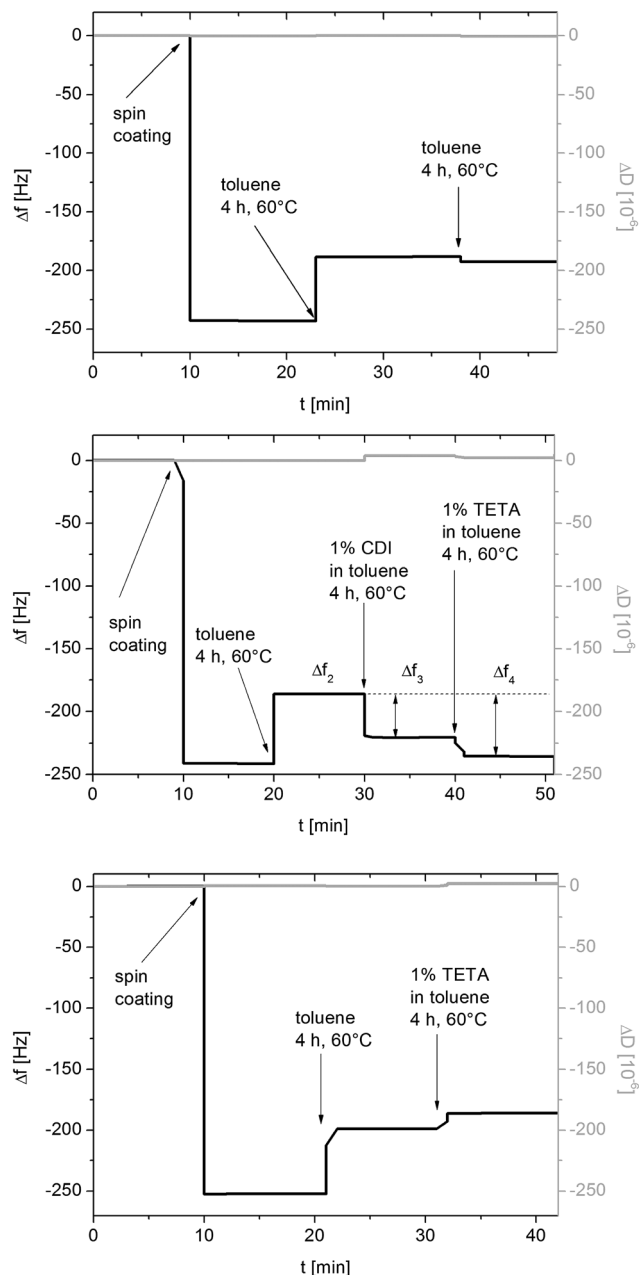
Fig. 4 FT-IR ATR spectra of thin films of hydroxyethyl cellulose furoate (**2**), hydroxyethyl cellulose furoate 1*H*-imidazole-1-carboxylate (**3**), and hydroxyethyl cellulose furoate carbamate (**4**) recorded on QCM-D crystals.

Fig. 3 Stitched QCM-D measurements in air, Δf change in frequency (black), ΔD change in dissipation (gray); top: stability of the film in toluene, center: reaction with TETA after CDI activation, bottom: treatment with TETA without CDI activation.

crystals (Fig. 4). In addition to the typical C=O stretching vibration at 1730 cm^{-1} arising from furoate, a second C=O vibration for the 1*H*-imidazole-1-carboxylate[26] at 1773 cm^{-1} appears. The integral areas of these peaks allow the prediction of the DS$_{Im}$, which was found to be 0.96. This value is in accordance to QCM-D measurements.

XPS results allow the qualitative and quantitative evaluation of the activated film considering C1s- and N1s scans (Fig. 5). Next to the three peak components arising from hydroxyethyl cellulose furoate at 284.4 eV (C–H), 286.0 eV (C–O), and 288.6 eV
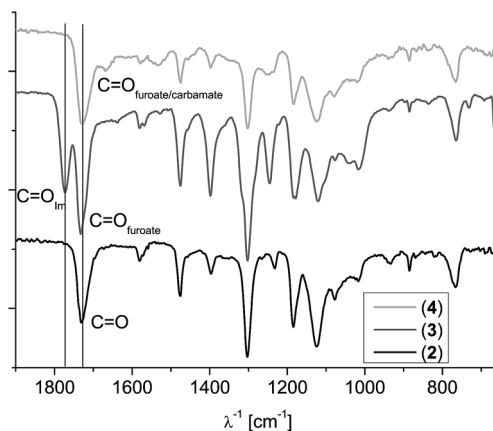
(O=C–O) an additional peak at 285.2 eV (C–N) occurs. Furthermore, the imidazolide is visible in the N1s scan; two peaks representing C=N and (C=O)N at 398.9 and 401.0 eV. These values are in accordance with literature data.[27,28] The elemental composition of the film indicates a DS$_{Im}$ of 0.91 (nitrogen content). Thus, the DS$_{Im}$ value is 0.9 as proved by three independent techniques (QCM-D, IR, XPS, Table 2).

The aminolysis of the activated polymer thin films (**3**) with TETA was also quantified with QCM-D and XPS. The increase of mass results in a frequency shift to −236 Hz (Fig. 3, center). Using analogous calculations to the previous example, the DS$_{TETA}$ was determined. M^*_{TETA} is the net molecular mass increase by triethylene tetramine carbamate (172.23 g mol^{-1}):

$$\mathrm{DS_{TETA}} = \frac{M_2 \dfrac{\Delta f(4)}{\Delta f(2)} - M_2}{M^*_{TETA}}$$

The change in frequency from −186 to −236 Hz could be interpreted as DS$_{TETA}$ 0.68. Thus, the conversion of the 1*H*-imidazole-1-carboxylate into the functional carbamate is about 80%. IR spectroscopy does not show C=O vibration of the imidazolide and thus, hydroxyl groups are regenerated. The formation of covalent bonds could not be proven by FT-IR spectroscopy unambiguously due to the overlapping of signals arising from the ester- (1730 cm^{-1}) and the carbamate moieties. The C=O stretching vibration for cellulose carbamates is usually observed at 1710 cm^{-1}.[7] However, in the spectrum of the N1s scan (XPS) of sample **4** one peak at 399.5 eV, arising from amine groups is visible. Considering the elemental composition the DS$_{TETA}$ was found to be 0.65 calculated from the nitrogen content of the XPS measurements.

The treatment of polymer films (**2**), not CDI-activated, with TETA results in no significant frequency shift (Fig. 3, bottom), *i.e.* the blank tests show that no significant amounts of amine were adsorbed on the surface. Moreover, no nitrogen could be detected by XPS in the samples.
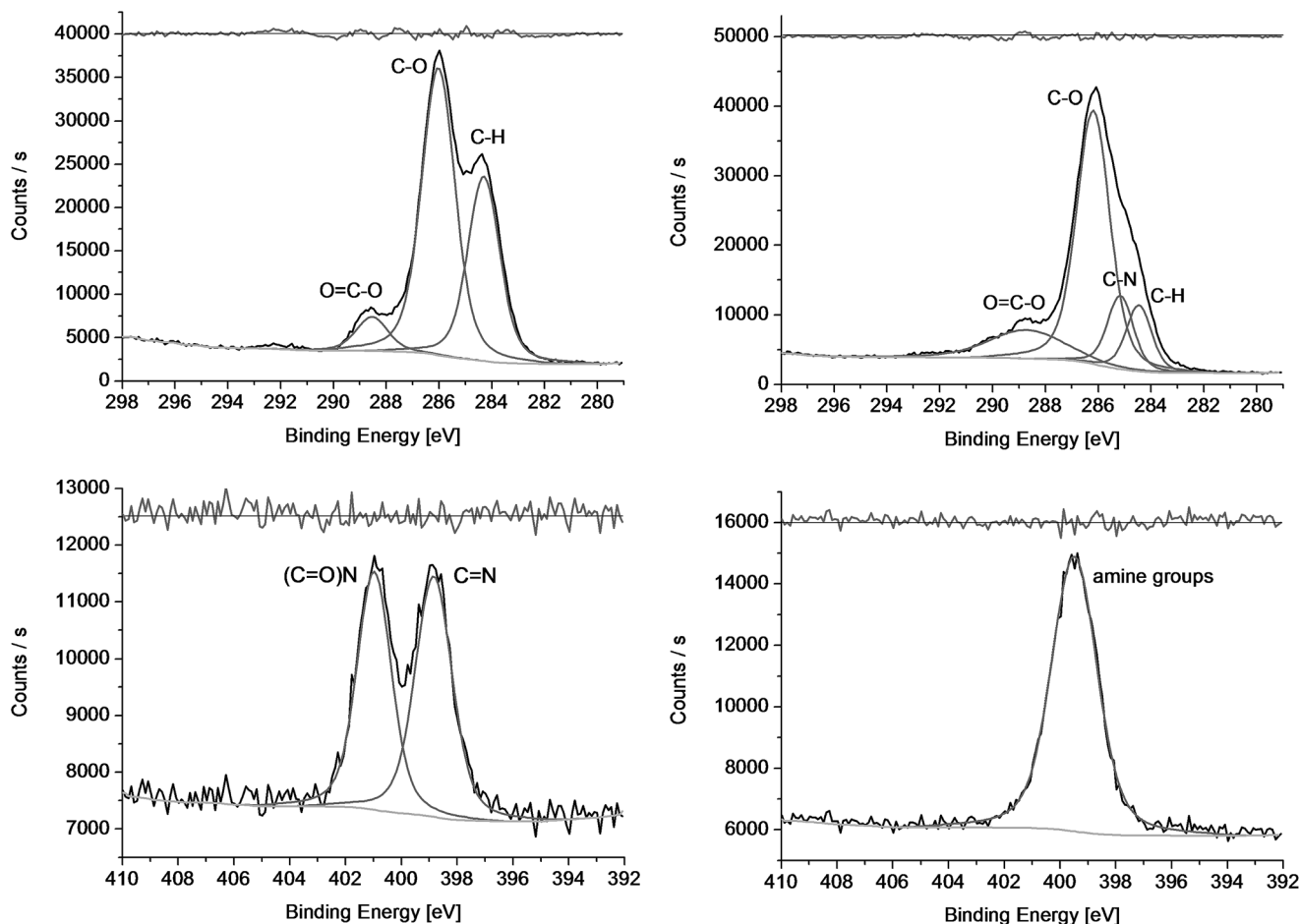
Fig. 5 Selected XPS results of thin films: C1s scan of hydroxyethyl cellulose furoate (2, top left), C1s scan of hydroxyethyl cellulose furoate 1*H*-imidazole-1-carboxylate (3, top right), N1s scan of 3 (bottom left), and N1s scan of hydroxyethyl cellulose furoate carbamate (4, bottom right); scans (black), fits (gray), residuals (offset, gray), background (light gray).

3.3.2 Change of surface properties. Furthermore, the post-modification of the thin films was detected by zeta-potential measurements using the principle of oscillating streaming potential.[24] A blank glass surface and the film of the cellulose derivatives (2, 3) show negative zeta potentials under alkaline and neutral conditions (Fig. 6). The negative zeta potential of these three materials can be caused by three effects. Adsorbed anions from the electrolyte solution, negatively charged carboxyl moieties from oxidized cellulose and dissociated sila-nol groups in the case of blank glass. The results are in accordance with literature.[29,30] The isoelectric point appears in acid medium due to the protonation of functional groups. However, zeta-potential measurements are appropriate to evidence the aminolysis with TETA. By this reaction amino groups are introduced in the thin film and a covalent carbamate linkage is formed. The obtained film (4) possesses a high density of amino groups resulting in a positive zeta potential, which increases
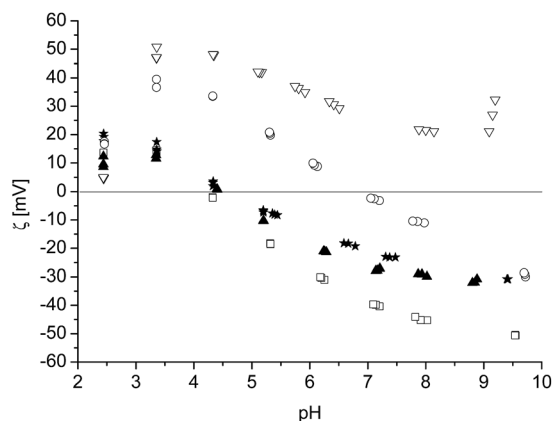

Fig. 6 Zeta-potential (oscillating streaming potential) in dependence on pH value of thin films measured on glass slides: □ piranha-cleaned glass, ▲ hydroxyethyl cellulose furoate (2), ★ hydroxyethyl cellulose furoate 1*H*-imidazole-1-carboxylate (3), ○ blank sample (2 was treated with TETA), ▽ hydroxyethyl cellulose furoate carbamate (4).

Table 2 Showing degree of substitution (DS) by three independent techniques

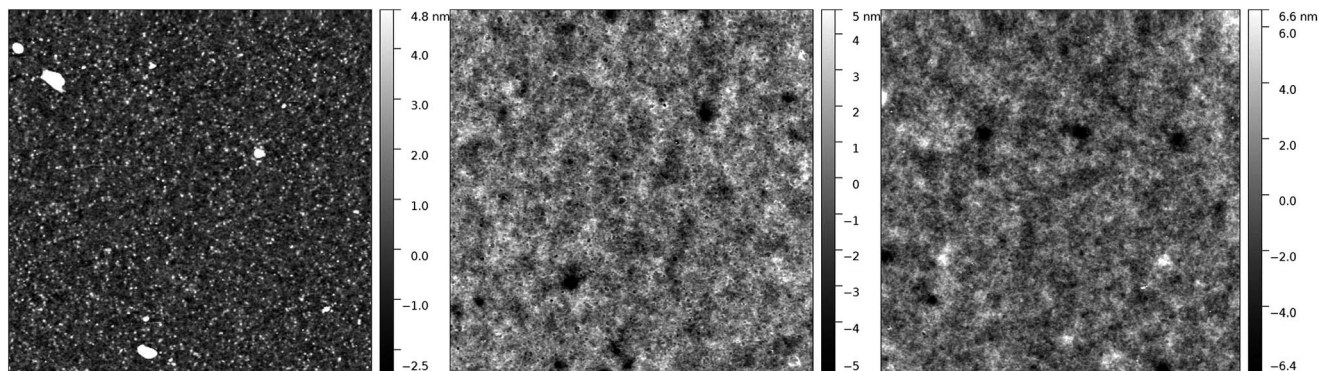| Sample	DS (QCM)	DS (IR)	DS (XPS)
3 (Im)	0.87 ± 0.06	0.96 ± 0.10	0.91 ± 0.01
4 (TETA)	0.68 ± 0.10	—	0.65 ± 0.03

Fig. 7 5×5 µm AFM images (height) of thin films of hydroxyethyl cellulose furoate **2** (left, rms 1.28 nm), hydroxyethyl cellulose furoate 1*H*-imidazole-1-carboxylate **3** (center, rms 1.49 nm), and hydroxyethyl cellulose furoate carbamate **4** (right, rms 1.67 nm).

with decreasing pH value that is related to the pronounced presence of ammonium groups in acidic medium. The zeta potentials of film **4** are significantly higher than the values of the blank sample (TETA adsorbed to non-activated film **2**). However, a very small amount could be adsorbed to the blank sample due to electrostatic interactions of a few negatively charged carboxylic groups and the amino groups of TETA.

Considering the surface energies of the thin films there are slight changes after performing the surface reactions. All films are hydrophobic cellulose derivatives. The total surface energy of the film is 37 mN m^{-1} for hydroxyethyl cellulose furoate (**2**), 39 mN m^{-1} for the 1*H*-imidazole-1-carboxylate (**3**), and 44 mN m^{-1} for the carbamate (**4**).

The changes in surface morphology could be evaluated by atomic force microscopy (Fig. 7). The thin film of cellulose ester (**2**) is smooth and uniform but some small particles stick to the surface. The surface reactions in toluene lead to a porous structure and the particles are removed from the surface (Fig. 7 center, right). In accordance with QCM-D measurements leaching of loosely bound polymer chains take place. Nevertheless, the film thickness increases from 19.7 ± 0.5 nm *via* 28.8 ± 1.3 nm to 31.9 ± 2.1 nm during the reactions, determined by profilometry. Thus, the film is probably expanded by changing the morphology and bounding of substituents to the polymer chains (increase of mass).

4 Conclusions

In the present work, hydroxyethyl cellulose furoate with high DS was synthesized by a mild and chlorine-free esterification applying CDI. Thin films of the biopolymer derivative were obtained by spin coating. The furoate moieties may undergo reversible cross-linking by (Retro)-Diels–Alder reaction with bismaleinimides and thus, these films are promising in field of self-healing materials. However, this topic will be a subject of further studies. In order to design advanced materials, multi-functionality was achieved by post-modification of the remaining hydroxyl groups. Beyond cross-linkable furoate moieties 1*H*-imidazole-1-carboxylate groups could be integrated into the film applying CDI, which provides a reactive platform coating for

various biological species by aminolysis. The model amine TETA was studied representing an example for an inexhaustible pool of amino compounds that may be covalently bound to the surface. The degree of substitution (DS) of the thin films was determined by means of QCM-D and proven with IR-spectroscopy as well as XPS. Thus, the surface sensitive technique QCM-D was applied for the determination of the DS of cellulose-based thin films for the first time. The change of the surface properties was measured by means of oscillating streaming potential. SEM and AFM imaging showed changed surface morphologies. In principle, hydrophobic, hydrophilic, charged, or responsive surfaces may be designed according to this concept, which will be investigated in subsequent studies in context with application as functional biomaterials. For example, self-healing films with antifouling properties could be used for coating of medical instruments. Therefore, we aim at developing a method that avoids harmful solvents in order to reduce the toxicity of the material.

Acknowledgements

References

1 C. Zhao, L. Y. Li, M. M. Guo and J. Zheng, *Chem. Pap.*, 2012, **66**, 323–339.
2 M. Tanaka, A. P. Wong, F. Rehfeldt, M. Tutus and S. Kaufmann, *J. Am. Chem. Soc.*, 2004, **126**, 3257–3260.
3 G. Decher, *Science*, 1997, **277**, 1232–1237.
4 C. S. Peyratout and L. Dahne, *Angew. Chem., Int. Ed.*, 2004, **43**, 3762–3783.
5 S. V. Orski, K. H. Fries, S. K. Sontag and J. Locklin, *J. Mater. Chem.*, 2011, **21**, 14135–14149.
6 V. Thakur and A. Singha, *Surface Modification of Biopolymers*, Wiley, 2015.
7 T. Elschner, K. Ganske and T. Heinze, *Cellulose*, 2013, **20**, 339–353.

8 T. Elschner and T. Heinze, *Macromol. Biosci.*, 2015, **15**, 735–746.

9 C. Wang, R. A. Venditti and K. Zhang, *Appl. Microbiol. Biotechnol.*, 2015, **99**, 5791–5799.

10 M. Schaub, G. Wenz, G. Wegner, A. Stein and D. Klemm, *Adv. Mater.*, 1993, **5**, 919–922.

11 T. Mohan, R. Kargl, A. Doliška, A. Vesel, S. Köstler, V. Ribitsch and K. Stana-Kleinschek, *J. Colloid Interface Sci.*, 2011, **358**, 604–610.

12 J. Eriksson, M. Malmsten, F. Tiberg, T. H. Callisen, T. Damhus and K. S. Johansen, *J. Colloid Interface Sci.*, 2005, **284**, 99–106.

13 S. M. Notley and L. Wagberg, *Biomacromolecules*, 2005, **6**, 1586–1591.

14 T. Elschner, F. Scholz, P. Miethe and T. Heinze, *Macromol. Biosci.*, 2014, **14**, 1539–1546.

15 R. Kargl, V. Vorraber, V. Ribitsch, S. Köstler, K. Stana-Kleinschek and T. Mohan, *Biosens. Bioelectron.*, 2015, **68**, 437–441.

16 M. I. Montanez, Y. Hed, S. Utsel, J. Ropponen, E. Malmstrom, L. Wagberg, A. Hult and M. Malkoch, *Biomacromolecules*, 2011, **12**, 2114–2125.

17 J. Ax and G. Wenz, *Macromol. Chem. Phys.*, 2012, **213**, 182–186.

18 C. M. Nimmo, S. C. Owen and M. S. Shoichet, *Biomacromolecules*, 2011, **12**, 824–830.

19 M. Andersson, J. Andersson, A. Sellborn, M. Berglin, B. Nilsson and H. Elwing, *Biosens. Bioelectron.*, 2005, **21**, 79–86.

20 T. Elschner, A. Doliška, M. Bračič, K. Stana-Kleinschek and T. Heinze, *Carbohydr. Polym.*, 2015, **116**, 111–116.

21 F. Hook, M. Rodahl, P. Brzezinski and B. Kasemo, *Langmuir*, 1998, **14**, 729–734.

22 S. Hornig, T. Liebert and T. Heinze, *Macromol. Biosci.*, 2007, **7**, 297–306.

23 T. Mohan, R. Kargl, A. Doliška, H. M. A. Ehmann, V. Ribitsch and K. Stana-Kleinschek, *Carbohydr. Polym.*, 2013, **93**, 191–198.

24 M. Reischl, S. Köstler, G. Kellner, K. Stana-Kleinschek and V. Ribitsch, *Rev. Sci. Instrum.*, 2008, **79**, 113902.

25 G. Sauerbrey, *Z. Phys.*, 1959, **155**, 206–222.

26 S. Alila, A. M. Ferraria, A. M. B. do Rego and S. Boufi, *Carbohydr. Polym.*, 2009, **77**, 553–562.

27 Y. Liu, T. T. Y. Tan, S. J. Yuan and C. Choong, *J. Mater. Chem. B*, 2013, **1**, 157–167.

28 Z. X. Xu, T. Li, Z. M. Zhong, D. S. Zha, S. H. Wu, Q. Liu, W. D. Xiao, X. R. Jiang, X. X. Zhang and J. T. Chen, *Biopolymers*, 2011, **95**, 682–694.

29 T. Ristić, T. Mohan, R. Kargl, S. Hribernik, A. Doliška, K. Stana-Kleinschek and L. Fras, *Cellulose*, 2014, **21**, 2315–2325.

30 C. Werner, U. König, A. Augsburg, C. Arnhold, H. Körber, R. Zimmermann and H. J. Jacobasch, *Colloids Surf., A*, 1999, **159**, 519–529.

SCIENTIFIC REPORTS

Direct-Write Fabrication of Cellulose Nano-Structures via Focused Electron Beam Induced Nanosynthesis

Thomas Ganner[1], Jürgen Sattelkow[1], Bernhard Rumpf[1], Manuel Eibinger[2], David Reishofer[3], Robert Winkler[4], Bernd Nidetzky[2,5], Stefan Spirk[3] & Harald Plank[1,4]

In many areas of science and technology, patterned films and surfaces play a key role in engineering and development of advanced materials. Here, we introduce a new generic technique for the fabrication of polysaccharide nano-structures via focused electron beam induced conversion (FEBIC). For the proof of principle, organosoluble trimethylsilyl-cellulose (TMSC) thin films have been deposited by spin coating on SiO_2 / Si and exposed to a nano-sized electron beam. It turns out that in the exposed areas an electron induced desilylation reaction takes place converting soluble TMSC to rather insoluble cellulose. After removal of the unexposed TMSC areas, structured cellulose patterns remain on the surface with FWHM line widths down to 70 nm. Systematic FEBIC parameter sweeps reveal a generally electron dose dependent behavior with three working regimes: incomplete conversion, ideal doses and over exposure. Direct (FT-IR) and indirect chemical analyses (enzymatic degradation) confirmed the cellulosic character of ideally converted areas. These investigations are complemented by a theoretical model which suggests a two-step reaction process by means of *TMSC → cellulose* and *cellulose → non-cellulose material* conversion in excellent agreement with experimental data. The extracted, individual reaction rates allowed the derivation of design rules for FEBIC parameters towards highest conversion efficiencies and highest lateral resolution.

Polysaccharides are a large class of biopolymers which exhibit a large structural and chemical diversity and, consequently, a variety of biological functions[1]. Among all polysaccharides, cellulose, a homopolymer of β-(1,4) linked D-glucose units, is of particular importance from both academic and industrial point of view. It is highly abundant since it is a major constituent of higher plant cell walls and some bacteria. Further, it offers a wide range of applications in many areas ranging from packaging, textiles, papers, housing to medicine, life sciences as well as advanced materials to mention just some examples[2–7]. In this context, cellulose nanomaterials such as nanofibrils, nanocrystals, aerogels or thin films have seen a tremendous rise during the past years, since it allowed materials scientists to shift polysaccharide materials from the micro- to the nanoscale world concomitant with new application areas of cellulosic materials[2]. However, for many applications (e.g. in electronics) thin films featuring well-defined patterns in the nanometer regime are required which are hardly realized so far for polysaccharides in general and cellulose in particular. A major problem in the processing of cellulose for this purpose is its poor solubility in common organic solvents. However, the use of soluble derivatives such as organosoluble trimethylsilyl cellulose (**TMSC**), which is converted to cellulose after the processing step via acid vapor hydrolysis, allows for a facile preparation of cellulose thin films. Introduced by Klemm and further developed by Kontturi, this method provides amorphous thin films with a flat and defined morphology in combination with easily adjustable film thickness ranging from a few nanometers to several micrometers[8,9]. Film properties have been exploited in numerous studies to elucidate the basic interaction principles of cellulose

[1]Institute for Electron Microscopy and Nanoanalysis, Graz University of Technology, Steyrergasse 17, A-8010 Graz, Austria. [2]Institute of Biotechnology and Biochemical Engineering, Graz University of Technology, Petersgasse 12, A-8010 Graz, Austria. [3]Institute for Chemistry and Technology of Materials, Graz University of Technology, Stremayrgasse 9, 8010 Graz, Austria. [4]Graz Centre for Electron Microscopy, Steyrergasse 17, A-8010 Graz, Austria. [5]Austrian Centre of Industrial Biotechnology, Petersgasse 14, A-8010 Graz, Austria. Correspondence and requests for materials should be addressed to S.P. (email: stefan.spirk@tugraz.at) or H.P. (email: harald.plank@felmi-zfe.at)

with other biomolecules such as proteins, DNA and other polysaccharides but also allowed for investigations into the interaction of cellulose with water[10–21]. However, in order to provide a convenient platform for integration in electronics, bio-sensing or diagnostic applications another key demand must be met: the defined lateral pre-structuring of cellulose on the macro-, micro- and nanoscale. First protocols were demonstrated by Tanaka et al.[22] who employed UV etching of regenerated cellulose films to create macro and micrometer sized pads as protein supports. However, a drawback of this approach is its intrinsic destructive nature creating defects at the edges of the patterns[22], which negatively impacts the performance at very small feature sizes. Later, Spirk et al. and Werner et al.[23] reported macrostructured cellulose pads derived from TMSC[24,25]. The patterning was achieved by applying a metal mask having holes onto the TMSC films during the acid vapor hydrolysis[24,25] or by using a novel lift-off technique to remove specific cellulose areas with a PEI coated cation stamp[23]. Cellulose microstructures using a combination of soft lithography and enzymes have been realized by Kargl et al. who used a microstructured mold having micrometer sized channels in combination with enzymes[25]. By pressing the mold onto the cellulose thin film and subsequent deposition of cellulose digesting enzymes micrometer patterns were obtained.[25] However, a major drawback is that large areas are difficult to pattern and further the procedure is rather laborious and difficult to upscale. To overcome this issue, an impressive study[26] was presented using photocatalytic regeneratoin of a TMSC/N-hydroxynaphtalimide triflate (**NHNA**) blend. At wavelengths higher than 300 nm (**UV**) photolysis of NHNA yields triflic acid. Thereby, the acidic proton performs nucleophilic attack of the TMS-O bond and leads to re-substitution to cellulose. Photo-regeneration proved to be a feasible method to obtain structures in the micrometer range and below. Additionally, two-photon lithography (**TPA**) was demonstrated at the same system which resulted in feature sizes of approx. 600 nm. Although simple in principle, the large feature size and traces of remaining NHNA might be detrimental for specific applications. Another approach to produce larger patterns within short times was introduced by Taajamaa et al.[27] by using a polysaccharid/polysterene blend. Although this technique allows fast and large scale structuring it slightly lacks lateral position control and size fidelity. In particular, applications in microelectronics[28,29,30], sensors[31–35] and nanofluidics[36] require the possibility to generate nanostructures below 100 nm. A recent study by Taskei et al.[37] which used a different cellulose based resist material showed that electron lithography on cellulose-derivates is a feasible method to fabricate, e.g., nanostructured masks for semiconductor industry and demonstrates the significance for industry.

Based on this motivation, we here demonstrate a highly localized, direct conversion of TMSC layers into cellulose via a nano-sized focused electron beam as used in classical scanning electron microscopes (**SEM**). The conversion effect resembles the basic principle of e-beam lithography where the electron beam chemically changes a thin photo-resist[38–40]. Depending on the resist type (positive or negative), the exposed areas are removed or remain on the surface via a wet chemical process. In our approach the focused electron beam directly transfers TMSC into cellulose. After removal of the unexposed regions via a final wet-chemical process, cellulose structures remain on the surface with features sizes below 100 nm. The study first focuses on the proof-of-principle by 1) using cellulose specific enzymes and atomic force microscopy (**AFM**) to quantitatively access converted cellulose; and 2) apply Fourier Transform Infrared (**FT-IR**) spectroscopy to gain more detailed chemical information of ideally converted regions. Next, a detailed parameter sweep during fabrication is presented which reveals three different regimes during conversion: *1)* incompletely converted, *2)* ideally converted, and *3)* over exposed. The gathered data is then combined with a theoretical model which explains the observed regimes and allow determination of ideal process parameters for efficient and chemically ideal conversion. The final part focuses on the downscaling which reveals that this method is indeed capable to produce cellulose structures in the sub−100 nm regime via this direct write conversion approach.

Results and Discussion

Preliminary Experiments.   During the last decade direct-write nanofabrication via focused electron beam induced deposition (**FEBID**) has attracted considerable attention[41–43]. This technology uses gaseous precursor molecules which absorb on practically any given surface in a classical SEM vacuum chamber. The interaction between these molecules and the focused electron beam leads to a highly localized chemical dissociation and immobilization which forms the functional deposit with spatial nanometer resolution. Similar in principle, electron beam lithography uses electron sensitive resists like poly(methyl methacrylate) (PMMA)[44] to achieve a structuring mask for a later development process. As a positive resist, electron irradiation causes degradation of PMMA in fragments of low molecular weight. It is conceivable that similar processes may be used to regenerate TMSC to cellulose. Traditionally, TMSC regeneration is achieved by use of acidic or basic reagents which catalyze the de-silylation of TMSC into cellulose via hydrophilic attack at the central silicon atom. During this process, volatile trimethylsilanol (TMSiOH) and hexamethyldisiloxane (TMSi$_2$O) are formed which can leave the films as suggested by Kontturi et al.[7,45]. On films, this reaction has been readily explored using a variety of techniques, either *in-situ* (QCM-D, GI-SAXS) or *ex-situ* (XRR, ATR-IR, wettability measurements, XPS)[9,17,46–48]. In the case of electron induced regeneration, the process still requires nucleophilic attack at the central silicon atom which may state a bottleneck as the reactive species have to be generated within the film. To bypass this problem we initially used a humid low vacuum atmosphere for preliminary experiments. The interaction of the beam and the water molecules may lead to dissociation and nucleophilic attack similar to the acidic reagents. For completeness we performed the same experiments in a high vacuum and thus water free environment (detailed results can be found in supplement 1). In brief, we achieved a contrary result to the proposed and hypothesized better regeneration under humid low vacuum atmosphere. We showed that using low vacuum conditions including water is rather detrimental to the process which primarily is caused by the so called curtaining effect. On the other hand, high vacuum conditions revealed that TMSC may be regenerated only by the interaction with the electron beam. A significant change in film height seen as a change of interference color is visible for the high vacuum patterns after application of cellulases (see supplement 1). We so far can only speculate about the exact mechanisms of the
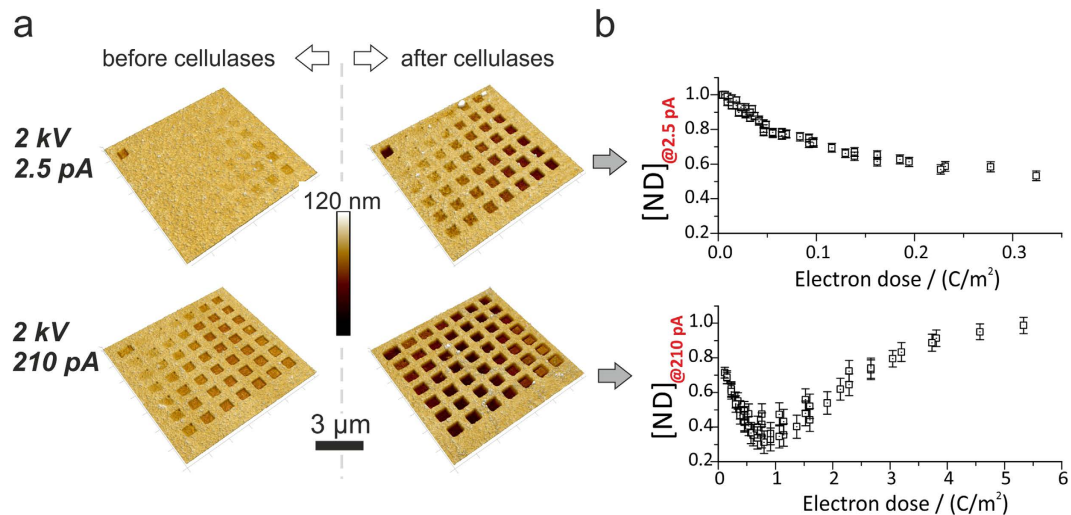
Figure 1. (**a**) AFM height images of test patterns before (left) and after enzyme exposure (right) for low and high beam currents of 2.5 pA (top) and 210 pA (bottom), respectively (2 keV primary energy). The different fields correspond to different electron doses via DT and frame number variations (see supplement 2). (**b**) Summary of the degraded volume fraction after enzyme exposure in dependency on the applied dose (see supplement 2). Note, this relative representation has been chosen for further correlation with the theoretical model.

generation of the protons required for the nucleophilic attack but it seems likely that the nucleophile is provided from the TMS moiety itself after cleavage. As proposed by Royall *et al.*[49] for water, electron beam interaction with in particular organic matter produces a large number of reactive compounds including protons needed for regeneration. As the TMS moiety is rich in hydrogen this process seems to be the likely cause of the regeneration in high vacuum. Despite the necessity to get a clearer understanding of process associated chemistry, we first have to unravel the relevant process parameters. From here on, we denote the process as Focused Electron Beam Induced Conversion (**FEBIC**) and provide a detailed process parameter study and its conversion implications in the following.

Parameter Space.   Based on the above mentioned observations, we transferred the FEBIC process to a dual-beam instrument (NOVA 200, FEI, The Netherlands) which provides a high-performance patterning engine for precise control of process parameters in order to determine ideal conditions for full conversion. Variables of interest are electron energy or beam voltage (U_{Beam}), beam current (I_{Beam}), pixel dwell-time (**DT**) and the pixel point-pitch (**PP**) between two consecutive patterning points. To allow comparable calculation of the applied electron doses, we kept the PP equal to 50% beam overlap in dependence on the beam diameter (see supplement 2 and 3). For each set of U_{Beam} and I_{Beam} (12 combinations in total) a 7×7 matrix of $1 \times 1\,\mu m^2$ fields has been structured on 100 nm thick TMSC films on SiO_2 / Si (5 nm / bulk) substrates with a systematic variation of DTs and frame-numbers (exact layout can be found in supplement 2). Subsequently, the structured films were immediately subjected to AFM imaging in ambient conditions for reference measurements (a graphical work-flow diagram concerning the experimental strategy can be found in supplement 2). Afterwards, the samples were exposed to a cellulase cocktail (produced by Hypocrea jeronica sp.) for 24 hours at 30 °C. (see experimental section for details). Finally, AFM was used again for detailed morphological characterization to quantify the bio-degraded material. To exclude the possibility of water swollen cellulose, respective films were carefully dried before post-incubation AFM measurements. Please note that Rehfeldt and Tanaka[51] demonstrated in dynamic experiments that film height is conserved before and after waters swelling. Figure 1a shows AFM height images of a parameter matrix before (left) and after enzyme incubation (right) structured at 2 keV beam energy with low (2.5 pA; Fig. 1a top) and high beam currents (210 pA; Fig. 1a bottom). The first remarkable detail is a dose dependent volume loss directly after patterning (left images). This is in agreement with previous findings by Kontturi and Lankinen[47] which reported a volume loss of up to 50% due to the loss of larger TMS groups upon regeneration to cellulose. The second detail is the clear volume loss after enzymatic incubation (right images) which has been quantified in a relative fashion (Fig. 1b). Here, each enzyme degraded pattern is normalized to its former height, thus specifying the amount of non-degradable (**ND**) material. Figure 1b shows the relative volume loss in dependency on the applied electron dose calculated from the constant process parameters I_{Beam}, PP and the variable DT. As evident, there is a clear minimum for the high-current sample (Fig. 1b; bottom) slightly below $1\,C/m^2$ electron dose followed by an increase, which indicates that higher doses might over-convert the TMSC into ND materials (discussed in detail later). For the lower beam current (Fig. 1b; top) we see no minimum but a steadily decreasing branch which, however, simply stems from too low doses ($<1\,C/m^2$) presumably required for ideal conversion (see 210 pA experiments). To investigate whether this behavior is generally valid, we expanded the experiments (*structuring → AFM → incubation → AFM*) to all combinations of U_{Beam}, I_{Beam}, PPs and DTs.

Figure 2 summarizes the results and shows the absolute height losses after enzyme exposure in dependence on the applied doses. Please note, as different beam energies imply different penetration depths of the electrons
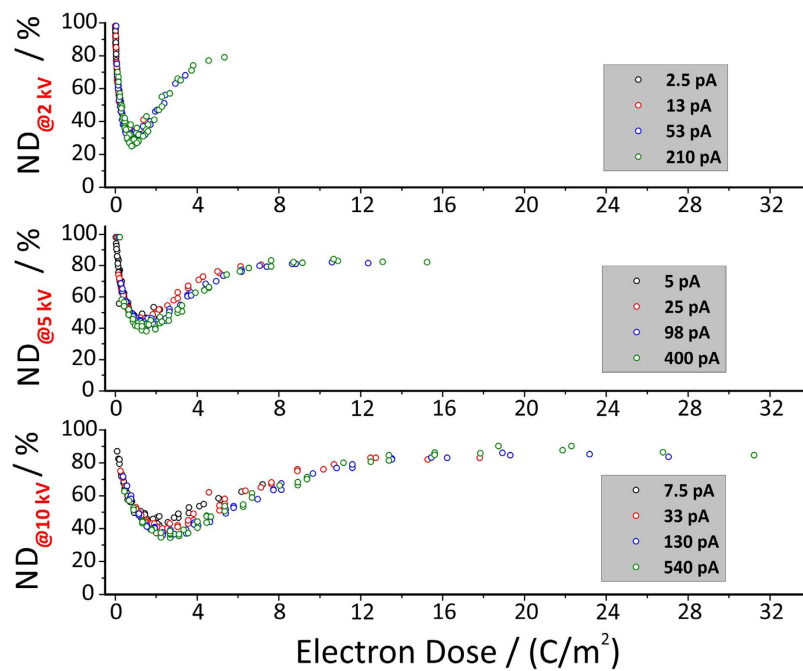
Figure 2. Absolute height loss after enzymatic incubation for 24 hours at 30 °C specifying the evolution of non-degradable material (ND). As evident, for a given primary electron energy U_{Beam} the behavior is predominantly dose dependent and barely affected by different beam currents and / or patterning parameters. The residual height, even at optimal doses, represents a characteristic feature of the presented approach as a consequence of simultaneously concurrent chemical reactions by means of TMSC → cellulose (wanted) and cellulose → non-degradable material (unwanted) as described in the main text.

the graphs have been separated accordingly. As evident from the results, each minimum mainly depends on the applied dose (at same primary energies) and is widely independent on the used beam currents and patterning parameters. It is known from literature that the applied enzyme cocktail is incapable to degrade TMSC with a substitution grade larger than 0.5[26]. Therefore, we can draw 2 conclusions: *1)* the electron beam indeed converts TMSC into cellulose with *2)* an dose dependent conversion efficiency. Although the degradation effect itself is a very strong indication for a successful *TMSC → cellulose* conversion[26,52], further evidence is required that the intermediate product is pure cellulose. Therefore, we conducted FT-IR spectroscopy investigations on $200 \times 200\,\mu m^2$ structured cellulose patches which have been structured at optimal doses (10 kV, 130 pA, 800 ns DT). Figure 3 shows spectra of TMSC (top, black), ideally converted FEBIC cellulose (center, red) and over-cured films (bottom, blue). The latter were exposed to a 30 fold electron dose and show no resemblance with the optimal cured patches (red). As expected no bands for the -O-H vibration are found in the over cured films while an increase in C=C vibrational bands is observed. This is in well agreement with the hypothesized beam damage of the formerly regenerated cellulose. The optimal dose patterns show a well resolved cellulose spectrum with the typical -O-H and -C-O-C bands[53,54]. More strikingly, however, is the absence of any TMSC residues which finally confirms full conversion into cellulose via focused electron beams in agreement with the enzymatic degradation experiments. Please note, FEBIC processes are only ideal for patterning fields up to a few tens of microns. Hence, the investigated regions are first small and second very thin which explains the low signal-to-noise ratio in the spectra.

In summary, direct chemical measurement and indirect enzymatic degradation show that optimally regenerated material is indeed cellulose without impurities from TMSC. Now, we can reconsider Fig. 2 and classify the observed behavior into 3 conversion regimes: *1)* electron-limited-regime (**ELR**) for low doses which lead to incompletely converted TMSC; *2)* optimum-regime (**OR**) for ideal conversion; and *3)* electron-excess-regime (**EER**) for high electron doses. First, we discuss the EER regime which converts the TMSC in non-degradable ND material (towards zero volume loss in Fig. 2). We attribute this over-conversion to classical electron beam damage of polymers[55–57] which is a well-known problem in electron-microscopy. Due to the strong evidences that ideal doses convert TMSC into cellulose (OR), it logically follows, that for very low doses an incomplete conversion takes place. This is consistent with the reduced height loss at low doses as the applied enzymes are incapable to degrade TMSC with a degree of substitution (DS) higher than 0.5[26]. Concerning the conversion itself, we refer to fundamental processes during FEBID processes, where low-energy electrons cause radiolysis of precursor molecules to a deposited and intended material[41–43]. TMSC usually requires acidic components to resubstitute the TMS moieties by hydrogen[46,58]. For FEBIC processes we hypothesize, that ionization effects and thus secondary electron generation provide a sufficient amount of H$^+$ for re-substitution. Here, further investigations are clearly needed to identify the responsible effects and origin of the required proton, which, however, is not in conflict with the present work as we have provided the evidence that the intermediate product is cellulose. The final detail to be explained concerns the increasing ideal electron dose for increasing beam energies as evident in Fig. 2. It is well
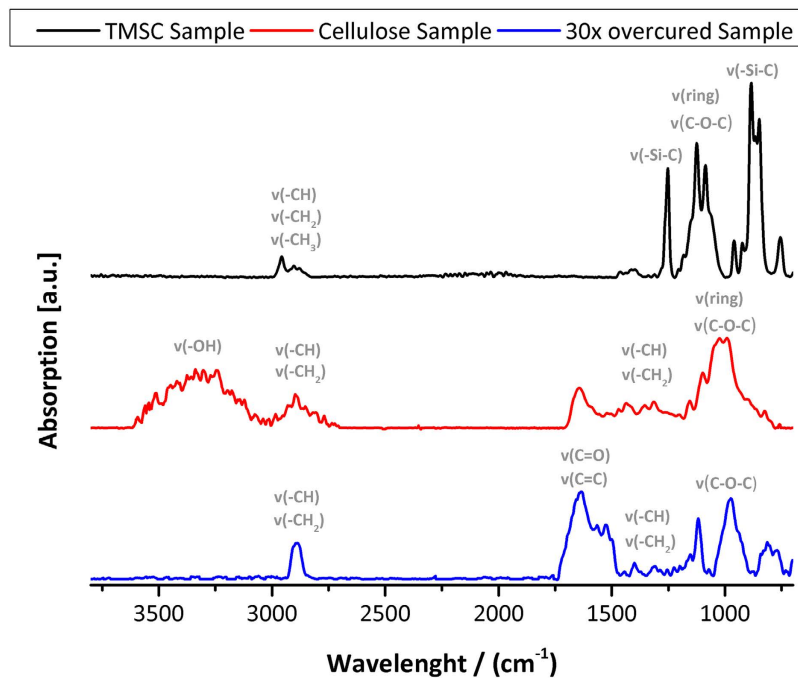
Figure 3. ATR-IR spectra of TMSC and focused electron beam processed cellulose films. The TMSC spectra after spin coating is shown on top (black) with clearly identifiable -Si-C bands at 849–883 cm^{-1} and 1252 cm^{-1}. After ideal conversion (center, red), no –Si-C bands are visible and clear cellulose bands at 3303 cm^{-1} (-OH) and 990–1032 cm^{-1} (-C-O-C-; -C-O-) are found. Dedicated experiments via 30 fold over-conversion (bottom; blue) proves the significant beam damage to the former generated cellulose structure. Here as proposed, no cellulose typical -O-H bands are visible. Spectra were obtained via a total of 1024 scan on a 100 x 100 x 0.6 μm^3 patch on gold covered SiO$_2$ substrates. The extremely low amount of material accounts for the low signal to noise ratio.
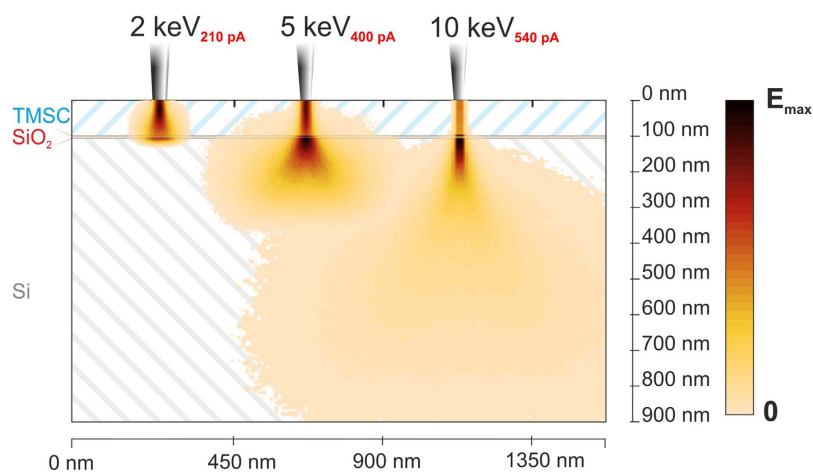
Figure 4. Monte Carlo simulation[59] of deployed energy for 2, 5, and 10 keV electrons in the x-z plane. The color of each pixel is the cumulative sum over the y-coordinate of deployed energy within this pixel. For 2 keV approximately 72.5% of the primary energy are deployed within the TMSC layer; For 5 keV and 10 keV primary energy this factor is reduced to 33.7% and 12.8%, respectively, which is in good agreement with the scaling factor of required doses for ideal conversion Fig. 2. Please note, backscattered electrons are not included in this visualization for more clarity.

known that higher primary electron energies entail higher penetration depths and feature larger so called interaction volumes. As a consequence, the content of "available" electrons within the TMSC film is decreasing for higher electron energies. Fig. 4 shows a Monte Carlo simulation of the mean energy loss in each pixel weighted with the electron energy at entry (Casino 2.48, Universite de Sherbrooke, Canada)[59]. The graph illustrates the situation for a 100 nm thick TMSC film on SiO$_2$ / Si (5 nm / bulk) substrate in a cross-sectional view. While for 2 keV electrons most electrons of a single pulse remain in the TMSC layer, a majority of 10 keV electrons are found in the substrate. More detailed calculations reveal an energy loss in TMSC of 72.5% for 2 keV while 33.7% and 12.8% were
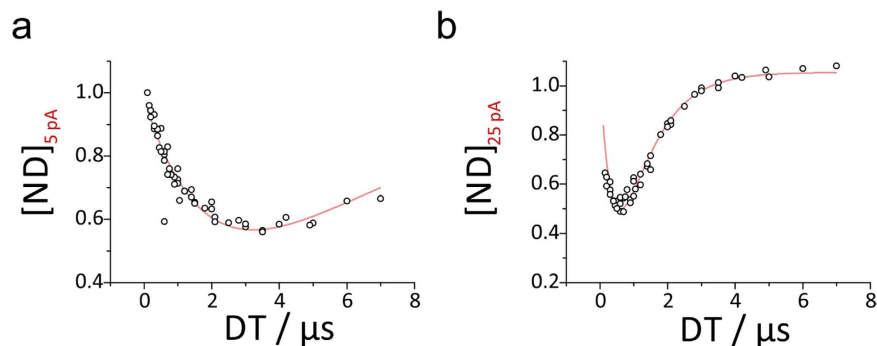
Figure 5. Experimental data of non-degraded material for 5 keV electrons at 5 pA (**a**) and 25 pA (**b**) beam current. The fit is shown in red and describes experimental data considerable well. Tabulated values of fit parameters and similar curves for each pair of U_{Beam} and I_{Beam} may be found in supplementary Table S3–S4 and supplementary Figure S4–S7.

found for 5 keV and 10 keV electrons, respectively. This roughly correlates with the scaling factor for increasing optimal doses in Fig. 2. Please note, for an exact determination, the dissociation cross-section of TMSC would be needed which is not available to date. Please note, a definite number concerning the ideal primary electron energy cannot be given as this criteria depends on the TMSC film thickness. To provide values as a starting point for successful reproduction, supplement 6 gives a table of minimum electron energies in dependency on the initial TMSC film thickness.

Conversion Process. In conclusion, the systematic characterization suggests a two phase process: *1)* conversion TMSC → cellulose; and *2)* cellulose → non-degradable carbon rich material which might be written in a two-step chemical formula:

$$TMSC + e_{acc}^- \rightleftharpoons_{k_{1-}}^{k_{1+}} \ cellulose + e_{acc}^- \rightleftharpoons_{k_{2-}}^{k_{2+}} \ Carbon \tag{1}$$
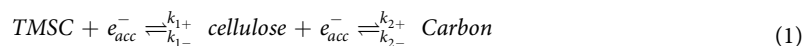
As a matter of fact, reaction constants k_{1-} and k_{2-} may be neglected as these are not likely to happen. Furthermore, electrons are constantly supplied by the electron beam and thus not diminished during individual beam pulses (DT)[60]. Such reactions may be described by pseudo-first order chemical reactions[60]. Using this formalism (full derivation can be found in supplement 4) we can deduce physical relevant fitting functions to obtain valuable parameters:

$$[ND] = a_1 + a_1 \cdot \frac{b_1}{b_1 - b_2}(e^{-b_1 \cdot t} - e^{-b_2 \cdot t}) \tag{2}$$

Here, a_1, b_1 and b_2 are fitting parameters and correspond to the normalized concentration of TMSC and to products of rate constants k_{1+} and k_{2+} with the concentration of electrons, respectively. The intention to shape this equation this way is the possibility to fit experimental curves in Fig. 4. Formulation of equation (2) bases on an assumed similar concentration of conversion relevant electrons for both reaction phases. This assumption is justified as the increasing material density is compensated by the volume loss during conversion as shown by Kontturi, Lankinen and Ehmann *et al.*[47]. Briefly, they used X-ray reflectivity to determine the increase of density from 0.99 g/cm³ to 1.51 g/cm³ and the corresponding decrease of film thickness by 50% during the regeneration of TMSC with hydrochloric acid vapors. The same data was used in Monte Carlo simulations as depicted in Fig. 4 and showed that energy loss within TMSC and denser but thinner cellulose films differ only by a few percent. *Hence, b_1 and b_2 are directly related to k_1 and k_2.* Applying now equation (2) to experimental data as shown in Fig. 1b, we can fit the curves to achieve the corresponding parameters and thus test the proposed two-phase process (equation (1)) on its validity. Figure 5 representatively shows such fits for 5 keV electrons for low (5 pA, (a)) and higher beam currents (25 pA, (b)). As evident, the proposed function (equation (2)) describes experimental data exceptionally well over all three regimes for 5 keV but also holds for all other pairs of U_{Beam} and I_{Beam} as shown in detail in supplement 4 (supplementary Figure S3–S6). Concluding, these results show the validity of the presented mathematical model of a two phase process. While we have already shown before that the intermediate and desired product is cellulose, beam damage also present from the beginning renders a fraction of the exposed materials non-degradable. The assumption of a carbon-rich residue at high doses is feasible as similar processes in FEBID and dedicated studies have been shown in literature[57,61]. The fitting model provides valuable information on the *rate-constants* and *reaction-speeds* (full summary can be found in supplement 4). Particularly interesting are the parameters b_1 and b_2 which are equivalent to reaction-rate constants for the first (TMSC → cellulose) and the second process (cellulose → ND carbon-rich material). Figure 6 shows both parameters against the current density for all beam energies used. Please note, a plot against the beam current may lead to misleading results, as each current has different beam profiles. First thing to notice is that both parameters (b_1 and b_2 in (a) and (b), respectively) saturate for higher current densities. This is expectable due to a limited number of relevant bonds in the TMSC / cellulose films which at some point is exceeded by the number of introduced electrons. Thus, fastest rates are achieved at current densities close to the transition point while higher doses provide much more electrons
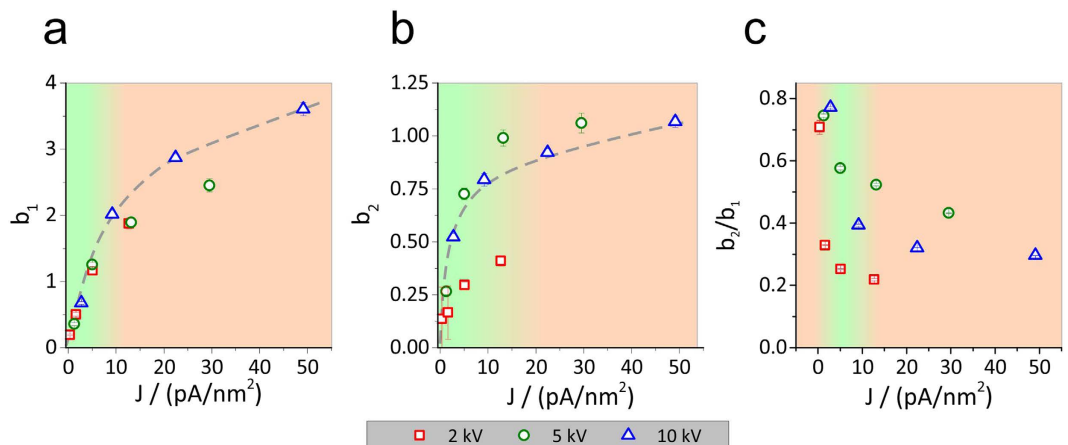
Figure 6. Fitting data for parameters b_1, b_2 and the ratio of b_2 / b_1 plotted against the current density. Data for b_1 and b_2 may be related to the reaction rate and shows that b_1 is significantly higher than b_2 which is extremely important for successful regeneration to cellulose. Moreover, exceeding current densities of 10 to 15 pA/nm^2 shows saturation tendencies for b_1 and b_2, respectively, which is expectable concerning the limited number of reaction sites.

than required and initiate EER conditions with strong formation of ND carbon material. For the TMSC → cellulose reaction (b_1 and thus k_1), this threshold lies around 15 pA/nm^2 while a value of about 10 pA/nm^2 is found for the proposed cellulose → ND carbon reaction (b_2 and k_2).

Several more and conclusive details can be extracted from these graphs. First, it is evident that absolute values of b_1 are much higher than for b_2 (~factor 3). This not only means that TMSC → cellulose reactions are faster but also explains the asymmetric behavior in Fig. 2. Second detail is that, although b_1 reaches larger values, the increase of b_2 is significantly faster. This provides evidence for radiation damage as soon as cellulose fragments are available. This nicely explains why it was not possible to degrade 100% of the structured fields as can be seen in Fig. 2. In this respect it is of advantage to consider the ratio b_2/b_1 which reflects the balance between both reactions. Figure 6c shows this ratio in dependency on the used beam current densities for different primary energies. As evident, the lowest values are found for lowest primary beam energies, which means, that the first and intended reaction (TMSC → cellulose) is dominating. This is in consistency with the observation that 2 keV structures resulted in highest volume losses (see Fig. 2). This is also the first indication that lower energies seem to be more appropriate for a fast and more complete conversion into cellulose. Please note, the exact value of the primary energy ultimately depends on the TMSC layer thickness which should be in the same range as the vertical interaction volume dimension (see supplement 6). Thus thicker films should be structured with tuned primary beam energy which can be evaluated by the use of Monte Carlo simulations (Casino 2.48; Fig. 4)[59]. Another detail in Fig. 6c is the observation that all b_2/b_1 ratios decrease with higher beam currents. This means that very low currents entail higher contents of unwanted ND carbon generation and therefore should be avoided. Although minor, this effect can nicely be seen in Fig. 2 for 10 keV structures where lowest currents lead to less degradable cellulose. Hence, in summary with data from Fig. 6a,b where saturation is found after approximately 10–15 pA/nm^2, we can state from a chemical point of view, that lower beam energies and intermediate beam currents are beneficial concerning the ideal cellulose conversion. With this elaborate and comprehensive analysis of reaction kinetics, reaction yield and evaluation of the corresponding chemistry, we proceeded by evaluating the highest attainable resolution.

Downscaling. For this purpose, we designed different patterns via black / white bitmaps which were further converted into interlacing stream files for direct use with the dual beam patterning engine[62–64]. To test the resolution capabilities, pattern geometries as depicted in Fig. 7 have been chosen together with process parameters of 2 keV primary electron energy, 53 pA beam current and DTs of 1500 ns to achieve ideal doses at optimum b_2/b_1 conditions. The decreasing line and space widths allow accurate analyses of the minimum distance of two un-structured areas and line-widths in between. Figure 7a shows the structured areas after patterning (top) and after enzymatic degradation (bottom). Multiple measurements on several samples revealed full-width-at-half-maximum (FWHM) line- and space widths of below 70 nm and 200 nm, respectively, as representatively shown by cross-sectional profiles in Fig. 7b (taken from indicated regions in Fig. 7a). These values can be rationalized by taking the back scattered electrons (**BSE**) into account as well. For structuring points at the pattern edge, this electron species leads to an intrinsic broadening effect as indicated by the brown shading in Fig. 7b (1). The exact broadening width is determined by the layer chemistry (TMSC) and the applied primary energy as studied in detail by Schmied *et al.* and Arnold *et al.*[65,66] for FEBID nano-structures. Hence, BSE proximity effects ultimately limit the achievable resolution for unstructured areas (Fig. 7b (1)). In contrast, fully converted regions can be made much smaller as BSE effects are of minor relevance for the patterned regions as confirmed via the cross-sectional profile in Fig. 7b (2). This immediately implies that lowest primary electron energies have to be used to minimize the BSE related broadening effect for highest lateral resolution. However, the thickness of the
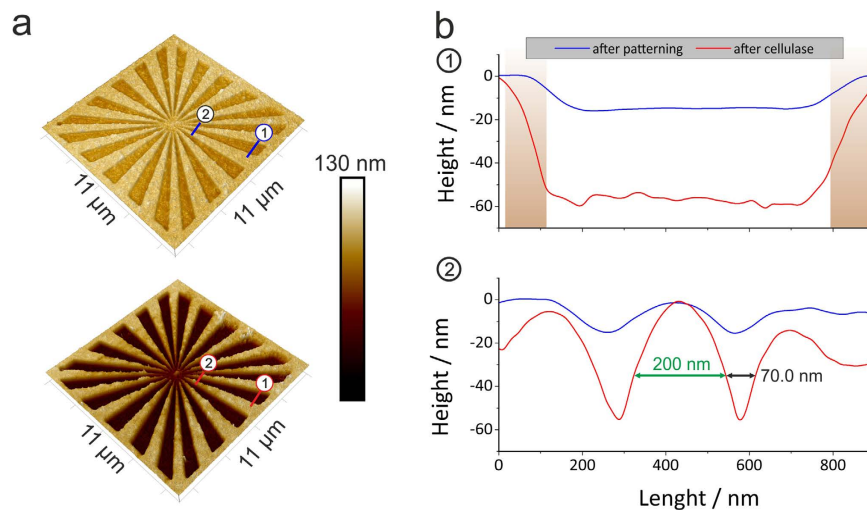
Figure 7. A FEBIC structured TMSC film visualized by AFM (**a**) imaging before (top) and after enzymatic treatment (bottom). In (**b**) section profiles near the center (2) show the minimal line width of 70 nm and a minimum distance of 200 nm. Near the edge (1) BSE effects lead to edge broadening effects as evident by the comparison of patterned and enzyme treated section lines (see brown shading).

TMSC layer has to be taken into account in such a way that the according interaction volume should entirely penetrate the precursor layer as shown in Fig. 3 for the 2 keV situation (see supplement 6). Lower energies would lead to unaffected TMSC regions at the bottom. In contrast, higher energies lead to electron-substrate interactions which entail substrate related BSE effects which further decrease the achievable lateral resolution (detailed analyses is found in supplement 5). By that, it can be stated that highest lateral resolution is achieved when the vertical dimension of the interaction volume fits to the TMSC layer thickness. This simply requires an initial simulation to find ideal primary electron energies with respect to the TMSC layer of interest. Concerning the ultimate FEBIC resolution it is expectable that very thin films might allow feature sizes below 100 nm for both line and space. The chemical limit might be given by the length of a typical cellulose chain which typically consist of hundreds of unit moieties leading to edge roughening (intrinsic limit).

Conclusions

In this study, we introduced focused electron beam induced conversion (FEBIC) as a feasible, mask-less, direct-write method to convert a cellulose precursor (TMSC) into cellulose with lateral resolution in the sub−100 nm regime. During conversion, we identified three regimes denoted as *electron-limited*, *optimal-* and *electron-excess-regime* (ELR, OR, EER). While ELR is characterized by incomplete TMSC → cellulose conversion, EER conditions lead to non-degradable (ND), non-cellulosic material due to overexposure. In the OR regime maximum regeneration of TMSC into cellulose is established as confirmed by direct and indirect experiments using FT-IR and enzymatic degradation, respectively. An elaborate modeling of the corresponding reaction mechanisms using pseudo-first order kinetics revealed a two-step conversion by means of *TMSC → cellulose* and *cellulose → ND materials*. The correlation with experimental data not only revealed excellent agreement but also allowed a deeper insight in reaction dynamics. It was found that lowest possible energies and intermediate beam currents are best suited for fastest conversion rates and highest volumetric conversion degree. Although in well agreement with experimental data, the exact reaction mechanisms are yet not understood in detail. In similarity to electron induced radical formation on water molecules[49], FEBIC is likely to cause multiple reaction pathways including silyl radicals, trimethylsilanol and hexamethyldisiloxane. Therefore, further studies are required to unravel the corresponding reaction products for a comprehensive process understanding. Finally, downscaling experiments revealed that converted areas below 100 nm can be achieved for ideal settings. A more detailed look further strengthened the demand for lowest possible primary electron energies to prevent any proximity effects from the underlying substrate. By that this study introduced a new approach for the defined structuring of cellulose with sub−100 nm resolution for the combination with electronic devices, microfluidic arrays, small scale bio-sensors or diagnostic tools. Finally, it should be mentioned that the structuring of chitin based films is now feasible which show a slightly different but highly interesting chemistry[67] for fundamental research.

Methods

Materials. All used materials and chemicals have been purchased in highest available purity unless otherwise stated. Pre-cut silicon wafers (10×10 mm^2) with 5 nm SiO$_2$ were kindly provided by AMS AG (Unterpremstätten, Austria). Glass vials (4 mL, Ø 15 mm, Rotilabo), microscopy slides, 2-propanol, ethanol (analytical grade, not denatured) and xylol were purchased from Carl Roth (Karlsruhe, Germany). Trimethylsilyl-cellulose (TMSC, DP = 2.8) was purchased from Thüringisches Institut für Textil- und Kunstoff-Forschung (TITK e.V, Germany).

Preparation of Trimethylsilyl-cellulose films.   Cellulose films were prepared according to protocols from literature[7,58]. Briefly, $20\,mg\cdot ml^{-1}$ of TMSC were dissolved in xylol and transferred to a sonification bath (Transsonic T560, Elma Schmidbauer GmbH, Germany) and treated until no residual particles were observable (typically 15 min). The resulting solution was drawn into a syringe and filtered through a nitro-cellulose filter with a nominal pore size of $5\,\mu m$ into a new capped glass vial. In a next step, silicon wafers (AMS AG, Unterpremstätten, Austria) were carefully removed in a flow box to prevent contamination with dust and transferred to the spin-coater (Laurell ws-650-S7-6NPP/LITE, Laurell Technologies Corporation, NW, USA). Approximately one hundred to two hundred μl of solution were pulled up into a glass pipette and transferred onto the silicon specimen, followed by immediate spin-coating. Parameters were: An acceleration period of 4 seconds to 3600 rpm, followed by constant spinning for further 25 seconds to ensure complete evaporation of the solvent. Specimens were removed from the coater and stored until further use in Parafilm sealed petri-dishes.

Focused electron induced regeneration.   TMSC thin film specimens were positioned on a conventional SEM holder (Ø 10 mm) by double sided adhesive carbon tape. A FIB Nova 200 microscope (FEI Company, The Netherlands) was used for the patterning of the TMSC thin films. Optimal parameter range was analyzed according Table S1 and Figure S2 as specified also in the results section. Here U_{Beam}, I_{Beam}, DT and PP were varied to find a set of optimal patterning parameters. Once optimal parameters were available, the patterning was performed as follows: For each structure, conventional drawing tools (CorelDraw X6, Corel Corporation, Canada) were used to design a black/white bitmap image with the corresponding non-patterend/patterned points, respectively. The image was then processed by the recently introduced SIL engine to gain a corresponding stream file[62]. Briefly, this engine was specially designed to minimize the thermal stress during FIB processing which is of essential relevance for low melting materials such as (bio-) polymers. Patterns were then structured in the specimens by the FIB patterning engine. Please note that the structuring was applied in "blind" mode as each electron would lead to regeneration effects. In this context the e-beam was blanked immediately before and after patterning within 20 ns. After patterning, specimens were removed from the vacuum chamber and stored in Parafilm capped petri-dishes for further characterization or further processing.

Enzymatic hydrolysis.   Complete cellulase system of *Hypocrea jeronica* mutant SVG 17 was prepared according to protocol from literature[68]. All hydrolysis experiments were performed using 2 ml of 50 mM sodium citrate buffer (pH 5.0) and $300\,\mu l$ of the cellulose supernatant (0.1 FPU/ml). Hydrolysis was performed at elevated temperatures (30 °C) and for 24 hours to ensure complete conversion of degradable material. Preliminary experiments confirmed complete degradation after a maximum time of 19 hours (the major part was already degraded after about 2 hours). Afterwards, specimen was carefully rinsed with deionized water for 5 minutes, followed by CO_2 spray drying.

Attenuated total reflection infrared spectroscopy (ATR-IR).   For ATR-IR experiments, silicon wafer specimens were preliminary covered with a 10 nm layer of chromium followed by 100 nm of gold. TMSC films were then prepared and structured according to the procedures above. For ATR-IR experiments an area of approximately $100 \times 100\,\mu m^2$ was fully regenerated by the electron beam at the optimal parameters (U = 2 kV; I = 53 pA; DT = 1200 ns; P = 1; $PP_{@50\%overlap}$ = 10.4 nm). The experiments were performed with an ALPHA FT-IR spectrometer (BRUKER; MA, USA). For the measurement an attenuated total reflection (ATR) attachment was used with 48 scans at a resolution of $4\,cm^{-1}$ and a scan range between 4000 and $400\,cm^{-1}$. The data were analyzed with OPUS 4.0 software.

Atomic force microscopy.   AFM investigations were carried out using a FastScan Bio AFM microscope (Bruker AXS, CA, USA) operated by a Nanoscope V controller. For all investigations FastScan C cantilevers (Bruker AXS, Santa Barbara, CA / USA) with nominal spring constants of 0.8 N/m and a tip radius of 5 nm were used. Experiments were conducted under ambient conditions at an air conditioned temperature of 20 °C. Films were analyzed in negative or positive structured manner, that is with still present TMSC layer or without, respectively. In order to produce the positive structures, films were immersed in xylol for 2 minutes prior to AFM measurement in order to remove the TMSC. For negative structured films carful scratching with ultra-sharp tweezers allowed a reference to the underlying silicon for height measurement. Setpoints, scan rates and controlling parameters were chosen carefully to ensure lowest possible energy dissipation to the sample and to exclude tip driven artifacts. Data analysis of images was performed using Nanoscope Analysis 1.50 (Build R2.103555, Bruker AXS, CA, USA) and Gwyddion 2.38 (Released 2014-09-18, http://gwyddion.net/). All images were plane fitted at 1st order unless otherwise stated.

References

1. Klemm, D., Philipp, B., Heinze, T., Heinze, U. & Wagenknecht, W. Comprehensive Cellulose Chemistry: Volume I: Fundamentals and analytical Methods. *Methods* **I,** 260 (1998).
2. Eichhorn, S. J. *et al.* Review: Current international research into cellulose nanofibres and nanocomposites. *J. Mater. Sci.* **45,** (2010).
3. Habibi, Y., Lucia, L. A. & Rojas, O. J. Cellulose Nanocrystals : Chemistry. Self-Assembly. and Applications. *Chem. Rev.* **110,** 3479–3500 (2010).
4. Moon, R. J., Martini, A., Nairn, J., Simonsen, J. & Youngblood, J. Cellulose nanomaterials review: structure, properties and nanocomposites. *Chem. Soc. Rev.* **40,** 3941–3994 (2011).
5. Olsson, R. T. *et al.* Making flexible magnetic aerogels and stiff magnetic nanopaper using cellulose nanofibrils as templates. *Nat. Nanotechnol.* **5,** 584–588 (2010).
6. McKee, J. R. *et al.* Healable, stable and stiff hydrogels: Combining conflicting properties using dynamic and selective three-component recognition with reinforcing cellulose nanorods. *Adv. Funct. Mater.* **24,** 2706–2713 (2014).
7. Kontturi, E., Tammelin, T. & Osterberg, M. Cellulose-model films and the fundamental approach. *Chem. Soc. Rev.* **35,** 1287–1304 (2006).

8. Schaub, M., Wenz, G., Wegner, G., Stein, A. & Klemm, D. Ultrathin films of cellulose on silicon wafers. *Adv. Mater.* **5,** 919–922 (1993).

9. Kontturi, E., Thüne, P. C. & Niemantsverdriet, J. W. (Hans). Cellulose Model Surfaces - Simplified Preparation by Spin Coating and Characterization by X-ray Photoelectron Spectroscopy, Infrared Spectroscopy, and Atomic Force Microscopy. *Langmuir* **19,** 5735–5741 (2003).

10. Orelma, H., Filpponen, I., Johansson, L. S., Laine, J. & Rojas, O. J. Modification of cellulose films by adsorption of cmc and chitosan for controlled attachment of biomolecules. *Biomacromolecules* **12,** 4311–4318 (2011).

11. Orelma, H., Johansson, L. S., Filpponen, I., Rojas, O. J. & Laine, J. Generic method for attaching biomolecules via avidin-biotin complexes immobilized on films of regenerated and nanofibrillar cellulose. *Biomacromolecules* **13,** 2802–2810 (2012).

12. Orelma, H., Teerinen, T., Johansson, L. S., Holappa, S. & Laine, J. CMC-modified cellulose biointerface for antibody conjugation. *Biomacromolecules* **13,** 1051–1058 (2012).

13. Mohan, T. *et al.* Cationically rendered biopolymer surfaces for high protein affinity support matrices. *Chem. Commun.* (Camb). **49,** 11530–11532 (2013).

14. Mohan, T. *et al.* Triggering Protein Adsorption on Tailored Cationic Cellulose Surfaces. *Biomacromolecules* **15,** 3931–3941 (2014).

15. Kittle, J. D. *et al.* Equilibrium water contents of cellulose films determined via solvent exchange and quartz crystal microbalance with dissipation monitoring. *Biomacromolecules* **12,** 2881–2887 (2011).

16. Kontturi, E. *et al.* Amorphous Characteristics of an Ultrathin Cellulose Film. *Biomacromolecules* **12,** 770–777 (2011).

17. Ehmann, H. M. A. *et al.* Surface-Sensitive Approach to Interpreting Supramolecular Rearrangements in Cellulose by Synchrotron Grazing Incidence Small-Angle X-ray Scattering. *ACS Macro Lett.* **4,** 713–716 (2015).

18. Kontturi, K. S., Kontturi, E. & Laine, J. Specific water uptake of thin films from nanofibrillar cellulose. *J. Mater. Chem. A* **1,** 13655 (2013).

19. Tenhunen, T. M. *et al.* Significance of xylan on the stability and water interactions of cellulosic nanofibrils. *React. Funct. Polym.* **85,** 157–166 (2014).

20. Niinivaara, E., Faustini, M., Tammelin, T. & Kontturi, E. Mimicking the Humidity Response of the Plant Cell Wall by Using Two-Dimensional Systems: The Critical Role of Amorphous and Crystalline Polysaccharides. *Langmuir* **32,** 2032–2040 (2016).

21. Azzam, F. *et al.* Reversible modification of structure and properties of cellulose nanofibril-based multilayered thin films induced by postassembly acid treatment. *Langmuir* **31,** 2800–2807 (2015).

22. Tanaka, M., Wong, A. P., Rehfeldt, F., Tutus, M. & Kaufmann, S. Selective Deposition of Native Cell Membranes on Biocompatible Micropatterns. *J. Am. Chem. Soc.* **126,** 3257–3260 (2004).

23. Werner, O., Persson, L., Nolte, M., Fery, A. & Wågberg, L. Patterning of surfaces with nanosized cellulosic fibrils using microcontact printing and a lift-off technique. *Soft Matter* **4,** 1158 (2008).

24. Spirk, S. *et al.* Surface modifications using a water-stable silanetriol in neutral aqueous media. *ACS Appl. Mater. Interfaces* **2,** 2956–2962 (2010).

25. Kargl, R. *et al.* Functional patterning of biopolymer thin films using enzymes and lithographic methods. *Adv. Funct. Mater.* **23,** 308–315 (2013).

26. Wolfberger, A. *et al.* Photolithographic patterning of cellulose: a versatile dual-tone photoresist for advanced applications. *Cellulose* 717–727, doi: 10.1007/s10570-014-0471-4 (2014).

27. Taajamaa, L., Rojas, O. J., Laine, J., Yliniemi, K. & Kontturi, E. Protein-assisted 2D assembly of gold nanoparticles on a polysaccharide surface. *Chem. Commun.* (*Camb*). **49,** 1318–1320 (2013).

28. Yun, S., Jang, S. D., Yun, G. Y., Kim, J. H. & Kim, J. Paper transistor made with covalently bonded multiwalled carbon nanotube and cellulose. *Appl. Phys. Lett.* **95,** (2009).

29. Fujisaki, Y. *et al.* Transparent nanopaper-based flexible organic thin-film transistor array. *Adv. Funct. Mater.* **24,** 1657–1663 (2014).

30. Seo, J.-H. *et al.* Microwave flexible transistors on cellulose nanofibrillated fiber substrates. *Appl. Phys. Lett.* **106,** 262101 (2015).

31. Mahadeva, S. K. & Kim, J. Conductometric glucose biosensor made with cellulose and tin oxide hybrid nanocomposite. *Sensors Actuators, B Chem.* **157,** 177–182 (2011).

32. Montañez, M. I. *et al.* Bifunctional dendronized cellulose surfaces as biosensors. *Biomacromolecules* **12,** 2114–2125 (2011).

33. Kim, J.-H., Mun, S., Ko, H.-U., Yun, G.-Y. & Kim, J. Disposable chemical sensors and biosensors made on cellulose paper. *Nanotechnology* **25,** 092001 (2014).

34. Credou, J. & Berthelot, T. Cellulose: from biocompatible to bioactive material. *J. Mater. Chem. B* **2,** 4767 (2014).

35. Qi, H., Mäder, E. & Liu, J. Unique water sensors based on carbon nanotube-cellulose composites. *Sensors Actuators, B Chem.* **185,** 225–230 (2013).

36. Zhang, C., Shao, P. G., van Kan, J. a. & van der Maarel, J. R. C. Macromolecular crowding induced elongation and compaction of single DNA molecules confined in a nanochannel. *Proc. Natl. Acad. Sci. USA.* **106,** 16651–16656 (2009).

37. Takei, S. *et al.* Inedible cellulose-based biomass resist material amenable to water-based processing for use in electron beam lithography. *AIP Advances 5,* **077141,** 1–8 (2015).

38. Owen, G. Electron lithography for the fabrication of microelectronic devices. *Reports Prog. Phys.* **48,** 795–851 (1999).

39. Ito, T. & Okazaki, S. Pushing the limits of lithography. *Nature* **406,** 1027–1031 (2000).

40. Thompson, L. F. & Kerwin, R. E. Polymer Resist Systems for Photo- and Electron Lithography. *Annu. Rev. Mater. Sci.* **6,** 267–301 (1976).

41. Utke, I., Moshkalev, S. & Russel, P. *Nanofabrication Using Focused Ion and Electron Beams: Principles and Applications*. (Oxford University Press, 2012).

42. Van Dorp, W. F. & Hagen, C. W. A critical literature review of focused electron beam induced deposition. *J. Appl. Phys.* **104,** (2008).

43. Van Dorp, W. F., Hansen, T. W., Wagner, J. B. & De Hosson, J. T. M. The role of electron-stimulated desorption in focused electron beam induced deposition. *Beilstein J. Nanotechnol.* **4,** 474–480 (2013).

44. Duan, H. *et al.* Sub-10-nm half-pitch electron-beam lithography by using poly(methyl methacrylate) as a negative resist. *J. Vac. Sci. Technol. B Microelectron. Nanom. Struct.* **28,** C6C58 (2010).

45. Mohan, T. *et al.* Enzymatic digestion of partially and fully regenerated cellulose model films from trimethylsilyl cellulose. *Carbohydr. Polym.* **93,** 191–198 (2013).

46. Mohan, T. *et al.* Watching cellulose grow – Kinetic investigations on cellulose thin film formation at the gas–solid interface using a quartz crystal microbalance with dissipation (QCM-D). *Colloids Surfaces A Physicochem. Eng. Asp.* **400,** 67–72 (2012).

47. Kontturi, E. & Lankinen, A. Following the kinetics of a chemical reaction in ultrathin supported polymer films by reliable mass density determination with X-ray reflectivity. *J. Am. Chem. Soc.* **132,** 3678–3679 (2010).

48. Mohan, T. *et al.* Exploring the rearrangement of amorphous cellulose model thin films upon heat treatment. *Soft Matter* **8,** 9807–9815 (2012).

49. Royall, C. P., Thiel, B. L. & Donald, A. M. Radiation damage of water in environmental scanning electron microscopy. *J. Microsc.* **204,** 185–195 (2001).

50. Ganner, T. *et al.* Dissecting and reconstructing synergism: *in situ* visualization of cooperativity among cellulases. *J. Biol. Chem.* **287,** 43215–43222 (2012).

51. Rehfeldt, F. & Tanaka, M. Hydration forces in ultrathin films of cellulose. *Langmuir* **19,** 1467–1473 (2003).

52. Bash, E. Biological degradation of cellulose derivatives. *Ind. Eng. Chem.* **1,** 89–93 (2015).

53. Köhler, S., Liebert, T. & Heinze, T. Interactions of Ionic Liquids with Polysaccharides. VI. Pure Cellulose Nanoparticles from Trimethylsilyl Cellulose Synthesized in Ionic Liquids. *J. Polym. Sci. Part A Polym. Chem.* **46,** 4070–4080 (2008).
54. Fengel, D. & Strobel, C. FtIR Spectroscopic Studies on the Heterogeneous Transformation of Cellulose I into Cellulose II. *Acta Polym.* **45,** 319–324 (1994).
55. Egerton, R. F., Li, P. & Malac, M. Radiation damage in the TEM and SEM. *Micron* **35,** 399–409 (2004).
56. Ohno, T., Sengoku, M. & Arii, T. Measurements of electron beam damage for organic crystals in a high voltage electron microscope with image plates. *Micron* **33,** 403–406 (2002).
57. Kitching, S. & Donald, A. M. Beam damage of polypropylene in the environmental scanning electron microscope: An FTIR study. *J. Microsc.* **190,** 357–365 (1998).
58. Kontturi, E., Thüne, P. C. & Niemantsverdriet, J. W. Novel method for preparing cellulose model surfaces by spin coating. *Polymer (Guildf)*. **44,** 3621–3625 (2003).
59. Drouin, D. *et al.* CASINO V2. 42 — A Fast and Easy-to-use Modeling Tool for Scanning Electron Microscopy and Microanalysis Users. *Scanning* **29,** 92–101 (2007).
60. Housecroft, E. C. & Constable, C. E. In *Chemistry* (*Easton*). 1285 (Pearson Educatin Limited, 2006).
61. Geier, B. *et al.* Rapid and Highly Compact Purification for Focused Electron Beam Induced Deposits: A Low Temperature Approach Using Electron Stimulated H 2 O Reactions. *J. Phys. Chem C* **118,** 14009–14016 (2014).
62. Orthacker, A. *et al.* Chemical degradation and morphological instabilities during focused ion beam prototyping of polymers. *Phys. Chem. Chem. Phys.* **16,** 1658–1666 (2014).
63. Schmied, R., Chernev, B., Trimmel, G. & Plank, H. New possibilities for soft matter applications: eliminating technically induced thermal stress during FIB processing. *RSC Adv.* **2,** 6932 (2012).
64. Schmied, R. *et al.* A combined approach to predict spatial temperature evolution and its consequences during FIB processing of soft matter. *Phys. Chem. Chem. Phys.* **16,** 6153–6158 (2014).
65. Schmied, R., Fowlkes, J. D., Winkler, R., Rack, P. D. & Plank, H. Fundamental edge broadening effects during focused electron beam induced nanosynthesis. *Beilstein J. Nanotechnol.* **6,** 462–471 (2015).
66. Arnold, G. *et al.* Fundamental resolution limits during electron induced direct write synthesis. *ACS Appl. Mater. Interfaces* **6,** 7380–7387 (2014).
67. Kittle, J. D. *et al.* Ultrathin Chitin Films for Nanocomposites and Biosensors. *Biomacromolecules* **13,** 714–718 (2012).
68. Bubner, P., Dohr, J., Plank, H., Mayrhofer, C. & Nidetzky, B. Cellulases dig deep: *in situ* observation of the mesoscopic structural dynamics of enzymatic cellulose degradation. *J. Biol. Chem.* **287,** 2759–2765 (2012).

Acknowledgements

Author Contributions

H.P. and T.G. designed the research. T.G., B.R., J.S. and R.W. performed FIB and AFM experiments and analyzed the data. D.R. and S.S. performed FT-IR experiments and data analysis. M.E. and B.N. provided enzymes, helped with the discussion and revised the manuscript. T.G., S.S. and H.P. wrote the paper.

Additional Information

Supplementary information accompanies this paper at http://www.nature.com/srep

Competing financial interests: The authors declare no competing financial interests.

How to cite this article: Ganner, T. *et al.* Direct-Write Fabrication of Cellulose Nano-Structures via Focused Electron Beam Induced Nanosynthesis. *Sci. Rep.* **6**, 32451; doi: 10.1038/srep32451 (2016).